NASA Experimental Program to Stimulate
Competitive Research

South Carolina

Cooperative Agreement
NCC5-643

Final Report

June 30, 2004

Table of Contents

Management and Coordination

MANAGEMENT AND COORDINATION

The South Carolina NASA/EPSCoR program, Grant Number NCC5-643, transferred from the University of South Carolina (USC) to the South Carolina Research Authority (SCRA), effective April 1, 2002. The SC EPSCoR State Committee and the SC Space Grant Consortium continued to implement the project management plan developed at the beginning of the grant (under NCC5-174) to provide consistent, efficient, and effective management of the NASA/EPSCoR program.

The SC EPSCoR State Committee maintained overall responsibility for grant management and the SCRA assumed fiscal responsibility of the grant. In November 2002, the State Office of the SC EPSCoR program moved into the same building occupied by the corporate offices of the SCRA. SCRA is a 501(c)(3) organization whose mission is focused on technology-based economic development. The SC Space Grant Consortium continued to aid in the development of outreach and evaluation initiatives for the NASA/EPSCoR research projects.

SC EPSCoR State Committee

During the final reporting period, the SC EPSCoR State Committee, consisting of representatives from academia, state government, and industry, attended biannual meetings to stay informed on federal solicitations and reports and discuss South Carolina's EPSCoR initiatives. John R. Raymond, MD, Vice President for Academic Affairs & Provost at the Medical University of South Carolina, serves as Chair of the State Committee.

Through an Executive Committee, the State Committee provided direction and oversight for the NASA/EPSCoR grant through monthly conference calls to Larry Druffel, PhD, Project Director, and the State Office of the SC EPSCoR program. The Committee assigned full management responsibility for the NASA/EPSCoR program to both Dr. Druffel and Mitchell Colgan, PhD, SC Space Grant Consortium Director. Scott Little, PhD, SC EPSCoR State Manager, and Tara Scozzaro, MPA, SC Space Grant Consortium Program Manager, assisted in the administration of the NASA/EPSCoR program.

SC NASA/EPSCoR Program Management

Effective April 1, 2002, Dr. Druffel, State Director of the SC EPSCoR program, began serving as the SC NASA/EPSCoR Project Director. Dr. Druffel is responsible for implementing the terms and conditions of the cooperative agreement and overseeing the grant's research activities, reporting to the State Committee and NASA. Drs. Little and Druffel met weekly to discuss NASA/EPSCoR activities and specific achievements.

NASA/EPSCoR program initiatives in South Carolina, in coordination with the SC Space Grant Consortium, were centrally managed from the State Office of the SC EPSCoR program, which operates through four full-time staff members, including Dr. Little, State Manager, a Fiscal Manager, a Program Manager, and an administrative assistant. One undergraduate student provides part-time assistance in administrative activities. The State Office staff provided centralized fiscal and program monitoring, implementation of outreach activities, and serve as a liaison to faculty and student participants.

The State Office worked closely with members of the state's Commission on Higher Education (CHE), representatives from the PhD granting institutions, and state congressional leaders to secure state funds to help meet the cost-share commitments required on active EPSCoR awards in the state. During the final reporting period, more than $350K in state matching funds were awarded to the research activities supported under this NASA/EPSCoR grant.

During the final reporting period, the State Office continued to maintain NASA/EPSCoR program data; updated the SC EPSCoR website; arranged logistics for meetings, conferences/workshops/

symposia, site reviews, and presentations to the SC General Assembly; prepared annual reports; established, maintained and monitored all federal and cost-share accounts; and managed review logistics for the participant support programs. These programs include seed funding for multi-institutional sustainable research clusters conducting research in support of NASA's strategic research areas, while simultaneously supporting SC EPSCoR goals. The SC EPSCoR program and the SC Space Grant Consortium announce the annual call for applications in early spring, with receipt of applications by late spring in the Space Grant Consortium office. The State Office of the SC EPSCoR program identifies and confirms at least three faculty with expertise in the technical area of the proposal to conduct a thorough review of the application by mail. The State Office sits a three-member panel to resolve any conflicts from the mail reviews, rank the proposals, and make funding recommendations.

SC Space Grant Consortium

The SC Space Grant Consortium and the SC EPSCoR State Committee worked closely to organize, plan, and manage South Carolina's NASA/EPSCoR program. Dr. Colgan and Ms. Scozzaro worked with Drs. Druffel and Little to oversee the progress of the program and assist in the evaluation and assessment of the research projects. The SC Space Grant Consortium continued to help integrate the NASA/EPSCoR program activities into its outreach and educational activities.

The SC Space Grant Consortium, through seminars and faculty exchanges, also disseminated information about EPSCoR-related research to institutions and scientists not presently involved in the NASA/EPSCoR program. Members of the SC EPSCoR State Committee and State Office were invited to attend SC Space Grant Consortium biannual meetings and were included on the consortium's mailing list to be kept abreast of the latest news and opportunities from NASA.

Project Milestones and Reporting

SC NASA/EPSCoR grant recipients adhered to several reporting requirements. In addition to submitting financial and technical progress reports, the SC Space Grant Consortium and the NASA/EPSCoR Directors prepared semi-annual progress reports for the SC EPSCoR State Committee. These reports included details on research tasks, projected milestones, resources to be used, and anticipated results, and were reviewed by the State Committee during their biannual meetings. In addition, the Principal Investigators (PIs) of the research activities were required to present a formal progress report to the State Committee on an annual basis and to provide periodic "bullets of achievement." These reports and achievement data served as a forum to review progress and plan for future activities.

During the final reporting period, Dr. Colgan continued to maintain a NASA/EPSCoR program file that serves as a reference tool for project staff, SC EPSCoR and Space Grant representatives, and NASA. This file contains copies of the grant instrument, copies of the technical and cost proposals, financial reports, progress reports, correspondence, meeting summaries, technical notes, and other related project information.

NASA/EPSCoR PIs prepared quarterly cost summary reports, which were used by Drs. Druffel and Little to track overall program status and to meet NASA disbursement reporting requirements. Dr. Little and his staff also identified expenditure trends, potential problem areas and their effects on the project timetable and funding schedule through these reports.

Subject Inventions: None

Inventory Report of Federally-Owned Property: None

SCRA®

Trident Research Center
5300 International Blvd.
North Charleston, SC 29418
TEL (843) 760-2700
http://www.scra.org

June 30, 2004

Diane Detroye, Technical Officer
NASA Headquarters, Code FE
Washington, DC 20546-0001

RE: South Carolina NASA EPSCoR Grant Number NCC5-643 Matching Funds Report

Dear Ms. Detroye:

Consistent with the Special Conditions of NASA Cooperative Agreement "South Carolina EPSCoR Grant" Number NCC5-643, the cost share commitment for the period 4/1/2002 – 3/31/2004 is $1,790,576.00.

To date, $1,791,056.79 non-federal funds have been matched to SC NASA EPSCoR Grant Number NCC5-643.

If you have any questions or need any additional information, please do not hesitate to contact K. Allyn Graham at 843-760-3235 or me at 843-760-3369.

Sincerely,

Jon P. Monson
Vice President
Chief Financial and
Administrative Officer

Development and Enhancement of Research Capability for Aircraft Structures and Materials

Summary Report for Year 5 Activity

University of South Carolina Cluster on Aeronautics

Dr. Michael A. Sutton, PI
Department of Mechanical Engineering
University of South Carolina
Columbia, SC 29208

Narrative

This is the final report for the USC portion of the 1996-2002 (1 year extension) South Carolina NASA EPSCoR program, with consortium agreement number NASA NCC-5-174. Even though recent changes within the NASA Langley Research center organization have resulted in major changes in focus for both our program and NASA Langley's areas of interest, without any doubt the USC portion of the EPSCoR program has been a complete success. In the last year of the program, the following areas have been the focus of our research activity work;

1. Damage Tolerance studies for friction stir welded joints (Michael Sutton, Anthony Reynolds)
2. Applications of 3D computer vision to structures (Michael Sutton, Jeffrey Helm, Stephen McNeill)
3. Mixed mode fracture experiments (Michael Sutton, John Ward)
4. Mixed mode fracture simulations through development of a computational predictive tool for general 3D crack simulations in aerospace structures (Michael Sutton, Xiaomin Deng, Jianzheng Zuo)
5. Development of 3D measurement tool for micro-scale structures (Michael Sutton, Dorian Garcia, Hubert Schreier)
6. Development of a 3D measurement tool for nano-scale structures (Michael Sutton, Hubert Schreier, Dorian Garcia)
7. Development of nano-scale pattern application methods (Michael Sutton, Wally Scrivens)
8. Development of molecular dynamic simulation capabilities (Xiaomin Deng)
9. Ultra high speed computer vision for deformation measurements during impact (Stephen R. McNeill, Michael Sutton)

Specifically, through the support provided by NASA EPSCoR, our faculty have developed national and international recognition in the following areas

Dr. Anthony Reynolds	Friction Stir Welding for Aerospace Structures
Dr. Michael Sutton	Computer vision for 2D and 3D deformation measurements in aero-structures

In addition, through the support provided by NASA EPSCoR, our faculty are beginning to develop national and international recognition in the following areas

Dr. Xiaomin Deng	Molecular Dynamic Simulations
Dr. Yuh Chao	Weld modeling
Dr. Stephen McNeill	High speed computer vision
Dr. Michael Sutton	Micro-scale and nano-scale measurement Technology

Below is a summary of the papers, faculty and students supported by NASA EPSCoR

Faculty:	*A.P. Reynolds*
	M.A. Sutton
	S.R. McNeill
	Wei. Zhao
	Xiaomin Deng
	J.S. Lyons
	M.A. Sutton
Staff:	*Daniel Wilhelm*
Post-doctoral fellows:	*Jianzheng Zuo*
	Bangcheng Yang
MS Students	*Ruiyun Wu (to graduate 8/2004*
	Robert Taylor (graduated 2002
	Ning Yuan (graduated 2003)
	Darin Lockwood (graduated 2001)
	Elmoiz Mahgoub (graduated 2003)
PhD Students:	*Hubert Schreier (graduated, 2003)*
	*Nicolas Cornille (graduates, 12/*2004)
	Paul Peterson (graduated, 2001)
	Weiming Lan (in progress)
	Yunhui Yan (graduated 2004)
	Peng Cheng (graduated 2001)

Scientific Accomplishments:

1. Three-dimensional Stress and Deformation Fields Around Flat and Slant Cracks Under Remote Mode I Loading Conditions (Mahgoub, Deng and Sutton)

The phenomenon of slant fracture observed in stable tearing tests of many ductile materials is investigated, where an initially flat crack, loaded under remote Mode I conditions, tends to grow into a slant crack and stay in the slant configuration until final fracture. In an effort to identify potential reasons why cracks prefer to grow in a slant manner, three-dimensional (3D) finite element analyses of crack-front stress and deformation fields in Arcan-type specimens containing a flat or slant crack are performed under elastic-plastic and remote Mode-I loading conditions. In particular, the crack-tip opening displacement (COD) at a position behind the crack tip, the mean stress, the effective stress, and a constraint factor (defined as the ratio of the mean stress and effective stress) are studied and compared for the two types of cracks.

Analysis results reveal several stress/deformation field variations around flat and slant cracks under identical remote loading conditions. First, close to the crack front, the COD of a slant crack is greater than that of a flat crack. Second, at the specimen's mid-plane, a flat crack leads to a higher constraint value ahead of the crack than a slant crack. Third, the effective stress ahead of a slant crack is greater than that ahead of a flat crack, especially close to the crack front. The above results seem to suggest that slant fracture may be preferred because a slant crack enhances the driving force in the form of a higher near-tip COD value and because a shearing type of failure is promoted in the case of a slant crack compared to a tensile type of failure in the case of a flat crack

2. A Novel Method to Investigate FRP Composite-Concrete Bond Toughness (Wan, Petrou, Harries, Sutton and Yang

A novel experimental method using modified double cantilever beam specimens and a customized test frame are introduced to evaluate bond characteristics and toughness of fiber reinforced polymer (FRP) composite overlays and a concrete substrate under mixed modes loading. A computer vision system is used to measure the crack location, near-tip deformations and crack opening displacement during the crack growth process. Digital image correlation is used to determine the crack opening displacement (***COD***) for flaws growing in the vicinity of the FRP-concrete interface.

Results from this study indicate that during crack growth, (a) the Mode I component of ***COD*** is dominant for all angles of specimen loading, (b) the magnitude of the local Mode I component of ***COD*** is maximized when good bond quality is present and crack extension occurs within the mortar/concrete near the FRP-concrete interface and (c) good agreement exists between independent energy release rate estimates based upon both an approximate elastic double cantilever beam formulation and also use of the measured components of ***COD*** in a classical linear elastic expression.

3. Basic studies of ductile failure processes and implications for fracture prediction (Zuo, Deng and Sutton)

Fracture of ductile materials has frequently been observed to result from the nucleation, growth and coalescence of microscopic voids. Experimental and analytical studies have shown that both the stress constraint factor and the effective plastic strain play a significant role in the ductile failure process. Experimental results also suggest that these two parameters are not independent of each other at failure initiation. In this study, a methodology for characterizing the effect of stress constraint (which is defined to be the ratio of the mean stress and the effective stress) on ductile failure is proposed. This methodology is based on experimental evidence that shows the effective plastic strain at failure initiation has a one-to-one relationship with stress constraint.

Numerical analyses based on plane strain and three-dimensional unit-cell models have been carried out to investigate failure initiation of the unit cell under different constraint conditions. Results from the numerical studies indicate (a) for each void volume fraction, there exists a local failure locus in terms of mesoscopic quantities, σ_m and σ_e, that adequately predict incipient local micro-void link-up, (b) the results are fully consistent with a failure criterion that maximizes mesoscopic effective stress for a constant level of constraint defined by the ratio $A_m = \sigma_m/\sigma_e$, (c) for high to moderate constraint A_m, the link-up envelope values for σ_m and σ_e are consistent with limit load conditions where the critical principal stress σ_{1c} corresponds to the maximum principal stress in the loading history and (d) for low constraint, the link-up envelope values for σ_m and σ_e correspond to link-up conditions having high levels of plastic strain and a principal stress σ_1 that is lower than the maximum value for this loading history.

Thus, the results suggest that a two-parameter ductile fracture criterion is plausible, such as critical crack opening displacement (COD) and constraint, for predicting the process of stable tearing in materials undergoing ductile void growth during the fracture process.

4. Deformations in wide, center-notched, thin panels: Part I: Three-dimensional shape and deformation measurements by computer vision (Helm, Sutton, McNeill)

The response of wide, thin, center-notched, 2024-T3 aluminum panels undergoing far-field tensile load is investigated. Three panels with a notch length to panel width of 0.33 and widths of 305 mm, 610mm and 1016 mm were subjected to far-field tensile loading. As part of the experimental program, two pairs of cameras were configured into separate stereovision systems and used to capture simultaneously both the global response of the sheet and the local response near a notch tip. Global areas, ranging in size from 250 mm x 250 mm to 550 mm x 550 mm, were imaged for each panel. A second stereo-vison system recorded images of a small area, 10 mm x 20 mm, ahead of one notch tip. Post-processing of the stereovision measurement data from global and local systems using three-dimensional digital image correlation was used to obtain the complete displacement field at each point in the region of interest.

In general, results demonstrate that the combination of stereovision and three-dimensional digital image correlation is capable of accurately measuring true, three-dimensional structural deformations in regions undergoing both large out-of-plane displacements and large displacement gradients. Furthermore, 3D measurements on the panel specimen near the grip location are shown to provide an independent assessment of the true boundary conditions, with specimen slippage clearly noted in the 1016mm specimen.

Results from the extensive notched, wide panel experimental program demonstrate that (a) each panel has an initial shape that deviates up to 3mm from planarity, with the greatest deviations occurring at the center of the notch, (b) the global load-displacement response is essentially linear for load levels that are well beyond the onset of large, out-of-plane displacements in the notch region, (c) increasing the size of the notched, thin panel specimen results in distinctly different surface deformations and deformed shapes, with three separate maxima/minima in the out-of-plane component of the largest panel and (d) local strain measurements near the termination hole are consistent with a plane stress condition. The region where tensile opening strains are above 2% extend several millimeters ahead of the hole, while compressive strains parallel to the notch direction are contained within a few millimeters of the hole. The in-plane shear strains are concentrated along circular lobes at +/-45° from the horizontal direction, a trend which is generally consistent with plane stress conditions.

5. Deformations in wide, center-notched, thin panels: Part II: Finite element analysis and comparison to experimental measurements (Helm, Sutton, McNeill)

For comparison to the experimental measurements, finite element analyses were performed for each panel. Results indicate that (a) for the 305-mm and the 610-mm panels, the finite element predictions and experimental measurements for two of the displacement components (U(x,y), W(x,y)) are in good agreement, with the finite element predictions for the grip displacement (V(x,y=L/2) being 5% lower than the measurements. For the 1016-mm panel, the finite element predictions did not match the experimental measurements; the full-field measurements demonstrated that the panel was slipped by 0.5 mm during the experiment, resulting in significant changes in the panel's deformation.

In summary, the results indicate that the FE method is effective in modeling the overall behavior of wide, flawed panels up to the onset of flaw growth. The combination of FEA and three-dimensional measurements for accurate prediction of displacement boundary conditions is shown to be a viable hybrid approach for predicting flawed panel response.

6. Advances in stereo light microscopy (Schreier, Garcia, Sutton)

The increasing research focus on small--scale mechanical systems has generated a need for deformation and strain measurement systems for micro--scale applications. Optical measurement systems, such as digital image correlation, present an obvious choice due to their non--contacting nature. However, the transfer of measurement technology developed for macro--scale applications to the micro--scale presents unique challenges due to the differences in the required high--magnification optics. This article illustrates the problems involved in calibrating a stereo microscope using traditional techniques and presents a novel methodology for acquiring accurate, three-dimensional surface shape and deformation data on small--scale specimens.

Experimental results demonstrate that stereo microscope systems can be accurately and reliably calibrated using \Latin{a priori} distortion estimation techniques in combination with traditional bundle-adjustment. The unique feature of the presented methodology is that it does not require a precision calibration target but relies solely on point correspondences obtained by image correlation. A variety of experiments is presented to illustrate the measurement performance of a stereo-microscope system. It is shown that the surface strains obtained from the full-field, three-dimensional measurements on tensile specimens undergoing large rigid body motions are within ±50 microstrain of strain gage measurements for strains ranging from 0 to 2000 microstrain.

7. Effect of Higher Order Displacement Fields on DIC Displacement Component Estimates (Schreier, Sutton)

Digital image correlation techniques are commonly used to measure specimen displacements by finding correspondences between an image of the specimen in an undeformed or reference configuration and a second image under load. To establish correspondences between the two images, numerical techniques are used to locate an initially square image subset in a reference image within an image taken under load. During this process, shape functions of varying order can be applied to the initially square subset. Zero order shape functions permit the subset to translate rigidly, while first order shape functions represent an affine transform of the subset that permits a combination of translation, rotation, shear and normal strains

In this article, the systematic errors that arise from the use of undermatched shape function, i.e., shape functions of lower order than the actual displacement field, are analyzed. It is shown that under certain conditions, the shape functions used can be approximated by a Savitzky–Golay low–pass filter applied to the displacement functions, permitting a convenient error analysis. Furthermore, this analysis is not limited to the displacements, but naturally extends to the higher–order terms included in the shape functions. This permits a direct analysis of the systematic strain errors associated with an undermatched shape function. Detailed numerical studies are presented for the case of a second–order displacement field and first and second order shape functions. Finally, the relation of this work to previously published studies is discussed.cross–correlation coefficient

8. On systematic errors in digital image correlation (Schreier, Braasch, Sutton)

Digital image correlation as a tool for surface deformation measurements has found widespread use and acceptance in the field of experimental mechanics over the recent years. The method is known to reconstruct displacements with a sub–pixel accuracy depending on various factors such as image quality, noise, and the correlation algorithm chosen. However, the systematic errors of the method have so far been neglected.

In this work, we address the systematic errors of the iterative spatial domain cross correlation algorithm caused by grey value interpolation. We investigate the position dependent bias in a numerical study and show that it can lead to apparent strains on the order of fifteen percent of the actual strain level. Furthermore, we present ways to reduce this bias to acceptable levels.

9. Banded microstructure in 2024-T351 and 2524-T351 aluminum friction stir welds. Part I: Metallurgical studies (Yang, Yan, Sutton, Reynolds)

Results from careful investigation of the banded microstructure observed on horizontal transverse cross-sections in all AA2024-T351 and AA2524 aluminum FSW joints indicate the presence of periodic variations in (a) the size of equiaxed grains, (b) micro-hardness and (c) concentration of base metal impurity particles (e.g., constituent particles) that correlate with the observed band spacing. The latter trend is more distinct in AA2024-T351, which has a higher volume fraction of constituent particles resulting in easily recognized particle rich regions on horizontal cross-sections near the mid-thickness of the joint and well-defined variations in hardness. In AA2524, the trends are more muted but clearly visible.

Results from recent numerical simulations of the FSW process enable interpretation of the trends in grain size along the weld centerline in terms of the time-temperature cycle experienced by the material. Specifically, the AA2524 FSW joints having low power and high input energy (i.e., the slow FSW) exhibit micron-size grain structure across both bands. Conversely, the fast and medium FSW in AA2524 have higher maximum temperatures and a corresponding six-fold increase in grain size.

10. Banded microstructure in 2024-T351 and 2524-T351 aluminum friction stir welds. Part II: Metallurgical studies (Sutton, Yang, Reynolds, Yan)

A series of micro-mechanical experiments have been performed to quantify how the friction stir weld (FSW) process affects the material response within the periodic bands that have been shown to be a common feature of FSW joints. Micro-mechanical studies employed sectioning of small samples and micro-tensile testing using digital image correlation to quantify the local stress-strain variations in the banded region.

Results indicate that the two types of bands in 2024-T351 and 2524-T351 aluminum FSW joints (a) have different hardening rates with the particle-rich bands having the higher strain hardening exponent (b) exhibit a periodic variation in micro-hardness across the bands and (c) do not change the initial yield stress of the material in the different bands.

11. Mixed Mode I/II Fracture of 2024-T3 Friction Stir Welds (Sutton, Reynolds, Yang, Taylor)

For the first time, a series of mixed mode I/II fracture experiments have been performed on both base material and three families of friction stir welds (FSWs) in 7 mm thick, 2024-T3 aluminum plate; the FSW joints are designated hot, medium and cold due to the level of nominal heat input during the joining process.

Results from the fracture tests indicate that the measured critical COD at a fixed distance behind the crack tip properly correlates both load-crack extension response and microstructural fracture surface features for both the base metal and all friction stir welds, providing an accurate measure of toughness. In addition, the COD values indicate that transition from mode I to mode II dominant crack growth occurs at lower loading angles for hotter FSW joints, with a truly mixed mode I/II COD measured during crack growth in the medium FSW joint. Also, using results from recent detailed FSW metallographic studies, specific features in the fracture process are correlated to the resulting FSW microstructure. Finally, the observed ductile crack growth path in all three welds tends to leave the under-matched FSW weld region as the far-field applied shear loading is increased, with the medium FSW being the only case where the flaw remained within the FSW region for all combinations of shear and tensile loading

12. Mode I Fracture and Microstructure for 2024-T3 Friction Stir Welds (Sutton, Reynolds, Yang, Taylor)

Detailed microstructural studies and mode I fracture experiments have been performed on both base material and friction stir welds (FSWs) in 7 mm thick, 2024-T3 aluminum plate. Three sets of FSW process parameters, designated cold, medium and hot to describe the relative amount of heat input to the FSW region, have been investigated.

Microstructural studies indicate that (a) the FSW nugget grain structure is relatively uniform in all welds, (b) grain size decreases by 25% when the global power input is increased 125%, (c) a banded microstructure exists on horizontal cross-sections traversing the weld region, where the band wavelength corresponds to the tool advance per revolution, (d) particles in the banded microstructure have the same elemental content as the impurities in the base metal, implying that the weld process is responsible for the observed particle redistribution and microstructural banding, (e) all welds exhibit a decrease in particle size and reduced particle volume fraction on the advancing side of the weld nugget and an attendant increase in particle volume fraction on the retreating side of the weld nugget, (f) hardness minima are present in the HAZ region outside of the weld nugget on both the advancing side and retreating side for all welds and (g) the hot weld has the lowest overall weld hardness.

Results from mode I fracture tests indicate that (a) macro-scale parameters (e.g., COD, yield stress) appear to be adequate for characterizing the observed fracture behavior in the under-matched FSW, (b) critical COD measured at a fixed distance behind the crack tip is a viable fracture parameter for FSW joints, with COD demonstrated as being capable of properly ordering the load-crack extension response for both the base metal and the welds, (c) the FSW joint has a through-thickness variation in toughness, (d) the observed ductile crack growth path remains in the softer nugget region of the FSW throughout the fracture process, though the microstructure variations appear to have an effect on the local fracture process and (e) the fracture path can be correlated with the locations of the hardness minima and, for the medium weld, with observed changes in the weld nugget due to FSW process

13. Full-field Speckle Pattern Image Correlation with B-Spline Deformation Function (Cheng, Sutton, McNeill and Schreier)

A full-field speckle pattern image correlation method is presented that will determine directly the complete, two-dimensional deformation field during the image correlation process on digital images obtained using computer vision systems.

In this work, a B-Spline function is used to represent the object deformation field throughout the entire image area. This is an improvement over subset-based image correlation methods by implicitly maintaining position and derivative continuity constraints among subsets up to a specified order. The control point variables within the B-Spline deformation function are optimized iteratively with Levenberg-Marquardt method to achieve minimum disparity between the predicted and actual deformed images. Results have shown that the proposed method is computationally efficient, accurate and robust. The general framework of this method can be applied to n-dimensional image correlation systems that solve for multi-dimension vector fields.

14. A Study of Residual Stresses and Microstructure in 2024-T3 Aluminum Friction Stir Butt Welds (Sutton, Reynolds, Wang and Hubbard)

Three-dimensional residual stress mapping in an aluminum 2024-T3 arcan specimen, butt-welded by friction stir technique at a low welding speed (), was performed by neutron diffraction. Results indicate that the residual stress distribution profiles across the weld region are asymmetric with respect to the weld centerline, with the largest gradients in residual normal stress occurring on the advancing side of the weld. Relative to Longitudinal stress is the largest tensile component with a maximum tensile stress (~100 MPa) at 7.5 mm from the weld centerline, and larger residual stresses are located close to the top surface.

Transverse stress is almost a tensile component but has a lower level of stress (max. ~60 MPa), except that four compressive residual stress regions are obtained at ±12.5 mm from the weld centerline near both the top and bottom surfaces. The normal stress component is in the range from –40 to 25 MPa, with compressive stress regions across the weld centerline within 15 mm. A relieve of the residual stresses in the section closer to the edge of the arcan specimen was observed.

15. Basic Studies of Welds in a Tank Car Steel: Residual Stress Measurements and Weld Characterization for TC-128B Steel Plate (Abdelmajid, Sutton, Wang and Hubbard)

Welding is the primary joining process used in the construction and repair of railroad tank cars. Since both fatigue crack growth and fracture of tank car structures are often initiated in the vicinity of welds, the effects of residual stress should be considered. Thus, for the first time, the enclosed work reports neutron diffraction results for all six components of the three-dimensional residual stress field on a transverse weld cross section in a widely used railroad tank car steel, TC128-B.

Results for a non-heat treated specimen indicate that (a) the longitudinal residual stress approaches 70% of the uniaxial yield stress, (b) the residual effective stress ranges from 250 Mpa to 450 Mpa in the weld region and (c) the residual shear stresses are of the same order as the smaller residual principal stresses in the weld region. Finally, initial fatigue crack growth predictions for weld flaws indicates that the residual stresses can reduce the fatigue life by a factor of two.

Archival articles since 2002 with NASA EPSCoR acknowledgment:

1. E. Mahgoub, X. Deng and M.A. Sutton, “Three-dimensional stress and deformation fields around flat and slant cracks under remote Mode I loading conditions”, **Engineering Fracture Mechanics**, 70 2527-2542 (2003).
2. B. Wan, M.F. Petrou, K.A. Harries, M.A. Sutton, and B. Yang, “A Novel Method to Investigate FRP Composite-Concrete Bond Toughness”, **ASCE Journal for Engineering Mechanics** (in press).
3. JZ Zuo, MA. Sutton and X Deng, "Basic studies of ductile failure processes and implications for fracture prediction", **Fatigue and Fracture of Engineering Materials (in press).**
4. Helm JD, Sutton MA and McNeill SR, "Deformations in wide, center-notched, thin panels: Part I: Three dimensional shape and deformation measurements by computer vision", **Optical Engineering**, 42 (5), 1293-1305 (2003)
5. Helm JD, Sutton MA and McNeill SR, "Deformations in wide, center-notched, thin panels: Part II: Finite element analysis and comparison to experimental measurements", **Optical Engineering**, 42 (5), 1306-1320 (2003)
6. H. W. Schreier, D. Garcia and M.A. Sutton, “Advances in Stereo Light Microscopy”, **Experimental Mechanics: An International Journal**, 44 (3) 278-289 (2004)
7. H.W. Schreier, M.A. Sutton, "Effect of Higher Order Displacement Fields on Digital Image Correlation Displacement Component Estimates", **Experimental Mechanics: An International Journal**, 42 (3) 303-311 (2002).
8. BC Yang, JH Yan, MA Sutton and AP Reynolds, "Microstructure and banding in 2024-T351 and 2524-T351 aluminum friction stir welding joints. Part I: metallurgical studies, accepted for publication in **Material Science and Engineering A**, 364, 55-65 (2004).
9. MA Sutton, BC Yang, JH Yan and AP Reynolds, "Microstructure and banding in 2024-T351 and 2524-T351 aluminum friction stir welding joints. Part II: mechanical characterization", **Material Science and Engineering A**, 364,66-74 (2004).
10. M.A. Sutton, A.P. Reynolds, B. Yang and R. Taylor, "Mixed mode I/II crack growth in 2024-T3 aluminum friction stir welds", **Engineering Fracture Mechanics**, 70, 2215-2234 (2003).
11. M.A. Sutton, A.P. Reynolds, B. Yang and R.K. Taylor III, "Mode I Fracture and Microstructure for 2024-T3 Friction Stir Welds", **Material Science and Engineering A**, 354, 6-16 (2003).
12. M.A. Sutton, A.P. Reynolds, B. Wang and R. Taylor, "Microstructure evolution in 2024-T3 aluminum friction stir welds and effect on mixed mode fracture", **Material Science and Engineering A**, Vol A323, 160-166 (2002).
13. M.A. Sutton, A.P. Reynolds, D.Q. Wang and C. Hubbard, "A Study of Residual Stresses and Microstructure in 2024-T3 Aluminum Friction Stir Butt Welds", **ASME Journal of Engineering Materials and Technology**, Vol 124, 215-221 (2002).
14. P. Cheng, M.A. Sutton, S.R. McNeill and H.W. Schreier, ”Full-field Speckle Pattern Image Correlation with B-Spline Deformation Function", **International Journal of Experimental Mechanics**, 42(3) 344-353 (2002).
15. M.A. Sutton, W. Zhao, C. Hubbard and D.Q. Wang, " Basic Studies of Welds in a Tank Car Steel: Residual Stress Measurements and Weld Characterization for TC-128B Steel Plate, **ASME Journal for Pressure Vessels and Piping**, 124 405-414 (2002).

South Carolina NASA EPSCoR Program at Clemson University
Report on Year 5 Activity

The research being conducted at Clemson can be broadly characterized as development of advanced materials, analysis methods, and design concepts for improving the performance of aircraft structures. Material investigations include studies of advanced titanium alloys, TiC reinforced titanium composites, and hybrid mixed-tow epoxy composites. Analysis methods are being developed that are applicable to these and conventional advanced materials. The effect of cyclic loads and presence of initial damage and defects on material behavior and structural response, as well as the damage tolerance of these materials and structures subject to monotonic and cyclic loads are common elements in many of the investigations of the four faculty participants and their graduate students. The effort is approximately equally divided between experimental and analytical investigations. A description of progress made during the past year on the four research projects is given below.

(1) Damage Progression Analysis, Residual Strength Prediction, and Finite Element Development for Laminated Plates

Sherrill Biggers, Jr., Professor of Mechanical Engineering, Clemson Univ.
De Xie, Ph.D., Engineering Mechanics, currently Univ. Michigan
Mohan Rathinasabapathy, M.S., Mechanical Engineering, currently ABAQUS Inc.

Summary

The objective of this project is to develop efficient and accurate analysis methods that can be used to predict the progression of damage in laminated composite structures and the residual strength of damaged structures. In particular, the interaction of local damage and global structural response is of primary interest. Application of these analysis methods to develop design concepts that improve damage tolerance and residual strength is also a goal of this project. Therefore, both computational efficiency and accuracy are of major concern. Damage can progress in different ways in different plies according to the ply properties and fiber orientation, the ply-level stress state and the condition of the interlaminar bond. Questions arise as to how damage affects the local properties of the material, how these changes in properties affect the global response of the structure, and how the global response affects further development of damage. Models are needed which are both computationally inexpensive as well as accurate. Research in the first four years included development of finite element analysis methods for postbuckled composite plates using a higher-order zig-zag theory and investigation of damage progression in tailored plates with and without cutouts. During the past year, work has focused on (1) the efficient and accurate modeling of delamination progression in plates and sandwich panels and (2) modeling of through-the-thickness stitching in a way that can be incorporated in the delamination modeling. Dr. Xie was supported by this grant and received his Ph.D. in December 2002. Mr. Rathinasabapathy was also supported by this grant and received his Masters in August 2003.

Section I: Narrative

Description of Research and Accomplishments

The research on delamination progression builds on investigations during previous years which focused on (1) evaluation of local damage evolution models, (2) simulation of damage progression under both monotonic and cyclic loading, (3) damage progression in postbuckled plates, and (4) damage progression and residual strength of tailored flat and curved plates with a cutout. During the past year particular attention has been given to (1) modeling of delamination growth after buckling, and (2) modeling stitching as a delamination growth control device. These last two topics are discussed briefly.

(1) STRAIN ENERGY RELEASE RATE CALCULATION FOR A MOVING DELAMINATION FRONT OF ARBITRARY SHAPE BASED ON THE VIRTUAL CRACK CLOSURE TECHNIQUE

Introduction

The onset and growth of delaminations are of great interest in the applications of composite structures since delaminations are one of the major failure modes. A delamination has usually been treated as a 2D or 3D crack so that facture mechanics can be utilized. Among the variables of fracture mechanics, the strain energy release rate (G_I, G_{II} and G_{III}) has been used most frequently as the criterion in determining the initiation and growth of delaminations in composite materials. Several closed-form expressions for (G) have been derived through analytical approaches for specific cases [1-4]. For more general and complicated problems in engineering applications, numerical approaches such as finite element methods are required in conjunction with the virtual crack closure technique that was developed to calculate the strain energy release rate numerically.

The virtual crack closure technique (VCCT) was proposed for 2D crack configurations by Rybicki and Kanninen [5] and was extended to three dimensions (3D-VCCT) by Shivakumar, Tan and Newman [6]. Usually VCCT is applied by using orthogonal meshes that have sides either normal or parallel to the delamination front. This can be easily achieved when the delamination front is fixed by adjusting FEA meshes to fit the pre-existing shape of the crack front, though this kind of matching between meshes and the geometry may require fine mesh patterns.

When studying delamination growth in composite structures, using orthogonal mesh patterns becomes problematic due to the changing position and shape of the delamination front. This kind of mesh adjustment together with the associated nonlinear iterations makes the analysis prohibitively large in most cases. Furthermore, delaminations in practical situations are not likely to grow in a self-similar manner due to the uneven distribution of the strain energy release rate (G) across the delamination front and due to the interaction of local and global response. For example, a straight delamination front does not stay totally straight in a double cantilever beam; a circular delamination tends to become an elliptical one under compression loading. A delamination due to impact damage is often irregular and grows in an irregular manner. It is not practical to create a new mesh for the newly predicted delamination front at each increment in order to keep the meshes orthogonal to the delamination front. This is a major obstacle in studying delamination growth in realistic cases.

This study presents a method to calculate the strain energy release rate at the delamination front accurately and efficiently without using orthogonal meshes. Towards this end, an 18-node special element was developed to calculate the strain energy release rate based on 3D-VCCT once the delamination front lies within the element.

Methodology

3D-VCCT and G-calculation Interface Element

The 3D-VCCT can be used to calculate the components of strain energy release rate (G_I, G_{II} and G_{III}) for node N shown in Figure 1 with an orthogonal mesh are as follows:

$$
\begin{aligned}
G_I &= \lim_{\Delta A\to 0}\frac{1}{2\Delta A}\int_{s_a}^{s_b}\int_0^{\Delta_2}\sigma_z(r,s)\overline{w}(\Delta_1,s)\,dr\,ds \\
G_{II} &= \lim_{\Delta A\to 0}\frac{1}{2\Delta A}\int_{s_a}^{s_b}\int_0^{\Delta_2}\tau_{rz}(r,s)\overline{u}_r(\Delta_1,s)\,dr\,ds \qquad (1)\\
G_{III} &= \lim_{\Delta A\to 0}\frac{1}{2\Delta A}\int_{s_a}^{s_b}\int_0^{\Delta_2}\tau_{sz}(r,s)\overline{u}_s(\Delta_1,s)\,dr\,ds
\end{aligned}
$$

where $\sigma_z(r,s)$, $\tau_{rz}(r,s)$ and $\tau_{sz}(r,s)$ are the stress components ahead of the crack front and $\overline{w}(\Delta_1,s)$, $\overline{u}_r(\Delta_1,s)$ and $\overline{u}_s(\Delta_1,s)$ are the components of crack openings behind the crack front. The parameters r and s are the local coordinates normal to and along the crack front, respectively. ΔA is the virtually closed area.

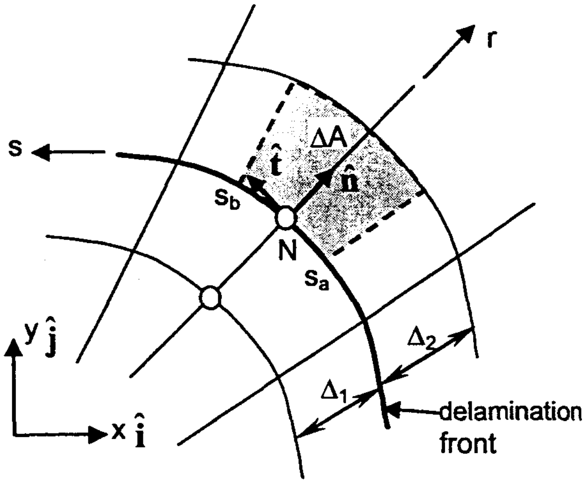

Figure 1. ***G*** **Calculation by 3D-VCCT at Node N**

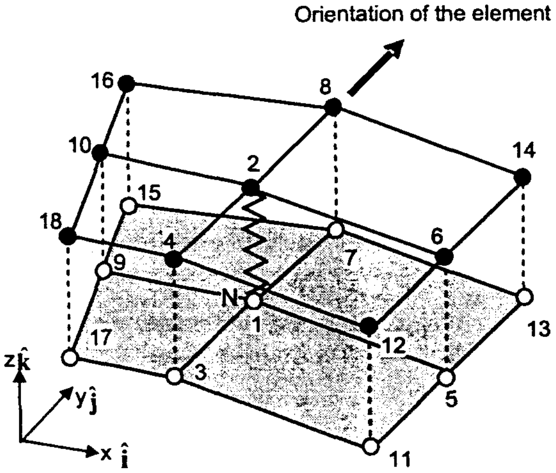

Fig. 2. Element definition and node numbering

To evaluate equations (1) numerically, a special 18-node element is proposed herein. Figure 2 shows the element definition and the node numbering. The element consists of two sets of node groups: the top set (filled circles in Figure 2) and the bottom set (open circles in Figure 2). When the element is placed at an interface between layers, the nodes in the top set are from the upper portion of the interface while the nodes in the bottom set are from the lower portion of the interface. The elements above or below an interface element can consist of four 8-node solids or four 4-node shell elements. If the interface is perfectly bonded, i.e., there is no delamination, the nodes in the top set will have the same coordinates as their corresponding partners in the bottom set. In this case, the gap between the top node set and the bottom node, set, exaggerated in Figure 2, does not exist. The element has zero thickness.

Since the element has been defined to calculate the strain energy release rates G_I, G_{II}, and G_{III} at the point where node pair (1,2) is located, three very stiff springs are placed between nodes 1 and 2 to evaluate the forces in the springs in the x, y, and z directions in the global coordinate system. In all the applications of this element made to date, the value chosen for the spring stiffnesses has not been a critical choice. Large values should be selected and no numerical solution problems have been detected for a wide range of values. Thus the element is robust in its numerical application. Let k_x, k_y, and k_z be the stiffness of the springs. The total strain energy in the spring is

$$U = \tfrac{1}{2}k_x(u_1 - u_2)^2 + \tfrac{1}{2}k_y(v_1 - v_2)^2 + \tfrac{1}{2}k_z(w_1 - w_2)^2$$

The first variation of U is

$$\begin{aligned}\delta U &= k_x(u_1 - u_2)(\delta u_1 - \delta u_2) + k_y(v_1 - v_2)(\delta v_1 - \delta v_2) + k_z(w_1 - w_2)(\delta w_1 - \delta w_2)\\ &= \{\delta\mathbf{u}\}[\mathbf{K}]\{\mathbf{u}\}^T\end{aligned}$$

where $\{\delta\mathbf{u}\} = \{\delta u_1, \delta v_1, \delta w_1, \delta u_2, \delta v_2, \delta w_2\}$, $\{\mathbf{u}\} = \{u_1, v_1, w_1, u_2, v_2, w_2\}$. The stiffness matrix for the element is

$$[\mathbf{K}] = \begin{bmatrix} \mathbf{K}_s & -\mathbf{K}_s \\ -\mathbf{K}_s & \mathbf{K}_s \end{bmatrix}$$

where

$$[\mathbf{K}_s] = \begin{bmatrix} k_x & 0 & 0 \\ 0 & k_y & 0 \\ 0 & 0 & k_z \end{bmatrix}$$

The stiffness matrix [K] is implemented within ABAQUS by means of a user defined element subroutine, UEL.

All the information necessary to calculate the three energy release rate quantities is present in the element without additional post processing. The further advantage of this element is its capability of predicting delamination growth since an energy release rate based criteria can also be easily implemented into the user subroutine of the special element.

Calculation of G for a Delamination Front having an Arbitrary Shape

The delamination front within an element that is centered on node N can be located by defining the two of the eight vectors pointing away from point N (Figure 3(a)) that divide the bonded nodes from the debonded nodes. Let these two vectors be defined as $\vec{\mathbf{R}}_b$ and $\vec{\mathbf{R}}_e$ where the "*b*" and "*e*" subscripts stand for the *"beginning"* and *"end"* of the bonded region where one moves counterclockwise from $\vec{\mathbf{R}}_b$ to $\vec{\mathbf{R}}_e$ in sweeping out the bonded region. The damage state for the surrounding nodes is defined by a variable referred to herein as the damage index,

$$m_i = \begin{cases} 0 & \text{for perfectly bonded nodes} \\ 1 & \text{for separated nodes} \end{cases}$$

The center node N is considered to be bonded. Knowing the damage indices, the delamination front can be located within an element having one or more values of damage index equal to one by defining the two special vectors

$$\vec{\mathbf{R}}_b = \sum_{i=1}^{8} m_{i-1}(1-m_i)\vec{\mathbf{R}}_i \qquad \vec{\mathbf{R}}_e = \sum_{i=1}^{8}(1-m_i)m_{i+1}\vec{\mathbf{R}}_i$$

Here, $m_0 = m_8$ and $m_9 = m_1$. These two vectors form a close approximation to the delamination front that passes through point N within the element. Figure 3(b) gives one example in which all nodes except 3 and 4 are bonded and therefore $b = 5$ and $e = 2$.

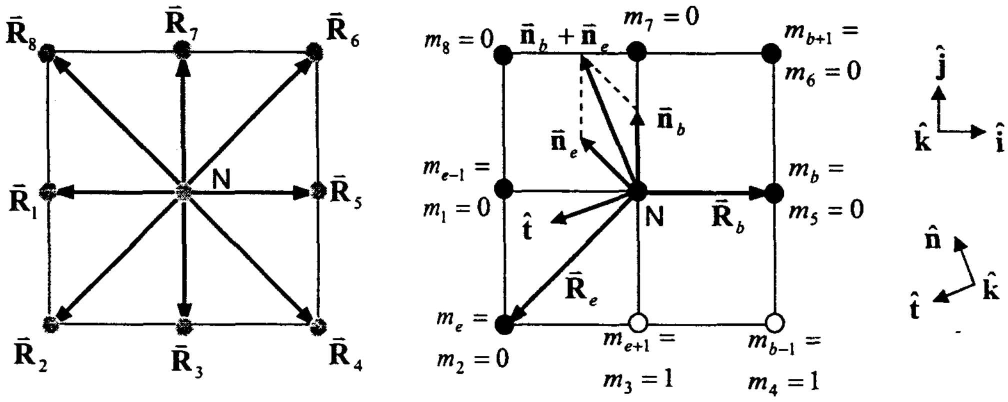

(a)

(b) For this example, *b*=5, *e*=2

Figure 3. Vectors that Form a Delamination Front

Determination of the vector that is normal to the delamination front at N is fundamental for the further calculation of strain energy release rates. The normal vector here is approximated as the resultant of the two vectors $\vec{\mathbf{R}}_b$ and $\vec{\mathbf{R}}_e$. Following the right-hand-rule for the cross product, we have

$$\hat{\mathbf{n}}_b = \hat{\mathbf{k}} \times \vec{\mathbf{R}}_b = \hat{\mathbf{k}} \times \sum_{i=1}^{8} m_{i-1}(1-m_i)(R_{ix}\hat{\mathbf{i}} + R_{iy}\hat{\mathbf{j}}) = \sum_{i=1}^{8} m_{i-1}(1-m_i)(-R_{iy}\hat{\mathbf{i}} + R_{ix}\hat{\mathbf{j}})$$

$$\hat{\mathbf{n}}_e = -\hat{\mathbf{k}} \times \vec{\mathbf{R}}_e = -\hat{\mathbf{k}} \times \sum_{i=1}^{8}(1-m_i)m_{i+1}(R_{ix}\hat{\mathbf{i}} + R_{iy}\hat{\mathbf{j}}) = \sum_{i=1}^{8}(1-m_i)m_{i+1}(\ R_{iy}\hat{\mathbf{i}} - R_{ix}\hat{\mathbf{j}})$$

where the unit vectors $\hat{\mathbf{i}}$ and $\hat{\mathbf{j}}$ correspond to the natural coordinate (ξ,η) directions and $\hat{\mathbf{k}}$ is the unit vector normal to $\hat{\mathbf{i}}$ and $\hat{\mathbf{j}}$. Therefore, the sum of the two vectors is

$$\vec{\mathbf{n}}_b+\vec{\mathbf{n}}_e=\sum_{i=1}^{8}(1-m_i)(m_{i+1}-m_{i-1})(R_{iy}\hat{\mathbf{i}}-R_{ix}\hat{\mathbf{j}})$$

The vector is then normalized as a unit vector. The unit normal vector and its corresponding tangent vector are

$$\hat{\mathbf{n}}=\frac{\vec{\mathbf{n}}_b+\vec{\mathbf{n}}_e}{\left\|\vec{\mathbf{n}}_b+\vec{\mathbf{n}}_e\right\|}=n_x\hat{\mathbf{i}}+n_y\hat{\mathbf{j}}$$

$$\hat{\mathbf{t}}=\hat{\mathbf{k}}\times\hat{\mathbf{n}}=-n_y\hat{\mathbf{i}}+n_x\hat{\mathbf{j}}$$

The three unit vectors $(\hat{\mathbf{n}},\hat{\mathbf{t}},\hat{\mathbf{k}})$ form a base for the local coordinate system. The components of strain energy release rate (G_I, G_{II} and G_{III}) will be calculated within this local coordinate system.

To determine G_I, G_{II} and G_{III}, the virtually closed area needs to be calculated first. The calculation is carried out in the space of the natural coordinates (ξ,η), see Figure 4(a). The shape functions for the element in Figure 4(b) are

$$N_1(\xi,\eta)=(1-\xi^2)(1-\eta^2);$$

$$N_2(\xi,\eta)=\tfrac{1}{2}(1-\xi^2)(-1+\eta)\eta;\ N_3(\xi,\eta)=\tfrac{1}{2}(1-\eta^2)(-1+\xi)\xi;$$

$$N_4(\xi,\eta)=\tfrac{1}{2}(1-\xi^2)(\ 1+\eta)\eta;\ N_5(\xi,\eta)=\tfrac{1}{2}(1-\eta^2)(\ 1+\xi)\xi;$$

$$N_6(\xi,\eta)=\tfrac{1}{4}(1-\xi)(1-\eta)\xi\eta;\ N_7(\xi,\eta)=-\tfrac{1}{4}(1+\xi)(1-\eta)\xi\eta;$$

$$N_8(\xi,\eta)=\tfrac{1}{4}(1+\xi)(1+\eta)\xi\eta;\ N_9(\xi,\eta)=-\tfrac{1}{4}(1-\xi)(1+\eta)\xi\eta$$

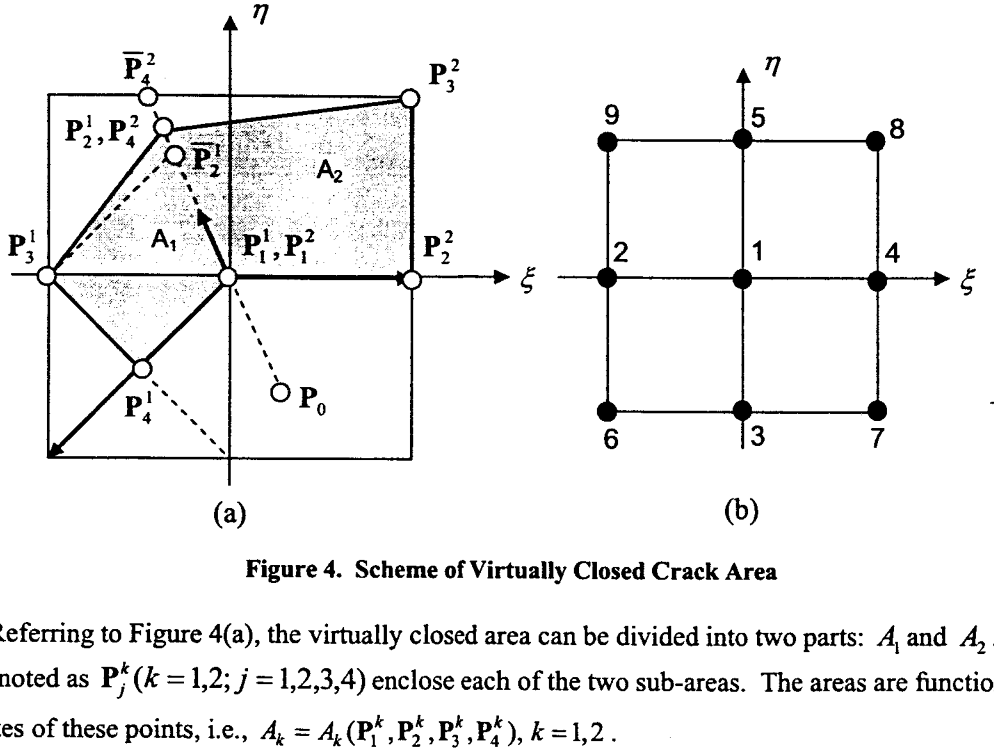

(a) (b)

Figure 4. Scheme of Virtually Closed Crack Area

Referring to Figure 4(a), the virtually closed area can be divided into two parts: A_1 and A_2. Four points denoted as $\mathbf{P}_j^k\,(k=1,2; j=1,2,3,4)$ enclose each of the two sub-areas. The areas are functions of the coordinates of these points, i.e., $A_k=A_k(\mathbf{P}_1^k,\mathbf{P}_2^k,\mathbf{P}_3^k,\mathbf{P}_4^k)$, $k=1,2$.

For the area A_1, the three known points are

$$\mathbf{P}_1^1=(0,0)\qquad \mathbf{P}_3^1=(\xi_{e-1},\eta_{e-1})\qquad \mathbf{P}_4^1=(\tfrac{1}{2}(\xi_{e-1}+\xi_{e+1}),\tfrac{1}{2}(\eta_{e-1}+\eta_{e+1}))$$

and the following three points are known for defining area A_2.

$$\mathbf{P}_1^2=(0,0)\qquad \mathbf{P}_2^2=(\tfrac{1}{2}(\xi_{b-1}+\xi_{b+1}),\tfrac{1}{2}(\eta_{b-1}+\eta_{b+1})\qquad \mathbf{P}_3^2=(\xi_{b+1},\eta_{b+1})$$

To obtain the two unknown points $\mathbf{P}_2^1$ and $\mathbf{P}_4^2$, two temporary points $\overline{\mathbf{P}}_2^1$ and $\overline{\mathbf{P}}_4^2$ are obtained first. The point $\overline{\mathbf{P}}_2^1$ is the intersection of (1) the line parallel to the vector $\hat{\mathbf{n}}$ passing through point $\mathbf{P}_1^1$ and (2) the line parallel to the vector $\vec{\mathbf{R}}_b$ passing the point $\mathbf{P}_3^2$. Therefore, the two linear equations

$$\begin{cases} n_x\bar{\xi}_2^1 - n_y\bar{\eta}_2^1 = 0 \\ R_{ey}\bar{\xi}_2^1 - R_{ex}\bar{\eta}_2^1 = R_{ey}\xi_{e-1} - R_{ex}\eta_{e-1} \end{cases}$$

can be solved to obtain the coordinates of $\overline{\mathbf{P}}_2^1$ as

$$\begin{cases} \bar{\xi}_2^1 = \dfrac{n_y}{d_1}(R_{ey}\xi_{e-1} - R_{ex}\eta_{e-1}) \\ \bar{\eta}_2^1 = \dfrac{n_x}{d_1}(R_{ey}\xi_{e-1} - R_{ex}\eta_{e-1}) \end{cases}$$

where

$$d_1 = -n_x R_{ex} + n_y R_{ey}.$$

The same procedure is then applied to obtain the coordinates of $\overline{\mathbf{P}}_4^2$ as

$$\begin{cases} \bar{\xi}_4^2 = \dfrac{n_y}{d_2}(R_{by}\xi_{b+1} - R_{bx}\eta_{b+1}) \\ \bar{\eta}_4^2 = \dfrac{n_x}{d_2}(R_{by}\xi_{b+1} - R_{bx}\eta_{b+1}) \end{cases}$$

where

$$d_2 = -n_x R_{bx} + n_y R_{by}.$$

As an approximation, the actual $\mathbf{P}_2^1$ and $\mathbf{P}_4^2$ are taken as a single point that is the average of points $\overline{\mathbf{P}}_2^1$ and $\overline{\mathbf{P}}_4^2$, that is,

$$\mathbf{P}_2^1 = \mathbf{P}_4^2 = \left(\tfrac{1}{2}(\bar{\xi}_2^1 + \bar{\xi}_4^2), \tfrac{1}{2}(\bar{\eta}_2^1 + \bar{\eta}_4^2)\right)$$

Now all the points $\mathbf{P}_j^k = (\xi_j^k, \eta_j^k)$, $(j = 1,2,3,4; k = 1,2)$ necessary to calculate the virtually closed area have been determined in terms of the parameters (ξ, η). Using the following relations

$$x_j^k = N_i(\xi_j^k, \eta_j^k)\bar{x}_i \qquad y_j^k = N_i(\xi_j^k, \eta_j^k)\bar{y}_i$$

points (ξ_j^k, η_j^k) can be transformed into points in physical space (x_j^k, y_j^k) where $(\bar{x}_i, \bar{y}_i)$ are the nodal coordinates in physical space. Once the points (x_j^k, y_j^k) are determined, Gauss Quadrature is used to calculate the areas A_1 and A_2 with the total virtually closed area A given by

$$A = \{c_1 A_1(\mathbf{P}_1^1, \mathbf{P}_2^1, \mathbf{P}_3^1, \mathbf{P}_4^1) + c_2 A_2(\mathbf{P}_1^2, \mathbf{P}_2^2, \mathbf{P}_3^2, \mathbf{P}_4^2)\}$$

where c_1 = 1.0 when point $\mathbf{P}_4^1$ does not correspond to a node or 0.5 when the point does correspond to a physical node. The same can be said for c_2 but the governing point is $\mathbf{P}_2^2$. These two points, as well as point $\mathbf{P}_1^1$, are always points on the delamination front. The c_i constants as defined here prevent double counting of the virtually closed area as the special element is centered at each node on the delamination front.

Next, the three nodal force components at node pair (1,2) are computed by

$$\bar{F}_x = k_z(u_2 - u_1) \qquad \bar{F}_y = k_y(v_2 - v_1) \qquad \bar{F}_z = k_z(w_2 - w_1)$$

$\bar{F}_z$ is required to calculate G_I and can be used directly as calculated above. $\bar{F}_x$ and $\bar{F}_y$ must be transformed into the local system to calculate G_{II} and G_{III} as

$$\bar{F}_2 = n_x\bar{F}_x + n_y\bar{F}_y \qquad \bar{F}_3 = n_y\bar{F}_x - n_x\bar{F}_y$$

The opening behind the delamination front is defined as the point anti-symmetric to points $\mathbf{P}_2^1$ and $\mathbf{P}_4^2$ about (0,0) in (ξ,η) space as

$$\mathbf{P}_0 = (\xi_0,\eta_0) = (-\tfrac{1}{2}(\bar{\xi}_2^1 + \bar{\xi}_4^2), -\tfrac{1}{2}(\bar{\eta}_2^1 + \bar{\eta}_4^2))$$

Therefore, the displacement components for the delamination opening in the global system are

$$\Delta u = N_i(\xi_0,\eta_0)\Delta u_i \qquad \Delta v = N_i(\xi_0,\eta_0)\Delta v_i \qquad \Delta w = N_i(\xi_0,\eta_0)\Delta w_i$$

The Δw is required to calculate G_I and can be used directly as calculated above. The Δu and Δv must be transformed into the local system to calculate G_{II} and G_{III} as

$$\Delta u_2 = n_x\Delta u + n_y\Delta v \qquad\qquad \Delta u_3 = n_y\Delta u - n_x\Delta v$$

The strain energy release rate based on equation (1) can be approximated as the product of the nodal forces at node pair (1,2) and the nodal displacement opening at point $\mathbf{P}_0(\xi_0,\eta_0)$ in the region enclosed by A_1 and A_2. Therefore, the equivalent of equation (1) is

$$G_I \approx \frac{1}{2A}\bar{F}_z\Delta w \qquad G_{II} \approx \frac{1}{2A}\bar{F}_2\Delta u_2 \qquad G_{III} \approx \frac{1}{2A}\bar{F}_3\Delta u_3$$

Numerical Results

The validity of the present approach was first assessed by four examples, each with a fixed delamination front. Two of these delaminations represent mode-I cracks while the other two are characterized as mixed-mode cracks. They are selected to ensure the correct implementation of the 3D-VCCT into the user subroutine UEL of ABAQUS.

Several delamination growth problems were then studied using the present approach. The criterion for determining the initiation and growth of delamination based on strain energy release rate is selected as

$$E_d = \left(\frac{G_I}{G_{IC}}\right)^{\alpha} + \left(\frac{G_{II}}{G_{IIC}}\right)^{\beta} + \left(\frac{G_{III}}{G_{IIIC}}\right)^{\gamma} \geq 1$$

where E_d is the delamination growth parameter. G_{IC}, G_{IIC}, and G_{IIIC} are the critical values corresponding to mode I, mode II and mode III cracks, respectively, and are assumed to be constant during delamination growth in this study. The exponents α, β, and γ were taken as 1 as suggested by Kutlu and Chang [7]. Once the $E_d \geq 1$, the delamination grows and the stiffness matrix of the interface element is set to zero, i.e., $[\mathbf{K}] = [\mathbf{0}]$. No difficulties have been encountered due to sudden reduction of the stiffness to zero as opposed to a more gradual reduction used by others to aid in numerical convergence.

Validation Examples for Fixed Delamination Front

In order to evaluate the accuracy of the present approach, the method was first applied to four benchmark problems: an end delamination in a double cantilever beam (DCB) test specimen, an embedded elliptical crack in a solid body, a through-the-width delamination in a buckled plate, and an embedded circular delamination in a buckled laminated plate. The first two are of typical mode-I dominated cracks while the later two are mixed-mode cracks. There are closed-form solutions or FEA predictions available for comparisons.

Figure 5 shows the results for the DCB. The analytical solution given by Kanninen [8] used classical beam on elastic foundation theory to model the one of the two layers and therefore imposed the assumption of a straight crack front due to the 2D configuration. The three dimensional ABAQUS standard element "C3D8I" was used to model the specimen. There was only one element in each layer across the width so that the delamination front was forced to be straight, consistent with Kanninen's assumption. Ten elements were used through the thickness of the delaminated layers and 90 elements were used along the length with the delamination occurring at the mid-surface. The mode-I strain energy release rate plotted in the figure was normalized with respect to the value G_{I0} as shown. Kanninen's results were given in terms of stress intensity factors were reproduced and converted to G_I to prepare these plots. The specimen has a width (into the paper) of "B" and the remaining parameters are defined in the subplot in Figure 5. The solid line shows the analytical solution and the values predicted by 3D-VCCT are shown as black dots. The difference between the analytical solution and the 3D-VCCT approximation is within 1.58%. The larger errors occur for the shortest crack lengths where the effects of transverse shear deformations, not accounted for in Ref. [8] but included in the current approach, are the greatest.

Figure 6 shows the distribution of the normalized G_I along the crack front of an embedded elliptical crack in a solid rectangular prism. The delamination shape and geometric parameters are shown in the subplot of the figure. The tensile stress σ was applied in the direction normal to the paper at a distance far from the embedded delamination. The proportions used in this example for the characteristic dimensions are W=T, c=2a, and c/W=0.2. The "C3D8" element was also used for the solid body and an orthogonal mesh was used in the region of the delamination. Results are shown only for $0^\circ \leq \Phi \leq 90^\circ$ due to the symmetry. The black dots show the distribution of G_I calculated from the 3D-VCCT and solid line represents the analytical expression given in Ref [9]. The G_I values plotted were normalized the by G_{I0} of circular delamination with radius "a". Accuracy similar to the previous example was observed, the difference between 3D-VCCT approximations and analytical solutions being within 1.33%.

Figure 7 compares the strain energy release rates of a buckled, through-the-width delamination given by the analytical approach developed by Chai, Babcock and Knauss [1] with that given by the present 3D-

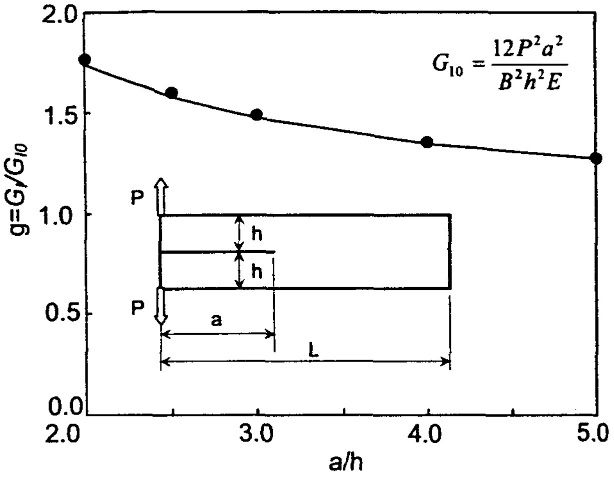

Figure 5. Comparison of Analytical Solution and 3D-VCCT for DCB

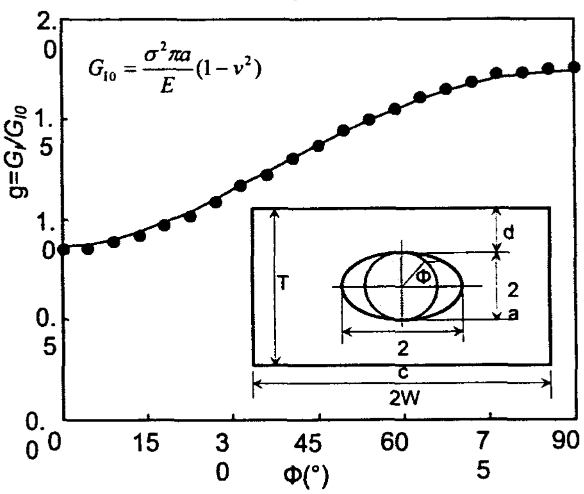

Figure 6. Comparison of Analytical Solution and 3D-VCCT for EEC in Solid Body

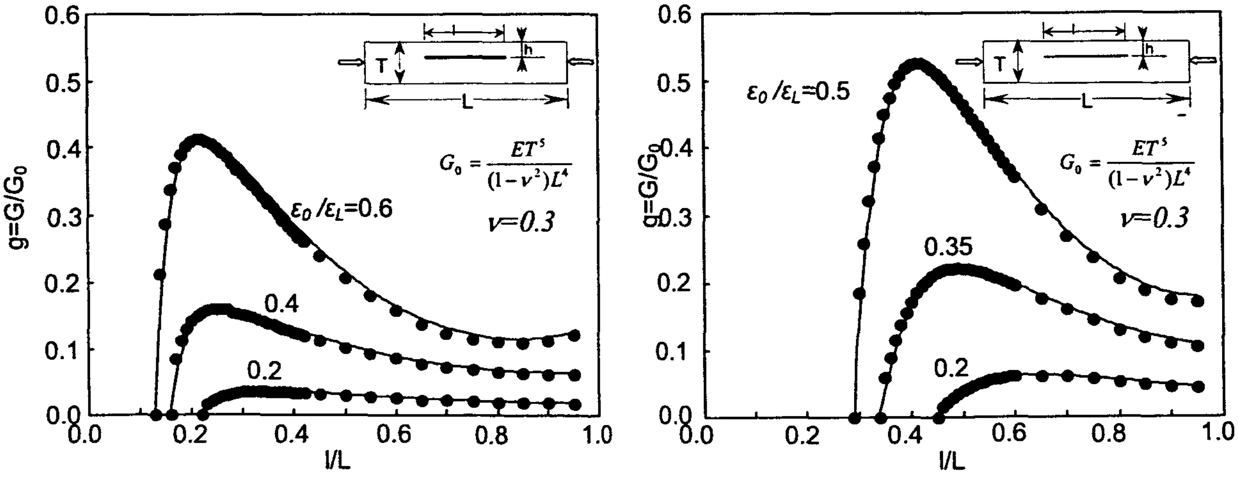

(a) h/T=0.1

(b) h/T=0.2

Figure 7. Comparison of Analytical Solution and Present Approximation for a 1-D Delamination

VCCT method. The black dots are the VCCT results. The energy release rate shown in the figure is the total energy contributed by both mode I and mode II because separate values were not computed in analytical approach. The total G is plotted against the delamination length (l/L) for two different delamination depths (h/T=0.1 and 0.2) and for three different compressive load levels ($\varepsilon_0/\varepsilon_L$). The present approach based on 3D-VCCT shows excellent accuracy compared to the analytical solutions.

The final validation example is reported in Figure 8. Whitcomb[10] also performed a finite element analysis based on 3D-VCCT. The sublaminate thickness (h) and the laminate thickness (H) are 0.4 mm and 4 mm, respectively. The radius of the delamination (a) is 15 mm and the half width of the laminate plate (W) is 50 mm. The load level corresponds to $\varepsilon_x = -0.005$. A "homogeneous quasi-isotropic" material with $(\pm 45/0/90)_s$ stacking sequence was selected in the study and the following mechanical properties for a typical graphite/epoxy were used:

$E_{11} = 134$ GPa $\quad G_{23} = 3.43$ GPa $\quad \nu_{23} = 0.49$
$E_{22} = E_{33} = 10.2$ GPa $\quad G_{12} = G_{13} = 5.52$ GPa $\quad \nu_{12} = \nu_{13} = 0.3$

The comparison in Figure 8 shows good agreement between 3D-VCCT employed by Whitcomb and the present 3D-VCCT method, especially in regions where the G_I and G_{II} values are maximum, i.e. where growth would occur. Larger relative differences occur in areas where the G_I and G_{II} values are small. This is likely due to differences in treatment of the contact in this area. Slight relaxation of the gap closure constraint very close to the delamination front caused much better agreement with Ref. [10] in the regions of small G while not affecting the excellent correlation in other regions around the circumference of the delamination front.

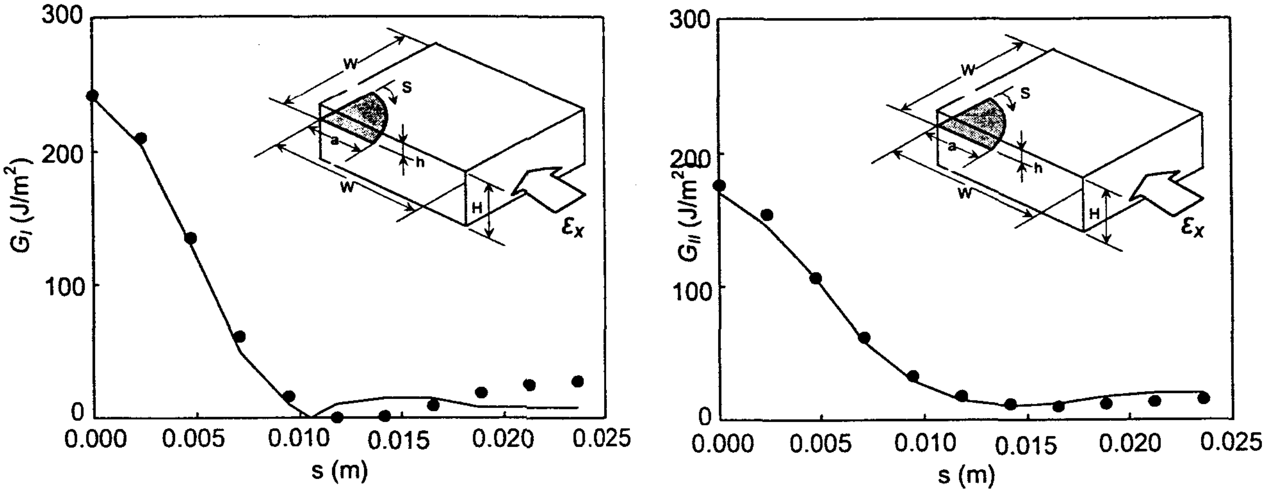

(a) G_I Distribution along the Delamination Front (b) G_{II} Distribution along the Delamination Front

Figure 8. Comparison of FEA Solution in Ref [9] and Present Approximation for an Embedded Delamination

Each of the four validation examples has shown excellent correlation between analytical solution or previous FEA analysis and the present approach. This confirms the accuracy of the 3D-VCCT for fixed delamination fronts and leads to consideration of the delamination growth studies discussed below.

Delamination growth in a double cantilever beam

Now consider the growth of a delamination in a double cantilever beam shown in Figure 9. The specimen is subjected to an end loading in the form of displacements that are constant across the specimen width. Initial studies were performed on other DCB models with mesh patterns aligned with the specimen geometry and oriented at 45 degrees to the specimen length. The current method produced strain energy release rates that were essentially independent of the mesh orientation. Here the method is applied to a specimen for which test results are available from Ref. [11]. The specimen is 150 mm long (L), 20 mm wide (B) and composed of two 1.98-mm-thick (h) plies of unidirectional materials. The initial delamination length (a) is 55 mm. The material is graphite/epoxy with the following properties:

$E_{11} = 150.0$ GPa
$E_{22} = E_{33} = 11.0$ GPa
$G_{12} = G_{13} = 6.0$ GPa
$G_{23} = 3.7$ GPa
$\nu_{12} = \nu_{12} = 0.25$
$\nu_{23} = 0.45$
$G_{IC} = 0.268$ N/mm
$G_{IIC} = 1.45$ N/mm

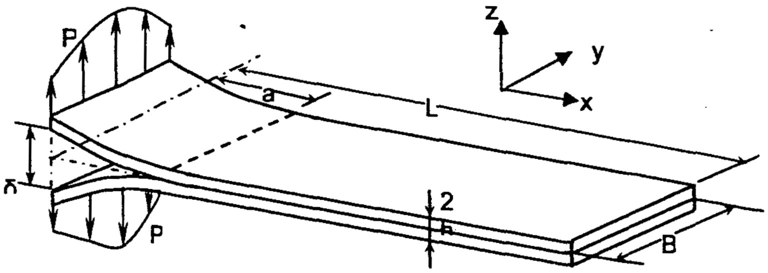

Figure 9. Geometry of Double Cantilever

The two models that were used are shown in Figure 10. ABAQUS standard "C3D8I" brick elements were used. Both models have 120 elements along the span and one element through the thickness of each of the two layers in the specimen. Two mesh sizes were used across the width: one (as in Ref. [11]) and ten elements, i.e., B01 and B10 mesh patterns, respectively. This allowed investigation of the importance of nonuniformity of the strain energy release rate across the specimen width and the associated curvature of the delamination front.

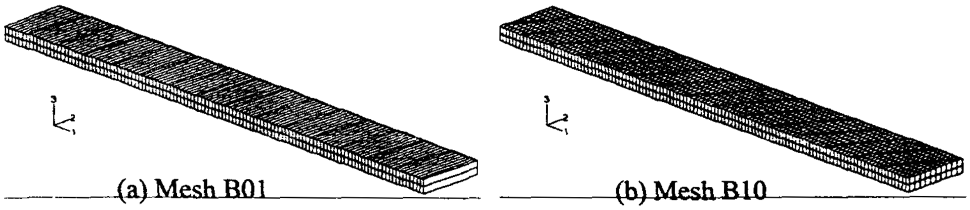
(a) Mesh B01 (b) Mesh B10

Figure 10. Two Finite Element Mesh Patterns

Plots of the end reaction force versus end deflection are shown in Figure 11 for the two models and also for the test data from Ref. [11]. The distribution of mode I strain energy release rate across the specimen width is shown in Figure 12 for the load level that creates the first growth in the delamination front. The B10 model shows a significant variation G_I across the specimen width. For this material, the G_{IC} value is remarkably close to the uniform G_I predicted by the simpler B01 model. This indicates that while the simpler model would accurately predict initiation of delamination growth of a pre-existing straight-front delamination, it might not do so well as the delamination grows and the front deviates from its straight form. This fact is illustrated by the much better correlation of the B10 results with the test data than for the B1 results. The first open circle on the plot corresponds to the initial delamination growth and if the front is artificially forced to retain the straight delamination front, the simple model considerably underestimates the

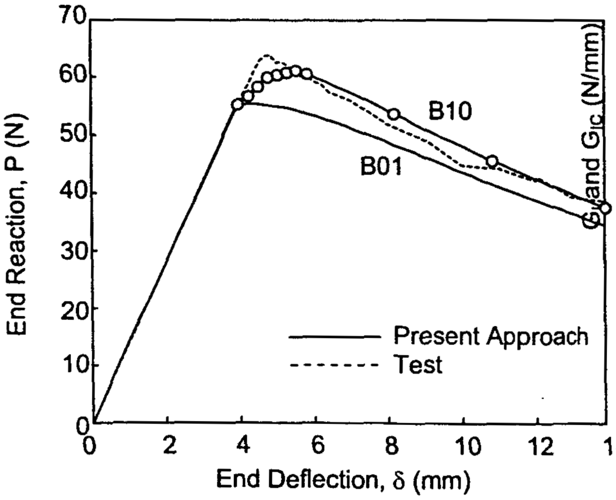

Figure 11. Load vs. Deflection Curves of DCB

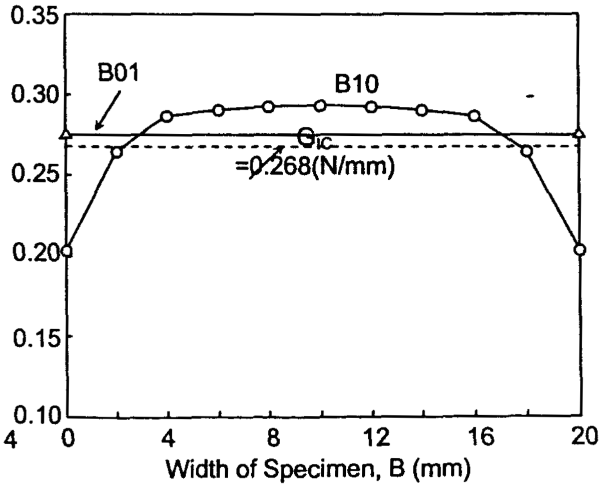

Figure 12. G_I Distribution at the Delamination Front

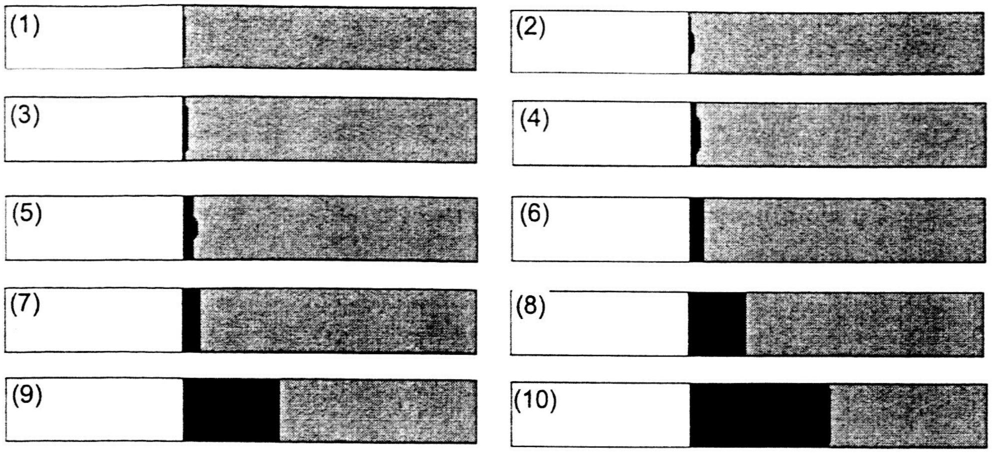

Figure 13. Delamination Front Shapes During Growth for B10 Mesh Pattern

ultimate load. The more refined model does an excellent job in predicting the test results. Since the current 3D-VCCT approach does not require the elements to be orthogonal to the delamination front, it does an excellent job in dealing with the change in delamination shape as growth proceeds. Figure 13 shows the progression of the delamination where the slight deviation from straightness of the front can be seen. These 10 patterns correspond to the 10 load-deflection points noted with circles in Figure 11.

Delamination Growth under Compressive Loading

To further study the sensitivity of the approach to the mesh pattern and the interface element orientation in the more difficult case of delamination buckling and post-buckling, three cases studies were examined. Their geometry and dimensions are shown in Figure 6 and Table 1. The delaminations are embedded in flat laminated plates and have the initial shapes shown in gray color in Figure 14. The three delaminated plates have the same stacking sequence, [0/90/90/D/0], with "D" referring to "Delamination". Therefore, the delamination is located at the interface between the top 0° and 90° plies. The mechanical properties are given in Table 2. The compressive load is applied horizontally (1-direction) on the edge of the plate as a uniform displacement. To initiate the out-of-plane deformation, an imperfection of 2% the plate thickness is prescribed in the center of the plate. The imperfection is imposed upward for the sublaminate above the delamination and downward for the sublaminate below the delamination. This imperfection does not significantly affect the post-buckling behavior of the sublaminates. Geometrically non-linear analysis (NLGEOM) was carried out to include large deformations in the post-buckling stage.

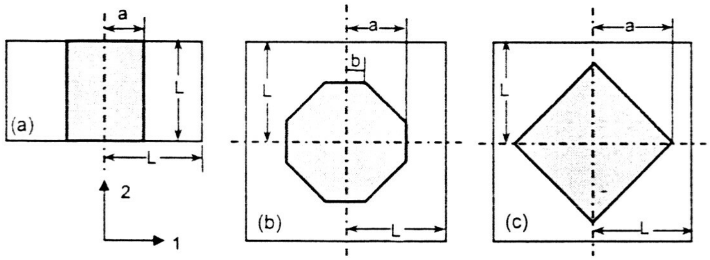

Figure 14. Geometrical Configurations of Delaminations

Each ply of the laminated plate is modeled using ABAQUS brick elements (C3D8) across the 1-2 plane and one element through the thickness. To employ the VCCT, the interface elements are placed

Table 1. Geometry Dimension

	t/L	a/L	b/L
Case (1)	0.02	0.4	N/A
Case (2)	0.0333	0.6	0.2
Case (3)	0.0333	0.8	N/A

Table 2. Mechanical Properties (Carbon/Epoxy)

Stiffness, Poisson's Ratio		Critical G (N/mm)	
E_{11} (GPa)	109.34	G_{IC}	0.306
E_{22}, E_{33} (GPa)	8.82	G_{IIC}	0.632
G_{12}, G_{13} (GPa)	4.32	G_{IIIC}	0.817
G_{23} (GPa)	3.20		
ν_{12}, ν_{13}	0.342		
ν_{23}	0.520		

between the sublaminates to hold the nodes together on opposite sides in the interlaminar region. To support the general loading, three springs are placed at each node to act in mutually perpendicular directions corresponding to the three global coordinates. The stiffness of the springs in the three directions is chosen to be the same value as "k". Due to the large out-of-plane deformation in the post-buckling stage, contact phenomena may be relevant in the delaminated regions. In order to prevent penetrations between the two contacting surfaces, gap elements (GAPUNI) were used to only allow separation of the node pairs in the out-of-plane direction.

Through-the-Width Delamination

The first example involves a through-the-width delamination that is investigated to gain some basic understanding of mesh sensitivity in a simple one-dimensional growth case. The geometrical configuration is shown in Figure 14(a). Due to the symmetry of the geometry and loading conditions, only one half of the structure is modeled. To perform the convergence study, four meshes with varying density were used and are shown in Figure 15. There is only one element across the width so that the delamination is forced to remain straight when it propagates along the 1-direction (local direction). For this specific mesh pattern, the enforced front approach and the front tracing approach using the adaptive normal vector direction predict identical results. Therefore, only one end load (N_x) vs. nominal strain (U/L) is plotted for each mesh density in Figure 16. Note that the four plots corresponding to four mesh refinements have the same initial slope prior to the buckling point. To help see the convergence clearly, the ultimate loads taken from the four plots in Figure 16 are plotted against the number of elements in Figure 17. It can be seen that the ultimate load decreases rapidly as the meshes are refined and tends to approach a constant after the number of elements reaches a certain degree of refinement. This indicates that the solution has converged.

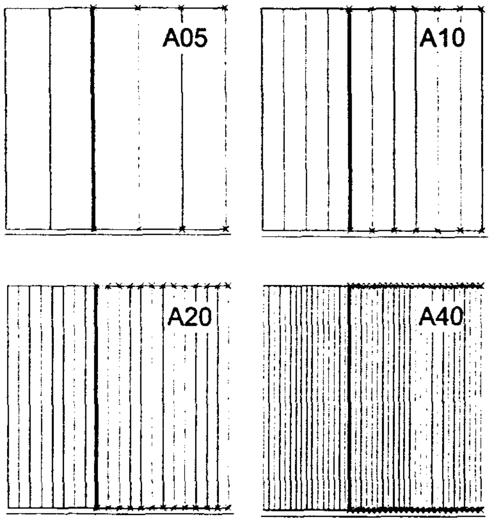

Figure 15. Four Refined Meshes for the Through-the-width Delamination.

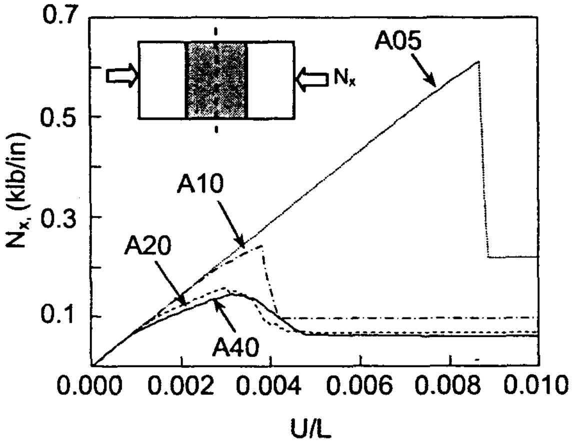

Figure 16. Avg. Running Load N_x vs. Nominal Strain U/L

Another concern is the importance of choosing a proper stiffness value for the spring of the interface element. In order to study this, a series of calculations were performed with varying spring stiffness. The ultimate load $(N_x)_u$ is plotted against the spring stiffness (k) normalized with respect to the longitudinal stiffness (E_{11}) in Figure 18. For each mesh density, there is a valid range for stiffness values that produce the same ultimate load. The calculations will encounter convergence difficulties if the stiffness falls out of the valid range. The finer the mesh, the broader the valid range will be. As expected, the stiffness used has almost no influence on the ultimate load for a wide range of numerical values. In other words, the approach is not sensitive to the interface element stiffness as long as a reasonable value is chosen. For this example, $\log(k/E_{11})=6.0$ or $k=109.34\times10^6$ GPa, which is valid for all of the mesh densities, would be one of many such reasonable values.

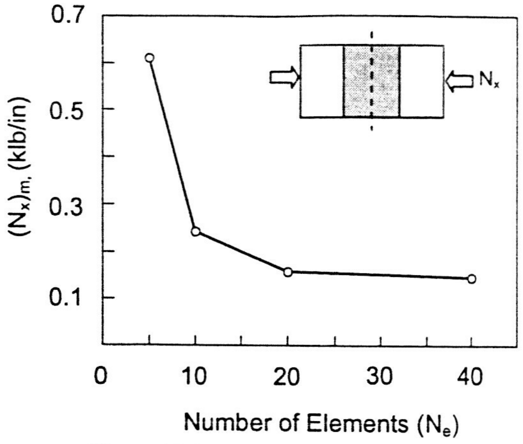

Figure 17. Mesh Convergence Study

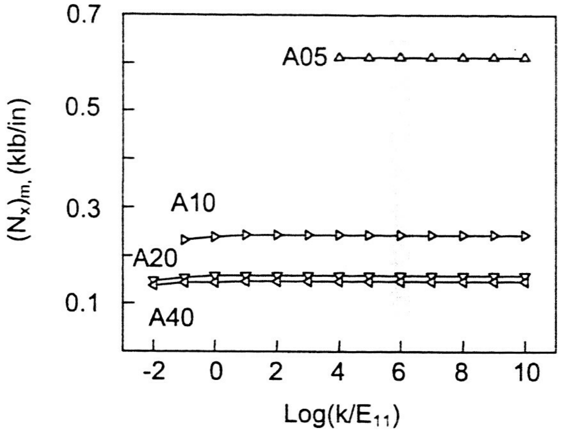

Figure 18. Effect of Spring Stiffness

Octagonal Embedded Delamination

Next, consider an embedded delamination having an octagonal shape shown in Figure 14(b). Due to the symmetry, only a quarter of the plate has been modeled. Two mesh patterns and two interface element orientations were adopted. Investigations were made for combinations of the mesh patterns and the interface element orientations to study the approach's sensitivities to them. Mesh pattern A (MA) and mesh pattern B (MB) are shown in Figures 19(a) and (b), respectively. Each mesh pattern has four meshes of varying densities.

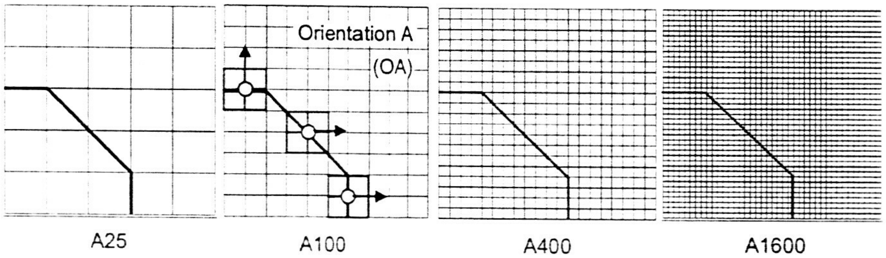

(a) Mesh Pattern A (MA)

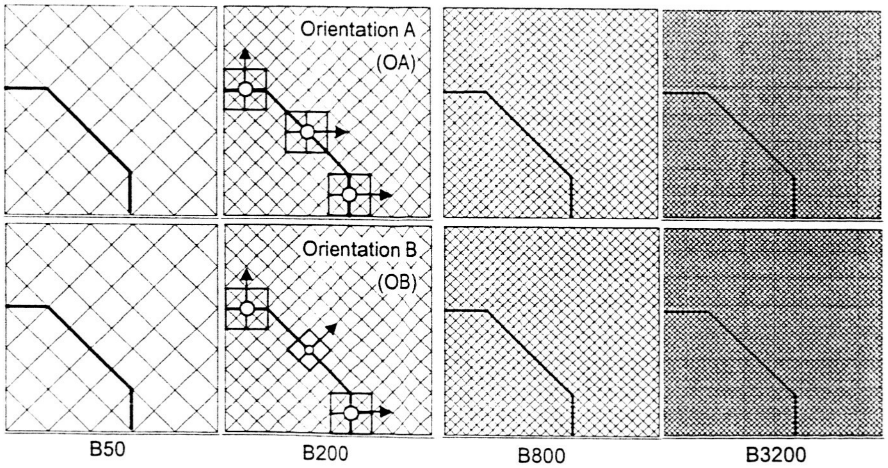

(b) Mesh Pattern B (MB)

Figure 19. Mesh Patterns and Interface Element Orientations for Octagonal Embedded Delamination

Only orientation A (OA) for the interface element was used together with mesh pattern A. This is the baseline problem and only the adaptive normal vector approach is used. Four plots of average running load (Nx) vs. nominal strain (U/L) are shown in Figure 20 for four different mesh densities. Some important features can be observed from the figures. First, the greater the number of elements, the larger the range of loading over which delamination growth can be predicted and followed. For a coarse mesh such as A25, the initial load $(Nx)_i$ at which delamination starts to grow, coincides with the ultimate load $(Nx)_u$. As a consequence, there is no delamination growth observed before the ultimate load. For a refined mesh such as A1600, significant delamination growth occurs between the initiation and ultimate loads. Second, the method converges with respect to mesh refinement for both delamination growth initiation load $(Nx)_i$ and the ultimate load $(N_x)_u$. These loads decrease rapidly as the meshes becomes finer but tend to approach constants after the number of elements reaches a certain degree of refinement.

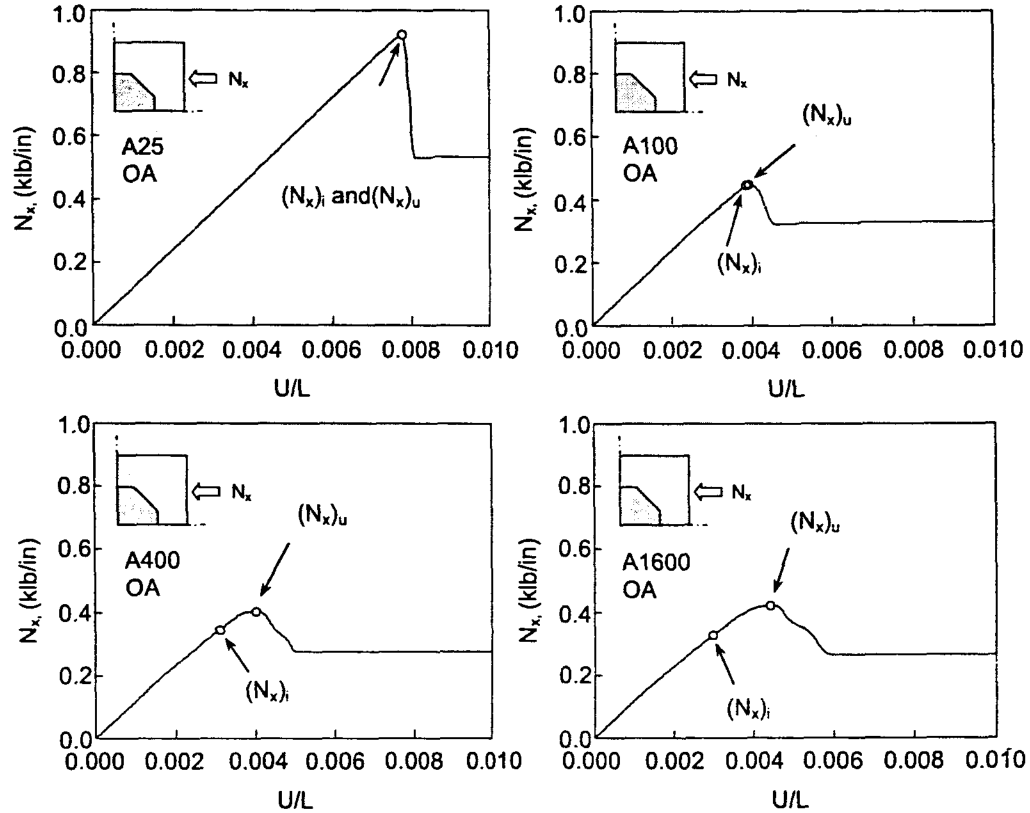

Figure 20. Avg. Running Load N_x vs. Nominal Strain U/L (MA with OA), Front Tracing Approach, Octagonal Embedded Delamination

To study the approach's sensitivity to the approximation of the delamination front normal direction, two orientations (OA and OB) of the interface element were applied to mesh pattern B. The plots of average running load (N_x) vs. nominal strain (U/L) curves obtained from the present approach are shown in Figure 21. Again, the finer the mesh, the larger the load range over which the delamination growth can be traced. It is clear that, regardless of the mesh refinement, the approach predicts two nearly identical curves with the two different orientations of the interface elements (OA and OB). Since the delamination starts to grow at the root of the top horizontal edge where the interface elements have the same orientation for OA and OB, the same growth initiation loads are predicted for mesh B3200. The ultimate loads have a relative difference of 1.64%. This excellent agreement shows that the approach is not sensitive to the orientation of the interface element. The approach works well in detecting the delamination front.

Comparing Figure 20 and Figure 21, the approach's sensitivity to the mesh pattern is clearly seen. There exists a significant difference between the ultimate end load vs. nominal strain curves of two coarse meshes (A25 and B50) because the problems have not converged yet at these mesh densities. As the mesh is refined to A1600 and B3200, the curves get closer. The relative difference between the two delamination growth onset loads for B3200 and A1600 is 2.99%. For the ultimate loads compared to A1600, the values for B3200 with OA and B3200 with OB have relative differences of 2.85% and 1.19%, respectively. The predictions from the two mesh patterns eventually converge to approximately the same constant. The conclusion can be drawn that the approach is not sensitive to the mesh pattern once the mesh is fine enough.

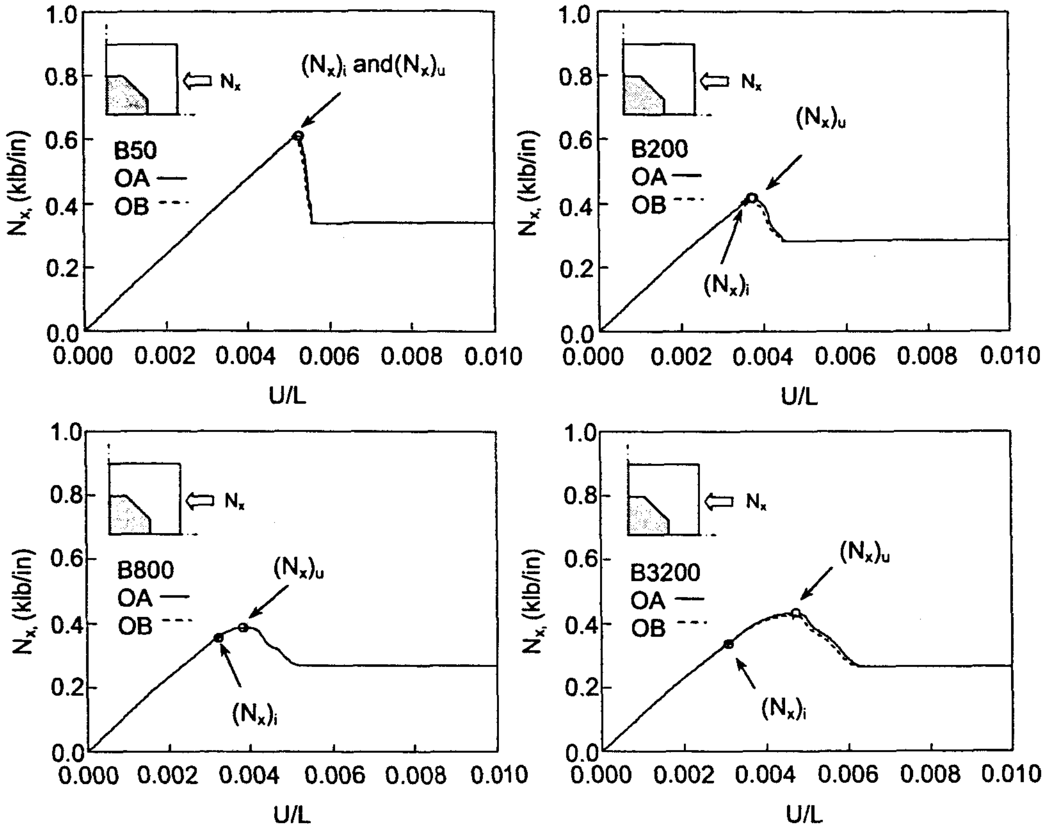

Figure 21. Avg. Running Load N_x vs. Nominal Strain U/L (Mb with OA and OB), Front Tracing Approach, Octagonal Embedded Delamination

It is desired to determine how the results would change if the normal vectors are forced to align with the mesh pattern established according to the delamination shape prior to loading. This approach is the "enforced front" approach. By comparing the dashed and solid lines in Figure 22, a significant difference can be seen between the results for the two different element orientation schemes. Furthermore, this difference is eliminated through mesh refinement. The enforced front algorithm obviously depends on the orientation of the interface elements. Therefore, assuming normal vectors prior to the analysis may prevent the correct result from being obtained even with very refined meshes.

To summarize the above discussion, the ultimate loads $(N_x)_u$ are plotted versus the number of elements (N_e) in Figure 23. One can see that all three meshes (MA with OA, MB with OA, and MB with OB) predict very similar results through using the front tracing approach. If the front is enforced in an appropriate way (such as MB with OB), it may predict a good result. If the front is not enforced correctly (such as MB with OA), it may predict a poor result. Of course, if the front is enforced, one cannot be certain that orientations that are good ones prior to delamination growth remain as good ones after growth. To help understand this behavior, the delamination shapes at U/L=0.004 for different combinations of mesh patterns and interface element orientations are shown in Figure 24. Three combinations using the front tracing approach and MB with OB generate a similar shape for the delamination front at this instant, see Figures 16(a)(b)(c) and (e). However, MB with OA using the enforced front approach predicts a totally different delamination shape as can be seen in Figure 16(d). Based on the above studies, the conclusion can be drawn that with front tracing, all mesh patterns and interface element orientations, even the very simple mesh pattern A with "OA" oriented interface element can achieve very good results.

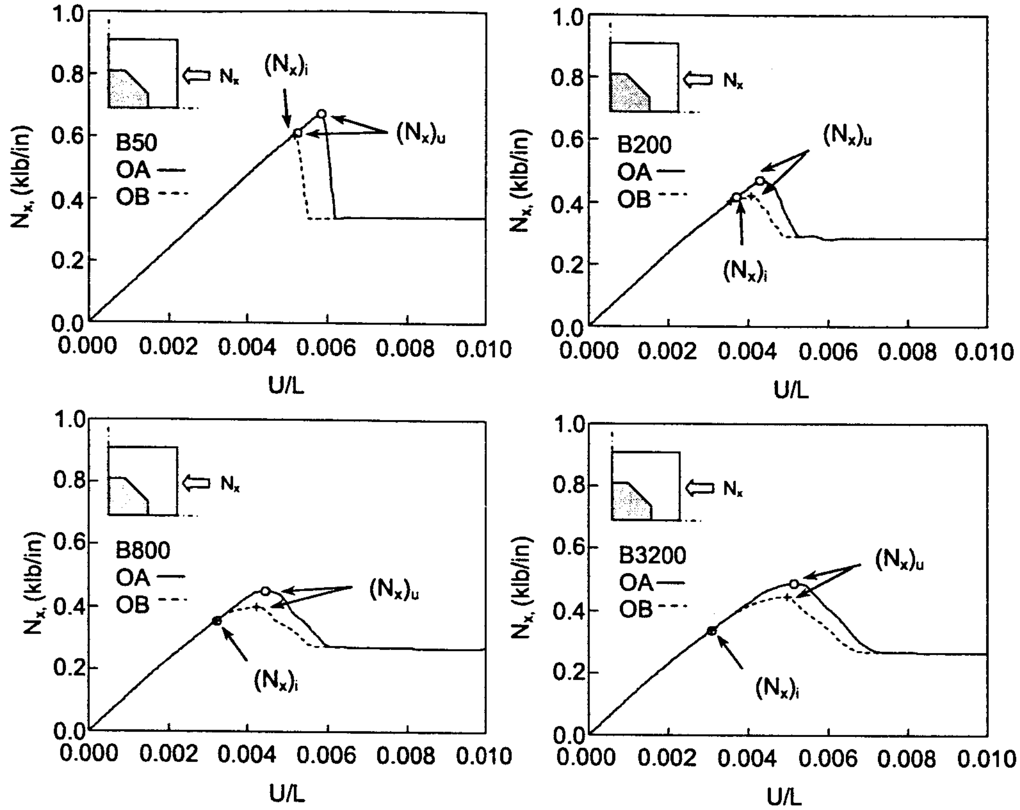

Figure 22. Avg. Running Load N_x vs. Nominal Strain U/L (MB with OA and OB), Enforced Front Approach, Octagonal Embedded Delamination

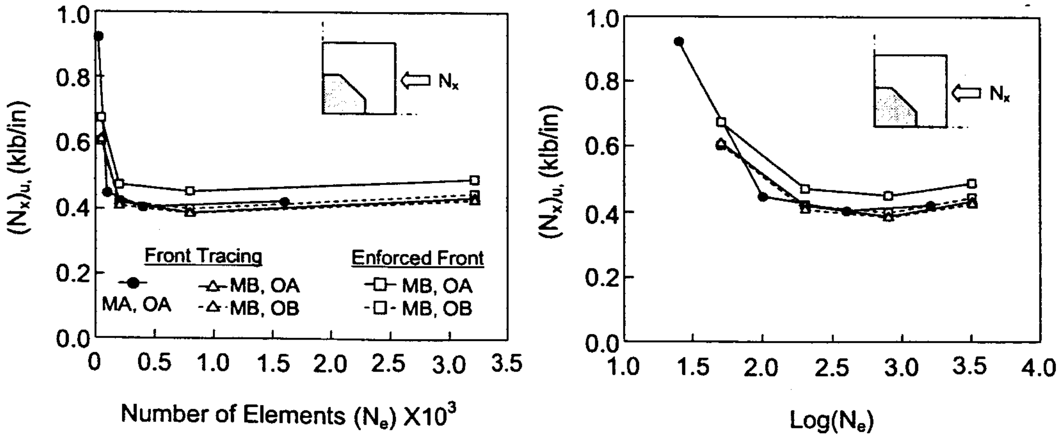

Figure 23. Summary for Octagonal Embedded Delamination

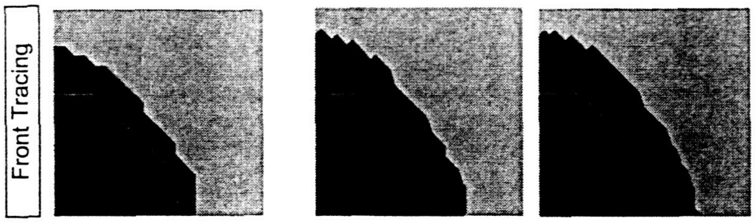

(a) A400, OA (b) B800, OA (c) B800, OB

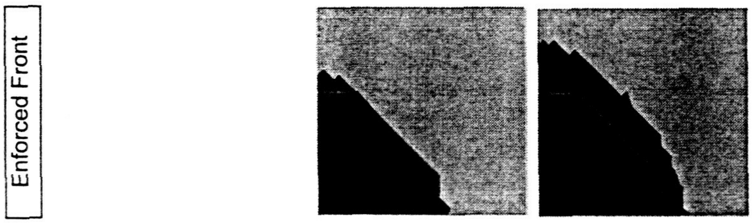

(d) B800, OA (e) B800, OB

Figure 23. Front shape for octagonal embedded delamination at U/L=0.004

3.3 Square Embedded Delamination

Finally, the same analysis procedure was also used to study a square shaped embedded delamination having the geometry shown in Figure 14(c). The definitions of the mesh pattern (MA and MB) and the interface element orientation (OA and OB) are the same as those for the octagonal embedded delamination discussed in the previous section. Again, "OA" oriented interface elements were imposed on mesh pattern A to provide a baseline problem and the front tracing approach was used. Results very similar to those discussed above were obtained for this delamination shape. As a summary, for all the cases considered here, the ultimate loads $(N_x)_u$ are plotted versus the number of elements (N_e) in Figure 24. These results once again demonstrate the ability of the current approach to capture significant aspects of the delamination front shape and location during delamination growth.

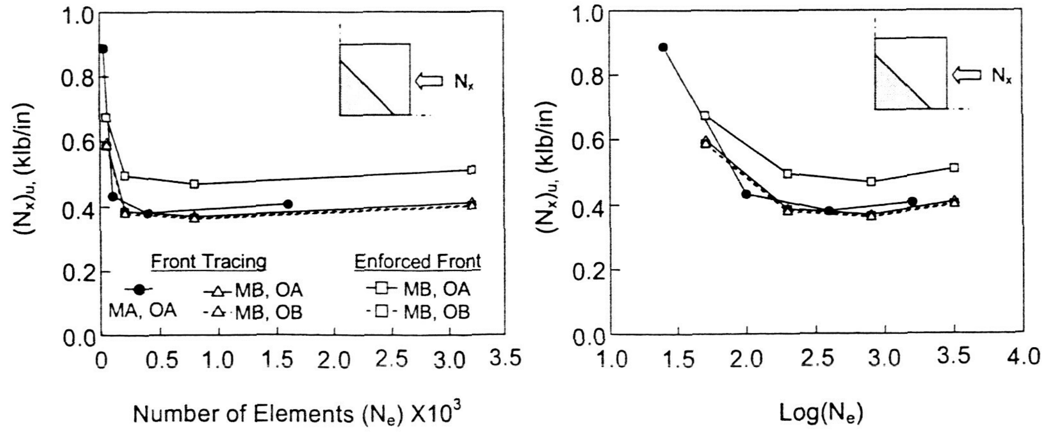

Figure 24. Summary for Square Embedded Delamination

Delamination growth in an irregularly shaped 2-D delamination

As a more difficult and realistic test of the present 3D-VCCT method, a delamination with an initially complex shape and its growth to laminate failure are considered here. De Moura[12] et al. presented a study of growth of a delamination created by a low-velocity impact event in a panel that is loaded in compression. Their experimental test data are used here for comparison. They also developed a computational method to track delamination growth based on an indirect usage of fracture mechanics, a material softening approach to damage development, and a penalty approach to prevent interpenetration of delaminated layers. The current approach differs in its direct application of mixed mode fracture mechanics through the 3-D VCCT method described earlier, immediate failure once the fracture criterion is satisfied, and standard gap elements to directly eliminate layer interpenetration.

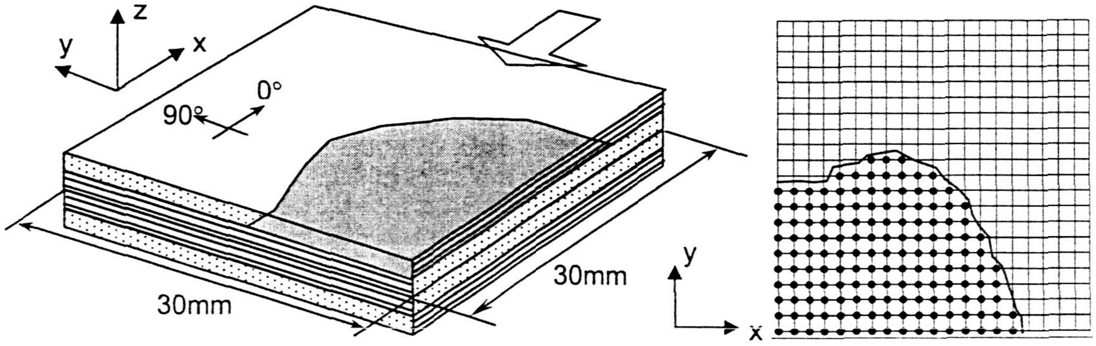

(a) Geometry and Load Direction, ¼ Plate

(b) Shape of Delamination

Figure 25. Delaminated Plate and Finite Element Mesh

This application uses the same $[0_4/90_4]_s$ graphite-epoxy laminate (see Figure 25(a)) loaded in compression in the 0°-direction that was presented in Ref. [12]. The laminate was impacted with a low-velocity mass resulting in the delamination between the outer 0/90 interface in the shape shown in Figure 25(b). The linear combination of energy release rate ratios

$$E_d = \frac{G_I}{G_{IC}} + \frac{G_{II}}{G_{IIC}} + \frac{G_{III}}{G_{IIIC}} \ge 1$$

was used as the fracture criterion. The same material properties, layer thicknesses, and initial imperfection stated in Reference [12] were used herein. The model used here contained 4 solid elements (ABAQUS C3D8I) through the thickness and a 20 x 20 mesh of elements across the plan of ¼ of the plate. Symmetry

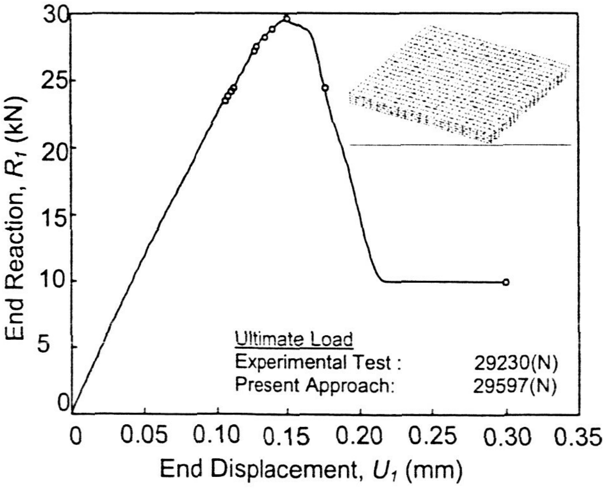

Figure 26. End Displacement vs. End Reaction

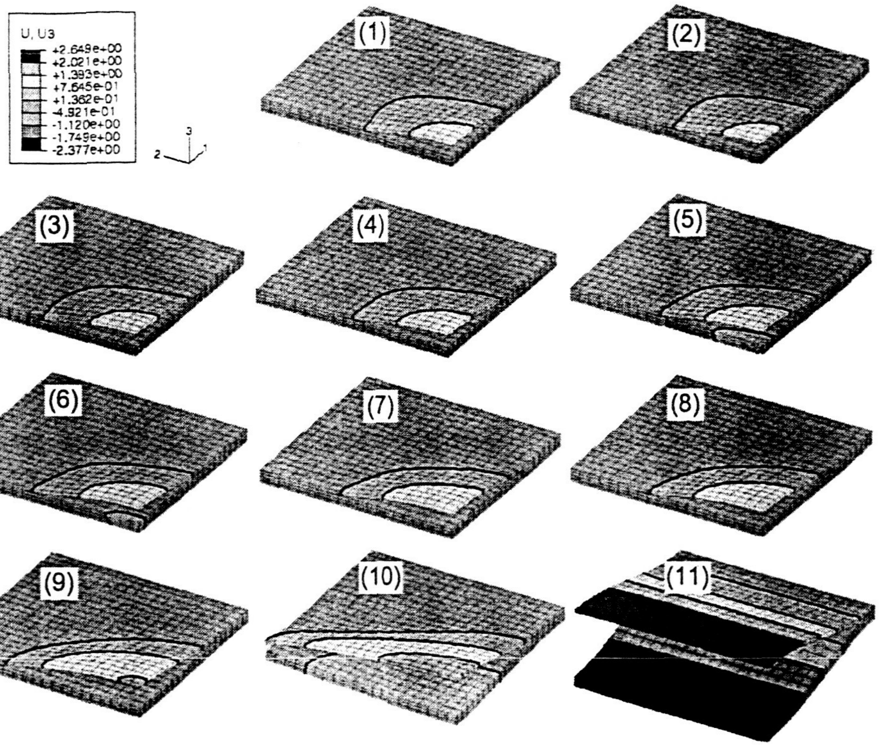

Figure 27. Contours of the U_3 During Delamination Growth

conditions were used at the plate center lines and the unloaded edge is free. Interface elements were included at the upper 0/90 interface.

Predicted load displacement data are plotted in Figure 26. The open circles are particular load levels selected for presentation of information on growth of the delamination in two later figures. The predicted ultimate load is within 1.3% of the measured test load reported in Reference [12]. This is somewhat better than the correlation (3.8% error) with the method presented in that reference. This excellent correlation is remarkable considering the complex shape of the initial delamination and the complex pattern of growth.

Deformed laminates are shown in Figure 27 for the 11 particular load levels identified in Figure 26 as noted above. These plots are oriented in the same way as shown in Figure 14 with the load direction being from lower left to upper right. Plot (1) shows the delamination buckling after the delamination grows to include one additional separated node pair. It is interesting to note that the lower, thicker sublaminate also tends to buckle upward initially. The delamination grows first in the load direction and then generally in the direction transverse to the load direction as the delamination buckle increases in size and separation height. At some point close to ultimate load, the lower sublaminate buckles downward. Plot (9) corresponds to the deformed shape at ultimate load. When additional end displacement is applied, the delamination grows rapidly to the free, unloaded edge of the plate (plot (10)) and then continues to grow until it encompasses the whole interface (plot (11)).

The progression of the delamination can be seen in more detail in Figure 28. The 11 plots here correspond to the same 11 plots shown in Figure 27. Here the initially delaminated node pairs are shown as black circles and the shape of the initial delamination is shown. The open circles indicate delaminated node pairs at increasing load levels. The progression of the delamination is easy to follow in this set of plots. The progression predicted here is slightly different from the one plot reported in Reference [12] although the general trend and the global characteristics are the same.

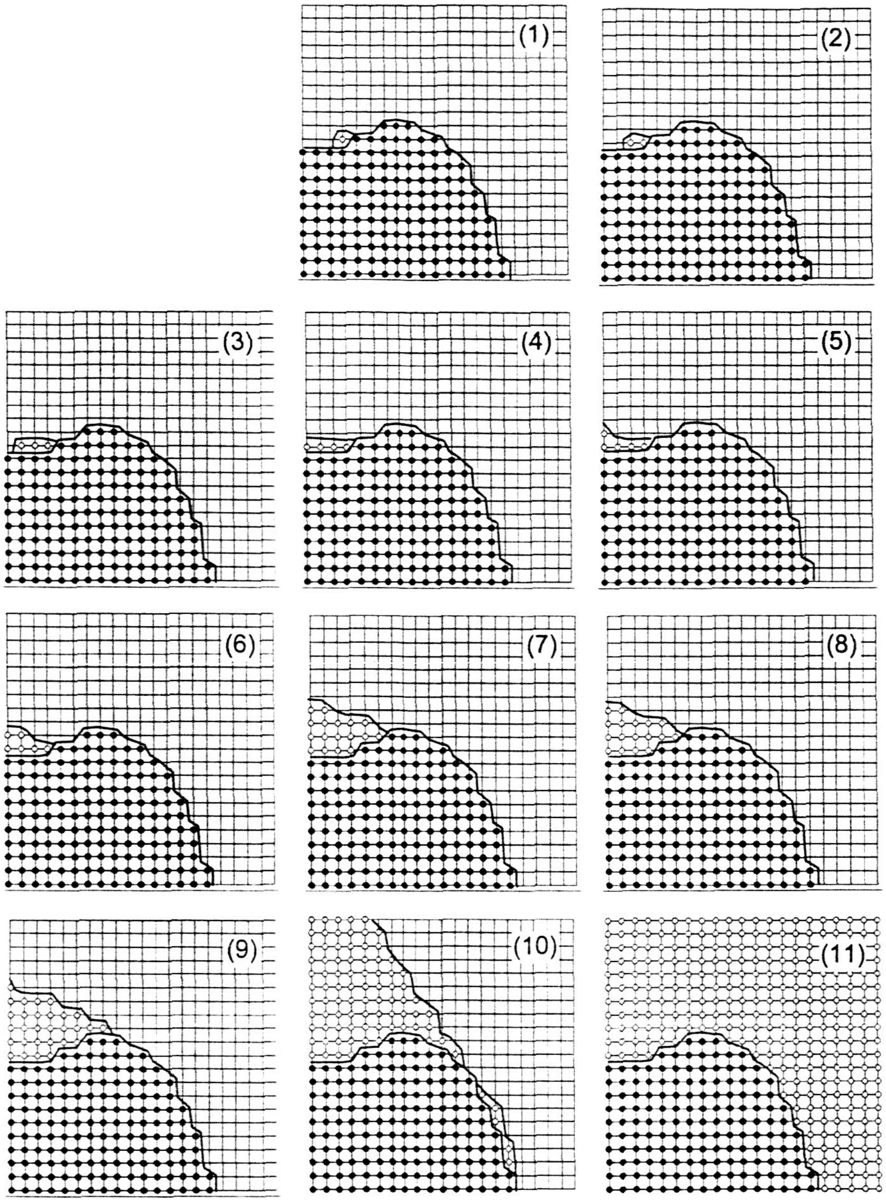

Figure 28. Delamination Front Shapes During Growth

Conclusions

This section of the report has shown that the proposed algorithm for tracing the front of a delamination growing in a non-self-similar way is not sensitive to the values used for the interfacial spring stiffness, the orientation of the interface element, or the mesh pattern if the mesh is reasonably fine. To study these sensitivities, three cases having different initial delamination shapes were examined. Using a simple through-the width delamination, the spring stiffness value was shown to have almost no influence on the predictions as long as the numerical value is selected with a very wide range. For the octagonal embedded delamination, the ultimate loads obtained from different interface element orientations and the same mesh patterns, have a relative difference of only 1.64%. This excellent agreement shows that the approach is not sensitive to the orientation of the interface element. When the mesh is reasonably fine, the relative difference is 2.99% for delamination growth initiation loads and 2.85% for ultimate loads between the two very different mesh patterns. This suggests that the front tracing approach is also not sensitive to the mesh pattern once the mesh has a reasonable density. The above observations are also true in the case of a square embedded delamination and the approach works well in detecting the delamination front. The proposed approach has been shown to be insensitive to the value chosen from the valid range for the interface spring stiffness, the orientation of the interface element, and the mesh patterns once a reasonable refinement has been achieved. This same case shows that an "enforced front" approach can yield very different results even after significant mesh refinement has been achieved.

Finally, it should be noted that no numerical difficulties have been encountered in the cases examined. This indicates that the approach is robust and easy to apply. The proposed front tracing method provides the capability of using relatively simple mesh patterns to simulate the moving delamination of an arbitrary shape without adapting the mesh as the delamination shape changes. The approach should prove to be valuable in future studies of delamination growth. In fact, it will be used in conjunction with the development of an approach to modeling through-the-thickness stitching described in the next section.

References for this section.

1. Chai, H., Babcock, C.D., and Knauss, W.G., One-Dimensional Modeling of Failure in Laminated Plates by Delamination Buckling, *International Journal of Solids and Structures*, **17** (1981): 1069-1083
2. Chai, H., and Babcock, C.D., Two-Dimensional Modeling of Compressive Failure in Delaminated Laminates, *Journal of Composite Materials*, **19** (1985): 67-98
3. Yin, W. -L., Recent Analytical Results on Delamination Buckling and Growth, Key Engineering Materials, **37** (1989): 253-268
4. Kardomateas, G.A., Postbuckling and Growth Behavior of Face-Sheet Delaminations in Sandwich Composites, Thick Composites for Load Rearing Structures, *AMD* Vol.**235** (1999): 51-60
5. Rybicki, E.F., and Kanninen, M.F., A Finite Element Calculation of Stress Intensity Factors by a Modified Crack Closure Integral, *Engineering Fracture Mechanics*, **9** (1977): 931-938
6. Shivakumar, K.N., Tan, P.W., and J.C., Newman, Jr., A Virtual Crack-Closure Technique for Calculating Stress Intensity Factors for Cracked Three Dimensional Bodies, *International Journal of Fracture*, **36** (1988): R43-R50
7. Kutlu, Z., and Chang, F.K., Modeling Compressive Failure of Laminated Composites Containing Multiple Through-the-Width Delaminations, *Journal of Composite Materials*, 1992(26): 350-387
8. Kanninen, M.F., An Augmented Double Cantilever Beam Model for Studying Crack Propagation and Arrest, *International Journal of Fracture*, **9** (1973): 83-92
9. Anderson, T.L., *Fracture Mechanics: Fundamentals and Applications*, Second edition, CRC Press, Boca Raton, FL., 1995
10. Whitcomb, J.D., Analysis of a Laminate With a Postbuckled Embedded Delamination, Including Contact Effects, *Journal of Composite Materials*, 1992(26): 1523-1535
11. Davila, C.G., Camanho, P.P., and de Moura, M.F., Mixed-Mode Decohesion Elements for Analyses of Progressive Delamination, *42nd AIAA/ASME/ASCE/AHS/ASC Structures, Structural Dynamics and Materials Conference*, Seattle, WA, April 16-19, 2001, AIAA-01-1486
12. de Moura, M.F.S.F., Gonçalves, J.P.M., Marques, A.T., and de Castro, P.M.S.T., Prediction of Compressive Strength of Carbon-Epoxy Laminates Containing Delamination by Using a Mixed-Mode Damage Model, *Composite Structures*, **50** (2000):151-157.

(2) FINITE ELEMENT SIMULATION OF STITCHING AS AN APPROACH TO DELAMINATION GROWTH CONTROL

Introduction

In laminated composites, the strength is often limited by their low interlaminar fracture toughness, which makes them sensitive to delamination. There are many causes of initial delamination and this initial delamination can grow into the undamaged area of the composite under certain loading conditions resulting in severe strength degradation. In many applications, the delamination alone may be the strength-limiting factor, especially if it leads to global instability. Therefore, it is very important to control the delamination growth in laminated composites and through-thickness stitching is a very effective way to do this.

Experimental studies [1-5] show that stitching improves the interlaminar fracture toughness up to 15 times under certain loading conditions depending on the stitch material and geometry. Due to this reason, stitching has already been used by many aircraft and composite structural parts industries. Several stitch geometries can be obtained by varying parameters such as stitch materials, fiber/yarn diameter, stitch pattern and stitch density and the interlaminar fracture toughness depends on the stitch geometry. For example, the interlaminar fracture toughness increases in proportion to the stitch density i.e. the number of stitches/unit area. For these reasons, it is important to simulate the delamination growth in laminated composites that are stitched through their thickness to study the effectiveness of stitches as well as to optimize the stitch geometry.

Lalit K. Jain and Yiu-Wing Mai [6] proposed a micromechanics based model to predict Mode I delamination toughness (KIC) for a given stitch parameters using finite difference approach. However, this model does not predict the delamination growth length for the applied load or applied opening displacement. Instead, the delamination growth value, Δa, has to be assumed and KIC can be found out for that particular Δa, for a given stitch parameters such as stitch density, thread material and thread diameter.

J. Byun et al. [7] tried to simulate Mode I regular and tabbed DCB tests conducted by Guenon [2,3] using 2D finite element analysis. Plane stress conditions were assumed. Through-thickness fibers were simulated using 3-noded beam elements. Fundamental inputs to the model were the z-axis fiber properties, fiber architecture, fiber volume fraction and the Mode I critical strain energy rate (GIC) for the 2D laminate. But, this simulation did not model the fiber fracture after elastic stretching. Hence, this analysis cannot be considered to be sufficient to model the Mode I delamination growth process.

Y. Tanzawa et al. [8] modified the model proposed by J. Byun et al. [7] to include the fiber fracture and carried out the numerical analysis. As Byun et al. they modeled the DCB specimen with 2D finite element mesh. The z-fiber bundle was modeled as a 3-noded rod element with a constant sectional area. This model simulates the Mode I delamination growth process reasonably well. However, this model will work only for Mode I DCB case with one particular stitch pattern since (a) it does not calculate GII and GIII and (b) does not model the specimen width.

Methodology

This section of the report proposes an approach to remove the deficiencies presented in the previous numerical simulation attempts mentioned above. This proposed approach models the fiber fracture and it is able to incorporate any stitch pattern since it models the specimen width using 3D elements. And more importantly, the present approach can simulate not only the unidirectional growth of the through-width initial delamination in the baseline Mode I case but also the multidirectional growth of an initial delamination of arbitrary shape in the mixed-mode case. Moreover, the stitch behavior and the delamination growth process have been modeled more realistically by incorporating the unstable crack growth between stitch rows by specifying two critical strain energy release rates such as GIC-unstitched and GIC-stitched at corresponding positions. Hence, in this present simulation methodology, whenever a stitch row breaks, the crack quickly grows and then can be arrested by the next row of stitches as observed in experiments [1-3].

The first step in simulating the delamination growth in laminated composites that are stitched through their thickness is to study how it is observed in experiments. Previous experimental studies showed that the delamination growth process in stitched laminated composites can be either (a) 3-step process as observed by Ogo [1] and Tanzawa et al. [5] or (b) 4-step process as observed by Guenon [2,3] and Dransfield et al. [4].

Figure 1 shows the 3-step delamination growth process. As shown in (A), a matrix crack passed round the thread, and then was arrested at approximately 5 mm past the thread. After loading, the thread was stretched and some debonding occurred along the thread as shown in (B). Finally, the thread failed as shown in (C) and the stored energy was released to propagate the crack at high speed until the next thread.

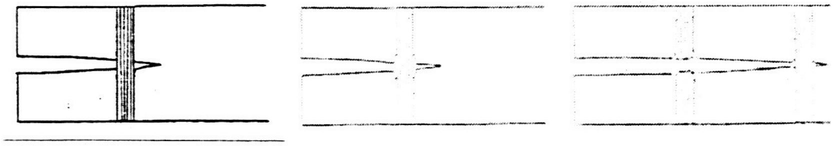

Figure 1. 3-step delamination growth process [1]

Figure 2 presents the 4-step delamination growth process. The first two steps were the same as Ogo's observation. However, in the third step, after debonding, the thread failure occurred inside the matrix material and not at the plane of crack. Finally, in the fourth step, the threads completely debonded and pulled out from the matrix material.

The method proposed herein is based on the following assumptions:

- Fiber fracture is based on Ogo's [1] 3-step delamination growth process as presented in Figure 1. That is, it has been assumed that the fiber fracture occurs at the plane of delamination growth – not inside the matrix material. Hence, the friction between the fractured stitch fiber and the matrix during pull-out is not modeled.
- Since the stitch fibers are flexible and they do not take up any bending loads, an individual stitch has been considered as 1D truss element and the horizontal connecting fibers as shown in Figure 3 are not modeled here.
- It has been assumed that each individual stitch is debonded from the matrix along the thread as shown in Figure 1 (B) as well as in Figure 2 but is attached to both the top surface of the top sublaminate and the bottom surface of the bottom sublaminate of the composite specimen. This attachment simulates the continuity of the horizontal connecting fibers that are not explicitly modeled here.

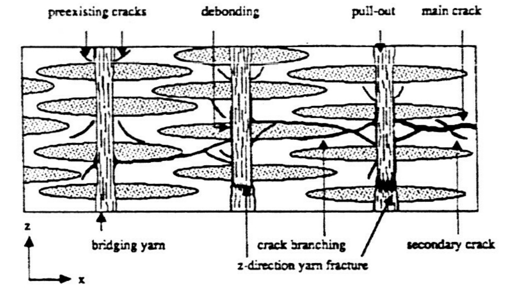

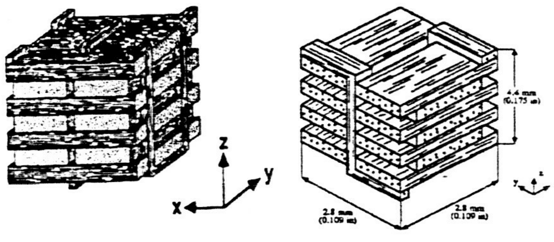

(a) (b)

Figure 3. (a) 3D fiber geometry of orthogonal interlocked fabric, (b) Unit cell of the orthogonal interlocked fabric composite [2,3]

Interface element

Xie [9,10] developed an 18-node "interface element" using the UEL option in ABAQUS to calculate the strain energy release rate (G) numerically based on 3D-VCCT and to simulate the delamination growth in unstitched laminated composites. The advantage of this element is that it can accurately calculate strain energy release rate components at an arbitrarily oriented delamination front and the predicted delamination front at each increment is not required. In other words, it can predict arbitrary multi-directional growth with a single mesh for the geometry throughout the analysis. The element properties i.e. fundamental inputs for this interface element are three spring stiffness values and three critical strain energy release rate (G_{IC}, G_{IIC}, and G_{IIIC}) values for unstitched laminated composites (or 2D laminated composites).

To simulate the delamination growth process in laminated composites that are stitched through their thickness, a new "stitch element" is developed using the UEL option in ABAQUS and this new stitch element has been combined with the previously developed interface element. Hence, the final finite element model for a stitched laminated composite (or 3D laminated composite) specimen, will have two user element definitions to simulate the delamination growth along with standard ABAQUS 8-node brick elements that model the specimen geometry.

While defining the element properties of interface elements for this analysis, two different sets of critical strain energy release rate (G_{IC}, G_{IIC}, and G_{IIIC}) values have to be defined depending on the position of those interface elements. For the interface elements that are located in the positions where the specimen has z-fiber stitch threads, the strain energy release rate of 3D laminated composites, i.e. G_C-stitched, has to be defined. For the other interface elements that are located in unstitched area, the strain energy release rate of 2D laminated composites, i.e. G_C-unstitched, has to be defined. This will simulate the real life situation, which is described as follows.

During Mode I fracture toughness tests, Ogo observed that the crack growth in unstitched DCB specimens was stable. For the stitched specimens, the crack growth was unstable after one row of stitch threads was broken, until it got arrested by the next row of stitch threads. That is, the crack growth in the matrix region between two rows of stitch threads was unstable. According to Ogo, this is because of the different critical energy release rate values, G_{IC}, between the stitched thread area and the unstitched area as shown in Figure 4. G_{IC} was not constant along the beam. Once the threads were broken, energy release rate G is larger than G_{IC} of the unstitched area, i.e. $G > G_{IC}$, which is an unstable condition. Then the energy was released and the crack propagated until the next stitching line in an unstable manner as shown from point A to point B in Figure 4. If there had not been another stitching line, the crack would have propagated until point C.

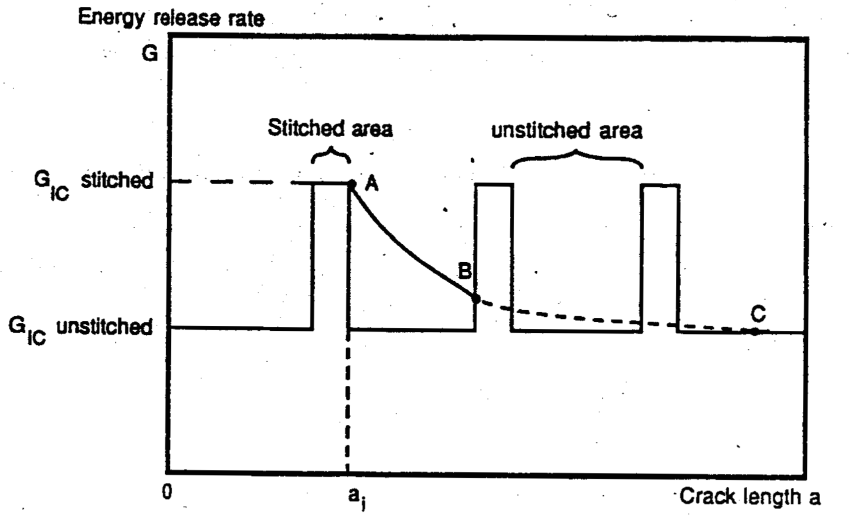

Figure 4. GIC for unstitched and stitched area [3].

Finally, the loads and boundary conditions are specified to the model and solved using ABAQUS/Standard solver. From the output results, the delamination growth area and/or total delamination area can be calculated. A general ABAQUS input file to simulate delamination growth processes in laminated composites that are stitched through their thickness will have a format as shown in Figure 5.

Stitch element

As observed in experiments, an individual stitch crossing a delamination undergoes elastic stretching and eventually fails when its axial stress exceeds the failure strength of the z-fiber yarn. A simple "stitch element" is developed to represent an individual stitch with this behavior. The formulation of this element is based on 2-node truss element. The standard ABAQUS 2-node truss element cannot be used for this purpose because it simulates only the elastic stretching and does not simulate fiber fracture. This necessitated the formulation and development of the stitch element that models the elastic stretching the same as the standard 2-node truss element and extends it to have the fiber fracture.

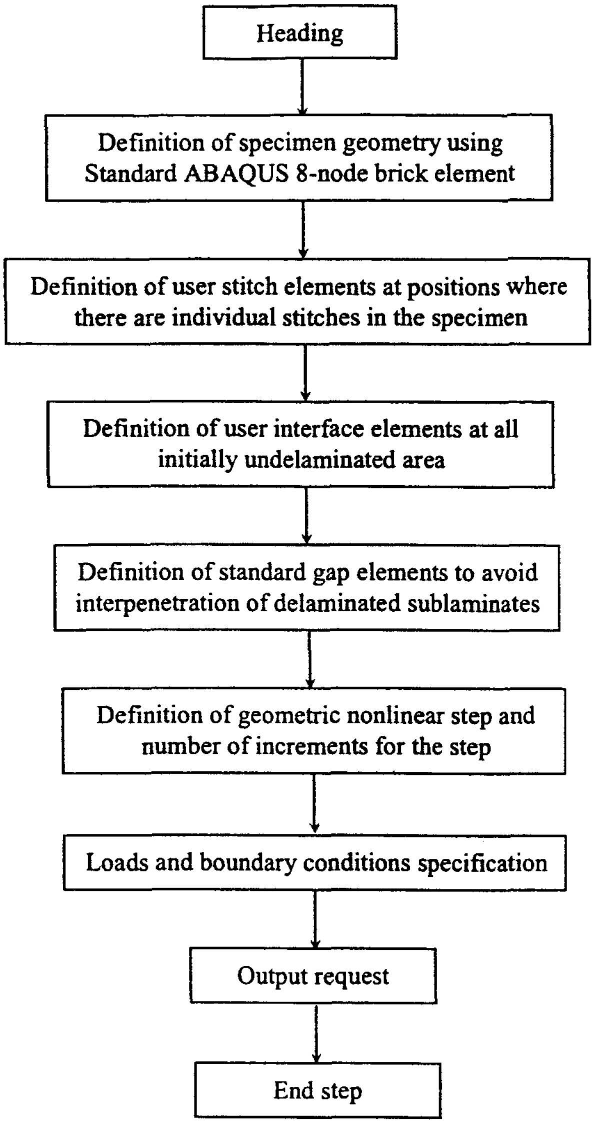

Figure 5. General ABAQUS input file format to simulate delamination growth process in stitched laminated composites.

The element is implemented using the user element subroutine UEL option in ABAQUS. A separate FORTRAN file has been written and is interfaced with the main ABAQUS input file. In UEL, the element is developed by defining the stiffness matrix. The material properties are defined as user element properties in main ABAQUS input file and these values are passed in by ABAQUS whenever it calls the subroutine during the solving process. The loads and boundary conditions are defined in the main ABAQUS input file and this definition accounts for the right hand side force vector. The nodal displacement vector for this element is found by using the ABAQUS/Standard solver. The axial strain and axial stress are secondary variables that are obtained from the derivatives of primary nodal displacement solution in the user subroutine.

The stitch fiber fracture is simulated by setting the element stiffness matrix to zero upon failure of the stitch. The maximum stress failure criterion has been used for this purpose. The fracture occurs when the axial stress of the fiber exceeds the fiber strength. In other words, the element stiffness matrix [K] becomes zero when $\sigma_z > \sigma_f$ where σ_f is the failure strength of the z-directional fiber material. Figure 6 presents the flow chart for the user subroutine UEL that simulates the stitch element. The subroutine is called by the main input file for every load increment. As the applied load increases for each increment, the axial stress σ_z increases. So, whenever the axial stress exceeds the failure strength in a particular increment, the stiffness matrix becomes zero and that element does not bear any load from the next increment until the loading process is complete.

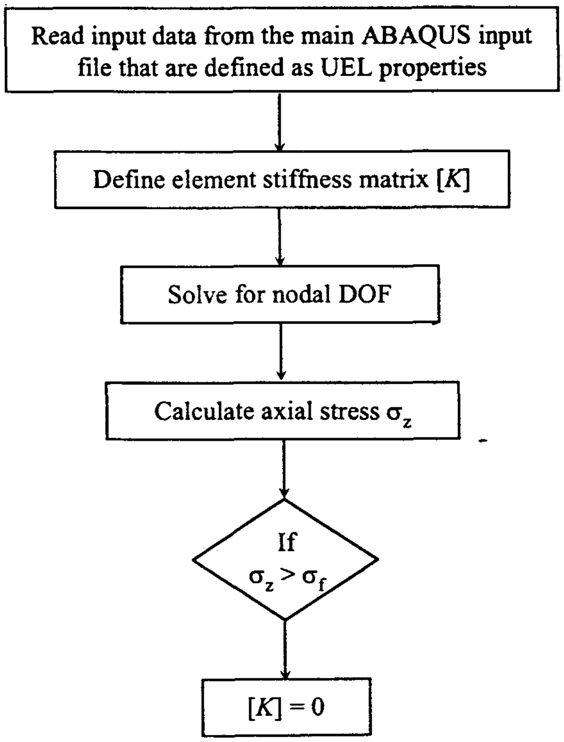

Figure 6. Flow chart for user subroutine UEL that simulates stitch element.

Mode I delamination growth

For the baseline case of Mode I delamination growth, Guenon's [2,3] experimental specimen as shown in Figure 7 was modeled in ABAQUS using 8-node incompatible mode (C3D8I) elements. In Figure 7, length 'L' is 152.4 mm, width 'B' is 19 mm, thickness '2h' is 4.44 mm and initial delamination 'a_0' = 25.2 mm. Gap elements were defined between the two sublaminates to eliminate the possible layer interpenetration after delamination. The stitch pattern as shown in Figure 8 was used for the stitched DCB case. This is the stitch pattern that was used by Guenon [3] for 3D laminate experiments. Stitch elements were defined at corresponding positions to represent individual stitches. Since Guenon's stitched specimen is 3D orthogonal interlocked woven fabric composite, it has carbon fibers in the z-direction as well. The diameter for the stitch element was calculated from the data given in reference [3]. The properties of the specimen and the user stitch element are given in Tables 1 and 2.

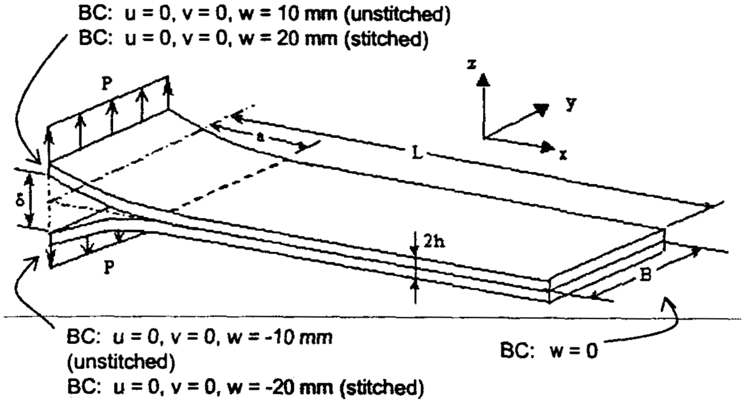

Figure 7. Mode I Double Cantilever Beam (DCB) specimen.

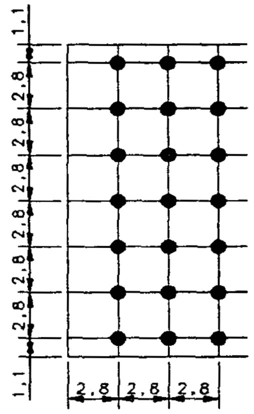

Figure 8. Stitch pattern used in stitched DCB model.

The user interface elements were defined in the initially undelaminated area. The user interface element properties that are specified for the unstitched DCB case is presented in Table 3. For the stitched DCB case, two G_{IC} values were specified. G_{IC} – stitched, which is the fracture toughness value obtained from experiments by Guenon [2,3] for a 3D composite laminate was specified for the interface elements that are in positions where stitch elements were defined. For the remaining interface elements that exist in the unstitched area, G_{IC} – unstitched value was specified. In other words, all the stitch row interface elements have G_{IC} – stitched values where as the interface elements between two stitch rows have G_{IC} – unstitched values. This was done to simulate the unstable crack growth between stitch rows observed by Ogo [1] as discussed before. The G_{IC} – stitched and G_{IC} – unstitched values that were used in the analysis are presented in Table 4. The other properties are the same as presented in Table 3 for all the interface elements in the stitched DCB model.

Displacement controlled analysis was performed for both stitched and unstitched cases. A linearly increasing vertical displacement 'w' was specified for the nodes at the initial delamination end of the specimen and the reaction force was requested as an output. The other displacements 'u' and 'v' in those nodes were restrained to simulate the hinge load condition. The vertical displacements 'w' for the nodes at the undelaminated end surface were restrained. The boundary conditions for both cases are shown in Figure 7. For both cases, the finite element mesh had 218 elements along x-direction, 8 elements along y- and 1 each for the sublaminate in the z-direction. Geometric nonlinear analysis was performed with direct control time incrementation.

Numerical Results

Figure 9 presents the load-displacement curve for the stitched DCB model. The delamination growth contour plots that show the total delamination length ‘a’ and the delamination growth area ‘ΔA’ corresponding to the positions shown in the load-displacement curve in Figure 9 are presented in Figure 10. The white area is the initial delamination, the cross marks represent broken stitches, and the dark gray area represents delamination growth. As the applied opening displacement increases, the reaction force increases steeply up to point 1 since the first row of stitches bear the load and

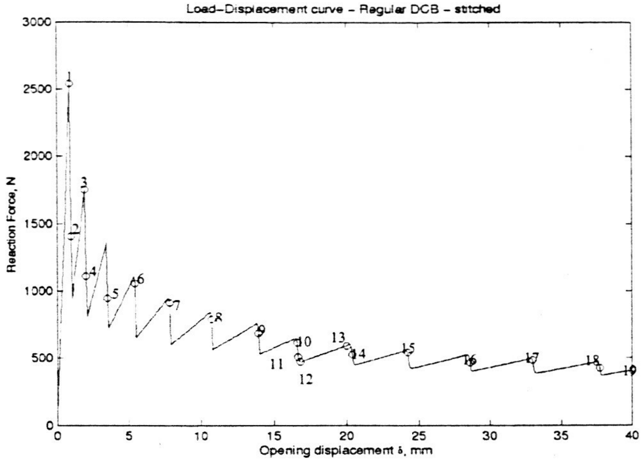

Figure 9. Load-displacement curve for the stitched DCB model.

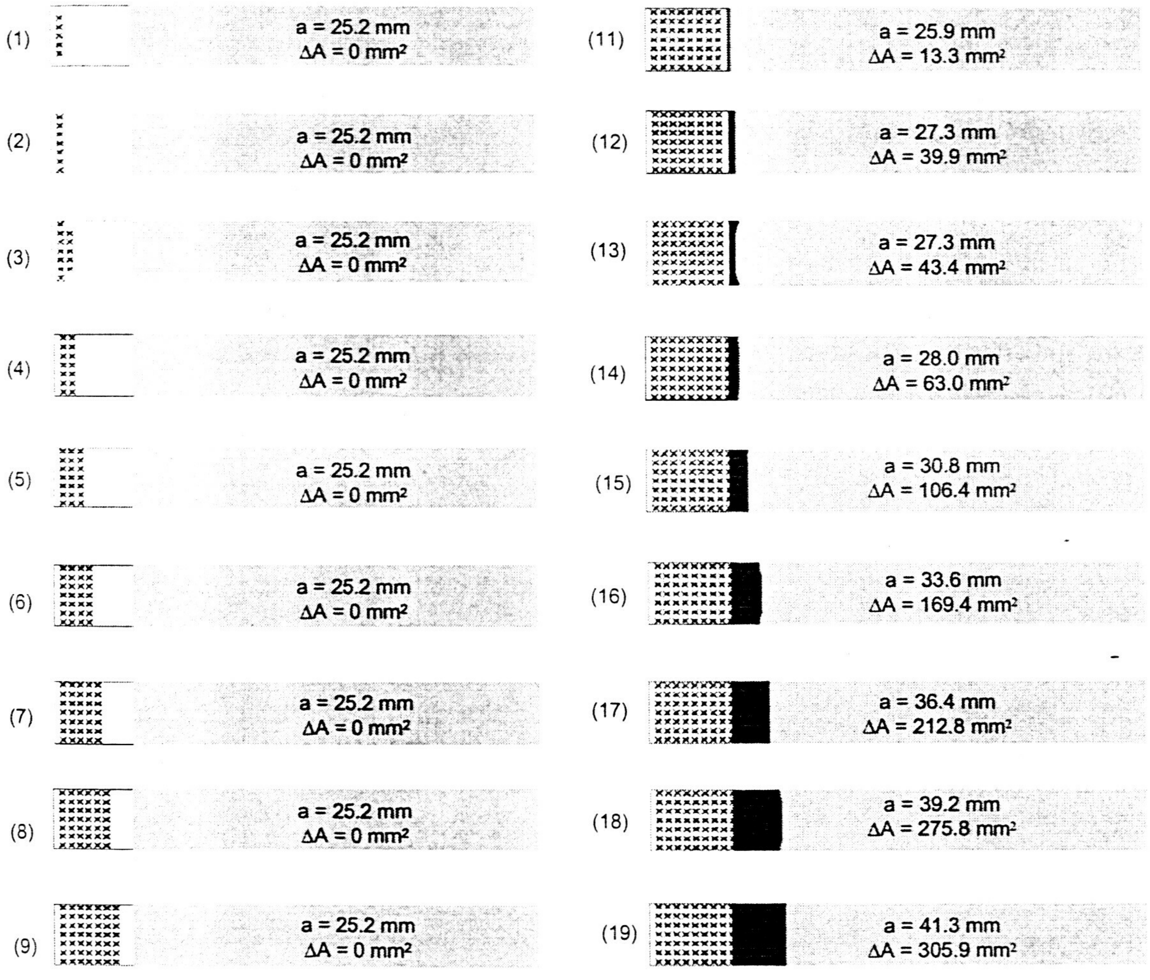

Stitches Breaking **Stitches Breaking & Delamination Growth**

Figure 10. Delamination growth contour plots at various load-displacement points – stitched DCB model.

elastic stretching of first row of stitches occurs during this period. At point 1, as shown in Figure 10, five center stitches in the first row fail and hence there is a sudden drop in reaction force after point 1. Furthermore, at point 2, the remaining two stitches in the first row break and the reaction force drops further. Again the reaction force increases up to point 3 and now the second row of stitches carries the load. When the applied opening displacement reaches point 3, the five center stitches in the second row fail as in the first row. Hence the reaction force drops down to point 4 and at that point, the rest of the stitches in the second row fail. This causes another drop in the reaction force after point 4. Similarly, the behavior of the laminate and the stitches for other points in the load-displacement curve can be observed from Figure 10.

The initial delamination in the specimen does not grow until the opening displacement reaches point 11, i.e. $\delta = 16.64$ mm. From this point onwards, the initial delamination starts growing as shown in Figure 10. At this instance, it can be observed that the 9th row of stitches, which are precisely located at the initial delamination front, have not failed yet. From Figure 10, it can be seen that these stitches still undergo elastic stretching at this opening displacement. Even at position 13, no stitches in that row have failed. Thus the method exactly simulates step one of the delamination growth process, i.e. the delamination grows past round the stitches and then gets arrested at some distance past those stitches, observed experimentally by Ogo [1], Guenon [2,3] and other researchers. Further increases in the opening displacement cause additional rows of stitches to fail and the delamination continues to grow in a controlled way. When the opening displacement $\delta = 40$ mm, the total delamination length 'a' is 41.3 mm and the delamination growth area 'ΔA' is 305.9 mm^2.

Figure 11 presents the behavior of the edge stitches in each row as the opening displacement increases from 0 to 40 m. As the applied opening displacement increases, the axial stress in the first row stitch increases until it breaks. This increase in axial stress is accompanied by the elastic stretching of that stitch. When the axial stress exceeds the failure strength 'σ_f' of the stitch material, the stitch fails. In Figure 11, the cross marks again indicate the stitch failure. Figure 12 presents applied opening displacement versus total delamination length 'a' plotted for the stitched DCB model. It can be observed that the initial delamination 'a_0' does not grow until applied opening displacement reaches the value of 16.64 mm. After this point, it quickly grows up to 27.3 mm and is then arrested by the next row of stitches. This shows that the simulation behavior conforms to the unstable growth behavior between stitch rows observed by Ogo [1].

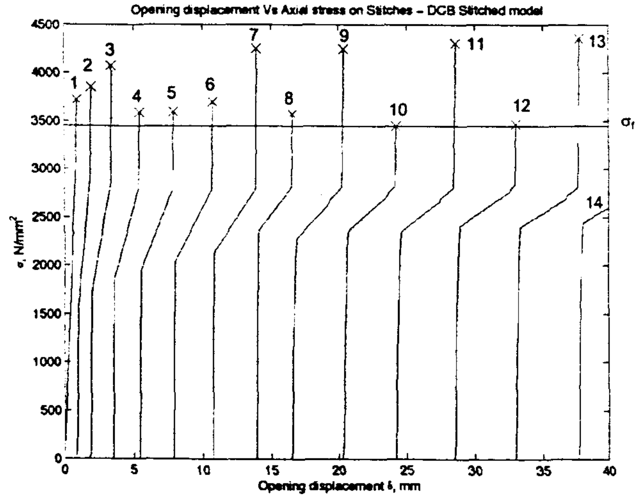

Figure 11. Elastic stretching and failure of stitches for $\delta = 0$ to 40 mm.

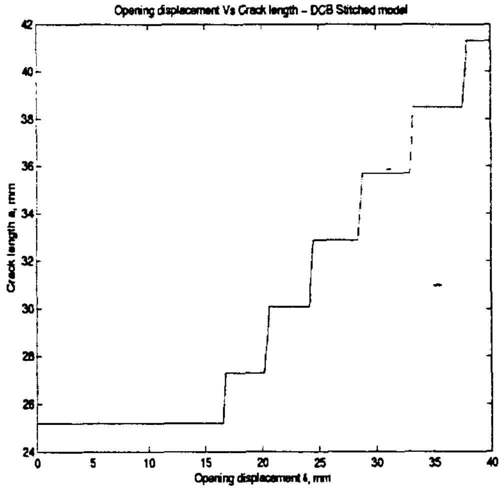

Figure 12. Applied opening displacement 'δ' versus total delamination length 'a'.

Effects of stitches

The effects of stitches can be observed by comparing the results of the stitched DCB model with those of the unstitched DCB model. The load-displacement curves of both unstitched and stitched DCB models for $\delta = 0$ to 20 mm have been plotted for comparison in Figure 13 where the dashed line represents the unstitched model and the solid line represents the stitched model. For the same applied opening displacement, there is a huge rise in the reaction force due to the inclusion of stitches. Hence, it can be concluded that the through-thickness stitches greatly improve the z-directional resistance of the specimen. Similarly, Figure 14 compares the variation of total delamination value 'a' as the opening displacement increases from 0 to 20 mm. In the unstitched model, the initial delamination starts growing from the applied opening displacement value of 2 mm, whereas in the stitched model, the initial delamination does not grow until the opening displacement reaches 16.64 mm. This is due to the improved resistance in the z-direction of the specimen provided by the inclusion of the through-thickness stitches. After the initial delamination starts growing, the growth is more rapid in the unstitched specimen than in the stitched specimen. When the applied opening displacement is at 20 mm, the total delamination in the unstitched specimen is 85.4 mm, whereas in the stitched specimen it is 27.3 mm. Hence, it can be concluded that the stitches effectively arrest the delamination growth and this simulation methodology works well.

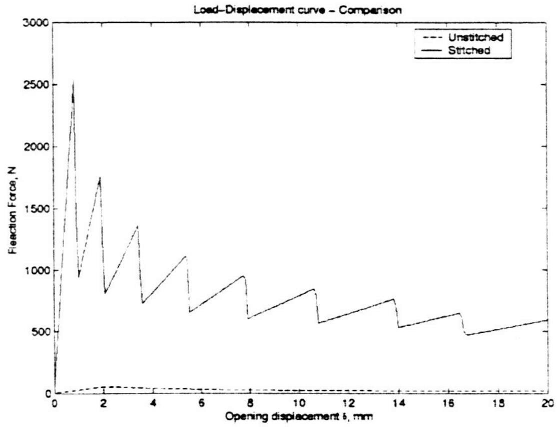

Figure 13. Comparison of load-displacement curves between unstitched and stitched DCB models.

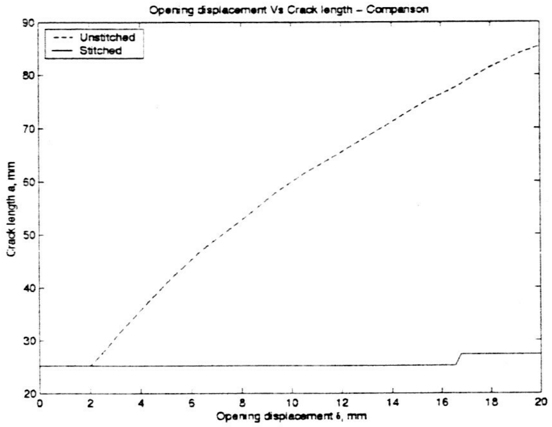

Figure 14. Comparison of total delamination length between unstitched and stitched DCB models.

Mixed-mode delamination growth

For the mixed-mode delamination growth, De Moura's [12] carbon/epoxy laminate specimen that contains an initial delamination of arbitrary shape created by low-velocity impact was modeled. One quarter of the laminate was modeled with C3D8I elements assuming symmetry about both x- and y-axes. The initial delamination of arbitrary shape exists at the interface of the top 0° and 90° sublaminates. The schematic diagram of the ¼ - plate model is presented in Figure 15. The stitch pattern used for the stitched mixed-mode case is also shown. Stitch elements were defined at corresponding positions to represent individual stitches. The properties of specimen and the user stitch element are given in Tables 5 and 6.

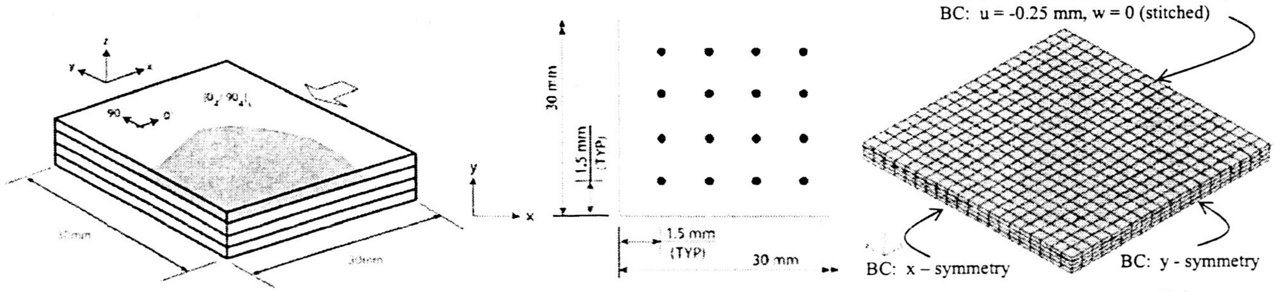

Geometry and applied displacement direction shown on ¼ plate.

Stitch Pattern

FEM mesh and boundary conditions

Figure 15. Geometry definition and modeling details for mixed-mode delamination growth problem.

Gap elements were defined between the top 0° and 90° sublaminates to eliminate the possibility of layer interpenetration after delamination. Also, the user interface elements were defined in the initially undelaminated area between these sublaminates. The user interface element properties specified for the unstitched case are presented in Table 7. For the stitched DCB case, two different G_{IC} and G_{IIC} values were specified. G_{IC} – stitched and G_{IIC} – stitched were specified for the interface elements that are in positions where stitch elements were defined. For the remaining interface elements that exist in the unstitched area, G_{IC} – unstitched and G_{IIC} – unstitched values were specified. The stitched and unstitched critical G values that were used in the analysis are presented in Table 8. All the critical G values were obtained from reference [12].

The finite element mesh and the boundary conditions for both stitched and unstitched cases are presented in the third part of Figure 15. The mesh has 20 elements along x-axis, 20 elements along y-axis and 4 elements through thickness. Displacement controlled analysis was performed, i.e. linearly increasing compressive end displacement along x-axis was applied and reaction force was requested as one of the outputs. Geometric nonlinear analysis performed with direct control time incrementation.

Figure 16 presents the load-displacement curve for the stitched mixed-mode model. The delamination growth contour plots that show the delamination growth area 'ΔA' corresponding to the positions shown in the load-displacement curve in Figure 16 and are presented in Figure 17. As the applied compressive end displacement 'u' increases, the reaction force increases almost linearly until position 1 in Figure 17. At point 1, due to the presence of stitches, the total laminate starts to buckle locally as a plate. Hence, after point 1, the slope of the load-displacement curve varies. No delamination growth occurs until point 3, i.e. u = 0.0985 mm. From this point onwards, the initial delamination starts growing and the load-displacement curve experiences more nonlinear behavior. No stitch has broken throughout the analysis. Instead, the delamination grew in a mixed-mode around the stitches. It has been observed that the specimen

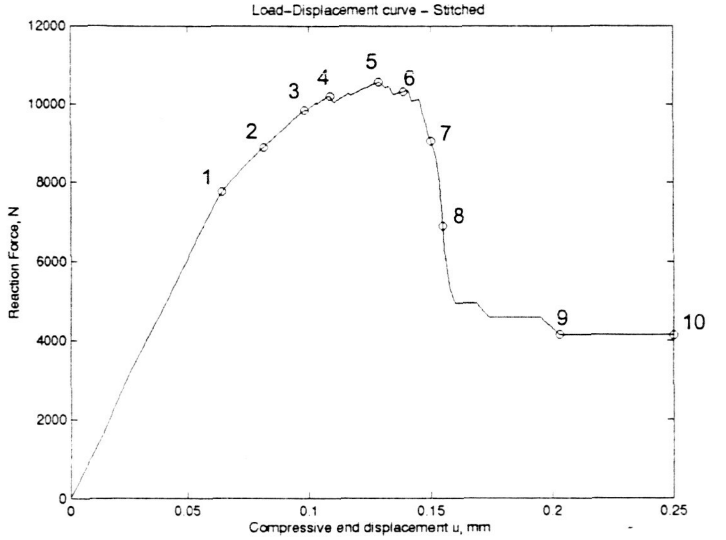

Figure 16. Load-displacement curve for the stitched mixed-mode model.

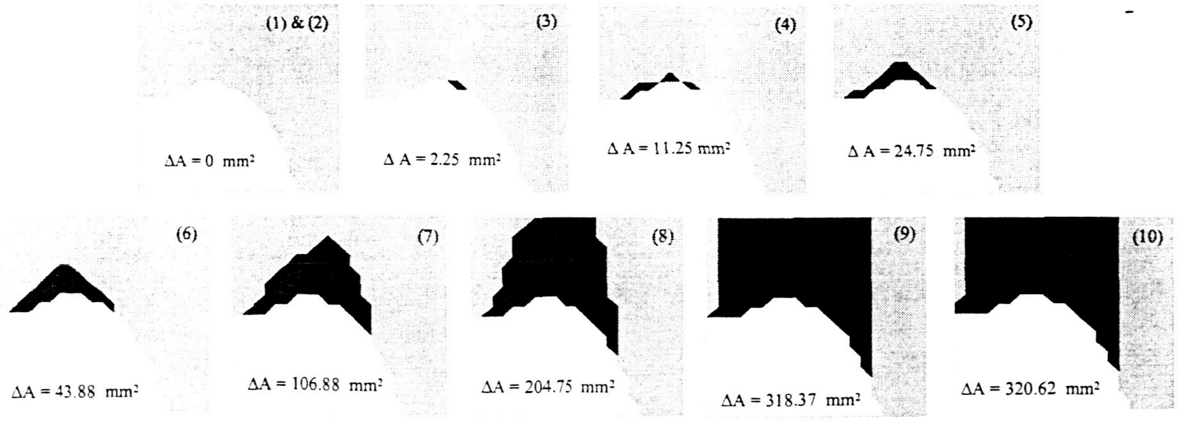

Figure 17, Delamination growth plots for points 1-10 on the load deflection curve.

experiences global wide column buckling from position 9, i.e. when u = 0.203 mm, in the load displacement curve. Also, it was inferred that the delamination growth in this stitched mixed-mode model is dominated by Mode II, which is in-plane shear. This has been discussed in detail in reference [11]. Figure 18 presents the applied compressive end displacement 'u' versus total (initial plus growth) delamination area 'A' plot for the mixed-mode stitched model for u = 0 to 0.25 mm.

The effects of stitches in the mixed-mode case can be observed by comparing the results of the stitched mixed-mode model with those of the unstitched mixed-mode model. The load-displacement curves of both unstitched and stitched mixed-mode models for u = 0 to 0.15 mm have been plotted for comparison in Figure 19. Similarly, Figure 20 compares the variation in total delamination area 'A' as the applied compressive end displacement 'u' increases from 0 to 0.15 mm.

The plot in Figure 19 shows that the peak compressive load increases by a factor of 1.41 due to the inclusion of stitches. Figure 20 shows that in the unstitched model, the initial delamination starts growing when the applied compressive end displacement 'u' is at 0.052 mm, whereas in the stitched model, the initial delamination does not grow until the compressive end displacement value of 0.0985 mm. After the initial delamination starts growing, the growth is more rapid in the unstitched specimen than in the stitched specimen. In the unstitched case, the specimen delaminates completely, which means the total delamination area in the ¼ - plate is 900 mm2 when the applied end displacement 'u' is 0.1045 mm, i.e. before 'u' reaches its applied maximum value of 0.15 mm. Whereas in the stitched case, the total delamination area 'A' in this ¼ - plate when 'u' is at 0.15 mm is 445.5 mm2. Hence, it can be concluded that the stitches effectively arrest the delamination growth and this simulation methodology works efficiently in the mixed-mode case as well.

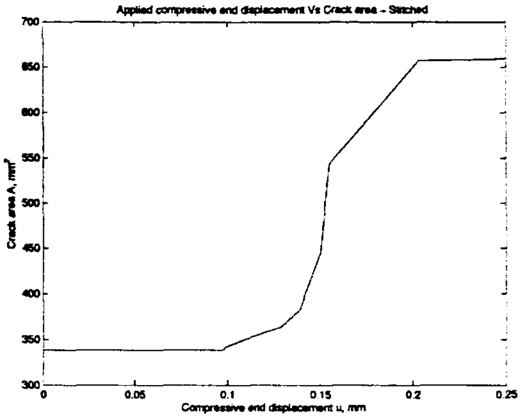

Figure 18. Applied "u" versus total delamination area.

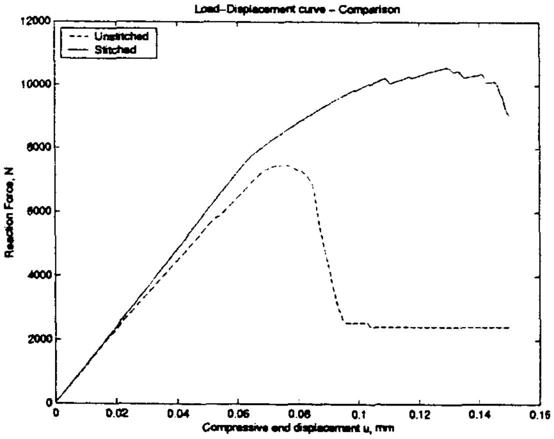

Figure 19. Stitched and unstitched load-displ curves.

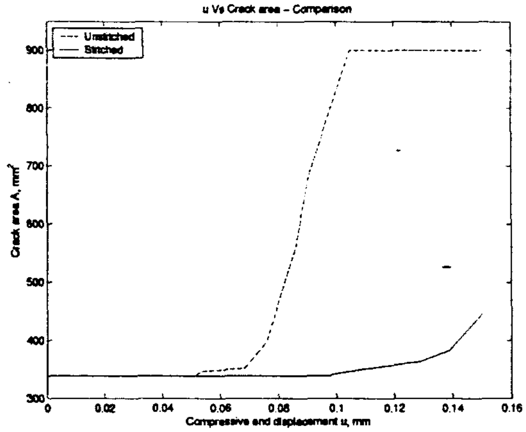

Figure 20. Stitched and unstitched delam-displ curves.

The method can also be used to evaluate the effects of stitching being applied less liberally and concentrated in certain geometric patterns. For example, consider the two patterns shown in Figure 21 for the quarter plate model. The initial delamination, loading, and boundary conditions are unchanged from the previous case. In Figure 22, load deflections plots for these new patterns (#2 and #3) are compared to results for the original grid stitching pattern (here identified as #1) and the unstitched plate. It is seen that the limited stitching can be used to with good effectiveness to increase the ultimate load.

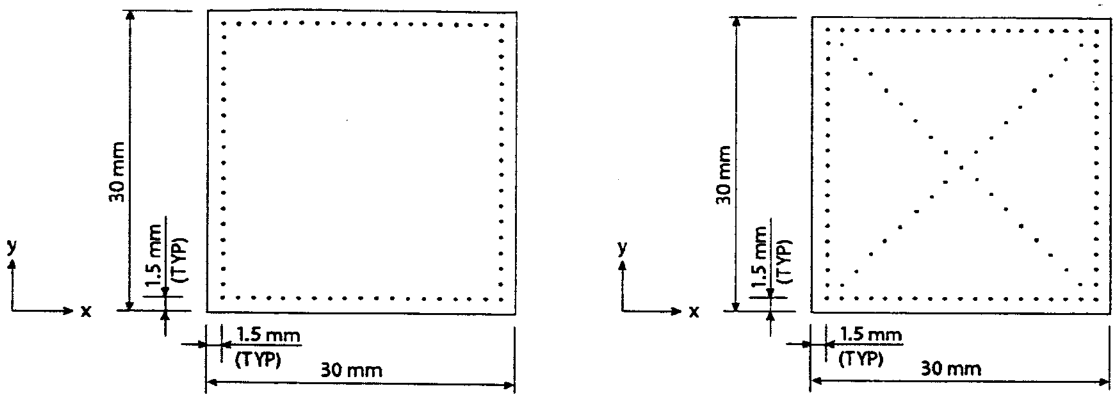

Figure 21. Stitch patterns #2 (left) and #3 (right) applied to the quarter plate model.

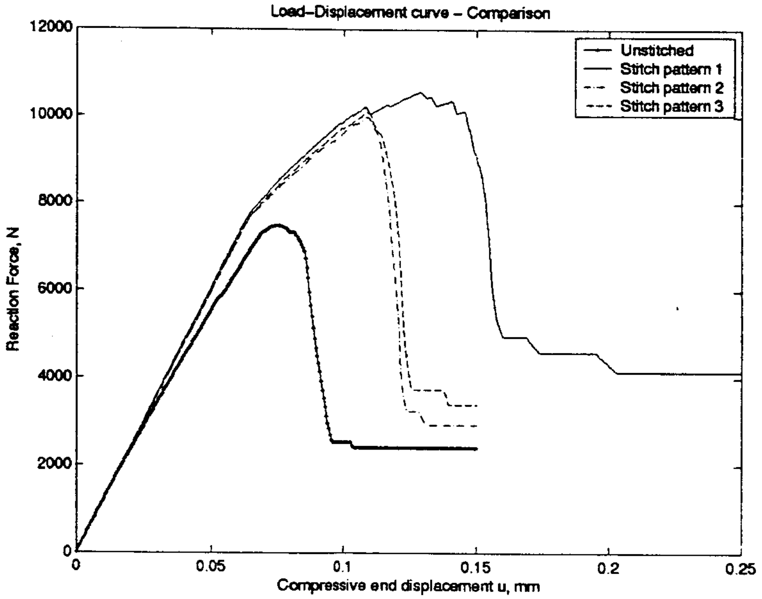

Figure 22. Load-displacment curves for three stitching patterns compared to no stitching.

Conclusions

The purpose of this research was to simulate the delamination growth process in laminated composites that are stitched through their thickness using finite element analysis so that this simulation can complement experimental techniques used to study the effectiveness of stitches as well as to optimize the stitch geometry by varying the parameters such as stitch materials, fiber/yarn diameter, stitch pattern and stitch density for any given loading case. ABAQUS/Standard was used for this purpose and a simple "stitch element" was developed using the UEL user element subroutine option. This "stitch element" was combined with a previously developed 3D-VCCT based algorithm that can trace the moving front of a delamination of arbitrary shape. The proposed methodology was successfully applied for both the baseline case of Mode I delamination growth and the mixed-mode delamination growth. The results showed that this methodology works effectively and simulates the behaviors observed in experiments. Due to the simplicity of this methodology, i.e. modeling an individual stitch and placing it in the laminate at corresponding positions depending on the stitch pattern, various stitch materials, patterns, and densities can also be easily evaluated to optimize the stitch geometry depending on the applications and/or boundary conditions.

References for this section

1. Ogo, Y., “The Effect of Stitching on In-plane and Interlaminar Properties of Carbon/Epoxy Fabric Laminates”, Master’s Thesis, University of Delaware, 1987.
2. Guenon, V. A., Chou, T. W., and Gillespie, Jr., J. W., “Toughness Properties of a Three-Dimensional Carbon-Epoxy composite”, Journal of Material Science, vol. 24, pp. 4168-4175, 1989.
3. Guenon, V. A., “Toughness Properties of a Three-Dimensional Carbon-Epoxy Composite”, Master’s Thesis, University of Delaware, 1987.
4. Dransfield, K. A., Jain, L. K., and Mai, Y. W., “On the Effects of Stitching in CFRPs-I. Mode I Delamination Toughness”, Composites Science and Technology, vol. 58, pp. 815-827, 1998.
5. Tanzawa, Y., Watanabe, N., and Ishikawa, T., “Interlaminar Fracture Toughness of 3-D Orthogonal Interlocked Fabric Composites”, Composites Science and Technology, vol. 59, pp. 1261-1270, 1999.
6. Jain, L. K., and Mai, Y. W., “On the Effect of Stitching on Mode I Delamination Toughness of Laminated Composites”, Composites Science and Technology, vol. 51, 331-345, 1994.
7. Byun, J. H., Gillespie, Jr., J. W., and Chou, T. W., “Mode I Delamination of a Three-Dimensional Fabric Composite”, Journal of Composite Materials, vol. 24, pp. 497-518, 1990.
8. Tanzawa, Y., Watanabe, N., and Ishikawa, T., “FEM Simulation of a Modified DCB Test for 3-D Orthogonal Interlocked Fabric Composites”, Composite Science and Technology, vol. 61, pp. 1097-1107, 2001.
9. Xie, D., and Biggers, S. B., “Strain Energy Release Rate Calculation for a Moving Delamination Front of Arbitrary Shape Based on the Virtual Crack Closure Technique”, Submitted to “Engineering Fracture Mechanics”, 2004.
10. Xie, D., “Damage Progression in Tailored Laminated Panels with a Cutout and Delamination Growth in Sandwich Panels with Tailored Face Sheets”, Ph.D. dissertation, Clemson University, 2002.
11. Rathinasabapathy, M., “Finite Element Simulation of Through-Thickness Stitching as a Means for Delamination Growth Control”, Master’s Thesis, Clemson University, 2003.
12. de Moura, M.F.S.F., Goncalves, J.P.M., Marques, A.T., and de Castro, P.M.S.T., “Prediction of Compressive Strength of Carbon-Epoxy Laminates Containing Delamination by Using a Mixed-Mode Damage Model”, Composite Structures, vol. 50, pp. 151-157, 2000.

Table 1. Carbon/Epoxy laminate properties.

Properties	Values
E_{11}	21.07 GPa
E_{22}	20.76 GPa
E_{33}	8.27 GPa
ν_{12}	0.0357
ν_{13}	0.0426
ν_{23}	0.0426
G_{12}	2.5 GPa
G_{13}	2.0 GPa
G_{23}	2.0 GPa

Table 2. Stitch element properties.

Properties	Values
Cross section area, A	0.151 mm^2
Young's modulus, E	228.0 GPa
Poisson's ratio, ν	0.21
Failure strength, σ_f	3.45 GPa

Table 3. Interface element properties.

Properties	Values
K_1	1.0 E+07 N/mm
K_2	1.0 E+07 N/mm
K_3	1.0 E+07 N/mm
G_{IC}	0.307 N-mm/mm^2
G_{IIC}	0.632 N-mm/mm^2
G_{IIIC}	0.817 N-mm/mm^2

Table 4. Interface element properties.

Properties	Values
GIC – stitched	3.850 N-mm/mm2
GIC – unstitched	0.307 N-mm/mm2

Table 5. Carbon/Epoxy laminate properties.

Properties	Values
E11	109.34 GPa
E22	8.82 GPa
E33	8.82 GPa
ν12	0.342
ν13	0.342
ν23	0.52
G12	4.32 GPa
G13	4.32 GPa
G23	3.20 GPa

Table 6. Stitch element properties.

Properties	Values
Cross section area, A	0.151 mm^2
Young's modulus, E	235.0 GPa
Poisson's ratio, ν	0.21
Failure strength, σ_f	3.73 GPa

Table 7. Interface element properties.

Properties	Values
K_1	1.0 E+07 N/mm
K_2	1.0 E+07 N/mm
K_3	1.0 E+07 N/mm
G_{IC}	0.306 N-mm/mm^2
G_{IIC}	0.632 N-mm/mm^2
G_{IIIC}	0.817 N-mm/mm^2

Table 8. Interface element properties.

Properties	Values
G_{IC} – stitched	3.850 N-mm/mm^2
G_{IIC} – stitched	6.320 N-mm/mm^2
G_{IC} – unstitched	0.306 N-mm/mm^2
G_{IIC} – unstitched	0.632 N-mm/mm^2

Section II: Measurables

Publications during this reporting period:

1. Xie, De, and Sherrill B. Biggers, Jr. "Damage Progression Analysis in Tailored Laminated Plates and Shells with a Cutout," 16th Annual Technical Conference of the American Society for Composites, Virginia Tech, Sept. 2001.
2. Li, Chaodi, Christopher E. Granger, H.D. Schutte, Sherrill B. Biggers, Robert A. Latour, Jr., and John M. Kennedy, "3-D Progressive Failure Analysis Method for Composite Material Applications in Hip Replacements," 16th Annual Technical Conference of the American Society for Composites, Virginia Tech, Sept. 2001.
3. Granger, Christopher E., Chaodi Li, Robert A. Latour, Jr., John M. Kennedy, H.D. Schutte, and Sherrill B. Biggers, "Fatigue Characterization of a Carbon Fiber/PEEK Composite Femoral Component for Hip Joint Arthroplasty Using an Optimized Test Fixture," 16th Annual Technical Conference of the American Society for Composites, Virginia Tech, Sept. 2001.
4. Li, C., Granger, C., Schutte, H.D., Biggers, S.B., Jr., Kennedy, J.M., and Latour, R.A., "Progressive Failure Analysis of Laminated Composite Femoral Prostheses for Total Hip Arthroplasty," Journal of Biomaterials, 23(21):4249-4262 (2002).
5. Xie, D. and Biggers, S.B. , Jr., "Postbuckling Analysis with Progress Damage Modeling in Tailored Composite Plates and Shells with a Cutout," Composite Structures, 59(2):199-216 (2003).
6. Li, C., Granger, C., Schutte, H.D., Biggers, S.B., Jr., Kennedy, J.M., and Latour, R.A., "Failure Analysis of Composite Femoral Components for Hip Arthroplasty," Journal of Rehabilitation Research and Development, V40, No.2, March/April 2003, pp 131-146.
7. Morgan, Dwayne R., Sherrill B. Biggers, and Mica Grujicic, "Carbon Foam Thermal Protection Systems for Space Applications," Earth and Space 2004 Conference, Houston TX, March 2004.
8. Rathinasabapathy, M, and Biggers, S.B., "Finite element simulation of through-thickness stitching as a means for delamination growth control," 2004 ABAQUS Users Conference, Boston, MA, May 2004.
9. Xie, De, and Sherrill B. Biggers, Jr. "Strain Energy Release Rate Calculation for a Moving Delamination Frontof Arbitrary Shape Based on the Virtual Crack Closure Technique," submitted, Engineering Fracture Mechanics (2004).

Proposals during this reporting period:

1. Structures & MataerialsMaterials and Aerodynamic, Aerothermodynamic & Acoustics Technology for Aerospace Vehicles, NASA, participant in team lead by Dynacs, Inc. (submitted, 2004)
2. SRTC Center of Excellence for Metal Hydride Research and Development for Hydrogen Storage/Clemson University, DOE, (submitted, not funded, 2004)
3. Thermal Protection Systems for Space Application, Touchstone Research Lab, $28K (funded, 2003)
4. Advancing Carbon Foam Technology for Thermal Protection Systems, Touchstone Research Lab, 2003, $132K (funded, 2003)

Grants and Financial Awards during this reporting period:

Partly as a result of the work done under Task 1 of this grant, funding was received associated with the proposals 3 and 4 listed above to develop a new material for space application. Work was completed on a multi-year Navy grant spawned by this EPSCoR grant and discussed in previous reports.

Section IV: Participants during this reporting period:

Graduate Students:

Ph.D. Graduate:

De Xie (Chinese, Male)

M.S. Graduate:
Mohan Rathinasababapathy (Indian, Male)

Faculty:
Sherrill B. Biggers, Jr.

Section V: Collaborations

NASA Centers:
NASA Langley Research Center, Hampton, VA:
Dr. Damodar Ambur

Navy Centers:
NSWC Carderock Division, Bethesda, MD:
Patrick Potter

Business and Industry:
Touchstone Research Laboratory, Ltd., Tridelphia, WV:
Dwayne Morgan
ABAQUS Inc., Pawtucket, RI:
Dr. A. Baranski
Bath Ironworks, Inc., Bath ME:
Peter Melhorn, Michael McAleenan
Seeman Composites, Inc., Gulfport, MS:
Dana Ladnier

(2) Damage Tolerance of Mixed-Tow Hybrid, Composite Laminates

John M. Kennedy, Professor of Mechanical Engineering, Clemson Univ.
Josh Stewart, Graduate, Mechanical Engineering, Clemson Univ.

Summary

The objective of this research is to investigate damage tolerance and durability concepts for mixed-tow hybrid (MTH) composites as well as buffer strip panels. An experimental study on MTH composites was completed in the first two years of this project. The data from the experimental program provide the basis for developing a model that can predict the failure behavior of MTH composites. Presently, a two-dimensional finite element code is being developed to predict damage accumulation and progression in a notched buffer strip panel subject to tensile loading. The model must be capable of identifying stress levels in each ply of the laminate as well as predict ply level failures near stress concentrations. The models, once completed, will account for material inhomogeneities, anisotropy, and to some extent characteristic damage.

Another objective of this research is to experimentally examine the combined effect of buffer strips or MTH configurations with through-the-thickness (TTT) reinforcement. Studies in which both techniques have been used together have been limited. This project involves carbon fiber material systems with both techniques employed.

Section I: Narrative

The use of mixed-tow or intraply hybrids as a damage tolerance concept has been investigated at Clemson University. Research is being conducted under two subsets as described below:

(1) Finite Element Analysis of Buffer Strip Panels

An experimental investigation of damage mechanisms in mixed-tow hybrid, center-cracked tension panels was conducted. Five mixed-tow combinations were studied. All mixed-tow plies in the panels were made with uniweave cloth containing periodic placement of glass and carbon tows. A quasi-isotropic and 0°-dominated laminate were evaluated. Results of radiographs and COD measurements indicated that the introduction of glass fibers into carbon fiber panels improved the fracture resistance of those panels. A decreasing carbon tow/glass tow ratio cause the predicted critical-damage zone size to become larger; therefore, the critical strain intensity factor increased, and the panels were less notch sensitive.

Damage tolerance and durability criteria for metals allow damaged structures to be in service until the damage reaches a specified size determined by the critical damage size. Only when a similar durability criterion for composites is established will it be feasible for composites to be the primary structural material in aircraft. The bridge to achieving that standard lies in the incorporation of novel material design concepts other than using excessive material, which increases cost.

Mixed-tow hybridization (often referred to as intraply hybridization) has been shown to improve damage tolerance characteristics over all-carbon systems in tension-loaded composite laminates [1-5]. In [1], it was confirmed that notch sensitivity of a material might be reduced by mixed-tow hybridization with higher failing strain fibers (i.e., S-Glass), as had been previously observed in buffer strip panels [6,7]. In addition to the fiber with higher failing strain, this reduction in notch sensitivity was attributed to the extensive damage that occurred in the notch-

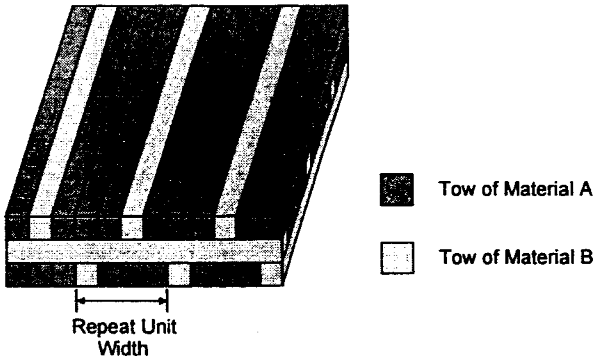

Figure 1. Schematic of mixed-tow hybrid laminate.

tip region prior to final fracture. The introduction of the higher strain and lower modulus fibers into the carbon material system induced more pre-catastrophic damage. A mixed-tow hybrid involves a repeating pattern of a hybridizing tow or tows in some or all plies of a laminate as shown in Figure 1. The hybridizing tows can be readily introduced into the composite fabric in a weaving process.

In [2], S2-glass was used as the hybridizing material since the buffer strip studies found S2-glass buffer-strip material gave the most damage tolerance improvement over all-carbon panels [6]. Further, including hybridizing tows in all plies resulted in a higher strength and fracture toughness than including tows in only the primary load-bearing plies for panels with central slits.

The objective of this paper is to examine the effect introducing hybridizing high failing strain glass tows has on damage mechanisms and consequently, fracture properties of center-cracked tension panels. Two laminate orientations and several mixed-tow combinations were investigated which were not investigated in [1-5]. Mechanisms that result in improved fracture toughness of mixed-tow hybrid composites were identified. The development of subcritical damage at the crack tip was studied using x-radiography. Panel strengths are compared to predictions from a linear elastic fracture mechanics (LEFM) model.

EXPERIMENTAL PROCEDURES

Materials and Specimens

The specimens were made with IM7-6K carbon manufactured by Hexcel and 449 S-2 Glass fiber roving manufactured by Owens Corning. The fibers were woven into a uniweave composite fabric using a 220-denier polyester fill yarn manufactured by Trevira of Hoechst Celanese. Cloth was woven with five mixed-tow combinations: all-carbon, all-glass, and three hybrid system ratios with carbon tow to glass tow ratios of 10:2, 6:2, and 2:2. Figure 2 shows pictures of the uniweave cloth with the five mixed-tow combinations. The tow size was such that there were about seven tows per centimeter. The resin system used in the material was 3501-6 manufactured by Hexcel. Ten sheets were manufactured at NASA

(a) All-carbon (b) 10:2 (c) 6:2 (d) 2:2 (e) All-glass

Figure 2. Composite fiber mixed-tow combinations.

Langley Research Center with a constant mass fraction of 32%. Thus, the fiber volume fraction, V_f, varied due to the different densities of the carbon and glass. All results have been normalized to a common fiber volume fraction.

Two laminate orientations were manufactured using uniweave cloth for every ply. One laminate was a quasi-isotropic layup, $[+45/0/-45/90]_S$, representative of that used in fuselage structure, while the other was a 0°-dominated layup, $[+45/-45/0_2/90/0_2/-45/+45]_T$, representative of that used in wingskin structure. Test panels were cut from the sheets to the sizes shown in the test matrix in Table 1. Two sizes of fracture panels were tested with the notch lengths indicated in the table. Two replicate tests were conducted for each configuration.

Test Procedures and Equipment

All tests were conducted at room temperature in a 250-kN servo-hydraulic testing machine. Panels were loaded to failure at a loading rate of 8.9 kN/min. Load, crack opening displacement (COD), and strain (selected samples) were recorded using a computer-based data acquisition system. COD data was measured with a clip-gage. A steel fixture was clamped to the small panels to prevent out-of-plane displacement at the center of the notch that minimized Mode III loading at the notch tips. For the large panels, an aluminum fixture that spanned the width of the specimen was used to prevent out-of-plane displacement.

Representative results are presented since the large number of tests conducted prevents the presentation of all test results in this paper; however, complete results may be found in [9] including those of unnotched coupons.

Fracture Tests Evaluation

Figure 3 shows the basic COD behavior of the mixed-tow hybrid panels. The

TABLE I. SPECIMEN GEOMETRIES

	2a/W				
	0.063	0.250	0.625	0.313	0.625
Specimen length (mm):	304.8	304.8	304.8	609.6	609.6
Specimen width (mm):	101.6	101.6	101.6	203.2	203.2
Notch length, 2a (mm):	6.4	25.4	63.5	63.5	127

glass in the panels caused arrest-crack behavior represented by the jumps in the curves, much like buffer strip panels. The panels with longer notches generally had more COD and consequently, more precatastrophic damage in the notch-tip region. Also, the 203.2-mm wide panels with a 63.5-mm notch underwent more COD than the 101.6-mm wide panels with the same notch length. There was also more precatastrophic damage in these panels.

Typical radiographic and COD results are shown in Figure 4 for a mixed-tow hybrid panel. The black bar in the middle of the radiographs is the out-of-plane displacement constraint mentioned previously. The damage growth indicated in the radiographs was quantified by sudden increases in COD.

Figure 4 shows the significance of the initial notch-tip location relative to the glass tows and the impact it has on damage modes and the damage-zone size. The first radiograph, taken at 58% of failing stress, shows that little damage developed at the notch tips prior to a significant jump in COD. The left notch tip was adjacent to glass tows in one of the primary load-bearing (0°) plies. At higher stress, some significant matrix cracking in the 90° plies is evident with some delamination close to the notch tip. There is also minimal cracking in the 45° plies, while there is a large axial split parallel to the 0° plies. Conversely, for the right notch tip that was located some distance away from the 0° glass tows, there were no axial splits. The damage developed as matrix cracks in the 45° plies and delamination. The damage did not extend outboard of the 0° glass tows.

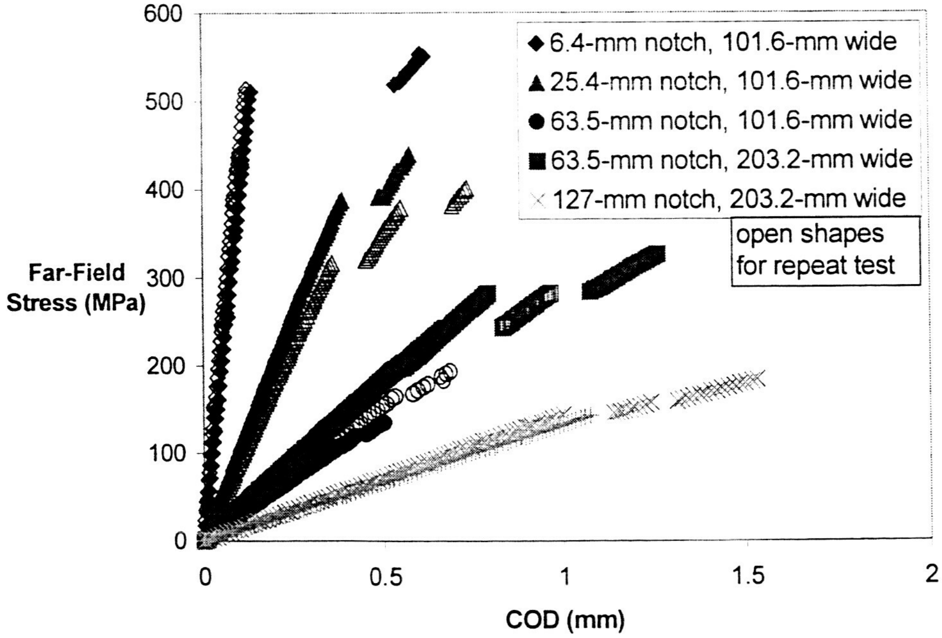

Figure 3. Stress vs. COD for 6:2 ratio, $[+45/-45/0_2/90/0_2/-45/+45]_T$ panels.

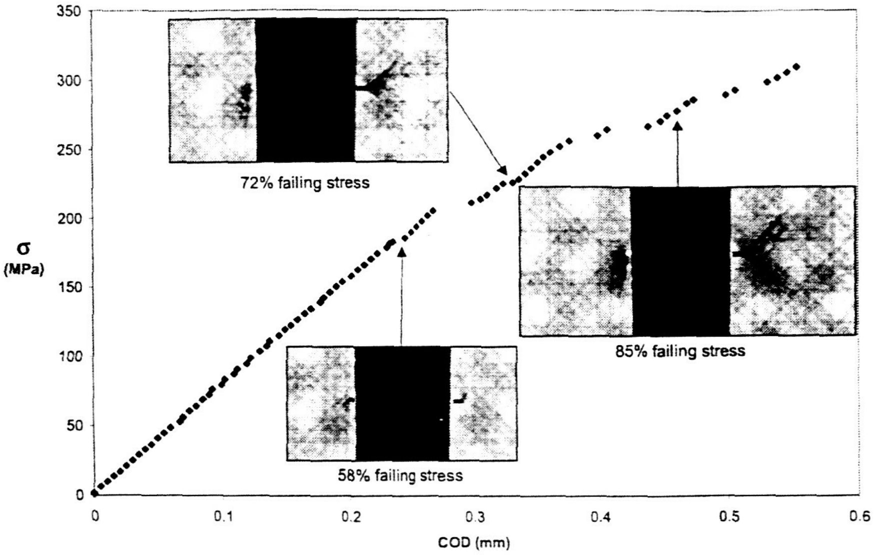

Figure 4. Stress vs. COD and radiographs (6:2 ratio, quasi-isotropic, 4-inch wide, 1-inch notch).

Figure 5 shows that the damage-modes and size at both notch tips in the 2:2 ratio panel were very similar. For these panels the initial location of the notch tip was less significant and the damage in the panel was symmetric, similar to the behavior observed in the all-carbon and all-glass systems. The close spacing and the fact that the glass tow architecture was not aligned in plies of the same angle resulted in approximately the same amount of glass in both notch-tip regions.

The presence of glass in the notch-tip region generally increases the amount of pre-catastrophic damage. Figure 6 shows evidence of this trend with mixed-tow combinations of 10:2 and 6:2 at 92% of failing stress. The damage-zone for the 6:2 ratio is larger at both notch tips. There are large axial splits along the 0° and 45° plies accompanied by extensive delamination. Pre-catastrophic damage in the notch-tip region redistributes the stress away from the notch tip; thus the panel becomes less notch sensitive. The radiographs of the 6:2 ratio panel suggests that damage development was affected by glass tows at the notch tip and the next set of tows outboard from the notch tips. This is not evident in the 10:2 ratio panel. The reason for the large amount of damage in the 6:2 panel is that the failing strain of glass fibers is two to three times higher than that of the carbon fibers and the matrix

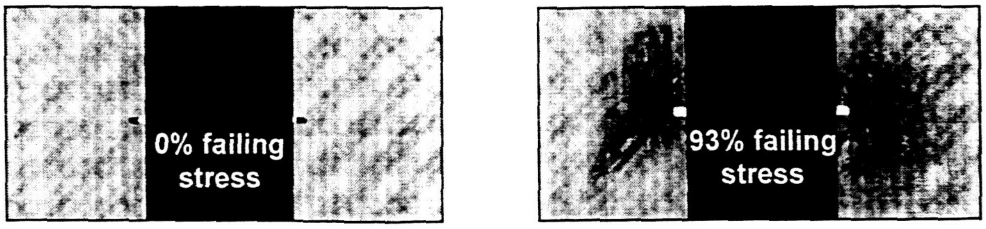

Figure 5. Radiographs of a $[+45/-45/0_2/90/0_2/-45/+45]_T$ 2:2 ratio mixed-tow panel 101.6-mm wide, with 25.4-mm notch. σ_f=444.7 MPa

material, which have about the same failing strain. Therefore, the matrix fails while the glass fibers stay intact, whereas in the all-carbon panel, the matrix and the fibers fail at about the same strain levels. This explains the general trend in the panels for which pre-catastrophic damage increased as the carbon tow/glass tow ratio decreased.

The increased strain that occurs in the glass tows during a significant damage event was evident from the failing strains of the mixed-tow hybrid panels. Figure 7 shows that the failing strains of the panels increased with a smaller spacing of the glass tows, which also meant there was more glass in the panels. For each notch length, the failing strain was generally highest for 2:2 ratio panels and lowest for 10:2 ratio panels.

Fracture toughness was determined for each panel using a LEFM model developed for composites [8]. The stress intensity factor equation for a centrally cracked sheet of infinite width, $K_\sigma = \sigma\sqrt{\pi a}$, was the basis for these calculations. A critical damage-zone size ρ_c was incorporated into this equation such that the

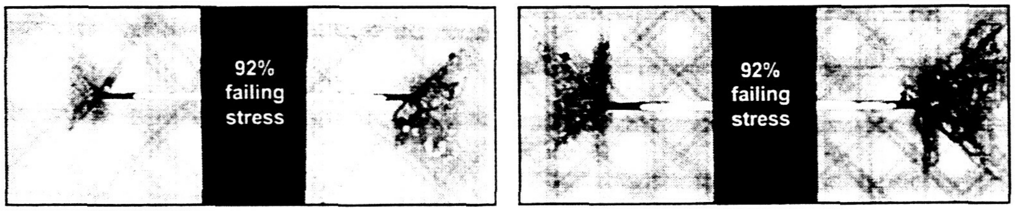

(a) 10:2 (b) 6:2

Figure 6. Quasi-isotropic 203.2-mm wide panels with 63.5-mm notches.

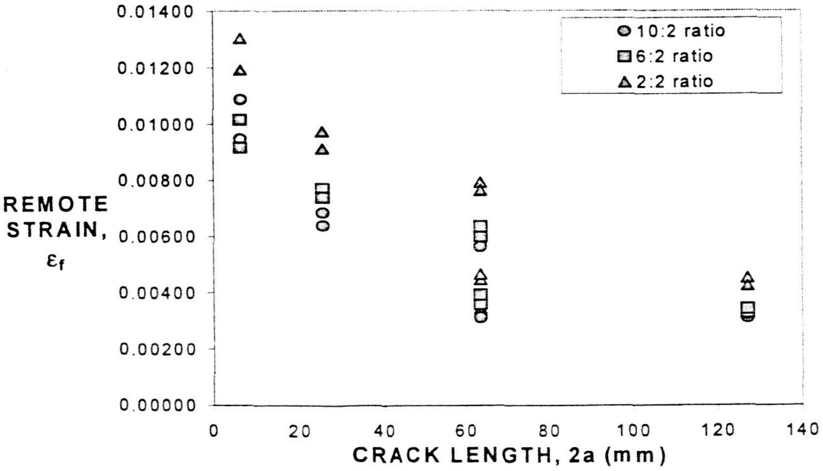

Figure 7. Failing strain results for $[+45/0/-45/90]_s$

critical stress intensity factor, $K_{\sigma Q}$, became

$$K_{\sigma Q} = \sigma_c \sqrt{\pi(a+\rho_c)} \qquad (1)$$

where σ_c is the far-field stress and a is the initial slit half-length. Then ρ_c, assuming $\rho_c>0$, reduced the predicted failing stress by assuming a longer crack than the initial machined slit. However, a complex damage-zone *did* exist in the notch-tip region, and using ρ_c to account for the effect of the damage-zone on failing stress was adequately effective.

The critical damage-zone ρ_c can be determined for a notch length of zero where σ is equal to the material ultimate tensile strength, F_{tu}. Thus, $K_{\sigma Q}$ was used to obtain ρ_c as follows.

$$\rho_c = \frac{\left(\dfrac{K_{\sigma Q}}{F_{tu}}\right)^2}{\pi} \qquad (2)$$

To determine the critical stress intensity factor for the panels tested, (2) was substituted into (1) to yield

$$K_{\sigma Q} = \frac{\sigma_c \sqrt{\pi a \sec\left(\dfrac{\pi a}{W}\right)}}{\sqrt{1-\left(\dfrac{\sigma_c}{F_{tu}}\right)^2 \sec\left(\dfrac{\pi a}{W}\right)}} \qquad (3)$$

Included in this equation is a widely used finite-width correction factor $\sqrt{\sec(\pi a / W)}$ where W is panel width.

The critical stress intensity factor was averaged for all the panels of a mixed-tow combination and laminate orientation. This provided a universal stress intensity factor for each mixed-tow combination and laminate orientation. Fracture is also characterized in terms of a strain intensity factor. The critical strain intensity factor, $K_{\varepsilon Q}$, was determined by dividing $K_{\sigma Q}$ by the material's elastic modulus. The fracture properties of each mixed-tow combination and laminate orientation are presented in Table 2.

The results in Table 2 show that there was no identifiable trend relating the carbon/glass tow ratio to the critical *stress* intensity factor. In terms of the stress intensity factor, the all-glass laminates exhibited the best fracture toughness followed by the 2:2 ratio. For the 0°-dominated lay-up, the all-carbon laminates had the third best $K_{\sigma Q}$ followed by the 10:2 ratio and the 6:2 ratio. For the quasi-isotropic lay-up, the 10:2 ratio had the third best $K_{\sigma Q}$ followed by the all-carbon and the 6:2 ratio. However, the *strain* intensity factor of the all-carbon material is the lowest and that of the all-glass is the highest. The decreasing elastic modulus with

TABLE 2. AVERAGE FRACTURE PROPERTIES.

Laminate orientation	**Mixed-Tow Combination**	**Average $K_{\sigma Q}$ (MPa$\sqrt{\text{mm}}$)**	**Average $K_{\varepsilon Q}$ ($\sqrt{\text{mm}}$)**
$[+45/-45/0_2/90/0_2/-45/+45]_T$	All-carbon	4451	0.05519
	10:2	4098	0.05715
	6:2	3515	0.05635
	2:2	4466	0.07930
	All-glass	5810	0.17585
$[+45/0/-45/90]_S$	All-carbon	3160	0.06209
	10:2	3224	0.06789
	6:2	2879	0.07081
	2:2	3625	0.09762
	All-glass	3680	0.17529

increasing percent glass in the laminates resulted in higher strain intensity factors for the mixed-tow combinations.

Although the all-glass laminates had the best fracture toughness, one of the primary benefits of carbon fiber composites must be kept in mind, that being the lightweight characteristic. This is an important consideration in the design of structural components for aircraft. Therefore, the density of each mixed-tow combination and laminate orientation was experimentally determined [9]. Realizing that the S-glass has a higher density than the carbon suggests that the best fracture toughness in terms of both stress and strain intensity factors may not make it the best material choice. Figure 8 displays bar graphs of the fracture toughness of each mixed-tow combination and laminate orientation. In this figure, the magnitude of each stress or strain intensity factor has been normalized by the density of its corresponding material's density. In addition, the data in each plot was normalized to the largest magnitude (the all-glass, 0°-dominated results) so that the fracture toughness parameters of the mixed-tow combination and laminate orientation that exhibited the highest magnitude were equal to unity.

Normalizing the fracture toughness parameters by the densities decreased the difference in magnitude among the laminates. The stress intensity factor in the quasi-isotropic laminates is now highest in the 2:2 ratio mixed-tow combination, with that of the all-glass system being next to last instead of the highest as it was before density-normalizing. The 0°-dominated laminate orientation still had the highest stress intensity factor in the all-glass system followed by the all-carbon system instead of the 2:2 ratio as before.

A decreased difference in critical stress intensity factors was noted in [8] in the study of carbon laminates. It was found that $K_{\sigma Q}$ was the same for all lay-ups with $E_x = E_y$. In the current study, $K_{\sigma Q}$ for the quasi-isotropic laminate (Table 2) varied by less than 10% for all mixed-tow combinations except the 6:2 ratio, which was approximately 13% below the mean. The variation among the mixed-tow combinations was even less when $K_{\sigma Q}$ was normalized by the density. There was significantly more variation in the 0°-dominated laminates; difference between the highest stress intensity factor (all-glass) and the lowest (6:2 ratio) was 40%.

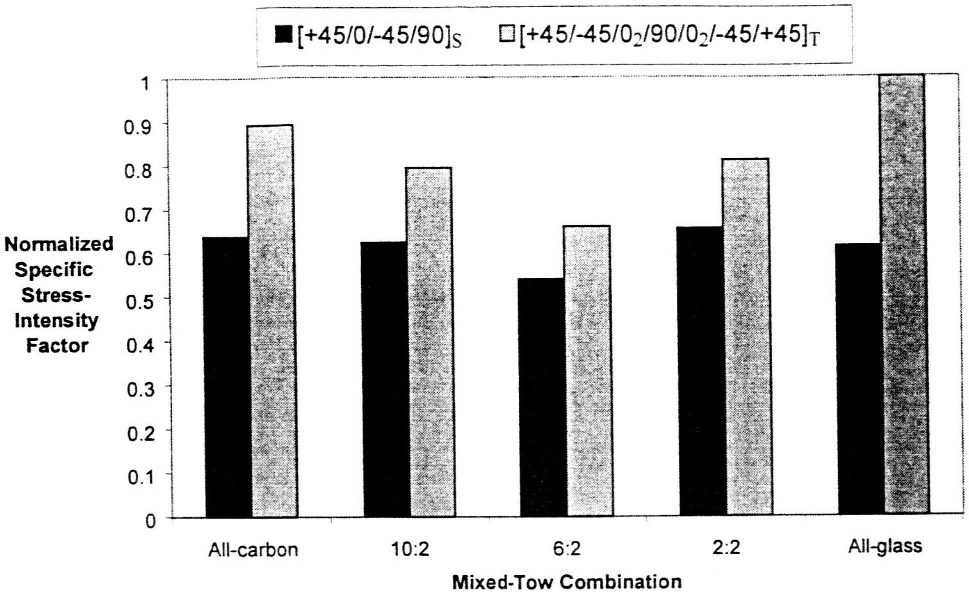

a. Density-normalized stress intensity factors.

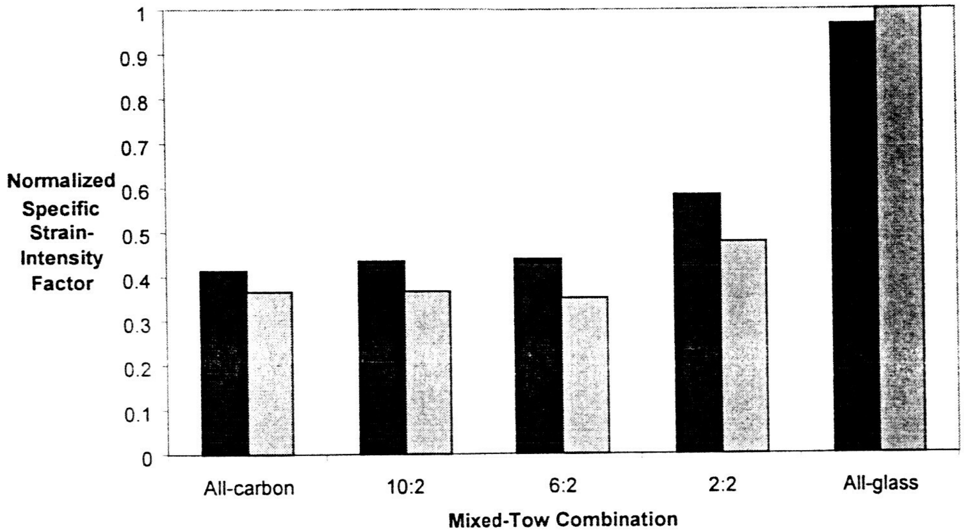

b. Density-normalized strain-intensity factors.

Figure 8. Fracture toughness parameters normalized by the density of the corresponding mixed-tow combination and laminate orientation with the highest magnitudes being unity.

The 0°-dominated laminate orientation generally had a lower strain intensity factor than the quasi-isotropic laminate orientation, indicating the 0°-dominated laminates are more notch sensitive than the quasi-isotropic laminates. This correlates with conclusions in [8] that an increased proportion of 0° plies results in an increased notch sensitivity of the laminate.

Using the average values from Table 2, the predictions from the model were compared to the experimental results. Solving (3) for σ_c gives

$$\sigma_c = \frac{K_{\sigma Q}}{\sqrt{\left(\pi a + \frac{K_{\sigma Q}^2}{F_{tu}^2}\right)\sec\left(\frac{\pi a}{W}\right)}} \tag{4}$$

for finite-width panels. Plots of far-field failing stress versus notch length (*2a*) were generated from this equation for each mixed-tow combination and laminate orientation. Plots were also generated from

$$\sigma_c = \frac{K_{\sigma Q}}{\sqrt{\pi a + \frac{K_{\sigma Q}^2}{F_{tu}^2}}} \tag{5}$$

for infinite plates. Figure 9 shows stress versus crack length predictions for the 0°-dominated, 6:2 ratio laminate. These results are typical of those for all the mixed-tow combinations. Predictions from (3), for two finite width plates, a 101.6-mm wide plate and a 203.2-mm wide plate are shown. Also included on the plot are data actual failing stresses of the panels. Figure 9 also contains two additional curves. These curves (dashed lines) represent the net section failing stress for the 101.6-mm and 203.2-mm wide panels. In all cases, the net section failing stress was higher than the failing stress of the panels, thus confirming the stress reduction caused by the stress concentration at the notch tips. The LEFM model predicted a higher failing stress than the net section model for large *2a/W*. This phenomenon is a result of the finite-width correction factor in the LEFM model.

The model predicts the failing stresses of the 203.2-mm wide panels well, but is not as accurate for the 101.6-mm wide panels. This inaccuracy is due to the stress intensity factors being generally much larger for the 203.2-mm wide samples. Since the stress intensity factor for the overall mixed-tow combination and laminate orientation is an average value, it was skewed upward a little by the values of the 203.2-mm wide panels. The cause of the stress intensity factor elevation for the larger panels stems from the large amount of crack-tip damage, discussed earlier.

This behavior is shown graphically in Figure 10, which displays the critical stress intensity factor for each of the 10:2-ratio mixed-tow panels. The figure shows the trend of panels with longer notches having higher stress intensity factors, while larger panels with longer notches had even higher stress intensity factors. A variation from the latter trend is evident for the 0°-dominated panels with a 63.5-mm notch where wider 203.2-mm wide panels had lower stress intensity factors than the 101.6-mm wide panels. This was observed in most of the mixed-tow combinations at the 63.5-mm notch length for the 0°-dominated laminate orientations. Also, there is a significant amount of variation among the tests, even among those of the same laminate orientation and notch length. This variation may not be surprising as the location of the notch tip relative to the 0° glass tows strongly affected pre-catastrophic damage. In light of these results, Figure 9 indicates the fracture strengths of the 203.2-mm wide laminates are more accurately predicted than those of the 101.6-mm wide laminates. Walker, et al discussed in [2]

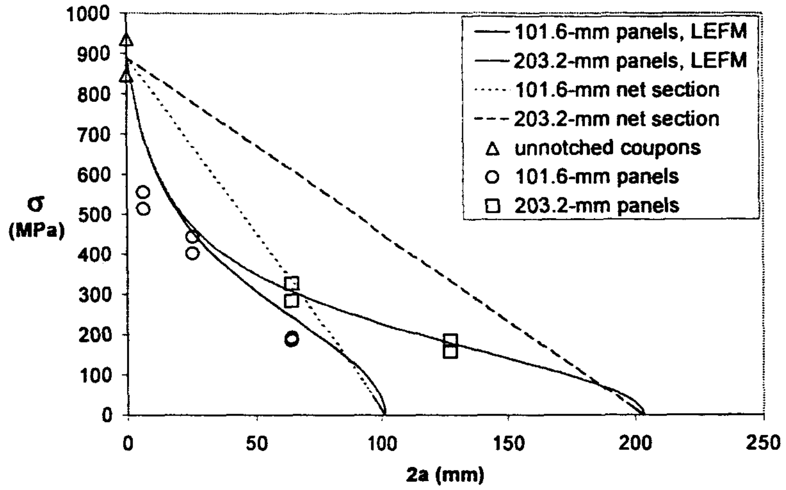

Figure 9. Failing stress versus crack length for 6:2 ratio, 0°-dominated panels.

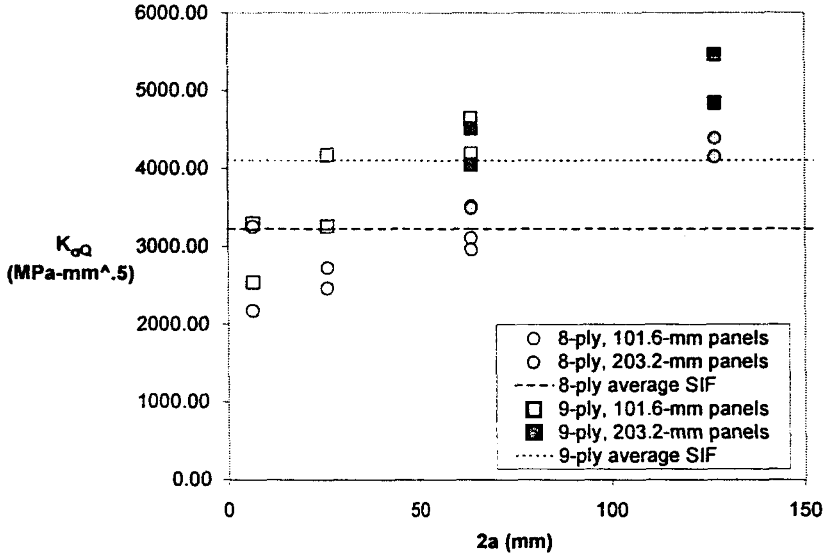

Figure 10. Stress-intensity factor versus 2a for 10:2 ratio laminates.

the likelihood that "methods based on the classical square-root stress-field singularity are not capable of predicting strengths for a large range of notch sizes, and that reduced-singularity methods may be more accurate." However, the LEFM-based predictions in the current study are within reasonable accuracy

The effect on fracture toughness of weaving various ratios of hybridizing S-glass tows into a carbon fiber material system was studied. Damage mechanisms were examined through study of crack opening displacement and x-radiography, while fracture-toughness parameters were determined using LEFM. The following general conclusions were reached from the results of this work.

- The critical strain intensity factor increased with the glass/carbon ratio in laminates; thus causing the laminates to become less notch sensitive.
- No trend was identifiable that related the carbon/glass ratio to the critical stress intensity factor.
- Panels with larger notches experience more pre-catastrophic damage than panels with shorter notches.
- Pre-catastrophic damage in the notch-tip region reduced notch sensitivity and increased the strain intensity factor.
- Alignment of the glass tow architecture among 0° plies along with initial notch-tip location relative to the nearest glass tows influenced non-critical damage.
- Mixed-tow panel crack-arrest behavior is like that of buffer strip panels.
- Using the critical stress intensity factor enabled the prediction of the failing stress in the laminates within reasonable accuracy. Generally, strength predictions for panels with short notches were unconservative.

REFERENCES

1. Walker, T. H., W. B. Avery, L. I. Ilcewicz, C. C. Poe Jr., and C. E. Harris. 1991. "Tension Fracture of Laminates for Transport Fuselage – Part I: Material Screening," *Second NASA Advanced Technology Conference,* NASA CP 3154.
2. Walker, T. H., L. B. Ilcewicz, D. R. Polland, and C. C. Poe Jr. 1992. "Tension Fracture of Laminates for Transport Fuselage – Part II: Large Notches," *Third NASA Advanced Technology Conference,* NASA CP 3178.
3. Walker, T. H., L. B. Ilcewicz, D. R. Polland, J. B. Bodine, and C. C. Poe Jr. 1993. "Tension Fracture of Laminates for Transport Fuselage – Part III: Structural Configurations," *Fourth NASA/DoD Advanced Technology Conference,* NASA CP 3229.
4. Ilcewicz, L. B., T. H. Walker, D. P. Murphy, B. Dopker, D. S. Cairns, and C. C. Poe Jr. 1994 "Tension Fracture of Laminates for Transport Fuselage – Part IV: Damage Tolerance Analysis," *Fifth NASA/DoD Advanced Technology Conference,* NASA CP 3229.
5. Walker, T., D. Scholz, B. Flynn, J. Dopker, J. Bodine, L. Ilcewicz, M. Rouse, D. McGowan, C. Poe Jr. 1996. "Damage Tolerance of Composite Fuselage Structure," *Sixth NASA/DoD Advanced Composites Technology Conference,* NASA CP-3326.
6. Poe, C. C., Jr., and J. M. Kennedy. 1980. "An Assessment of Buffer Strips for Improving Damage Tolerance of Composite Laminates," *J. Composite Materials Supplement,* 14(1):57-70.
7. Kennedy, J. M., 1991 "Damage Tolerance of Woven Graphite/Epoxy Buffer Strip Panels," *J. Composite Materials,* 25(9):1218-1241.
8. Poe, C. C., and J. A. Sova. 1980. "Fracture Toughness of Boron/Aluminum Laminates With Various Proportions of 0° and ±45° Plies," NASA TP-1707.
9. Lagrange, B. A. *Damage Mechanisms in Mixed-Tow Hybrid, Center-Cracked Tension Panels*; Master's Thesis, Clemson University, Clemson, South Carolina, May, 1999.

(2) Combined Effect of Buffer Strips or MTH Configurations with TTT Reinforcement

The objective of this research was to examine the effect of R-ratio on failure modes for through-the-thickness (TTT)-reinforced composite materials. It was anticipated that as the R-ration moved from one that was compression-dominated to one that was tension-dominated, the failure mode would at some point transition respectively. Tests were run in the range from predominaently tension to predominantly compression, and all samples failed with some form of longitudinal splitting around the open-hole, transverse cracks growing from the open-hole region to the outer boundaries, and delamination in the region local to the hole. Photomicrographs from a compression-dominated test showed local compression failures in plies and delamination.

As expected, the TTT-reinforcement decreased the intensity of the delaminations that occurred. Damage growth was more dependent on stress amplitude than on the maximum tensile or the maximum compressive stress. For instance, the fully-reversed tests, with a larger stress amplitude, always failed much earlier than the predominantly tension-dominated test, with a smaller stress amplitude, even though the maximum tensile stress was the same. Similar behvaior was observed with the compression-dominated tests; the fully-reversed tests failed much earlier than the predominantly compression-dominated test, even though the maximum compressive stress was the same. A larger stress amplitude caused localization of damage mechanisms around the open-hole area, whereas smaller stress amplitudes caused a more dispersed region of longitudinal and transverse splitting, sometimes as far as two hole diameters away.

Lastly, secant modulus degradation proved to be a good indicator for estimating fatigue life. Although all samples exhibited a gradual decrease in secant modulus, failure was imminent when a large and sudden decrease in secant modulus was observed.

Section II: Measurables

Publications:

Lagrange BA and Kennedy JM. "Damage Mechanisms in Mixed-Tow Hybrid, Center-Notched Tension Panels," No. 91 in *Proceedings of the American Society of Composites*, 16th Conference, Blacksburg, VA (2001).

Osborn, C.J. and Kennedy, J.M. "Progressive Damage in Mixed-Tow Hybrid Center-Notched Composite Tension Panels," No. Proceedings of the American Society for Composites 17th Technical Conference, West Lafayette, IN (2002).

Section IV: Participants:

Graduate Student:

Josh Stewart (W, M)

Faculty:

John M. Kennedy

Section V: Collaborations:

NASA Centers:

NASA Langley Research Center, Hampton, VA

(3) A Three Dimensional Fatigue Crack Closure Model of Surface Cracks

Paul Joseph, Associate Professor of Mechanical Engineering, Clemson Univ.
Magda Capitaneanu, M.S., Graduate, Engineering Mechanics
Adrian Loghin, Ph.D. Graduate, Engineering Mechanics

Summary

The original objective of this research was to develop a model to predict fatigue crack growth in the fuselage of metallic aircraft structures. A realistic model must include crack closure effects induced by plasticity and possibly other nonlinear issues that occur with fracture in metals. Due to the nonlinear, three-dimensional nature of the problem, it is highly desirable to use a simplified model with the ability to account for these nonlinear effects at every time step. The line spring model was chosen as the basis for this model. In building this model, several aspects of linear and nonlinear fracture have been investigated.

In order to account for a loss of K-dominance, a method was developed to accurately determine the coefficients of the higher order terms in the expansion of the stress field near the tip of a crack. For the case of an edge crack in a strip, which is the basic geometry required to implement the line spring model, the first four coefficients have been determined, where the first is the stress intensity factor, the second is the so-called T-stress, etc. A journal article describing the method and results is currently in preparation. The symmetric case has been completed, but due to our recent interest in mixed mode fracture, which is discussed below, the antisymmetric case will also be included in this article. A female M.S. student, Magda Capitaneanu, completed her thesis on this subject and graduated in May of 2000. The symmetric results will be implemented into the model to help approximate constraint variation along the crack front. In order to make use of the model to predict surface crack growth; it is necessary to extend the capability of the line spring model to characterize crack tip conditions near the endpoints of the crack, as well as in the center of the crack. Another accomplishment of this research has been the determination of the precise nature of the stresses and crack opening displacement predicted by the line spring model at the endpoints. It has been determined that it is necessary to include a second singular term in the numerical solution procedure. The current method that has been used for nearly thirty years is to use only one singular term. Given this result, it will now be possible to devise a method to approximate crack tip conditions all along the curved crack front.

In the last three years we have extended our work with higher order terms from linear material behavior to nonlinear material behavior. By far the most interesting work has been with higher order/mixed mode analysis of nonlinear material behavior. Adrian Loghin did his doctoral work on this problem, and graduated in August of 2001. We have discovered that multiple asymptotic solutions exist. The important point is that the stress-based, J-integral approach fails near mode I, and a CTOD approach might be better.

Section I: Narrative

Description of Research and Accomplishments – this section is divided into two parts: nonlinear mixed mode fracture and higher order linear elastic terms.

1. Nonlinear mixed mode fracture

The primary accomplishment of this research has been on understanding the effects of arbitrary loading on the asymptotic stress and strain fields in nonlinear fracture for a stationary crack tip. In this work the material behavior is modeled as pure power law hardening within the theory of J_2-deformation plasticity. Of particular interest is the role of two-parameter higher order solutions in "mixed mode" fracture, where each of the first two terms in the expansion of the displacement fields is variable-separable with real, but unequal eigenvalues. Such an asymptotic form is given below.

$$\begin{aligned}\frac{u_i(r,\theta)}{r_1\varepsilon_0} &= K_1(r/r_1)^{\lambda_1}\bar{u}_i^1(\theta) + K_2(r/r_1)^{\lambda_2}\bar{u}_i^2(\theta) + \ldots,\ \lambda_1 < \lambda_2 \\ &= \alpha A_1^n(r/r_1)^{ns_1+1}\bar{u}_i^1(\theta) + \alpha A_1^{n-1}A_2(r/r_1)^{ns_1+1+(s_2-s_1)}\bar{u}_i^2(\theta) + \ldots, \qquad (3.1)\end{aligned}$$

$$\frac{\varepsilon_{ij}(r,\theta)}{\varepsilon_0} = K_1(r/r_1)^{-(1-\lambda_1)}\bar{\varepsilon}^1_{ij}(\theta) + K_2(r/r_1)^{-(1-\lambda_2)}\bar{\varepsilon}^2_{ij}(\theta) + \ldots$$

$$= \alpha A_1^n (r/r_1)^{ns_1}\bar{\varepsilon}^1_{ij}(\theta) + \alpha A_1^{n-1}A_2(r/r_1)^{ns_1+(s_2-s_1)}\bar{\varepsilon}^2_{ij}(\theta) + \ldots, \qquad (3.2)$$

$$\frac{\sigma_{ij}(r,\theta)}{\sigma_0} = \alpha^{-\frac{1}{n}}K_1^{\frac{1}{n}}(r/r_1)^{-\frac{1}{n}(1-\lambda_1)}\bar{\sigma}^1_{ij}(\theta) + \alpha^{-\frac{1}{n}}K_1^{\frac{1}{n}-1}K_2(r/r_1)^{-\left[(1-\lambda_2)-(1-\lambda_1)\left(1-\frac{1}{n}\right)\right]}\bar{\sigma}^2_{ij}(\theta) + \ldots$$

$$= A_1(r/r_1)^{s_1}\bar{\sigma}^1_{ij}(\theta) + A_2(r/r_1)^{s_2}\bar{\sigma}^2_{ij}(\theta) + \ldots, \ s_1 < s_2 \ , \qquad i,j = r,\theta. \qquad (3.3)$$

where K_1 and K_2 (or A_1 and A_2) are arbitrary constants, λ_1 and λ_2 (or s_1 and s_2) are the eigenvalues with $0 < \lambda_1 < \lambda_2 < 1$ $(-1 < s_1 < s_2 < 0)$ that govern the singular behavior of stresses and strains at the tip of the crack (or wedge), and the barred functions are the eigenfunctions which define the angular dependence.

A displacement-based finite element method coupled with singular value decomposition is used to solve the nonlinear higher order eigenvalue problem for cracks and wedges. The versatility of this method to account for arbitrary loading and geometry is used to investigate homogeneous crack and interface crack cases by studying the limit as a wedge subjected to arbitrary loading becomes a crack. Two such limits are considered. The first when the total wedge angle is smaller than the crack case, and the second when it is larger. By using this approach, it has been determined that in homogeneous plane strain and plane stress fracture, and in plane strain fracture of an interface crack between a hardening material and a rigid substrate, there are two distinct asymptotic solutions. These solutions are referred to as mode I dominant and mode II dominant. In the linear elastic limit the solutions are identical, however, as the hardening exponent deviates from the linear elastic case, the asymptotic structures are different. The forms of the asymptotic solutions are presented in the table below.

Table 3.1. Asymptotic behavior of mixed mode loading cases in nonlinear fracture based on Equations (3.1 – 3.3), as determined by the current research (Loghin and Joseph, 2001).

	Plane strain homogeneous fracture	Plane strain interface fracture	Plane stress homogeneous fracture
Mode I dominant loading	Higher order, $s_1 < s_2$	Higher order, $s_1 < s_2$ Sharma and Aravas (1993)	Higher order, $s_2 < s_1$
Mode II dominant loading	Mixed mode, $s_1 = s_2$ Shih (1974)	Oscillatory	Higher order, $s_1 < s_2$

As seen from the table, each of the three fracture cases has one higher order solution where $s_1 < s_2$. In both plane strain cases this higher order solution is mode I dominant, while in plane stress the solution is mode II dominant. The mode I dominant interface crack higher order solution was first presented by Sharma and Aravas (1993). The "mode II dominant" solution for homogeneous plane strain fracture, first presented in a classic study by Shih (1974), is a mixed mode solution governed by a single real eigenvalue. Contrary to this mixed mode solution, there is strong evidence that the mode II dominant plane strain interface crack solution is oscillatory, i.e., non-separable with a form similar to that of the compressible linear elastic case that results from a complex eigenvalue. The mode I dominant plane stress is solution is the most unusual, as it is in a higher order form, but the antisymmetric portion is more singular that the symmetric portion. This unusual result is discussed in more detail later in the report. The plane strain case has been published (Loghin and Joseph (2003)) and the plane stress case will be submitted for publication soon. The key asymptotic results, which reveal these multiple asymptotic solutions, are given in the next three figures. The important point is that the J-integral term does not account for the mix of the loading in some cases. These cases include: Mode I dominant for plane strain (Figure 3.1), all loading in plane stress (Figure 3.2) and mode I dominant loading for the interface crack (Figure 3.3).

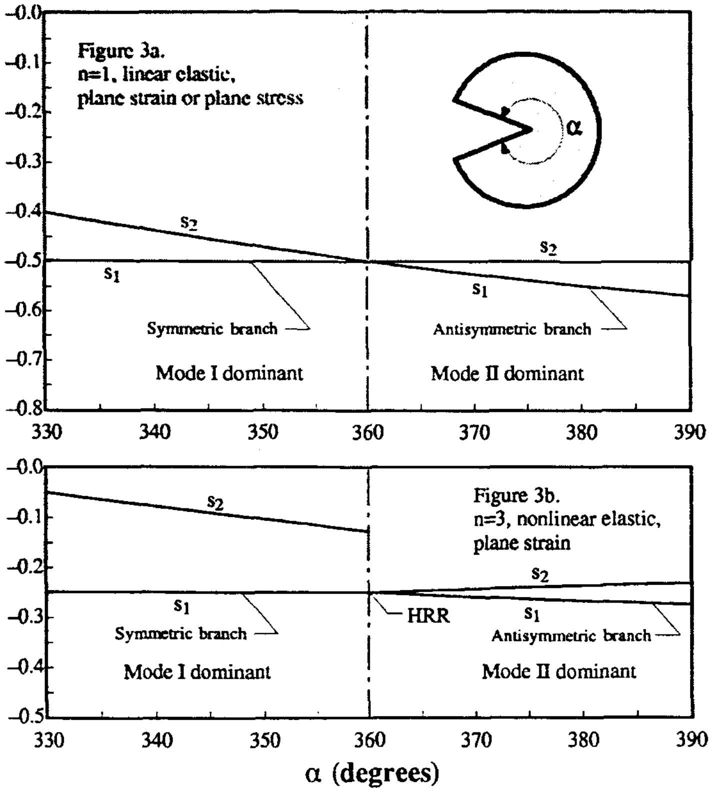

Figure 3.1. The first two eigenvalues for a linear elastic (n = 1, ν = 0.5) and a nonlinear elastic (n=3) free-free wedge. The nonlinear case shows multiple asymptotic solutions (see Eqn. 3.3) for the eigenvlaues for the case of a crack.

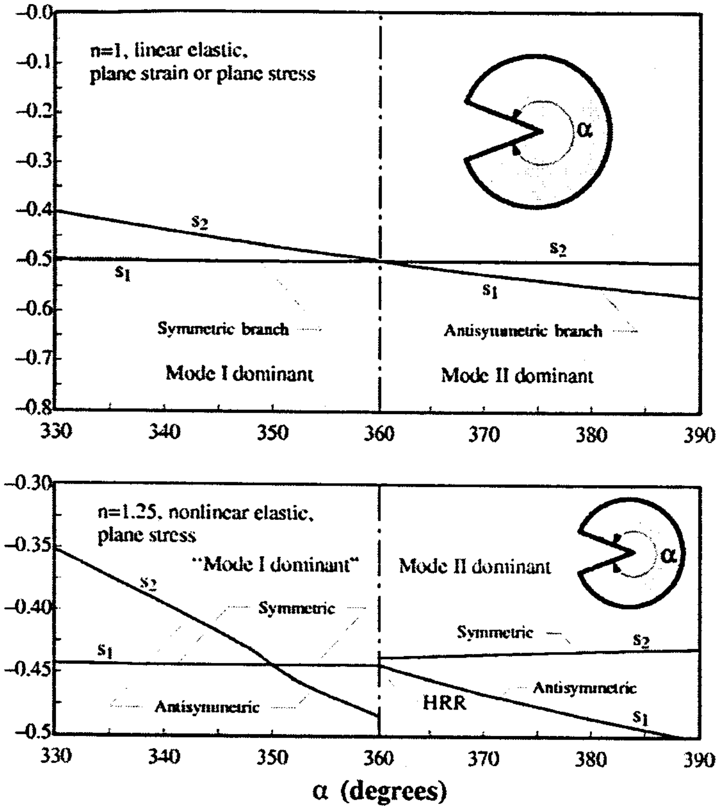

Figure 3.2. Same as Figure 3.1 for plane stress.

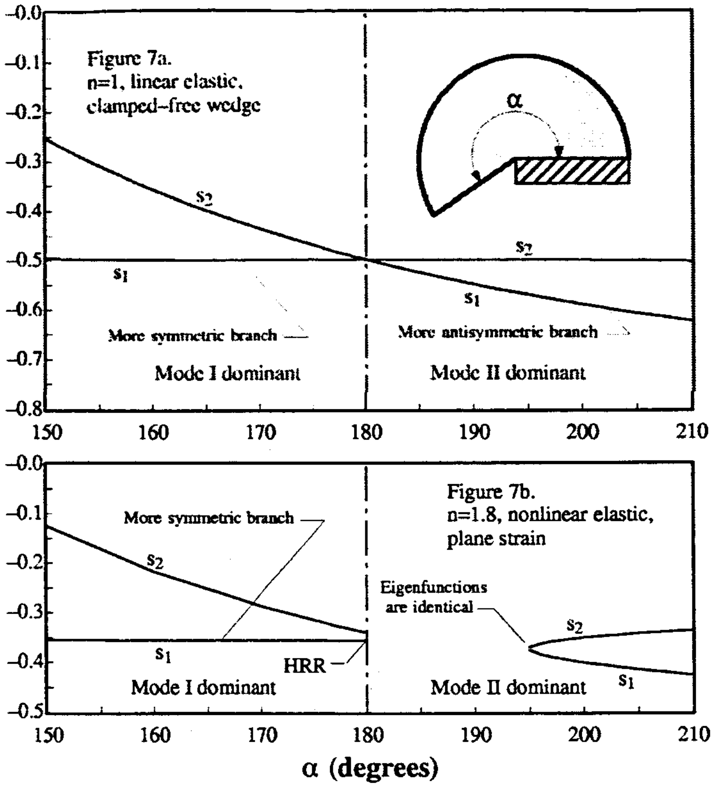

Figure 3.3. The first two eigenvalues for a linear elastic ($n = 1$, $\nu = 0.5$) and a nonlinear elastic ($n=3$) clamped-free wedge for plane strain loading conditions. A variable-separable solution cannot be obtained in the lower figure between $\alpha = 180^\circ$ and the angle at which the double root occurs. Again the figure shows multiple solutions for nonlinear material behavior for an interface crack ($\alpha = 180^\circ$).

The results in Figures 3.1 – 3.3 are asymptotic, and should be verified by full-field results. For the cases of plane strain and plane stress, we have confirmed the asymptotic results using full field finite element analysis. The asymptotic results for all cases predict that a switch in asymptotic structure takes place somewhere between pure mode I and pure mode II. For the case of plane strain this is demonstrated in Figures 3.4 and 3.5. In Figure 3.4 there is proof that near mode I, somewhere between a loading corresponding to $0.8 < M^e < 0.98$, where M^e is the loading parameter defined by Shih (1974),

$$M^e = \frac{2}{\pi} tan^{-1} \left| \frac{K_I}{K_{II}} \right| . \tag{3.4}$$

the asymptotic solution switches from mixed mode where symmetric and antisymmetric parts of the stress field have the HRR eigenvalue, to a higher order form where the antisymmetric part of the stress field has a weaker eigenvalue. The complicated way in which this occurs is demonstrated in Figure 3.5. For more details, see the paper by Loghin and Joseph (2003).

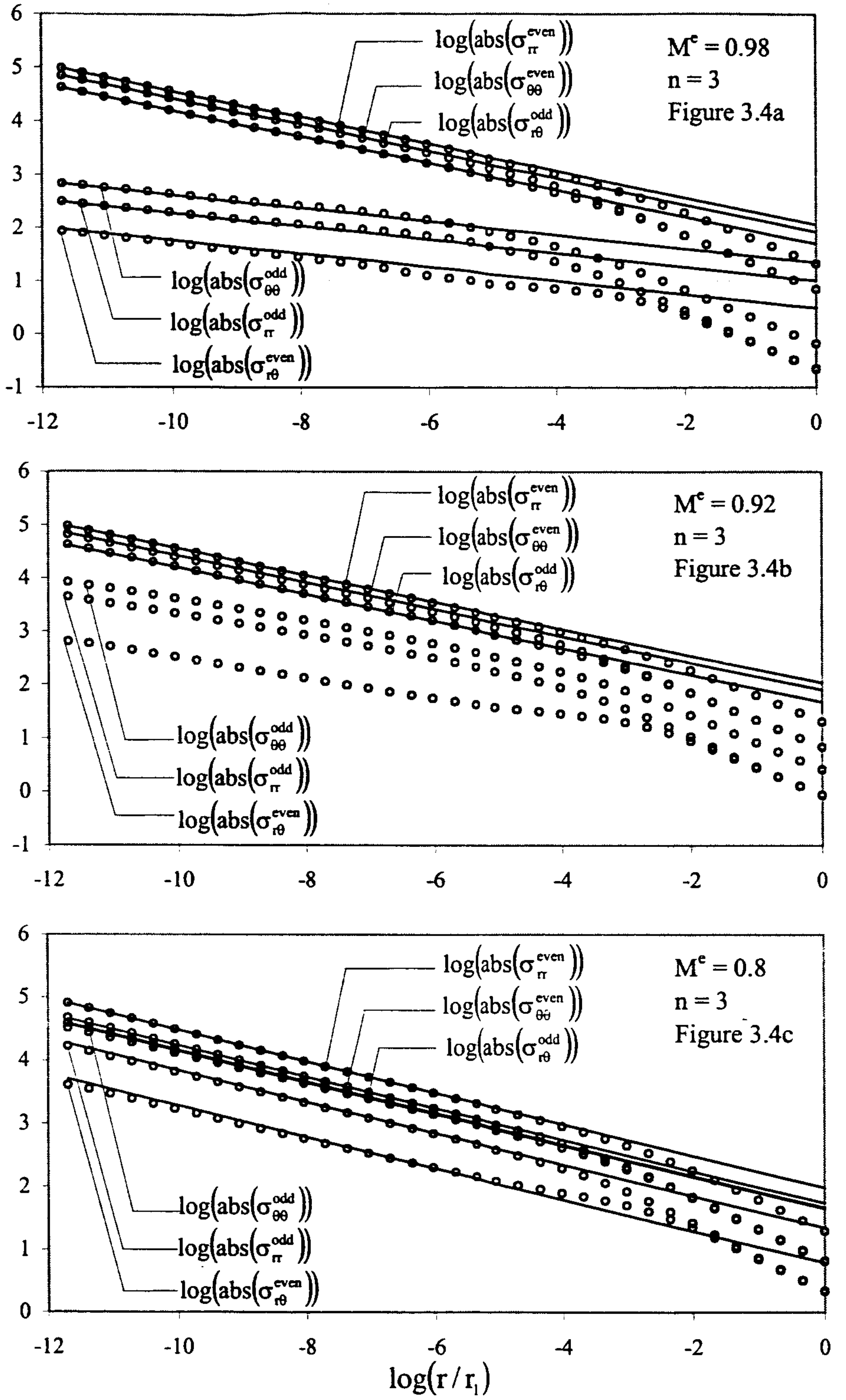

Figure 3.4. Comparison of the asymptotic solutions with the symmetric and antisymmetric parts of the full-field finite element results for n = 3 at $\theta = 90^\circ$ for different loading conditions. Figure 3.4a: $M^e = 0.98$, Figure 3.4b: $M^e = 0.92$, Figure 3.4c: $M^e = 0.80$.

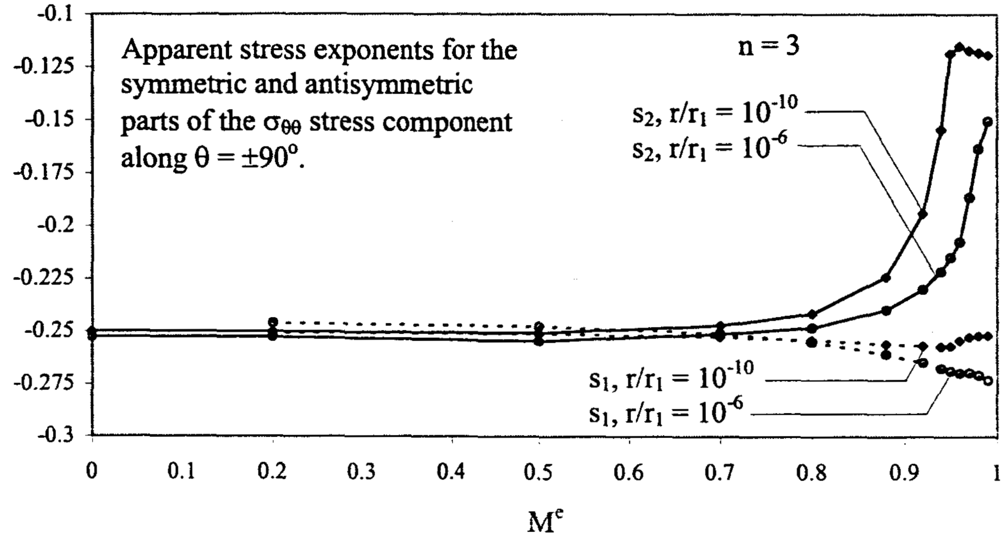

Figure 3.5. Full-field finite element results for the apparent stress exponent of the antisymmetric portion of the stresses at $r/r_1 = 10^{-6}$ and 10^{-10} for a hardening exponent of $n = 3$ for plane strain. The results show the gradual transition from the HRR eigenvalue of –0.25 for mode II dominant loading to the eigenvalue $s_2 = -0.1275$ for mode I dominant loading. These results confirm the asymptotic results in Figure 3.1.

Similar results have been obtained by Loghin (2001) for the case of plane stress. This work is currently being prepared for journal paper submission. For this case the full-field verification of the two different asymptotic crack solutions corresponding to Figure 3.2 are presented as Figures 3.6 and 3.7.

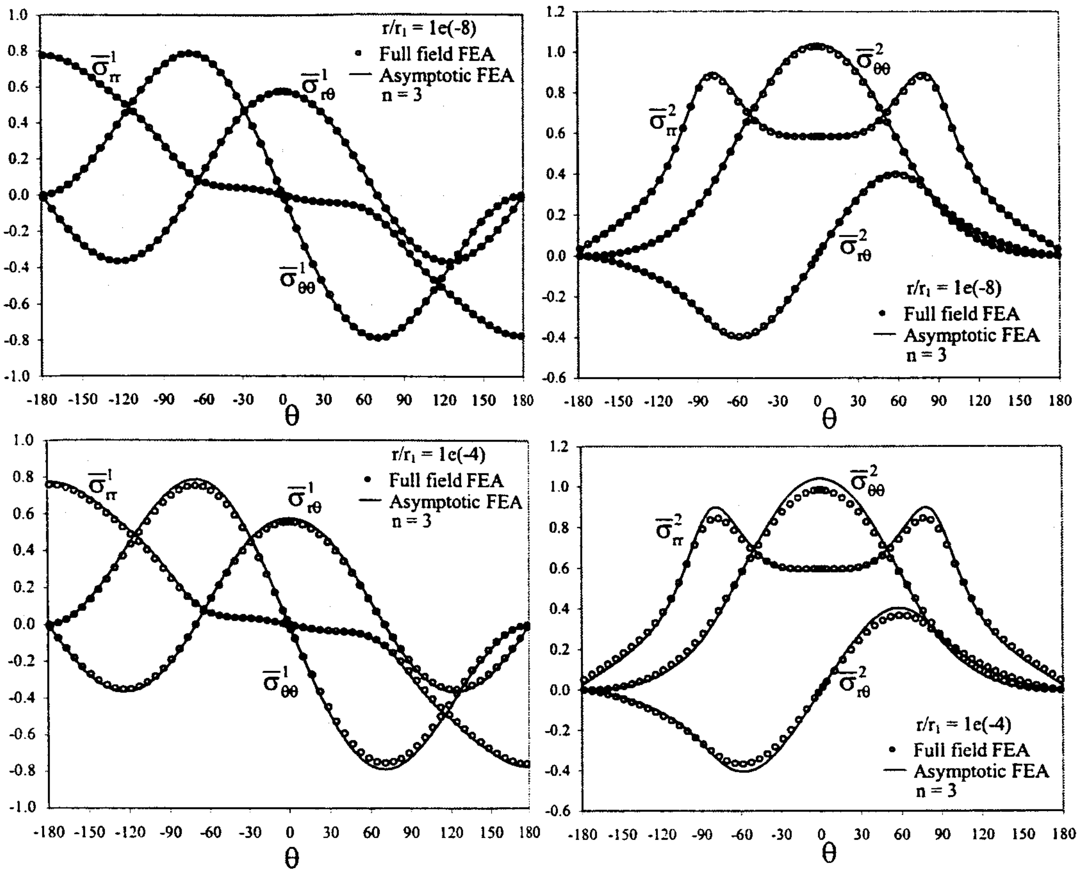

Figure 3.6. Comparison of the first and second terms of the mode II dominant asymptotic plane stress solution with the symmetric and antisymmetric parts of the full-field finite element solution at $r/r_1=10^{-8}$ and $r/r_1=10^{-4}$ for a hardening power of n = 3 and a mixed loading of $M^e = 0.1$.

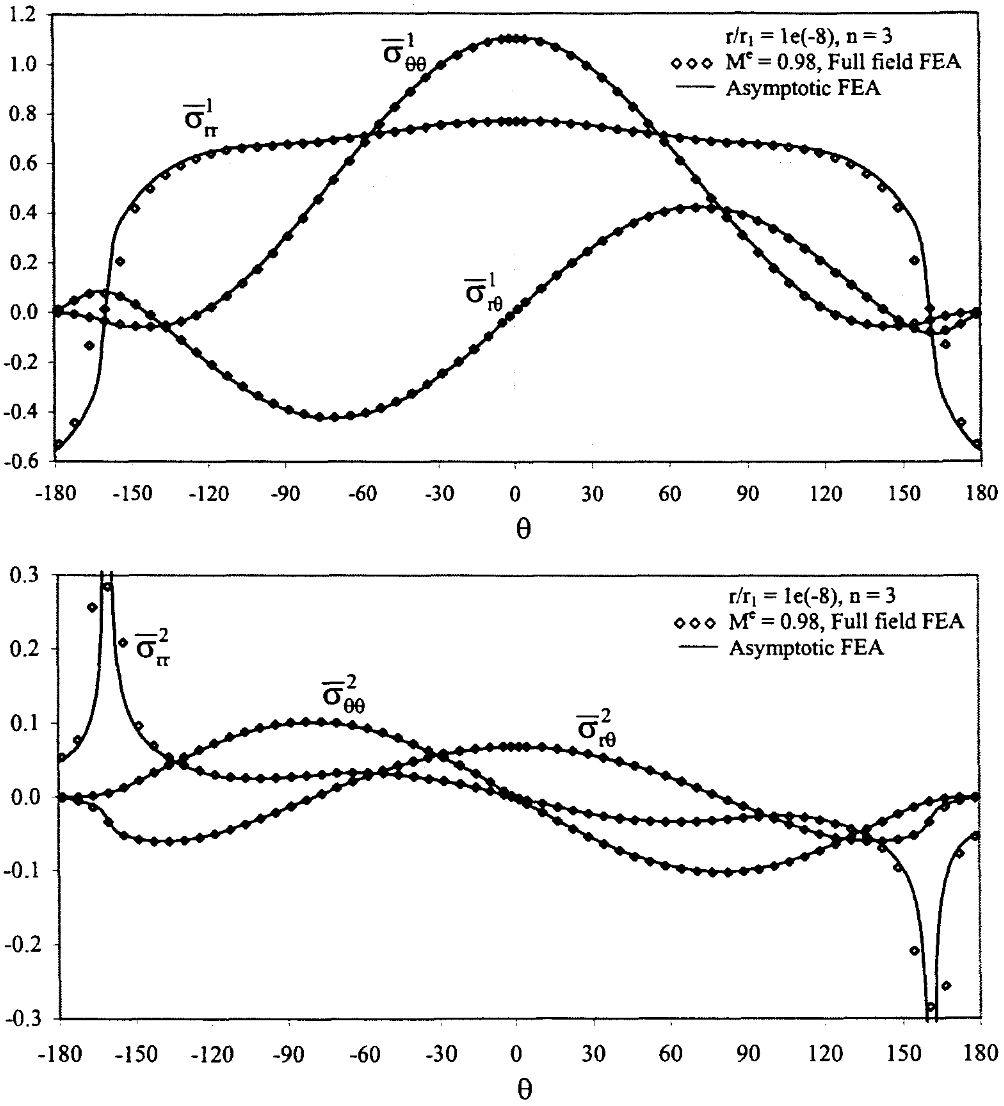

Figure 3.7. Comparison of the first and second terms of the mode I dominant asymptotic plane stress solution with the symmetric and antisymmetric parts of the full-field finite element solution at $r/r_1=10^{-8}$ for a hardening power of n = 3 and a mixed loading of $M^e = 0.98$.

This work is slow to be completed due to the rather confusing result of a singular power stronger than the HRR eigenvalue, for the antisymmetric part of the mode I dominant asymptotic response (see Figure 3.2). We believe this is explained by the fact that the asymptotic behavior is not actually valid in the mathematical limit as r approaches zero, in which case there is no violation of infinite energy. However, the result appears to be valid at extremely small values of r, well within the region where the HRR theory is no longer valid. To see this paradoxical behavior, in Figure 3.8 results analogous to those of Figure 3.5 are presented for plane stress. The smallest value of (r/r_1) where the theory can be applied is 10^{-5}, which is on the order of the crack tip opening displacement.

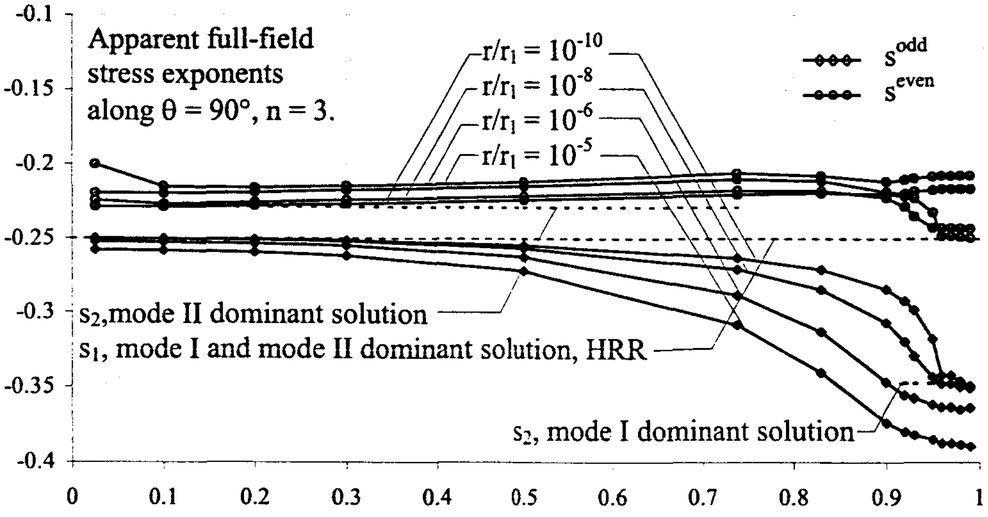

Figure 3.8. Plane stress case analogous to Figure 3.5. Apparent stress singularities from the full-field finite element analysis for a hardening exponent of n = 3 as a function of the loading parameter, M^e. The results at different values of r/r_1 are compared to the singularities given by asymptotic analysis in dashed lines.

2. Higher order linear elastic terms

A method to determine higher order terms from the numerical solution of a singular integral equation has been established. In addition to stress intensity factors and the T-stress, which are respectively the first and second terms, additional terms are determined. For the example of an edge crack or an internal crack in a half space, converged values of the first six coefficients have been determined, and for an edge crack in a finite width strip, the first four coefficients are given. Convergence of the results becomes more difficult for increasing numbers of terms. The results can be used to quantify the size of the K dominant zone and also the K-T dominant zone taking into account the entire region around the crack tip. The method can be used to determine cases where linear elastic fracture mechanics breaks down due to the loss of dominance of these zones.

Williams (1952) was the first to express stresses and strains near the tip of a crack in terms of an asymptotic series for small distances from the crack tip. Using the polar coordinate system in Figure 1, the asymptotic form of the stresses and displacements for the symmetric, mode I case of loading can be expressed as

$$\sigma_{ij}(r,\theta) = \sum_{n=0}^{\infty} k_n^I (2r)^{n-\frac{1}{2}} f_{ij}^{Ik}(n,\theta) + \sum_{n=0}^{\infty} T_n^I (2r)^n f_{ij}^{In}(n,\theta), \tag{3.5}$$

$$2\mu u_i(r,\theta)=\sum_{n=0}^{\infty} k_n^I (2r)^{n+\frac{1}{2}} g_i^{In}(n,\theta)+\sum_{n=0}^{\infty} T_n^I (2r)^{n+1} g_i^{In}(n,\theta),\ i=r,\theta\ ,. \tag{3.6}$$

where the angular functions for both the symmetric and antisymmetric (mode II) cases are known. By applying considerable mathematical details and analysis, the coefficients can be very accurately determined using a singular integral equation approach. For example, for an edge crack in a half space the coefficients an infinite strip, the coefficients for tension and bending are given in Tables 3.1 and 3.2.

Table 3.1 Asymptotic coefficients for an edge crack in a strip.
Uniform tension.

a/h	$\frac{k_0^I}{\sigma_0\sqrt{b}}$	$\frac{T_0^I}{\sigma_0}$	$\frac{k_1^I b}{\sigma_0\sqrt{b}}$	$\frac{T_1^I b}{\sigma_0}$
0.0	1.1215	-0.5260	0.2418	-0.1925
0.1	1.1892	-0.5502	0.2460	-0.19865
0.2	1.3673	-0.5890	0.21695	-0.1994
0.3	1.1699	-0.6103	0.08426	-0.1754
0.4	2.1114	-0.57825	-0.2873	-0.09055
0.5	2.8246	-0.4217	-1.2293	0.1617
0.6	4.0331	0.03814	-3.6968	0.9509
0.7	6.3549	1.3614	-11.1150	3.8845
0.8	11.9553	6.0074	-41.2088	19.3852
0.9	34.6326	35.7433	-297.664	213.725
0.95	99.1303	166.299	-1876.35	1972.07

Table 3.2 Asymptotic coefficients for an edge crack in a strip.
Bending.

a/h	$\frac{k_0^I}{\sigma_1\sqrt{b}}$	$\frac{T_0^I}{\sigma l}$	$\frac{k_1^I b}{\sigma_1\sqrt{b}}$	$\frac{T_1^I b}{\sigma_1}$
0.0	1.1215	-0.5260	0.2418	-0.1925
0.1	1.0472	-0.3779	0.07967	-0.08952
0.2	1.0553	-0.2382	-0.1112	0.01899
0.3	1.1241	-0.07917	-0.3773	0.14665
0.4	1.2606	0.1208	-0.7909	0.3138
0.5	1.4972	0.3975	-1.51245	0.5772
0.6	1.9140	0.8339	-2.9719	1.1199
0.7	2.7252	1.67525	-6.6091	2.6732
0.8	4.6764	3.9269	-19.3929	9.5643
0.9	12.4621	15.8057	-116.047	84.4986
0.95	34.3061	63.2085	-674.261	713.191

For the case of an edge crack in a half-space, which is presented to show convergence capability, the first six coefficients are presented in Table 3.3.

Table 3.3 Asymptotic coefficients for an edge crack in a half space.

Term in Series n	$\frac{k_n^I b^n}{\sigma_0 \sqrt{b}}$	$\frac{T_n^I b^n}{\sigma_0}$
0	1.1215222552	-0.5259676011
1	0.241774599	-0.1924915
2	0.027990	0.0535?

Section II: Measurables

Publications this reporting period:

1. Loghin, A. and Joseph, P.F., "Asymptotic Solutions for Mixed Mode Loading of Cracks and Wedges in Power Law Hardening Materials," Engineering Fracture Mechanics, Vol. 68. pp. 1511-1534, (2001).
2. Loghin, A. and Joseph, P.F., "Near mode I fracture in power law hardening materials," International Journal of Fracture, Vol. 123, pp. 81-106, (2003).
3. P.F. Joseph and M. Capitaneanu, "Determination of higher order coefficients from a singular integral equation approach," in preparation.
4. M. Capitaneanu, "Higher order terms in linear elastic fracture mechanics," MS Thesis, Clemson University, May 2000.
5. Loghin, A. and Joseph, P.F., "Mixed mode fracture in power law hardening material behavior for plane stress," in preparation.
6. A. Loghin, "The effects of arbitrary loading in nonlinear fracture mechanics," Ph.D. Dissertation, Clemson University, August 2001.
7. A. Aurora, P.F. Joseph, J.D. DesJardins, M. LaBerge, "The effect of lubricant composition on the fatigue properties of ultra high molecular weight polyethylene (UHMWPE) for total knee replacement (TKR)," submitted for publication, 2004.

Grants and Financial Awards:

Dr. Joseph has had one project initiate after the NASA EPSCoR project. This project is funded by the National Science Foundation through the NSF EPSCoR program. The total funding amount from the NSF is $499,000 over two years for five faculty. The research area is wear of polymers. Dr. Joseph's research area in this NSF grant includes contact and fracture.

Section III: Other Publications and Proposals:

Presentations:

1. P.F. Joseph, "Some complications in singular stress analysis," University of Miami, Invited seminar, April, 2000.

Section IV: Participants

Graduate Students:

Magda Capitaneanu (W,F) Earned MS degree in May 2000
Full NASA funding, switched from Ph.D. program to MS.
Adrian Loghin (W,M) Earned Ph.D. degree in August 2001
Final year of Ph.D. program funded by NASA
Amit Aurora (W,M) Earned MS degree in December 2003
Funded by NASA for 6 months

Undergraduate Students:
David Suttles (W,M)

Faculty:
Paul F. Joseph

Section V: Collaborations

NASA Centers:
NASA Langley Research Center, Hampton, VA
Dr. James C. Newman

(4) High Performance Titanium Alloys For Aerospace Applications

H. J. Rack, Professor Materials Science and Engineering, Clemson University
Dr. J. Qazi, Research Associate H.C. Bellum, M.S. Candidate
I. Duta, M. S. Candidate S. Vignesh, M. S. Candidate

Summary

This task has examined a broad range of issues that limit the applicability of advanced titanium alloys for aerospace structures. Included are studies designed to define those factors that (a) control the deep hardenability and thus the heavy section capability of α + ß and metastable ß titanium alloys, (b)limit the high cycle fatigue behavior of metastable titanium alloys and (c) control the high temperature, high strain deformation behavior of α + ß and metastable ß titanium alloys. Finally the feasibility of designing a high modulus, high strength titanium alloy through coupled thermodynamic and solid mechanics modeling is being examined.

Continued progress has been made in attaining the goals set forth in the original proposal. The study of phase transformations occurring during cooling of Ti-6Al-4V, IMI 550 and Ti-6-22-22 has been concluded. This have shown the importance of β phase stability in controlling type of martensite formed on rapid cooling, slower cooling resulting progressively in massive transformation, Widmanstatten, basket-weave and patchy α formation. Further the deep hardenability of metastable β titanium alloys has been shown to be limited by progressive nucleation of primary α at grain boundary triple points, grain boundary edges/surfaces and dislocation sub-boundaries – the critical cooling rates for each being dependent upon alloy composition.

During this final reporting period studies of Ti-15V-3Cr-3Al-3Sn have shown that a 50% enhancement in high cycle fatigue performance can be achieved through controlled rolling/recrystallization and aging to form a bi-modal microstructure. Additionally it has been found that dynamic spheroidization in lamellae α–β titanium alloys initially involves dynamic recovery/recrystallization of individual α lamellae followed by α/α grain boundary sliding and grain rotation, while flow stability in equiaxed α + ß microstructures associated with dynamic recovery/recrystallization, unstable flow associated whith localized shear and strain assisted dissolution and coarsening of primary alpha phase.

Finally coupled thermodynamic and solid mechanics modeling has been utilized to define a range of wrought Ti-Mo-Al/TiC alloys that have the potential of achieving both high modulus and high strength.

Section I: Narrative

Description of Research and Accomplishments

The objective of this task is to establish an understanding of the factors that limit the development of advanced aerospace titanium alloys. These studies include examinations of

- phase transformations in α + ß and metastable ß titanium alloys,
- the high cycle fatigue behavior of metastable ß titanium alloys,
- deformation processing of α + ß and metastable ß titanium alloys, and
- high modulus, thermally stable TiC reinforced titanium alloys.

Phase Transformations

This sub-task is presently examining phase transformations in α + ß (IMI 550, Ti-6Al-4V) and metastable ß (TIMET LCB and Beta-C) titanium alloys.

α + βAlloys: Previous year's studies have shown that the transition from a hexagonal, α' to an orthorombic, α", martensite which occurs with increasing beta stabilizing content, and which limits the ability to attain high strength with adequate tensile ductility in solution treated and aged *α + β* titanium alloys, is related to the degree of short-range developed within the parent β phase, increasing degree of order promoting the formation of α" martensite. Qualitative agreement with this suggestion was achieved utilizing in-situ high temperature neutron diffraction at AECL, Chalk River, Canada.

Examination of the phase transformations taking place in IMI 550 during cooling from above or below the beta transus temperature as a function of cooling rate concluded. X-ray diffraction analysis of samples cooled from 1010°C (above the β-transus temperature) showed that the metastable β phase goes through the following transformation sequence with decreasing cooling rate, $\beta \rightarrow \alpha'$ (martensite) $\rightarrow \alpha' + \alpha + \beta \rightarrow \alpha + \beta$. Microstructure analysis by optical and scanning electron microscopy of samples cooled at different rates showed that the samples also went through following microstructural changes; α' laths$\rightarrow$ Widmanstatten $\alpha \rightarrow$ basket weave $\alpha \rightarrow$ basket weave + patchy α structure. The presence of α' martensite in the samples cooled from 1010°C at 450°C/sec detected by x-ray diffraction and optical microscopy was confirmed by transmission electron microscopy. The α' martensite laths in the samples cooled from 1010°C at 450°C/sec has a highly dislocated structure, Figure 1, in agreement with the earlier work. X-ray diffraction analysis also revealed the presence of α and α' in the samples cooled at a rate in the range of 450 to 100°C/sec, with the volume fraction of α' decreasing with slower cooling rates. Transmission electron microscopy of samples cooled at a rate of 100°C/sec confirmed the presence of α' and α, Figure 2; α being differentiated from α' by the presence of highly dislocated structure. Qualitative spot and line chemical analysis of these laths by STEM/EDX analysis showed partitioning of Mo and Al in the α' and α laths respectively. Based on these results it is proposed that α' forms at M_s temperature, further cooling resulting in auto-tempering of the α' martensite.

X-ray diffraction analysis also revealed that on cooling from 900°C (below the beta transus temperature) IMI 550 goes through following phase transformations $\alpha_{primary}$ + orthorhombic α'' martensite $\rightarrow \alpha_{primary} + \alpha'' + \beta \rightarrow \alpha_{primary} + \alpha_{secondary} + \beta$. Cooling from 900°C at a rate of 15°C/sec or faster resulted in the formation of orthorhombic α'' martensite, with the volume fraction of α'' decreasing with slower cooling rates. The microstructural changes were however too fine to be detected by optical or scanning electron microscopy, e.g., the α'' martensite could not be detected by SEM analysis, Figure 3. The presence of α'' martensite was confirmed by transmission electron microscopy, Figure 4. These fine α'' needles have a highly twinned structure, in agreement with earlier work.

The effect of cooling rate on the phase transformations in Ti-6A-4V on cooling from below the β-transus temperature has also been examined. Two temperatures, 940°C and 884°C, were selected to examine the role of primary α content and β phase composition on the phase transformation observed in this alloy. X-ray diffraction revealed that cooling from both these temperatures at 350°C/sec or faster resulted in the formation of α' martensite. Additionally, XRD analysis showed that with slower cooling rates the β phase became stable and its volume fraction increased with decreasing cooling rate. TEM analysis of samples cooled at 350°C/sec from 940°C or 884°C confirmed the presence of α' martensite, having high dislocation density, stacking faults along with some twins. Additionally, TEM analysis of primary α in these samples confirmed its hexagonal structure its composition remaining unchanged at all cooling rates. Based on this it is suggested that for phase transformation purposes, primary α and the metastable β phases can be considered as two alloys, the former remains unchanged on cooling and later goes through α' to α+β transformation sequence with decreasing cooling rates.

Metastable β Alloys: These studies during the final year of this program have focused on the transformations occurring during cooling of TIMET LCB and Beta-C. Transmission electron microscopy of TIMET LCB, as summarized in Figure 5, has shown that α phase nucleation initially occurs at grain boundary triple points, decreasing cooling rates resulting in progressive nucleation of α at grain boundary edges and surfaces, with homogeneous nucleation being observed at the slowest cooling rates examined. In contrast α nucleation during cooling in Beta-C occurs at substantially slower cooling rates with grain boundary, dislocation associated and homogeneous nucleation occurring progressively with decreasing cooling rate.

High Cycle Fatigue Behavior of Metastable β Titanium Alloys:

The previous results of this sub-task have shown that processing history can have a major impact on the high cycle fatigue performance of metastable β titanium alloys. Scanning electron microscopy has now shown that fatigue crack initiation is associated with the free surface for Ti-15V-3Cr-3Al-3Sn lot A sheet, Figure 6. In contrast, evidence of sub-surface initiation was found in lot B sheet, Figure 4. Fatigue crack initiation in lot B also appeared to be associated with former α grain boundaries. Indeed, the transition in fracture appearance shown in Figure 7(insert) suggested that initiation in this sample occurred at a Type I(coarse α)/Type II (fine α) interface. Examination of the fracture profile, also showed that fatigue crack propagation occurred predominantly through the Type I regions.

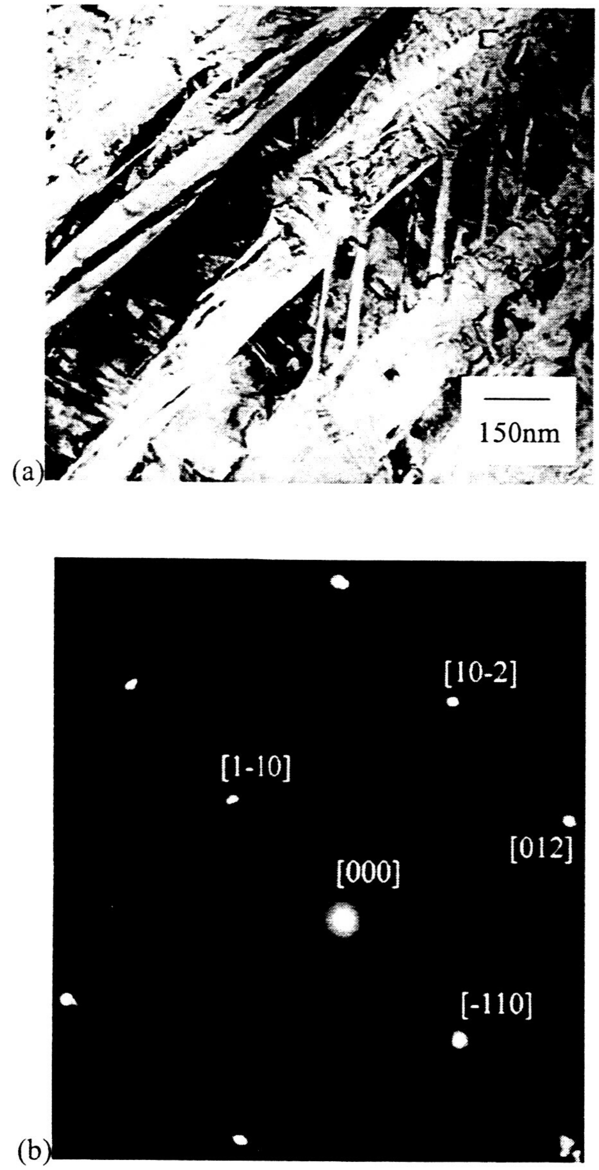

Figure 1. Transmission electron micrograph of IMI 550 solution treated at 1010°C followed by cooling at a rate of 450°C/sec showing (a) α' laths, and (b) selected area diffraction pattern from these laths.

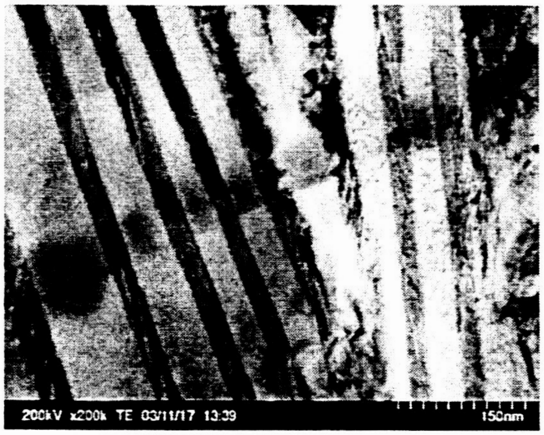

Figure 2. Scanning transmission electron micrograph showing α and α' needles, carbon deposit on the laths show the location of EDX.

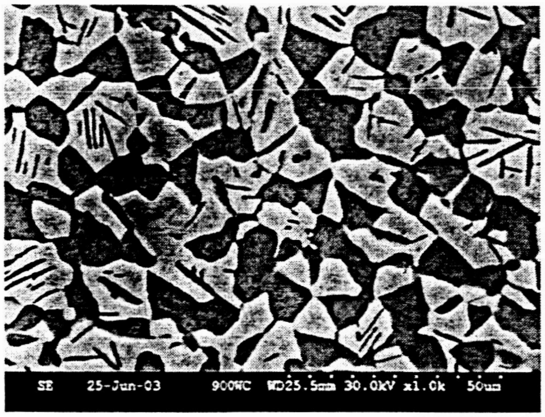

Figure 3. Secondary scanning electron micrograph showing primary α particles in IMI 550 sample cooled from 900°C at 150°C/sec.

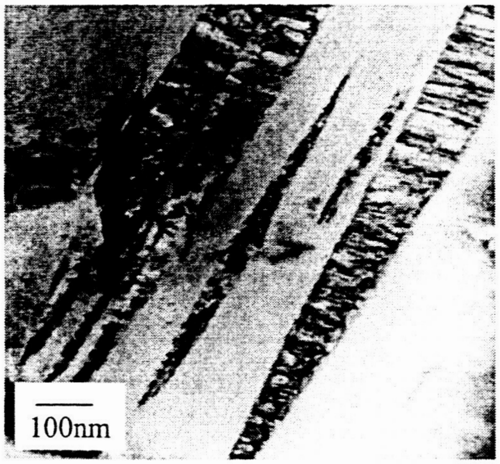

Figure 4. Transmission electron micrograph showing α'' martensite needles in IMI 550 sample cooled from 900°C at 150°C/sec.

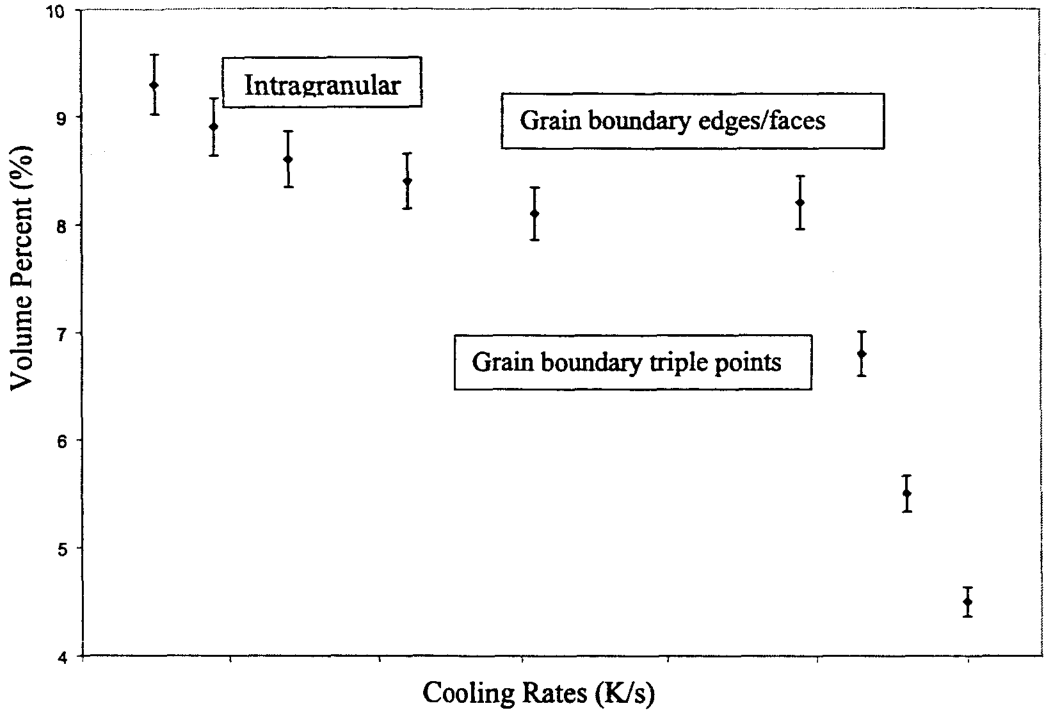

Figure 5: Influence of cooling rate on α nucleation site in TIMET LCB.

Nano-indentation measurements, Figure 8, of lot A specimens cycled at σ_{max}= 620 MPa, i.e., at the fatigue limit, demonstrated that failure at this stress level was associated with fatigue damage accumulation, that is cyclic hardening was observed in finite life fatigue samples, while cyclic softening was observed in samples where run-out occurred. Further measurements of lot B fatigue specimens, again cycled at the fatigue limit, σ_{max}= 827 MPa, indicated that the response in this material was dependent upon local microstructure. The cyclic response of Type I regions was similar to that of sheet A, while a continuous decrease in nano-hardness with increasing number of cycles was observed in Type II regions. These results indicate that enhancements in fatigue behavior within metastable β titanium alloys may be achieved through development of a bi-modal α microstructure.

Deformation Modeling:

The effort during this past year within this task has focused on achieving an understanding of the high temperature, high strain deformation processes in lamella Ti-6Al-4V and equiaxed α+β Corona-X, the latter a higher toughness alloy developed in support of the HSCT program. Microstructural examination has shown that the flow behavior of lamellar Ti-6Al-4V under these conditions involves dislocation generation (from lamellae α/β interfaces), dynamic recovery and flow softening. Flow softening can be related to lamellae bending, kinking and dynamic spheroidization. The flow instability region defined by Dynamic Material Modeling at low temperatures and high strain rates has been related to the combined effect of shear localization and strain induced porosity at grain boundary α/ β interface. Finally electron back-scattered diffraction of individual α lamellae suggests that dynamic spheroidization involves dynamic recovery/recrystallization of α lamellae, followed by grain boundary sliding and rotation of these new α grains.

High temperature, high strain deformation of eqiuaxed microstructures has also been concluded. . These studies of Corona-X in the equiaxed $\alpha+\beta$ condition showed that stable flow, as defined by Dynamic Material Modeling techniques, can be associated with dynamic recovery and recrystallization, unstable flow being associated with localized shear(low temperature and high strain rate), dynamic grain growth(high temperature and low strain rate) and strain assisted dissolution and coarsening of the primary α phase(low strain rates at all temperatures examined).

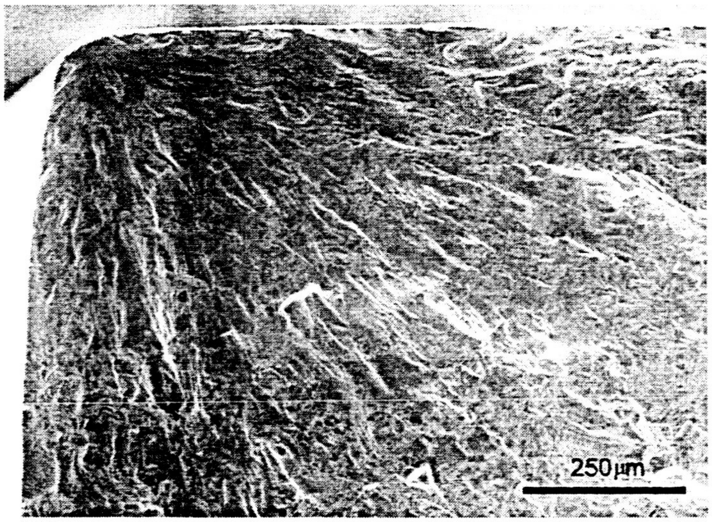

Figure 6: Scanning electron fractograph of Ti-15V-3Cr-3Al-3Sn lot A sheet in the solution-treated (ST) condition, aged condition (σ_{max}= 620 MPa, N= 65,689 cycles).

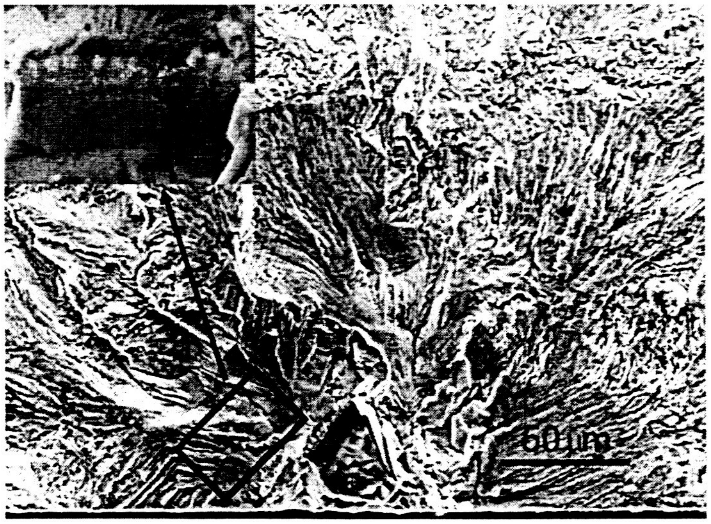

Figure 7: Scanning electron fractograph of Ti-15V-3Cr-3Al-3Sn lot B sheet in the solution-treated (ST) condition, aged condition (σ_{max}= 827 MPa, N= 29,511 cycles).

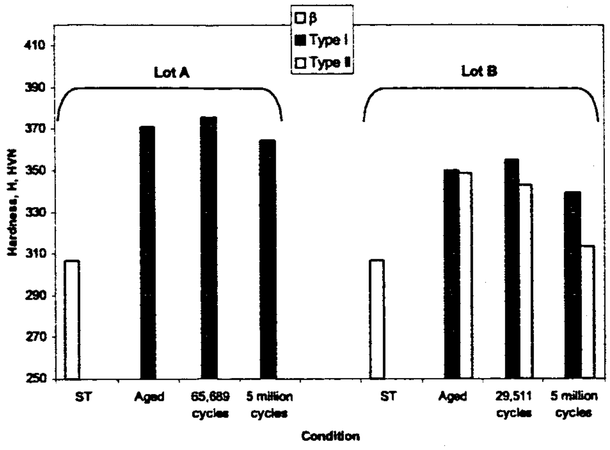

Figure 8: Nano-indentation measurements performed on Ti-15V-3Cr-3Al-3Sn in the solution-treated (ST) condition, aged condition and fatigued specimens cycled at σ_{max}= 620 MPa for lot A and σ_{max}= 827 MPa for lot B sheet.

Synthesis of TiC/Titanium Composites

This sub-task examined the feasibility of designing a high modulus, high strength α + ß titanium alloy utilizing particulate and dispersion strengthening techniques. Development of both Eshelby and finite element models of these three phase materials, containing α, ß and TiC has been completed. These have shown that attainment of high moduli will depend upon control of carbide/alpha/beta phase size and distributions. The Ti-Mo-Al/TiC system has been selected for this investigation. Thermodynamic simulations of this quaternary system using Thermo-Calc have shown that at elevated temperature approximately 1 wt pct C can be taken into solid solution, subsequent exposure at lower temperatures resulting in the precipitation of TiC dispersoids and reinforcements. Small buttons of the required compositions have been prepared and confirmed these predictions.

Technology Transfer

Phase Transformation in titanium alloys: Information on effect of cooling rate on phase transformations in IMI 550, Ti-6-22-22 and T-6Al-4V supplied to Boeing – Seattle to support F-22 program. Information on cooling rate effects on IMI 550 have been transmitted to GE Engine-Evandale, OH, that of TIMET LCB to TIMET.

Fatigue Behavior of Metastable ß Titanium Alloys: Information transmitted to TIMET. This information together with phase transformation studies on TIMET LCB being used to assist in implementation of TIMET LCB for automotive springs.

Deformation Processing of Titanium: details of Ti-6Al-4V results provided to TIMET and ALLVAC to support internal processing activities.

TiC Reinforced Titanium Alloys: Agreement signed with TIMET to provide support and scale-up of promising compositions as identified. Assistance has also been provided to Dynamet Technology, Burlington, MA to define optimized heat treatment schedule for TiC reinforced Ti-6Al-4V prepared from elemental powders.

Honors and Awards

National Materials Advisory Board, 2000 -
Clemson University Board of Trustees Award for Faculty Excellence - 1997
Humboldt Research Prize – 1997

Section II: Measurables

Refereed Publications:

1. R. R. Boyer, H. J. Rack and V. Venkatesh, THE INFLUENCE OF THERMOMECHANICAL PROCESSING ON THE SMOOTH FATIGUE PROPERTIES OF Ti-15V-3Cr-3Al-3Sn, Mat'l Sci. Eng., Vol. A243, 7(1998).
2. I. Philippart and H. J. Rack, HIGH TEMPERATURE DYNAMIC YIELDING IN BETA TITANIUM ALLOYS, Mat'l Sci. Eng., Vol. A243, 196(1998).
3. T. Ahmed and H. J. Rack, PHASE TRANSFORMATIONS DURING COOLING IN α + ß TITANIUM ALLOYS, Mat'l Sci. Eng., Vol.A243, 206(1998).
4. I.Philippart and H. J. Rack, HIGH TEMPERATURE HIGH STRAIN DEFORMATION OF Ti-6.8Mo-4.5Fe-1.5Al, Mat'l Sci. Eng., Vol. A254, 253(1998).
5. S. Azimzadeh and H. J. Rack, PHASE TRANSFORMATIONS IN Ti-6.8Mo-4.5Fe-1.5Al, Met. Trans., Vol. 29A, 2455(1998).
6. M. Long, R. Crooks and H. J. Rack, HIGH-CYCLE FATIGUE BEHAVIOR OF SOLUTION TREATED METASTABLE ß TITANIUM ALLOYS, Acta Met., Vol.47, 661(1999).
7. S. Menon and H. J. Rack, FLOW STABILITY IN BINARY Al-Li ALLOYS, Mat'l Sci. Eng., Vol. 297, 244(2001).
8. S. Menon and H. J. Rack, HIGH TEMPERATURE, HIGH STRAIN FORGING BEHAVIOR OF BINARY Al-2Li, Mat'l Sci. & Tech., Vol. 17, 836(2001).
9. K. Kharia and H. J. Rack, THE INFLUENCE OF SOLUTION TREATMENT TEMPERATURE ON THE MARTENSITIC PHASE TRANSFORMATIONS IN IMI 550(Ti-4Al-4Mo-2Sn-0.5Si), Met. Trans., Vol. 32A, 671(2001).
10. A.Roussel, I. Duta and H. J. Rack, GRAIN GROWTH PHENEOMENA IN Ti-15V-3Al-3Cr-3Sn, <u>Microstructural Modeling and Prediction during Thermomechical Processing,</u> R. Srinivasan and S. L. Semiatin, eds., TMS, Warrendale, PA, 2001, pp. 157-165.
11. A. Roussel, L. Reister and H. J. Rack, HIGH CYCLE FATIGUE RESPONSE OF SOLUTION TREATED AND AGED Ti-15V-3Al-3Cr-3Sn, <u>FATIGUE 2002</u>, Proc. 8th Int. Fatigue Congress, Stockholm, Sweden, June 2002, A. F. Blom, ed., Vol. 3, pp. 1823-1832.
12. M. Gheorghe, J.I. Qazi and H. J. Rack, ANISOTHERMAL ALPHA PHASE FORMATION IN Ti-6.8Mo-4.5Fe-1.5Al, Proc. 10th World Titanium Conference, DGM, Hamburg, 2003, in press.
13. J. Qazi, D. Hobson and H. J. Rack, PHASE TRANSFORMATIONS DURING COOLING OF Ti-6Al-2Mo-2Cr-2Sn-2Zr-0.12Si, Met. Trans., in preparation.
14. J. Qazi and H. J. Rack, PHASE TRANSFORMATIONS DURING COOLING OF IMI 550, Met. Trans., in preparation.
15. J. Qazi and H. J. Rack, PHASE TRANSFORMATIONS DURING COOLING OF SUB-TRANSUS SOLUTION TREATED Ti-6Al-4V, Met. Trans., in preparation.
16. M. Gheorghe, J.I. Qazi and H. J. Rack, ANISOTHERMAL ALPHA PHASE FORMATION IN BETA – C TITANIUM, in preparation.
17. T. Ahmed and H. J. Rack, PHASE TRANSFORMATIONS DURING COOLING OF Ti-5Al-2Sn-4Zr-2Cr-1Fe(β-CEZ), Mat'ls Sci. & Tech., in preparation
18. I. Duta and H. J. Rack, DYNAMIC SPHEROIDIZATION OF LAMELLAR TI-6Al-4V, in preparation..
19. S. Vignesh and H. J. Rack, High Temperature, High Strain Deformation of Equiaxed α+β CORONA –X, in preparation.

Section III: Other Publications and Proposals

Publications:

1. M. Long and H. J. Rack, TITANIUM ALLOYS IN TOTAL JOINT REPLACEMENT - A REVIEW, Biomaterials, Vol. 19,1621(1998).
2. V. Venkatesh and H. J. Rack, ELEVATED TEMPERATURE STRAIN HARDENING OF INCONEL 690, Mech. of Mat'ls, Vol. 30, 69(1998).

3. V. Venkatesh and H. J. Rack, INFLUENCE OF MICROSTRUCTURAL INSTABILITIES ON ELEVATED CREEP DEFORMATION OF INCONEL 690, Mat'ls Sci. & Tech., Vol.15, 408(1999).
4. V. Venkatesh and H. J. Rack, A NEURAL NETWORK APPROACH TO ELEVATED TEMPERATURE CREEP-FATIGUE LIFE PREDICTION, Int. Jn Fatigue, Vol. 21, 225(1999).
5. A. C. Geiculescu, H. G. Spencer, H. J. Rack and B. Sullivan, AQUEOUS SOL-GEL MODIFICATION OF THE FIBER-MATRIX INTERFACE IN GRAPHITE FIBER ALUMINUM MATRIX COMPOSITES, Adv. Mat'ls & Man., Vol. 14, 489(1999).
6. X. Tang, T. Ahmed and H. J. Rack, MARTENSITIC PHASE TRANSFORMATION IN Ti-Nb-Ta and Ti-Nb-Ta-Zr ALLOYS, Jn. Mat'ls Sci., Vol. 35, 1805(2000).
7. J. Fitzgerald, P. D. Rack, A. C. Geiculescu and H. J. Rack, DEPOSITION OF CERAMIC MATERIALS USING POWDER AND PRECURSOR VEHICLES VIA DIRECT WRITE PROCESSING, Materials Development for Direct Write Technologies, MRS Proc. Vol. 624, 2000, pp. 29-34.
8. A. C. Geiculescu and H. J. Rack, ATOMIC-SCALE STRUCTURE OF WATER-BASED XEROGELS BY X-RAY DIFFRACTION, Jn. Sol-Gel Sci. & Tech., Vol. 30, 13(2001).
9. P. D. Rack, A. C. Geiculescu and H. J. Rack, GROWTH OF REACTIVE SPUTTER DEPOSITED TUNGSTEN-CARBON THIN FILMS, Jn. Vac. Sci. Tech., Vol. 19, 62(2001).
10. M. Long and H. J. Rack, FRICTION AND SURFACE BEHAVIOR OF SELECTED TITANIUM ALLOYS DURING RECIPROCATING-SLIDING MOTION, Wear, Vol.249, 158(2001).
11. A. C. Geiculescu and H. J. Rack, ATOMIC SCALE STRUCTURE OF ALCOHOL-BASED ZIRCONIA XEROGELS BY X-RAY DIFFRACTION, Jn. Non-Crystalline Solids, Vol. 289 53(2001).
12. H. J. Rack, I. Gheorghe, K. Kharia and A.C. Geiculescu, IN-SITU FABRICATION OF FIBER REINFORCED METAL MATRIX COMPOSITES, Affordable Metal Matrix Composites for High Performance Applications, A. Pendey, K. Kendig and T. Watson, eds., TMS, Warrendale, PA, 2001, pp. 211-221.
13. I.Gheorghe and H. J. Rack, INFLUENCE OF TiO_2 TO Al RATIO ON THE REACTION IN TiO_2/Al COMPOSITES, Mat'ls Sci and Tech., Vol. 18, 1079(2002).
14. I.Gheorghe and H. J. Rack, REACTIVE INFILTRATION OF 25 V/O TiO_2/Al COMPOSITES, Met. Trans., Vol. 33A, 2155(2002).
15. A. C. Geiculescu and H. J. Rack, SMALL ANGLE X-RAY SCATTERING STUDIES OF POLYMERIC ZIRCONIA AQUEOUS XEROGELS, Jn. Non-Crystalline Solids,Vol. 306, 30(2002).
16. G.G. Yapici, I. Karaman,Z. P. Luo and H. Rack, MICROSTRUCTURE AND MECHANICAL PROPERTIES OF SEVERELY DEFORMED POWDER PROCESSED Ti-6Al-4V USING EQUAL CHANNEL ANGULAR EXTRUSION, Scripta Materialia, Vol. 49,1021(2003).
20. M. Long, J.I. Qazi and H.J. Rack, RECIPROCATING SLIDING WEAR RESISTANCE OF β21SRx TITANIUM, Proc. 10th World Titanium Conference, DGM, Hamburg, 2003, in press.
21. J.I. Qazi, V. Tsakiris, B. Marquardt and H. J. Rack, THE EFFECT OF DUPLEX AGING ON THE TENSILE BEHAVIOR OF Ti-35Nb-7Zr-5Ta-(0.06-0.7)O ALLOYS, Proc. 10th World Titanium Conference, DGM, Hamburg, 2003, in press.
22. J. I. Qazi and H. J. Rack, EFFECTS OF THERMAL TREATMENT ON THE MECHANICAL PROPERTIES OF BIOMEDICAL TITANIUM ALLOYS, Mat'ls and Processes for Medical Devices I, ASM Int., in press.
23. R. Z. Valiev, V. V. Stolyarov, H. J. Rack and T. C. Lowe, SPD-PROCESSED ULTRA-FINE GRAINED TI MATERIALS FOR MEDICAL APPLICATIONS, Mat'ls and Processes for Medical Devices I, ASM Int., in press.
24. M. Kocan, T. Ludian, M. Ishii, H, J, Rack and L. Wagner, OPTIMIZATION OF MICROSTRUCTURE OF TIMETAL LCB FOR APPLICATION AS SUSPENSION SPRINGS, Light Materials for Transportation Systems(LIMAT), ed. O. Es-Said, 2003, in press.
25. E. Fu, H. C. Bellum, J. Qazi, H. J. Rack and V. Stolyaru, RECIPROCATING-SLIDING WEAR OF ULTRA-FINE GRAINED Ti-6Al-4V, Proc. 3rd Int. Sym. On Ultrafine Grained Materials, TMS, in press.
26. M. Long and H. J. Rack, RECIPROCATING-SLIDING WEAR AND SUBSURFACE BEHAVIOR OF TITANIUM ALLOYS, Met. Trans., in press.

27. A. C. Geiculescu, K. Siegamura and H. J. Rack, REACTIVE INFILTRATION OF 25 V/O Nb_3O_5/Al COMPOSITES, in preparation.

Presentations:

1. H. J. Rack, PHASE TRANSFORMATIONS IN METASTABLE BETA TITANIUM ALLOYS, Aeromat '97, Williamsburg, VA, May, 1997.
2. H. J. Rack, HIGH TEMPERATURE DEFORMATION PROCESSING OF $\alpha+\beta$ TITANIUM ALLOYS, Aeromat '97, Williamsburg, VA, May 1997.
3. R. Boyer, H. J. Rack and V. Venkatesh, THE INFLUENCE OF THERMOMECHICAL PROCESSING ON THE SMOOTH FATIGUE PROPERTIES OF Ti-15V-3Cr-3Al-3Sn, International Conference on Thermomechanical Processing of Steels and Other Materials, Univ. of Wollengong, Australia, July, 1997.
4. T. Ahmed and H. J. Rack, PHASE TRANSFORMATIONS DURING COOLING IN $\alpha+\beta$ TITANIUM ALLOYS, International Conference on Thermomechanical Processing of Steels and Other Materials, Univ. of Wollengong, Australia, July, 1997.
5. H. J. Rack and I. Phillipart, HIGH TEMPERATURE DYNAMIC YIELDING IN BETA TITANIUM ALLOYS, International Conference on Thermomechanical Processing of Steels and Other Materials, Univ. of Wollengong, Australia, July, 1997.
6. J. Brasell, P. Martin and H. J. Rack, PHASE TRANSFORMATIONS IN CORONA-X, Fall Mtg ASM/TMS, Indianapolis, Indiana, Sept. 1997.
7. X. Tang and H. J. Rack, KINETICS OF ORDERING IN Ti-6Al-2Mo-2Cr-2Zr, Fall Mtg ASM/TMS, Indianapolis, Indiana, Sept. 1997.
8. H. J. Rack, PRECIPITATION IN METASTABLE BETA TITANIUM ALLOYS, Tech. Univ. Hamburg-Harburg, June 1998.
9. K. Kharia and H. J. Rack, PHASE TRANSFORMATION IN IMI 550, TMS Annual Meeting, Nashville, Tenn., March, 2000.
10. H. J. Rack and C. Robinson, HIGH TEMPERATURE, HIGH STRAIN DEFORMATION OF BETA-CEZ TITANIUM, TMS Annual Meeting, Nashville, Tenn., March 2000.
11. I. Gheorghe and H. J. Rack, THERMODYNAMICS OF IN-SITU REACTIONS BETWEEN TiO_2 AND PURE AL, Annual Mtg, TMS, Nashville, Tenn., March, 2000.
12. A. C. Geiculescu and H. J. Rack, SHORT RANGE STRUCTURE OF ZIRCONIA XEROGELS, Am. Cer. Soc., Annual Mtg., St. Louis, Mo., April 2000.
13. J. Fitzgerald, P. D. Rack, A. C. Geiculescu and H. J. Rack, DEPOSITION OF CERAMIC MATERIALS USING POWDER AND PRECURSOR VEHICLES VIA DIRECT WRITE PROCESSING, MRS Mtg., San Francisco, CA, April, 2000.
14. H. J. Rack, ADVANCED METALLIC MATERIALS FOR BIOLOGICAL APPLICATIONS, INSA-Rennes, France, June 7, 2000 and TUMunich, Germany July 20, 2000.
15. H. J. Rack, HIGH TEMPERATURE, HIGH STRAIN DEFORMATION OF NEAR-BETA TITANIUM ALLOYS, BTU-Cottbus, Germany, June 29, 2000.
16. H. J. Rack, MARTENSITIC PHASE TRANSFORMATIONS IN ALPHA-BETA TITANIUM ALLOYS, BTU-Cottbus, Germany, July 3, 2000.
17. H. J. Rack, IN-SITU FORMATION OF HIGH TEMPERATURE COMPOSITES, BTU-Cottbus, Germany, July 5, 2000.
18. H. J. Rack, IN-SITU FORMATION OF LIGHT- WEIGHT FIBER REINFORCED COMPOSITES, ARL, Belvedere, Md, August 21, 2000.
19. H. J. Rack, J. Wendt, M. Hilpert and L. Wagner, DIRECTIONAL MECHANICAL PERFORMANCE OF WROUGHT AZ80 MAGNESIUM, Annual Mtg, TMS, New Orleans, Feb. 17, 2001.
20. H. J. Rack, TITANIUM IN THE 21ST CENTURY, BTU-Cottbus, Germany, October 26, 2001. H. J. Rack, ANISOTHERMAL ALPHA PHASE FORMATION IN Ti-6.8Mo-4.5Fe-1.5Al, 10th World Titanium Conference, DGM, Hamburg, July 11, 2003.
21. H.J. Rack, RECIPROCATING SLIDING WEAR RESISTANCE OF β21SRx TITANIUM, 10th World Titanium Conference, DGM, Hamburg, July 12, 2003.

22. H. J. Rack, THE EFFECT OF DUPLEX AGING ON THE TENSILE BEHAVIOR OF Ti-35Nb-7Zr-5Ta-(0.06-0.7)O ALLOYS, 10th World Titanium Conference, DGM, Hamburg, July 12, 2003.
23. H. J. Rack, EFFECTS OF THERMAL TREATMENT ON THE MECHICAL PROPERTIES OF BIOMEDICAL TITANIUM ALLOYS, Mat'ls and Processes for Medical Devices, Anaheim, Cal., Sept. 8, 2003.
24. H. J. Rack, SPD-PROCESSED ULTRA-FINE GRAINED TI MATERIALS FOR MEDICAL APPLICATIONS, Mat'ls and Processes for Medical Devices, Anaheim, CA, Sept. 8, 2003.

Proposals:

1. Phase Transformations in TiC Reinforced P/M Ti-6Al-4V, DOE, March 2002
2. Interrelationship between Microstructure and High Cycle Fatigue Performance of TIMET LCB, TIMET, July 2002(Funded).
3. Novel Titanium Materials for Orthopaedic Lumbar Implants, NIH, December, 2002(Funded).

Section IV: Participants

Current Participants

Graduate Students:

M. S. Candidates:

Ion Duta (M,W)
S. Vignesh(M, Asian)
H. C. Bellam(F, Asian)

Research Associates:

Dr. J. Qazi(M, Asian)

Faculty:

Henry J. Rack (W, M)

Former Participants

Undergraduate Students:

Rebecca. Hubbard (F, W)

Graduate Students:

M. S. Graduates:

John Brasell (M, W)[Nucor Steel, Darlington, SC]
Alex Rousell (M, W)[ALLVAC, Monroe, NC.]
Dale Hobson (M, W)[Oxford Instruments, Medford, Mass]
Krishna Kharia (M, Asian)[Tata Industries, India]
Mariana Gheorghe (F, W)(PhD Candidate Georgia Tech.)

Ph.D. Candidates:

Santosh. Menon (M, Asian)[LSI Logic, Portland, OR]

Research Associates:

Dr. T. Ahmed (M, Asian), SABIC, Riyadh, Saudi Arabia
Dr. X. Tang (F, Asian)[Carpenter Technology, Reading, Pa]

Section V: Collaborations

NASA Centers:

NASA Langley Research Center, Hampton, VA:

Mr. William Brewer – HSCT Program
Mr. Dennis Discus – HSCT Program
Ms. Terryl Wallace, serve on PhD committee at Univ. of Virgina
Dr. Roy Crooks, joint research on grain boundary misorientation effects on high cycle fatigue behavior of metastable beta titanium alloys

Academic:

Tech. University of Munich, Germany

Dr. Jean Gregory, high cycle fatigue performance of metastable β titanium alloys

BTU- Cottbus/TUClausthal , Germany

Dr. Lothar Wagner, fatigue and fracture of titanium alloys

INSA-Rennes, France

Dr. Jean Debuigne, phase transformations in metastable β titanium alloys

Business and Industry:

Titanium Manufacturers:

TIMET, Las Vegas, NV:

Dr. Steve Fox, Design of TiC/Ti Composites, fatigue performance of metastable beta titanium alloys.

Dr. Vasisht Venkatesh, former graduate student

RMI, Niles, Ohio:

Mr. James Ferraro, processing of IMI 550, Ti-6-22-22, Beta-C

Teledyne ALLVAC, Monroe, NC:

Mr. Alex Roussel (former student), Dr. Richard Kennedy, Mr. J. R. Wood, Mr. J. R. Wood, Mr. Michael Volas, processing of titanium alloys

Airframe Manufacturers:

Boeing Commercial Airplane, Seattle, WA:

Dr. Jim Cotton, Mr. Rodney Boyer, thermomechanical processing of metastable beta titanium alloys

Boeing, St. Louis, MO:

Mr. Richard Lederich, phase transformations in Ti-6-22-22

Aircraft Engine Manufacturers:

General Electric, Evandale, Ohio:

Dr. Andy Woodfield, processing of α–ß titanium alloys.

Tom Broderick, processing of IMI 550

Other Federal/Governmental Agencies:

Oak Ridge National Laboratories, High Flux Reactor Site:

Dr. Stephan Spooner, Neutron Diffraction Analysis of Ordering in IMI 550

AECL, Chalk River, Canada

Dr. Kelly Conlon, High Temperature Neutron Diffraction

NASA EPSCoR Final Report

Name of PI – Nikunja K. Swain, Ph.D., P.E.

Cluster – Aeronautics

Section I: Narrative

I worked on this project during summer 2003 for only six weeks. My research focused on digital signal processing using Joint Time and Frequency Analysis technique.

Need for JTFA

A given signal can be represented either as a function of time, which shows how the signal amplitude changes over time or as a function of frequency, which tells us how frequently the amplitude changes. The bridge between time and frequency representations is the *Fourier transform*, which is one of the most important signal analysis methods. Using Fourier transformation, a signal can be easily decomposed as a weighted sum of sinusoid functions. This enables one to process either the signal time waveform or its corresponding set of sinusoid functions, depending on which form is more convenient. Fourier transform also used to compute power spectrum for a signal. The power spectrum usually has a simpler pattern than the time waveform, and as result it often serves as the fingerprint of the analyzed signal. But the Fourier transform possesses certain disadvantages that prevent its use to represent many signals encountered in real world effectively. Examples of some of these signals are seismic and ECG (electrocardiogram), speech and noise corrupted signals. To properly analyze this type of signals both time and frequency analysis are generally performed. This is called joint time-frequency analysis (JTFA). The main objective of this analysis is to determine the energy density of a signal, which indicates how much energy is contained within a certain time interval in a given frequency band. This information is then used to analyze the signal properties.

I continued designing and developing Virtual Instrument instructional modules for digital signal processing and digital filters. I also spend time on design and development of remote control and data acquisition modules using LabVIEW and Visual Basic (Object Oriented Programming).

I have prepared a manuscript entitled "Joint Time Frequency Analysis Using Virtual Instruments" and plan to present it in local/regional conference.

The project budget provided funding only for my summer salary and there was no set aside funding in my part of the proposal for involving students. Therefore, no student was involved in my part of the project.

Section II: Measurables

Publications -

1. N. K. Swain, J. A. Anderson, R. Korrapati, M. Swain, Ajit Singh, "IPAR – A Visual Basic Program to study IP Addressing and Routing" - Proceedings of the IEEE SECoN 2003, Jamaica, West Indies, April 2003.
2. N. K. Swain, Ajit Singh, J. A. Anderson, Mswain, et. all, "Remote Data Acquisition, Control, and Analysis using LabVIEW Front Panel and Real Time Engine" – Proceedings of the IEEE SECoN 2003, Jamaica, West Indies, April 2003.
3. N.K. Swain, Mrutyunjaya Swain, James A. Anderson, "Integrating Virtual Instruments into EET Curriculum – 2004 ASEE Annual Conference Proceedings, Salt Lake City, Utah, June 2004.

Patents – None

Grants and Financial Awards –

"Computer Based Virtual Engineering Laboratory – CBVEL" – DOD Infrastructure grant, 1999.

Section III – Other Publications and Proposals

None

Section IV – Participants

None

Section V – Collaborations

None

Monitoring Coastal Wetland Change and Modeling Ecosystem Health in South Carolina using Advances in Remote Sensing Digital Image Processing

NASA/EPSCoR Year 5 & FINAL Report

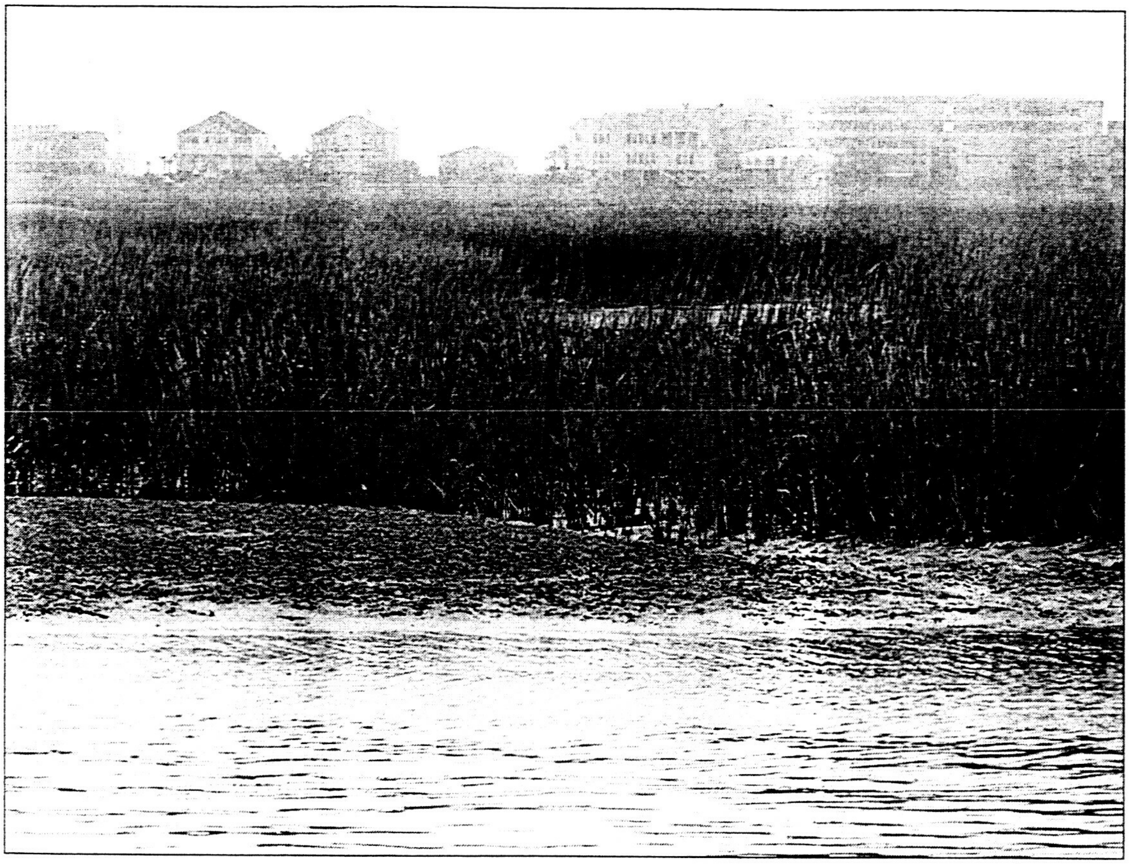

John R. Jensen and Dwayne E. Porter
University of South Carolina

Cassandra J. Runyon
College of Charleston

Jeff E. Allen
Clemson University

South Carolina EPSCoR – Wetlands Research Cluster

Section I: Executive Summary of the 5th and Final Year of NASA Sponsored EPSCoR Research in South Carolina

This report summarizes both the Wetlands Research Cluster's Year 5 activities and our research accomplishments over the full five years of our grant. This grant has been a tremendous asset to the colleges involved and a tremendous boost to environmental research within South Carolina.

Quite notably, our remote sensing cluster has matured through our NASA EPSCoR collaborative research and experiences. True to the program's intent, several of our team members have won additional competitive research awards totaling more than $4.5M from 6 non-NASA agencies an have additional proposals pending for an additional $5M. All members of our team were active in outreach: more than 30 presentations were delivered to local, state, regional and national audiences, and we published more than 50 papers and abstracts. We are very proud of the thirty-three M.S. and Ph.D. students we supported with this funding. Many of these students are now PI's and are now writing their own research grants. We also supported 9 undergraduate students who are now in graduate school or recently graduated from environmental science programs. Two student internship opportunities were also initiated; one corporate and one with SC Department of Natural Resources.

In addition to gathering and analyzing a variety of remote sensor data to evaluate the health of South Carolina's lowcountry wetlands, our team also looked at the effects of population growth on the environment. A full report of the culmination of 5 year's worth of modeling population growth is presented in Appendix 1.

Year 5 & Final Research Results: Incorporation of BRDF Characteristics of *Spartina alterniflora* to Model Estuarine-wide Biomass Characteristics and Perform a Change Detection Analysis.

Building upon our advancements in the use of innovative remote sensing and digital image processing techniques over the past four years, we performed a change detection analysis of biomass characteristics of *Spartina alterniflora* within the Murrells Inlet estuary. During the summer of 2003, we acquired high resolution multi-spectral data of the Murrells Inlet estuary using the same protocol for the acquisition of the remote sensing and in situ calibration data as developed during Year 1 of this project (Jensen et al., 1998).

Activity 1: Murrells Inlet 1997-2001 Change Detection Analysis

We quantified and investigated the changes in upland and vegetative cover in Murrells Inlet, SC over the five-year grant period. A change detection analysis will be conducted using ATLAS 3 x 3 m multispectral data acquired on October 7, 1997 and IKONOS 4 x 4 m multi-spectral data acquired in the fall of 2001. Potential anthropogenic-induced trends (i.e., rates of increases in impervious surface) were identified that demonstrate the correlations between estuarine vegetation stress and upland land cover changes. Research previously conducted of BRDF signatures of *Spartina alterniflora* were incorporated into the ATLAS and IKONOS data for improving image classification. Radiometric adjustments that account for solar and sensor zenith angles were used for deriving accurate surface albedos.

In addition, in-situ estuarine biophysical data (i.e., biomass, LAI, height, etc.) were acquired simultaneously with the IKONOS data collection for modeling changes in the biophysical parameters of the estuary between 1997 and 2001.

Activity 2: Evaluating ADAR or Hymap data for mapping intertidal oyster reefs.

The eastern oyster, *Crassostrea virginica*, serves prominent roles in the ecology of estuarine and coastal ecosystems (Bushek, et al., in press). This oyster, which lives in the intertidal portion of South Carolina's estuaries, is a reef-forming, filter feeding bivalve. Oyster reefs perform a variety of ecological roles that contribute significantly to the structure and function of the coastal ecosystems in which they exist. Oyster reefs form a unique habitat that supports and abundance of taxonomically diverse species. They stabilize creek banks and serve as both active and passive filters as waters pass over them. In South Carolina, the eastern oyster is both an important for commercial fishery and recreational fishery activities. The natural population of oysters has declined dramatically due to overfishing and habitat loss/degradation (Bushek 2001).

In South Carolina, the SC Department of Health and Environmental Control is responsible for regulating the opening and closing of shellfish reefs for commercial and recreational harvesting. The SC Department of Natural Resources (SCDNR) is responsible for managing state shellfish ground for commercial and recreational harvesting. Important to the efforts of both agencies is the ability to accurately map existing shellfish resources in a timely manner. Currently, the SCDNR maps shellfish reefs using a combination of Global Positioning System (GPS) surveys and field measurements and incorporates the information in a Geographic Information System (GIS). While much improved over historical techniques which involved extensive field surveys and laborious manual cartographic techniques are still manpower intensive and limit the ability of the agency to maintain and update oyster maps for the entire coast of South Carolina.

Therefore, the purpose of this study is to assess the utility of supervised classification of high spectral resolution imagery for mapping oyster beds in a South Carolina estuary. The proposed study site is the intertidal area of the North Inlet-Winyah Bay National Estuarine Research Reserve located north of Georgetown, SC. The imagery used in this study is a rectified and registered image acquired by Positive Systems, Inc. at low tide on November 4, 1999 and HYMAP hyperspectral imagery obtained on October 22, 2000. The ADAR 5500 digital camera was used to acquire 4 bands (band 1: 450-515 nm; band 2: 525-605 nm; band 3:630-690 nm; and band 4: 750-860 nm) at 0.7 x 0.7 m spatial resolution. The imagery was acquired in support of this project and an associated Environmental Protection Agency project.

Building upon a student project (Schmidt 2000) supported by this NASA grant, a GER 1500 spectroradiometer was used to acquire multiple spectral profile samples of oyster beds throughout the study area. Profiles of live and empty oyster shells, pure mud, mixed with dead oyster shells will be acquired. Profile information, logistic regression techniques, and image processing techniques, were used to develop a supervised classification of shellfish beds within the intertidal zone of the North Inlet study area. We also attempted to classify the health (i.e., living vs. dead) of the oyster beds using these techniques. The resultant map was ground-referenced to determine the accuracy of this use of remotely sensed imagery for mapping shellfish resources.

As part of this project, we established two student internship opportunities. One is with Geometrics, an engineering consulting firm specializing in coastal environmental issues, and the second with the Marine Resources Division of the SCDNR.

References

Bushek, D. 2001. http://marinescience.sc.edu/faculty/bushek.shtml

Schmidt, L. http://www.cla.sc.edu/geog/rslab/751/f00/schmidt/

Bushek, D., J. Kreesee, B. Jones, D. White, M. Neet, and D.E. Porter. In press. Shellfish health management: a system level perspective for *Perkinsus marinus*. Journal of Shellfish Research.

Activity 3: Evaluating the use of HYMAP imagery for mapping algal community composition and wetland biomass.

Qualification and quantification of algal community composition in estuarine systems can yield important information about overall water quality, eutrophication, and toxic and non-toxic algal blooms. Common sampling techniques have relied upon point sampling from land and watercraft sampling stations, and data analyses have depended upon highly trained individuals using microscopy. Although these techniques are effective, they are limited in spatial coverage and the time and effort required to analyze a large number of samples is prohibitive.

Recent advances in the use of high performance liquid chromatography (HPLC) have aided researchers to qualify algal community composition (Wright et al., 1996). Further research in the use of factor analysis to analyze HPLC results has led to a robust method to quantify each component of the algal community can be described by accessory pigment(s) or pigment ratios in relation to total chlorophyll *a* (Mackey et al, 1996). Thus, if the pigment characteristics of the local algal communities are adequately described from lab cultures, wild algal populations from estuaries along the South Carolina coast (White and Lewitus unpublished data).

The use of remotely sensed data from aircraft and spacecraft to quantify surface water algal biomass by monitoring chlorophyll a has become common, allowing for large spatial coverage repeatable over time. However, the available remote sensing platforms were limited to chlorophyll *a* detection. The advent of hyperspectral data may hold promise in the use of remotely sensed data may hold promise in the use of remotely sensed data to derive an overall pigment composition from a water body. The Airborne Visible InfraRed Imaging Spectrometer (AVIRIS) was the first of these platforms to be used to classify and map a mixed phytoplankton bloom (Richardson and Kruse).

The purpose of this study is to assess the HYMAP sensor (Hyperspectral Mapping) in describing surface water algal community composition in a well-mixed coastal estuarine system. The HYMAP sensor was deployed over North Inlet, South Carolina in October of 2000. This sensor has a range of 100 – 200 bands and a bandwidth of 10-20nm. In conjunction with this over flight, water samples were collected and a suite of environmental variables were analyzed including inorganic and organic nitrogen and phosphorus, algal pigments (*chl a* and accessory pigments), total sediment load and total organic carbon. A GER 1500 spectro-radiometer was used to acquire multiple spectral profile samples of the water surface from sampling stations. The in-situ spectroradiometer profile information and specialized hyperspectral digital image processing techniques were used to classify the imagery. The techniques included matched filtering, spectral feature fitting, and pixel purity index analysis. The hyperspectral data will also be analyzed and compared to HPLC and microscopy results to determine the accuracy of the remotely sensed data. If possible, the hyperspectral data were evaluated to determine the biomass of the smooth cordgrass (*Spartina alterniflora*) surrounding the estuarine water under investigation. Results are discussed more fully in Section II.

HYMAP Sensor Specifics

HyMAP sensor is a 126-band commercial hyperspectral scanner that is capable of acquiring data at spatial resolution between 3-10m. The spectral resolution is listed below:
VIS 0.45 – 0.89 um (15 nm sampling interval)
NIR 0.89 – 1.35 um (15nm sampling interval)
SWIR1 1.40-1.80 um (13 nm sampling interval) SWIR2 1.95 – 2.48 um (17 nm sampling interval)

Additional information:
http://www.analyticalimaging.com/data_acq/hymap_1999/hym_specs.htm

HyMAP Data report for 10-22-2000 North Inlet, SC

Geo: average alt: 2098.685895
Geo: Start line lat, lon, alt: 33.381052, -79.170670, 2087.392954
Geo: End line lat, lon, alt: 33.297326, -79.214087, 2102.480411
Geo: year, month, day: 2000, 10, 22
Geo: hour, minute, sec: 16, 17, 40
Geo: average scene elevation: 2.233238
Geo: UTM zone: 17, Datum: NAD-27
Geo: original pixel size: 4.500000
Geo: output pixel size: 4.00000
Geo: UTM upper left X coord (1,1) 665081.445414
Geo: UTM upper left Y coord (1,1) 3695302.511934

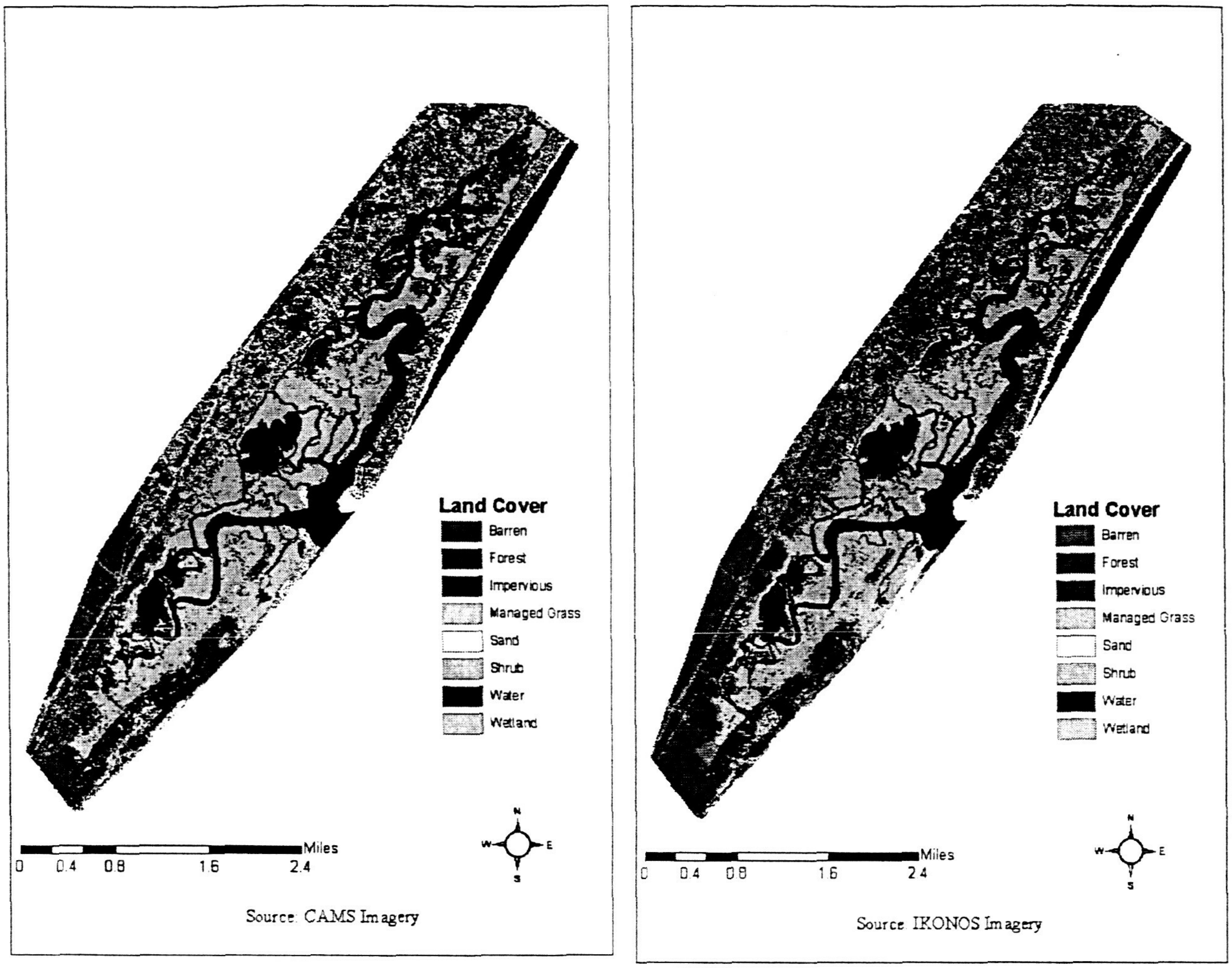

Figure 1. Murrells Inlet land cover for 1997 and 2001.

Section II: Measurables for Wetlands Remote Sensing Activities

Research efforts towards quantifying upland and vegetation cover in Murrells Inlet, SC succeeded in data acquisition and remote sensing data analysis. Changes in sensor availability and specific requests made by local resource management organizations, however, altered the choice of airborne sensor and specific tasks, though the original research requirements remained.

In support of a request from the Murrells Inlet 2005 Task Force and the NOAA-supported Murrells Inlet Special Area Management_Plan (MI-SAMP), an effort was undertaken to provide a land cover change detection analysis using imagery collected as part of this project and an additional NOAA-funded research effort. Using CAMS imagery acquired in August 1997 in support of this effort, and IKONOS imagery acquired in October 2001 in support of the NOAA-funded project, a change detection analysis was performed. The results of the change detection analysis suggest the most significant change within the Murrells Inlet area was an increase in impervious surfaces (Figures 1 and 2).

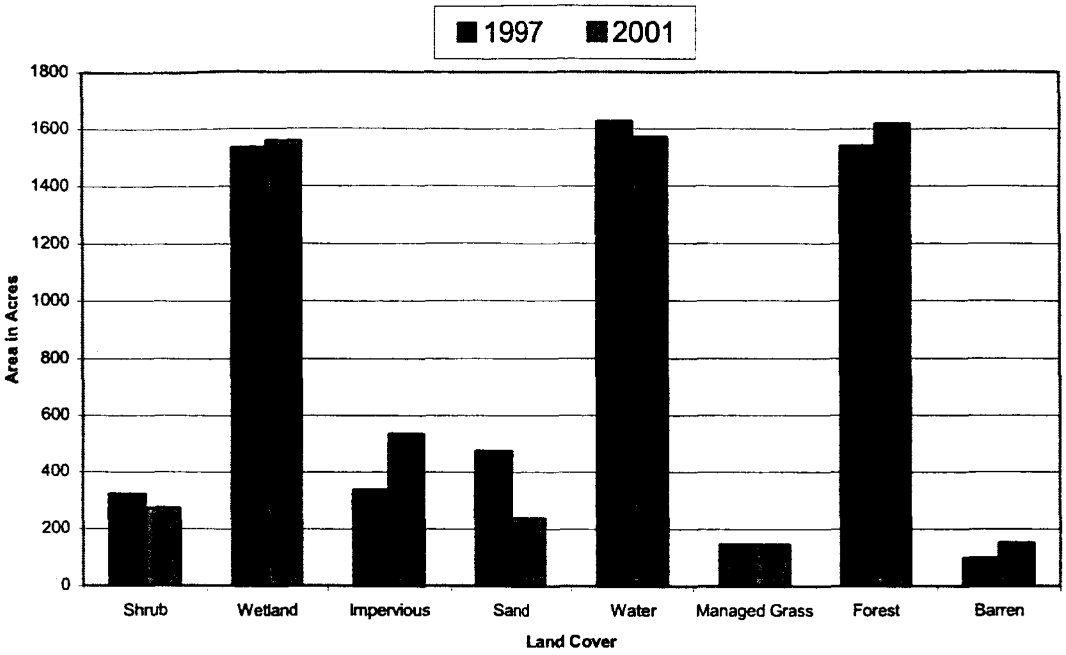

Figure 2. Results of 1997 to 2001 land cover change detection analysis.

As part of an ongoing coast-wide initiative to improve the ability to map and assess intertidal shellfish resources, the South Carolina Department of Natural Resources requested that we evaluate imagery acquired as part of this effort to determine utility for mapping the spatial distribution and characterizing the structure of mapped shellfish beds.

The selection of study sites was designed with the idea of gathering spectral signatures of shellfish in various environmental conditions. Conditions such as: abundance of shellfish, positions, (vertical and horizontal), and environmental condition, (wet/dry, various amount of mud present, algae, and detritus). Site characterization of oyster reefs utilized definitions from the Shellfish Management section of the South Carolina Department of Natural Resource's Intertidal Oyster Survey Field Data Sheet codes. These describe the reef strata with respect to bushels of live oysters per acre, presence or absence of vertical clusters, proportion of live oysters to shells and amount of mud present. Each of the 10 listed strata or classifications are identified by a letter code. Field collection using the hand-held GER spectroradiometer to gather spectral signatures of shellfish, vegetation, mud, and water took place over a 12-month period and constitute the core of the spectral library that will be used to derive spectral endmembers from remotely sensed imagery. Figure 3 showing the sample site, BOB4. Twenty-two sample points in total were established on BOB4 representing the various shellfish strata's present. Figure 3 shows five of those sample points and the next four figures illustrate the spectral signatures of mud, shellfish, mud and shellfish, and a combined chart of all spectral signatures including *Spartina alterniflora* as percent reflectances.

By comparing the percent reflectances of mud, shellfish and vegetation we see there is a difference between mud and shellfish and between shellfish, mud and vegetation percent reflectances. Although, the spectral curves of mud and shellfish are more alike than between vegetation and shellfish-mud spectral signatures.

Comparing the individual spectral signatures of the shellfish shows a percent reflectance difference within the shellfish group. BOB4-15 and 16 represent the "G" strata that are semi-wet with a thin film of mud. BOB4-1 and 2 represent a stratum that is more like the "D" strata with few vertical oysters and, some substrate showing and washed (dead) oysters on top of the shellfish reef that is dry. BOB4-1 and 2 show a greater amount of reflectance that may be due in part to being drier and the shells being in a reclined position. These initial spectral signatures show collectively is there are appreciable differences not only between mud and shellfish but there is a degree of variability within shellfish strata. More research will be done during the course of this research to ascertain the significance of wet versus dry between shellfish strata types.

Recent imagery of Murrells Inlet, SC, was acquired with the Airborne Imaging Spectrometer for Applications (AISA) sensor in September 2003. The AISA sensor has 35 bands in the visible and near-infrared portion of the spectrum (441 – 873 nm). AISA bandwidths are either 6 nm (441 – 500 nm) or 3nm (>500 nm) wide (Table 1).

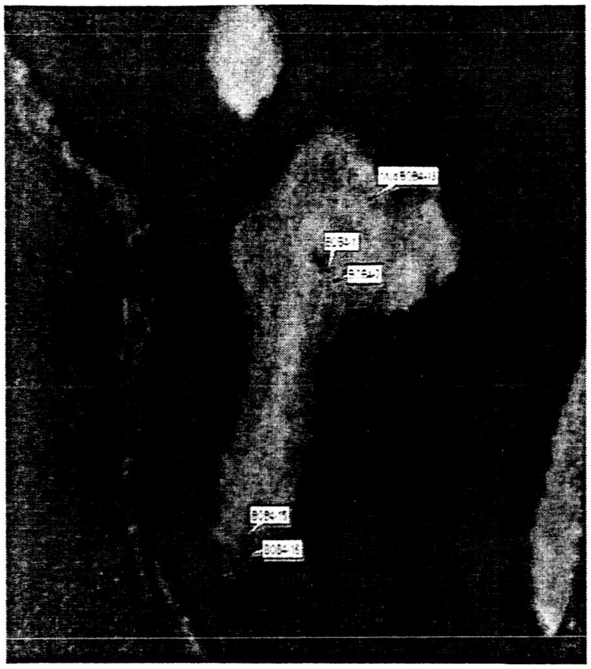

Figure 3. BOB4 monitoring site.

Imagery was acquired by the CALMIT Hyperspectral Aerial Monitoring Program in Lincoln, Nebraska. Spatial resolution of the imagery was 3 m x 3 m. Four flight lines were needed to cover the entire estuary and part of the uplands. Imagery was flown within 2 hrs of low tide on September 20, 2003. Conditions were cloud free. Figure 4 depicts 6 of the 8 flight line data files covering Murrells Inlet. The two files not shown cover upland areas to the west of the estuary.

Imagery has been processed to scaled percent reflectance and georegistered. We are awaiting radiance files and updated, more accurately georegistered imagery. IKONOS imagery was available for 1999 but was not available in 2003 for the Murrells Inlet location, under the atmospheric conditions specified.

Biophysical data was collected *in situ*, 24 hrs after the imagery collection. On September 21st, within a window of 2 hrs on either side of low tide, 6 different locations within the estuary were sampled. The locations represented areas adjacent to the varying conditions surrounding the estuary (developed, undeveloped, and to the center of the estuary) (Figure 5). At each of the 6 different locations, 5 sampling sites were chosen for biophysical sampling. The 5 sites formed an L-shape in order to capture variation within the *Spartina alterniflora* (Figure 5). A transect along the high berms of the low marsh consisted of 2 sample points (A and B). A Three additional samples (C, D, and E) were taken along a transect perpendicular to the first transect. The purpose of the second transect was to capture the variation in *Spartina* height from the low marsh along the stream berms to the higher elevations of the high marsh (Jensen et al., 1998). Sampling locations were approximately 10 meters apart. Each location was marked by a GPS point, taken with a Trimble GPS.

The *in-situ* biophysical measurements obtained included total above ground biomass and leaf area index (LAI). Total above ground biomass was harvested for 0.25 x 0.25 m quadrats and placed into labeled plastic bags.

Table 1. Comparison of the AISA Hyperspectral and ATLAS Multispectral Sensors

AISA Hyperspectral			**ATLAS Multispectral**		
Spatial Resolution	**3 x 3 m**		**Spatial Resolution**	**3.08 x 3.08 meters**	
Maximum number of channels	**35**			**9**	
Band Number	**Band Center**	**Bandwidth**	**Band Number**	**Band Center**	**Bandwidth**
1	441	6			
2	463	6			
3	474	6			
4	483	6	1	485	70
5	500	6			
6	542	3			
7	550	3			
8	561	3	2	560	80
9	585	3			
10	597	3			
11	609	3	3	615	30
12	622	3			
13	632	3			
14	639	3			
15	650	3	4	660	60
16	670	3			
17	685	3			
18	692	3			
19	700	3			
20	705	3			
21	709	3			
22	714	3			
23	719	3			
24	728	3	5	725	70
25	749	3			
26	757	3			
27	764	3			
28	774	3			
29	791	3			
30	808	3			
31	814	3			
32	819	3			
33	826	3	6	830	140
34	849	3			
35	873	3			
			7	1650	200
			8	2215	270
			9	11500	2000

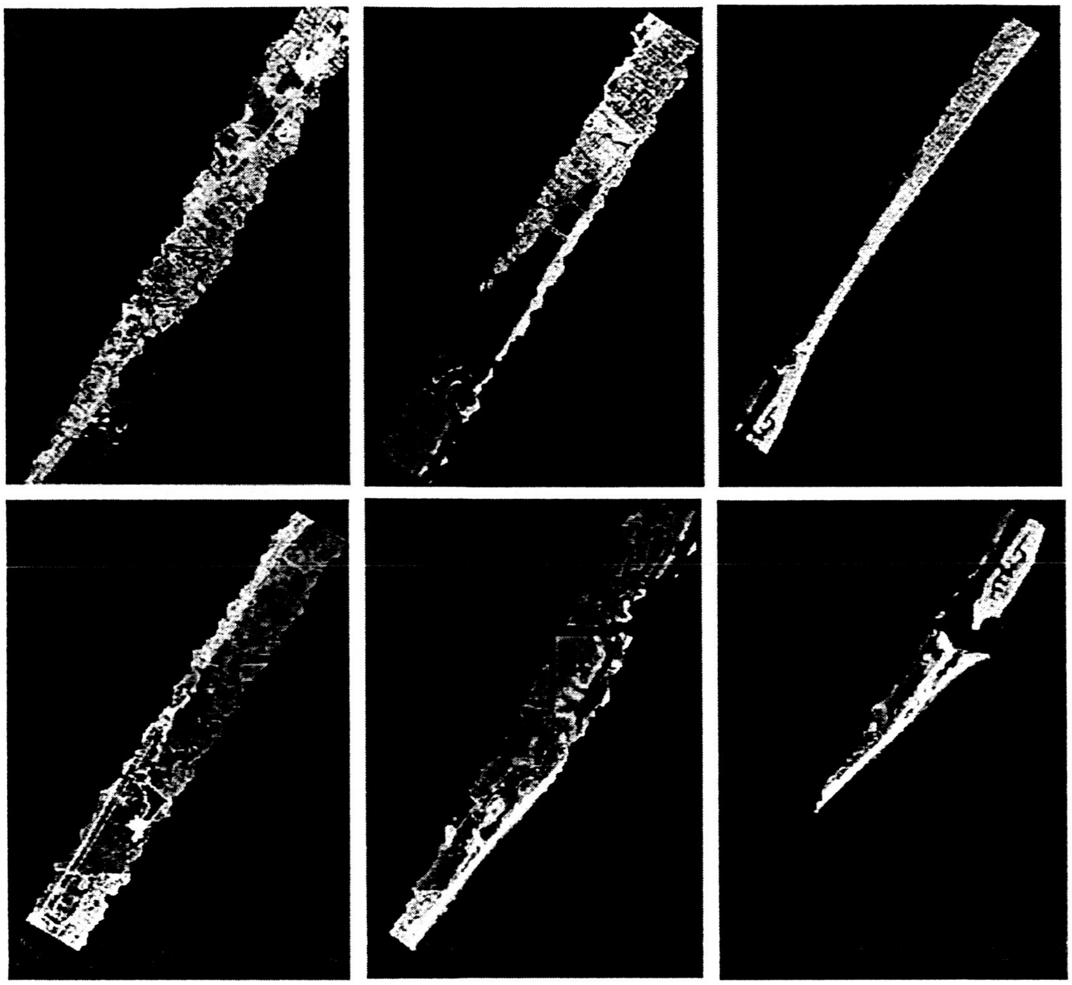

Figure 4. The Airborne Imaging Spectroradiometer for Applications (AISA) sensor was used to acquire imagery of Murrells Inlet, SC on September 20, 2003. The 6 datasets covering the estuary are presented above. The 2 remaining datasets cover additional upland areas to the west of the estuary. Each image is presented in units of scaled percent reflectance in band combination 34, 18, 2. Spatial resolution is 3 x 3m. North is oriented to the top of the page.

Figure 5. Ground referencing sampling pattern for the AISA hyperspectral data collection, September 20, 2003. The above sampling point location (site #7) representative of two transects for each of the six sampling locations: 1) a transect to capture the greater amounts of biomass along the berm, in the low marsh and 2) another transect to capture the transition in Spartina biomass from the low to high marsh, perpendicular to the berm. Inset graphic displays GPS points on an ADRG base map. AISA hyperspectral imagery displayed in band combination 32, 18, 2.

LAI was measured with a Decagon Ceptometer and included readings above and below the *Spartina alterniflora* canopy (Jensen et al., 2002). *Spartina* spectra readings were obtained using a handheld GER spectroradiometer with a spectral range of 290 to 1098 nm. Initial assessment of the LAI readings indicates capture of variation in *Spartina* LAI measurements from the high berms of the low marsh to the flat, slightly higher elevations of the low marsh (Figure 6). Harvested quadrats of *Spartina* were dried in a storage shed for approximately three months. The contents of each marked bag were transferred to another bag and weighed before being placed in a drying oven. Final dry weight was determined after 10 days.

Statistical relationships between *in situ* and AISA-derived spectra, LAI, and biomass are being established. Using these mathematical relationships, vegetation indices based on previously conducted BRDF signatures of Spartina alterniflora will be used to generate a biomass map of the peak 2003 Spartina in Murrells Inlet (Jensen et al., 2002; Meisburger, 2000; Shew and Linthurst, 1981; Thenkabail et al., 2000).

The AISA spectra also will be convolved to mimic the ATLAS multispectral bandwidths. Using the previously derived vegetation indices applied to the ATLAS 1997 data, the convolved AISA 2003 data will be used to generate a biomass map. These two biomass maps will be compared. Of particular interest will be whether or not change in the *Spartina* may be correlated to changes or stress in the upland land cover (Porter et al., 1996; Vernberg et al., 1992).

Further research questions will be addressed using this dataset. The AISA 2003 imagery and the convolved AISA imagery will be compared to quantify any improvement in the capture of *Spartina alterniflora* biophysical parameters from hyperspectral versus multispectral imagery.

References

Jensen, J. R., C. Coombs, D. E. Porter, B. Jones, S. R. Schill and D. White (1998). "Extraction of smooth cordgrass (*Spartina alterniflora*) biomass and leaf area index parameters from high resolution imagery." Geocarto International 13(4): 25-34.

Jensen, J. R., G. Olsen, S. R. Schill, D. E. Porter, J. Morris (2002). "Remote Sensing of Biomass, Leaf-Area-Index, and Chlorophyll a and b content in the ACE Basin national Estuarine Research Reserve Using Sub-meter Digital Camera Imagery." Geocarto International 17(3): 1-10.

Meisburger, J. (2000). *Quantification of Biomass and Leaf-Area-Index in a Charleston, SC Estuary Using Low-altitude AVIRIS Imagery.* Doctoral dissertation, Geography, University of South Carolina, Columbia, 110 pp.

Porter, D. E., W. K. Michener, T. Siewicki, D. Edwards and C. Corbett (1996). Geographic Information Processing Assessment of the Impacts of Urbanization on Localized Coastal Estuaries: A Multidisciplinary Approach. Sustainable Development in the Southeastern Coastal Zone. F. J. Vernberg, W. B. Vernberg and T. Siewicki. Columbia, SC, University of South Carolina Press. 20: 519.

Shew, D. M. and R. A. Linthurst (1981). "Comparison of Production Computation Methods in a Southeastern North Carolina *Spartina alterniflora* Salt Marsh." Estuaries 4(2): 97-109.

Thenkabail, P. S., R. B. Smith and E. De Pauw (2000). "Hyperspectral vegetation indices and their relationships with agricultural crop characteristics." Remote Sensing of Environment 71: 158-182.

Vernberg, F. J., W. B. Vernberg, E. Blood, A. Fortner, M. Fulton, H. McKellar, W. Michener, G. Scott, T. Siewicki and K. El Figi (1992). "Impact of urbanization on high-salinity estuaries in the southeastern United States." Netherlands Journal of Sea Research 30: 239-248.

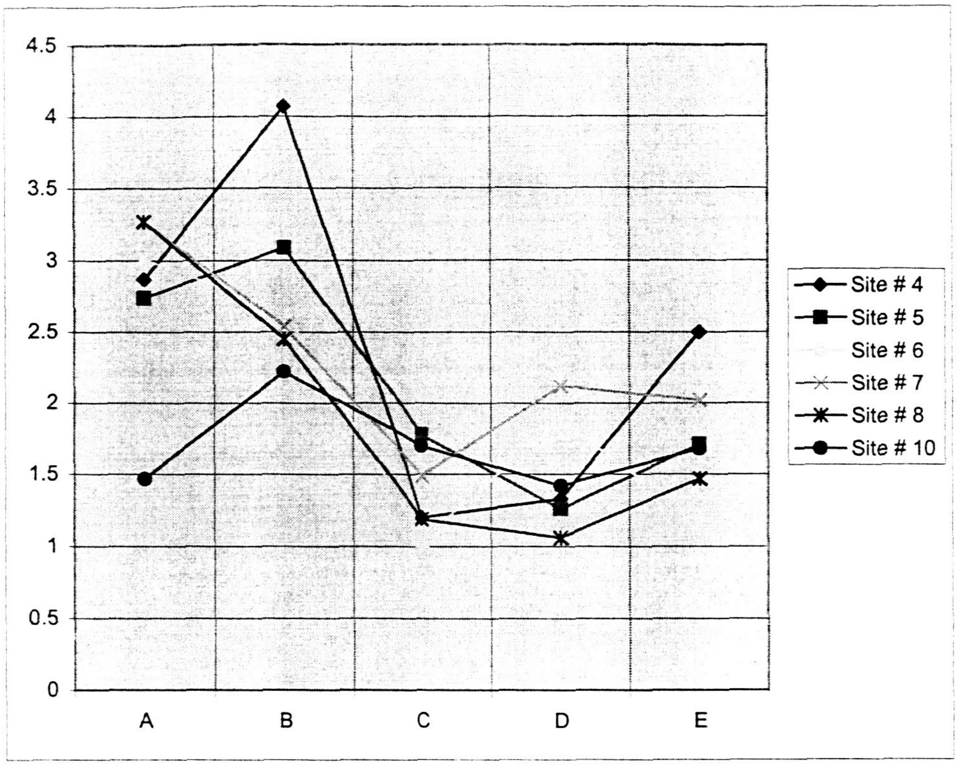

Figure 6. When compared by quadrat, the trends in LAI are similar. The observed increase in LAI reading for quadrat sites "E" may indicate that the sampling scheme placed quadrats far enough into the marsh that they perhaps represent the topographic trend back to "low" marsh near another creek. There was no sample site #s 1-3, 9.

Section II-1: Publications Related to & Resulting from this NASA EPSCoR Grant

Book

Jensen J.R. (2000) Remote Sensing of the Earth's Environment: An Earth Resource Perspective. Prentiss Hall, Saddle River, NJ, 576 pp.

Published Papers

Allen, J. and K. Lu (2003) Modeling and Prediction of Future Urban Growth in the Charleston Region of South Carolina: A GIS-based integrated approach. *Conservation Ecology* 8(2): 2.

Allen, J., Kang S. Lu, and Thomas D. Potts. (2002) A GIS-based analysis and prediction of land-use change in a coastal tourism destination area. In Miller, Marc I., Auyong, Jan, and Hadley, Nina P. (eds.). *Proceedings of the 1999 International Symposium on Coastal and Marine Tourism: Balancing Tourism and Conservation.* (26-29 April 1999, Vancouver, BC, Canada). Washington Sea Grant Program and School of Marine Affairs, University of Washington, Seattle, WA, Oregon Sea Grant College Program, Oregon State University, Corvallis, OR, and Oceans Blue Foundation, Vancouver, BC.

Alsup D.L., C.R. Coombs (1998) A Study of Plant Distribution Changes in Abandoned Rice Fields within Freshwater Estuaries, Georgetown-Horry Counties, South Carolina. *Proceeding First International Conference on Geospatial Information in Agriculture and Forestry.* pp. II-653-II-659.

Burdett L., C. Runyon, W. McFee (2003) Mapping of Marine Mammal Entanglement Wounds: Sources of Mortality in Commercial Fisheries Predicted with GIS. ArcNews, Fall 2003. http://www.esri.com/news/arcnews/fall03articles/sources-of-mortality.html

Born, K., D.E. Porter, M. Neet and S. Walker. In press. An Internet mapping system for coastal resource management and data dissemination in support of a Special Area Management Plan. *California and the World Ocean '02 Proceedings.*

Gardner, R. and D.E. Porter. (2001) Stratigraphy and geologic history of a southeastern salt marsh basin, North Inlet, South Carolina, USA. *Wetlands Ecology and Management.*

Hulin A., C.R. Coombs, D.E. Porter (1999) A Policy Analysis of the Safe Harbor Act to Protect the Endangered Red-Cockaided Woodpecker Using GIS and Remote Sensing. Jour. Forested Wetlands.

Jensen J.R., C.R. Coombs, D.E. Porter, B. Jones, S. Schill (1999) Smooth Cordgrass (*Spartina - alterniflora*) Biomass and Leaf Area Index Parameters from High Resolution Imagery. *Geocarto, v. 13*, no. 4, pp. 25-34.

Kleppel, G.S., D.E. Porter, M.R. DeVoe and R.H. Becker. Preserving biodiversity in rapidly urbanizing estuarine ecosystems. *Science.*

Nichols, C.C., T.C. Siewicki, and J.W. Daugomah, D.E. Porter, B. Jones and J.R. Jensen. 2000. Coastal land-cover classification using NASA's Airborne Terrestrial Applications Sensor (ATLAS) data. *Proceedings* of Sixth International Conference on Remote Sensing for Marine and Coastal Environments. pp. 279-286.

Savitsky B.G., J.S. Allen, K.F. Backman (1999) The role of Geographic Information Systems in Tourism Planning and Rural Economic Development. *Tourism Analysis.* Sagamore Publishing Co., Champaign-Urbana, IL

Schill S.R., J.R. Jensen, D.E. Porter, B.C. Jones, and C. Coombs (2000) A discriminant analysis on the biophysical characteristics of *Spartina alterniflora* and multispectral reflectance in remotely sensed data. *Proc. 6th International Conference on Remote Sensing for Marine and Coastal Environments.* May 1-3, Charleston, SC. pp. 89-102.

Schill, S.R., J.R. Jensen, G.T Raber, D.E. Porter, 2004, Temporal Modeling of Bidirectional Reflection Distribution Function (BRDF) in Coastal Vegetation, *GIScience and Remote Sensing.* 41(1):61-80.

White, D.L., D. Bushek, D.E. Porter and D. Edwards. (1999) Geographic Information Systems (GIS) and Kriging: Analysis of the Spatial and Temporal Distributions of *Perkinsus marinus* in a Developed and an Undeveloped Estuary. *Journal of Shellfish Research.* V. 17, no. 5, pp. 1473-1476.

White, D., D.E. Porter and A.J. Lewitus. 2004. Spatial and temporal analyses of water quality and phytoplankton biomass in an urbanized versus pristine salt marsh estuary. *Journal of Experimental Biology and Ecology.* 298:255-273.

Vincent, J.S., D.E. Porter, L.D. Coen, D. Bushek and S. Schill. 2003. Using hyperspectral remote sensing to map and assess intertidal shellfish resources in the southeastern US. *Journal of Shellfish Research.* Vol. 2(1):359. Reviewed abstract

Presentations

Conference Presentations (abstracts submitted for each)

Allen, J. (2000) Land-Use Change and Urban Growth Modeling for Coastal South Carolina." *South Carolina State Mapping Advisory Committee Biennial Conference.* Columbia, South Carolina. January 26-27, 2000.

Allen, J. and Lu, K. S. (1999) A GIS-Based Analysis and Prediction of Land-Use Change in a Coastal Tourism Destination Area. *1999 World Congress on Coastal and Marine Tourism.* Vancouver, British Columbia, Canada. April 26-29, 1999.

Allen, J.S. and S.L. Kang (1998) "Population and tourism growth and its relation to ecosystem health" Conference on Southeast Coastal Ocean Research. Savannah, GA., April 1998.

Alsup D.L., C.R. Coombs, M. Weiner (1998) The monitoring of wetland ecosystem health in impounded estuary communities using remote sensing. College of Charleston, April 1997.

Born, K., D.E. Porter, M. Neet and S. Walker (2003) An Internet mapping system for coastal resource management and information dissemination in support of a Special Area Management Plan. Coastal GeoTools '03. Charleston, SC. January 2003.

Burdett,L., W. McFee, C. Runyon (2004) Working Backwards: Using the rope impressions of entangled marine mammals to create GIS maps that identify potential sources of entanglement Southeast and Mid-Atlantic Marine Mammal Symposium held March 26-28 at Harbor Branch Oceanographic Institution, N.C.

Bushek D., D. White, D.E. Porter, B. Jones, J. Keesee and D. Edwards (1998) Relationships between land-use patterns and dermo disease in oysters from two South Carolina estuaries. 3rd International Symposium on Aquatic Animal Health. Baltimore, MD. August, 1998.

Bushek, D., D. White, D. Porter and D. Edwards (1998) "Land-use patterns, hydrodynamics and the spatial pattern of Dermo disease in two South Carolina estuaries". Aquaculture '98, Las Vegas, NV, February 1998.

Chose J.R. (1998) Tidal Creek Bank Erosion in Murrells Inlet, SC. Southeastern ARC/INFO Users Group Meeting, Charleston, SC, October, 1998.

Chose J.R. and C.R. Coombs (1998) Parameters influencing creek bank erosion in two *South Carolina tidal salt marshes. S.C. Acad. Sciences*, Clemson, SC. March 1998.

Chose J.R. and C.R. Coombs (1998) Creek bank erosion of the tidal salt marshes of Murrells Inlet and North Inlet, South Carolina. *Conference on Southeast Coastal Ocean Research.* Savannah, GA., April 1998.

Coombs C.R., J.R. Chose, D.L. Alsup, and J. Daugomah (1997) The monitoring of ecosystem health in South Carolina estuaries using remote sensing: *A NASA EPSCoR Project.* College of Charleston, April 1997.

Daugomah J. (1998) Natural and Anthropogenic Factors Affecting Spatial Palaeomonetes pugio Population Abundance in Murrells and North Inlets, SC. *Southeastern ARC/INFO Users Group Meeting*, Charleston, SC, October, 1998.

Goddard M. (2000) Integrating Landsat Thematic Mapper Data and BASINS Integrated Modeling for Water Quality Mapping and Prediction. *ASPRS Regional Meeting* Student Presentation, Clemson University.

Hay G. (2001) Modeling the Habitat Characteristics of Tidal Creeks Used by Recreationally Important Juvenile Finfish with a Geographic Information System. *Coastal GeoTools 2001.* Charleston, SC. January 2001.

Hulin A. (1998) Endangered Red-Cockaided Woodpecker's Foraging and Nesting Habitat. *Southeastern ARC/INFO Users Group Meeting*, Charleston, SC, October, 1998.

Kleppel G., D.E. Porter, J. Allen and M.R. DeVoe (1999) Implications of changing demographic and land use patterns to coastal ecosystem integrity in the southeastern United States. *9th Annual Meeting of SETAC-Europe*. Leipzig, Germany. May, 1999.

Meisburger, J.L., J.R. Jensen, S. Schill and D.E. Porter. (2000) Quantification of biomass and leaf are index in a Charleston, SC estuary using low-altitude AVIRIS data. *American Society for Photogrammetry and Remote Sensing Annual Convention.* Washington, DC. May 2000.

Nichols C.C., T.C. Siewicki, and J.W. Daugomah, D.E. Porter, B. Jones and J.R. Jensen. (2000) Coastal land-cover classification using NASA's Airborne Terrestrial Applications Sensor (ATLAS) data. *Sixth International Conference on Remote Sensing for Marine and Coastal Environments.* Charleston, SC. May 2000.

Olson, G., J. Jensen, S. Schill and D.E. Porter. (2001) Remote sensing of wetland biophysical variables in the ACE Basin National Estuarine Research Reserve. *Coastal GeoTools 2001.* Charleston, SC. January 2001.

Porter, D.E. (2000) Using innovative remote sensing and image processing techniques for assessing coastal ecosystem health. *NASA/EPSCoR Earth Science Enterprise Workshop. Clemson, SC.* August 2000. Invited presentation.

Porter D.E., G.T. Chandler, B.E. Jones and M.W. Williamson (1998) The use of spatial modeling to map estuarine areas susceptible to photo-induced toxicity. *Southeastern ARC/INFO Users Group Meeting*, Charleston, SC, October, 1998.

Porter, D.E. (1999) An overview of the role of geographic information processing techniques in support of coastal environmental decision making. Invited presentation. *Southeast Partnership for Environmental Technology Education Fourth Annual Resource Conference*. Charleston, SC. April 1999. Invited presentation.

Porter D.E., D. Bushek, D.L. White and J. Keesee (1998) Host-Parasite Relationships and Disease Status as a Measure of Ecosystem Health. *Conference on Southeast Coastal Ocean Research*. Savannah, GA., April 1998.

Porter, D.E., J. Allen, T. Siewicki, M. Gielazyn, D. Edwards and W.K. Michener (1998) Defining the Role of Database Management in Support of Long-term, Multidisciplinary Environmental Research Efforts. *Conference on Southeast Coastal Ocean Research*. Savannah, GA., April 1998.

Runyon, C.J., L. Burdett, W. McFee (2003) Using GIS as a Forensic Tool to Predict Sources of Marine Mammal Entanglement in Commercial Fisheries. *The 15th Biennial Conference on the Biology of Marine Mammals*, Joseph S. Koury Convention Center, Greensboro, NC. December 14-19, 2003.

Schill, S., J. Jensen and D.E. Porter. 2001. Measurement and modeling of the spectral and directional reflection properties of smooth cordgrass (*Spartina alterniflora*). *Coastal GeoTools 2001*. Charleston, SC. January 2001.

Schill, S., J. Jensen and D.E. Porter. 2001, Temporal modeling of BRDF patterns and phenological change in coastal vegetation. *2001 American Society of Photogrammetry and Remote Sensing Annual Convention and Exposition*. St. Louis, MO. April 2001.

Schill, S.R., D.E. Porter and J.R. Jensen. 2000. Acquiring and modeling BRDF in coastal environments. *Mid-South Region of the American Society of Photogrammetry and Remote Sensing Annual Meeting*. Clemson, SC. October 2000.

Schill S.R., J.R. Jensen, D.E. Porter, B.C. Jones, and C. Coombs. 2000. A discriminate analysis on the biophysical characteristics of *Spartina alterniflora* and multispectral reflectance in remotely sensed data. *Sixth International Conference on Remote Sensing for Marine and Coastal Environments*. Charleston, SC. May 2000.

Schill, S.R., D.E. Porter, and J.R. Jensen. 2000. Evaluating bi-directional reflectance distribution function (BRDF) of smooth cordgrass (*Spartina alterniflora*). *National Estuarine Research Reserve Association Annual Meeting*. Williamsburg, VA. October 2000.

Vaughan, D.F. and J. R. Jensen. Extraction of Spartina alterniflora biophysical parameters using narrow-band vegetation indices and high spatial resolution hyperspectral imagery. Association of American Geographers 2004 Annual Conference, March 14-19, 2004, Philadelphia, Pennsylvania.

Vaughan, D.F., J.R. Jensen, D.E. Porter, S. Walker, B. Hadley, and J. Tullis. Hyperspectral Change Detection of Spartina alterniflora in Murells Inlet, South Carolina. American Society of

Photogrammetry and Remote Sensing 2004 Annual Conforence, May 23-28, 2004, Denver, Colorado.

Vernberg, F.J., W.B. Vernberg, D.E. Porter, G.T. Chandler, H.N. McKellar, D. Tufford, T. Siewicki, M. Fulton, G. Scott, D. Bushek and M. Wahl. Impact of coastal development on land-coastal waters. 1999. Medcoast 99. Antalya, Turkey. November 1999.

Vincent, J.S., D.E. Porter, L. Coen, D. Bushek and S. Schill. 2003. Assessing and mapping shellfish resources using hyperspectral remote sensing. Coastal GeoTools '03. Charleston, SC. January 2003.

White, D.L., D.E. Porter and A.J. Lewitus. (2001) Spatial heterogeneity of nutrients and primary production in an urbanized estuarine system. *Coastal GeoTools 2001*. Charleston, SC. January 2001.

White, D., D.E. Porter, and A.J. Lewitus. (2000) Spatial and temporal analyses of water quality patterns in two well-mixed, high-salinity estuaries. *National Estuarine Research Reserve Association Annual Meeting.* Williamsburg, VA. October 2000.

White, D.L., D.E. Porter, A.J. Lewitus, M. Neet, D. Tufford and J.R. Jensen. (2000) Integrating in situ sampling and remote sensing techniques to assess and model spatial heterogeneity of nutrients and primary production in an urbanized estuarine system. *Mid-South Region of the American Society of Photogrammetry and Remote Sensing Annual Meeting*. Clemson, SC. October 2000.

White, D., D.E. Porter, J. Jensen, S. Schill and B. Jones. 1999. An evaluation of non-destructive techniques for estimating aboveground biomass of the cordgrass *Spartina alterniflora. 15th International Biennial ERF Conference*. New Orleans, LA. September 1999.

White D., D.E. Porter and D. Bushek (1997) A Comparison of Spatial and Temporal Patterns of *Perkinsus marinus* in Oyster Populations in a Developed Estuary and an Undeveloped Estuary in South Carolina. *Spatial Data and Remote Sensing in Invertebrate Fisheries Habitat, Research and Management Workshop.* Fort Walton Beach, FL. 19-20 April 1997.

Invited Presentations

Allen J.S. (2001) Growth Modeling and Growth Management in South Carolina. *Interview with News Channel* 7, Spartanburg, SC. January 2001.

Allen J.S. (2000) Using a Growth Prediction Model for Monitoring Coastal Ecosystem Health. *NASA/SC EPSCoR project workshop*. Clemson, South Carolina. August 21, 2000.

Allen J.S. (2000) Growth Management – What it Means to the Palmetto State. *South Carolina Association of Conservation Districts/USDA-NRCS/SCDNR Joint Conference.* Charleston, South Carolina. January 21, 2000.

Allen J.S. (1999) Growth Prediction Modeling: Lessons for Upstate South Carolina. *Reedy River Growth Management Conference*. Greenville, South Carolina. December 1, 1999.

Allen J.S. (1999) Forces Behind Land Use Planning: A GIS-Based Growth Prediction Model." *31st Annual Meeting of the South Carolina Forestry Association.* Myrtle Beach, South Carolina. November 3-5, 1999.

Allen J.S. (1999) Forces behind land use planning: A GIS-based growth Prediction model. *Annual S.C. Forestry Association*, Myrtle Beach, S.C., November, 1999.

Allen J.S. (1999) GIS and Predicting Growth. *Annual Conference of the South Carolina Association of Special Purpose Districts*, Myrtle Beach, S.C., October, 1999.

Allen J. and S.L. Kang (1999) GIS-based Analysis and Prediction of Land-Use Change in Coastal Tourism Destination Areas. *Proceedings of World Congress on Coastal and Marine Tourism.* April 29, 1999. Vancouver, British Columbia, Canada.

Coombs [Runyon] C.R. (1999) Monitoring Wetlands and Ecosystem health in coastal South Carolina using GIS and remote sensing, Denver, CO. *Annual GSA meeting*, October 1999.

Coombs [Runyon] C.R. (1999) Modeling Coastal Ecosystem Health Using Advanced Techniques of Remote Sensing and GIS. *Southeastern ARC/INFO Users Group Meeting*, Charleston, SC, October, 1998.

Coombs C.R., J.R. Jensen, D.E. Porter (1998) Use of remote sensing and GIS as monitoring tools for wetlands and ecosystem health. *Texas Tech University*, Lubbock, TX, February 20, 1998.

Coombs C.R. (1997) A new way to explore wetlands in the classroom. *KidSat (EarthCam) Training Workshop*, College of Charleston, July, 1997.

Jensen, J.R., D.E. Porter and C.R. Coombs (1998) Biophysical Remote Sensing of Coastal Wetlands. *AAAS Annual Meeting and Science Innovation Exposition*. Philadelphia, PA. February 1998.

Porter D.E. (1999) An overview of the role of geographic information processing techniques in support of coastal environment decision making. *Southeast Partnership for Environmental Technology Education Fourth Annual Resource Conference*. Charleston, SC, April 1999.

Porter, D.E. (1998) Murrells Inlet Under the Microscope: Preliminary Findings and Recommendations for Coastal Zone Management. *Murrells Inlet 2007 Task Force and community of Murrells Inlet.* January 1998.

Award-winning presentations

Allen J., Lu K.S. (2000) ***Most innovative use of technology in S.C.*** Awarded by SC Chapter of the American Planning Association for Charleston Area Urban Growth Model.

Dr. J. R. Jensen, 2004, **John E. Estes Award**, ASPRS, Sponsored by SAIC. American Society of Photogrammetry and Remote Sensing, Denver, Colorado

Porter D.E., G.T. Chandler, B.E. Jones and M.W. Williamson (1998) The use of spatial modeling to map estuarine areas susceptible to photo-induced toxicity. Southeastern ARC/INFO Users Group Meeting, Charleston, SC, October, 1998.

Schill S. (2000) BRDF Modeling in estuarine systems. Remote Sensing Division, ASPRS 2000, Washington D.C. *1st Place.*

White D. Geographic Information Systems (GIS) and Kriging: Analysis of the Spatial and Temporal Distributions of the Oyster Pathogen Perkinsus marinus in a Developed and an Undeveloped Estuary. Southeastern ARC/INFO Users Group Meeting, Charleston, SC, October, 1998.

Section IIIa: Spin-Off Projects (Funded)

Funding Period ***Amount ($)***	Granting Agency	PI (s)	Project Title
2004-2009 ***$500,000***	SC DNR	J. Allen et al.	Reedy River Watershed Education Program
2003-2005 ***$270,000***	VKR Foundation	J. Allen et al.	The Saluda-Reedy Watershed Consortium: Taking Action for Water Quality Improvement and Watershed Management
2003-2007 ***$2.4 million***	NASA/REASoN	J. R. Jensen M.E. Hodgson S. Cutter D. J. Cowen	Development of Remote Sensing-assisted Natural and Technological Hazards Decision Support Systems
2004-2005 ***$158,140***	NOAA CICEET	D. E. Porter J.R. Jensen V. Klemas	NERRS Remote Sensing Applications Assessment Project (RESSAP)".
2002-2004 ***$245,491***	NOAA CICEET	S. Schill D. E. Porter L. Coen	Development of an Automated Mapping Technique for Monitoring and Managing Shellfish Distributions
2000-2001 ***$113,130***	NOAA	Porter et al.	Urbanization and Southeastern Estuarine Systems
2000-2004 ***$617,359***	NOAA Coastal Ocean Program	Porter	Development of a GIS-based Database Management Program to Characterize Sources and Effects of Natural Parameters and Anthropogenic Impacts to Coastal Ecosystems
2000-2001 ***$19,500***	NSF	Porter et al.	Multidimensional Consequences of Urban Encroachment on Natural Ecosystems
2000 ***$10,000***	NASA/EPSCoR	Porter	Graduate Student Training Grant
1999-2002 ***$48,572***	EPA	Porter et al.	CISNet: Molecular to Landscape-scale Monitoring of Estuarine Eutrophication
1998 – 1999 ***$125,000***	NOAA Coastal Ocean Program	Porter et al.	Geographic Information Processing and Spatial Modeling on Urbanization in Southeastern Estuarine Systems
1997 – 1998 ***$33,744***	SC Sea Grant	Porter, Allen	A Spatial Data Assessment for LU-CES

Section IIIb: Spin-Off Projects (Proposed / Pending)

Funding Period/ Amount	Granting Agency	PI (s)	Project Title
2004 ***$2,975,576***	NSF	J. Allen et al.	Biocomplexity as an Integrative Concept for Interdisciplinary Graduate Education and Research
2004 ***$410,922***	NSF	J. Allen et al.	Impacts of Urbanization on social, economic and environmental values – Does typology matter?
2004 ***$2,000,000***	NSF	J. Allen et al.	Multiple Information Streams for Better Informed Policy Makers

Section IV: Participants

University of South Carolina *(J. Jensen, D. Porter)*

Student	Degree	Discipline	Thesis/Dissertation Title
George T. Raber	Ph.D., 2003	Geography	The Impact of Varied Nominal Posting Density Lidar Data on DEM Accuracy, hydraulic modeling and Flood Zone Delineation
Jason A. Tullis	*Ph.D., 2003*	Geography	Data Mining to Identify Optimal Spatial Aggregation Scales and Input Features: Digital Image Classification with Topographic Lidar and Lidar Intensity Returns
Steve R. Schill	*Ph.D., 2001*	Geography	Modeling hyperspectral Bidirectional Reflection Distribution Function (BDRF) data of smooth cordgrass (Spartina alterniflora) using a sandmeter field goniometer
Jeff Vincent	*Ph.D. Candidate*	Geography	Mapping Shellfish Distribution Using Hyperspectral Remote Sensing
David F. Vaughan	*Ph.D. Candidate*	Geography	Examination of Hyperspectral Data for Classification and Biophysical Parameter Measurement of Smooth Cordgrass (*Spartina altemiflora*)
Brian Gray	*Ph.D. Candidate*	Biostatistics & Epidemiology	Modeling spatially and temporally correlated oyster infection data
Mark Jackson	*Ph.D. Candidate*	Geography	On leave of absence
Jennifer Meisberger	*Ph.D.*	Geography	Quantification of Biomass and Leaf Area Index (LAI) Using AVIRIS Imagery
David L. White	*Ph.D. Candidate*	Marine Science	Land Cover and Water Quality: A Spatial Investigation of Phytoplankton community structure in two well mixed marsh ecosystems
Xinghe Yang	*Ph.D.*	Geography	Georeferencing CAMS Data: Polynomial Rectification and Beyond
Yingming Zhou	*Ph.D.*	Geography	Modeling Uncertainty of Areai Interpolation
Katherine Born	*M.S.*	Marine Science	Using GIS, Remote Sensing and Internet Mapping Systems for Mapping, Assessing and Monitoring Localized Coastal Estuaries
Gunner Olson	*M.S.*	Geography	Remote Sensing of Estuarine Salt Marsh: Assessment of Biophysical Variables Utilizing High Resolution Data
Judith Burgland	*M.S.*	Geography	Evaluating the Use of Radarsat SAR and JERS-1-SAR for Estimating LAI and Delineating Upland Land Cover and Tidal Freshwater Wetland Vegetation Species in the Tivoli North Bay Area, New York
Laura Schmidt	*M.S.*	Geography	Evaluation of the Utility and Accuracy of LIDAR and IFSAR Derived DEMs for Flood Plain Mapping
Jason Tullis	*M.S.*	Geography	Artificial Intelligence for Automated Housing Enumeration from Pan-Sharpened IKONOS Imagery
George Raber	*M.S.*	Geography	Vegetation Characterization and Improvement of Digital Surface model (DSM) Creation Using Multiple Return LIDAR

Student	Degree	Discipline	Thesis/Dissertation Title
Matthew Neet	*M.S.P.H.*	Environmental Health Sciences	Environmental Health Sciences Prototype Development of a GIS-based Web Presentation for Spatial Analysis and Promoting Increased Awareness of Fish Consumption Advisories for Lake Hartwell, SC
Margaret (Williamson) Vo	*M.S.P.H.*	Environmental Health Sciences	Integrating meiobenthic copepod bioassays and spatial modeling techniques to examine photo-enhanced toxicological hazard of Murrells Inlet sediments contaminated with polycyclic aromatic hydrocarbons
Heath Kelsey	*M.S.P.H.*	Environmental Health Sciences	Examination of Land Use and Fecal Coliform Bacterial Pollution From Human and Animal Sources in Murrells Inlet, South Carolina
Cameron Kerr	*M.S.P.H.*	Environmental Health Sciences	Using LIDAR in the development of watersheds and sub-watersheds for assessment and modeling of source loadings in natural resource management practices
Giannina Dimaio	*M.S.P.H.*	Environmental Health Sciences	A Review and Analysis of SC DHEC's OCRM Regulations for Permitting in Critical and Non-critical areas
Katherine Born	*M.S.P.H.*	Environmental Health Sciences	Development of a GIS-based resource management tool to assess anthropogenic activities and physiographic influences on the health and structure of the Murrells Inlet, South Carolina estuary
Cameron Kerr	*B.S.*	Marine Science	N/A
Giannina DiMaeo	*B.S.*	Marine Science	N/A
Gretchen Hay	*B.S.*	Marine Science	N/A

Clemson University *(J. Allen)*

Student	Degree	Discipline	Thesis/Dissertation/Internship Title
Kang Shou Lu	*Ph.D. Candidate*	Parks, Recreation & Tourism Mgmt.	Macro-level Land-Use Change Analysis and Prediction for Coastal Tourism Destination Areas
Jeffrey Allen	*Ph.D. Candidate*	Policy Studies	Urban Growth Modeling and its Policy Implications
Megan Goddard	M.S.	Environmental Toxicology	Land Use Changes and its affects on water quality in a coastal watershed
Heather Crean	M.S.	Planning Studies	Coastal South Carolina's Population and Development Trends

College of Charleston (*C. Runyon [Coombs]*)

Student	Degree	Discipline	Thesis/Dissertation/Internship Title
Marian Mitchell	*MES (2003)*	Policy / Geology	Using Geographic Information Systems Software to Analyze the Capacity of Wood Stork Nesting Colonies in Relation to Wetland Availability
Joy Parikh	*MES (2003)*	Geology	Integrating AutoCAD Facility Data into an Environmental GIS Database for Impact Assessment Using Marshall Space Flight Center as a Model
Robin Adams	*MES (2002)*	Policy / Geology	Modeling and Restoration of Water Quality in Two Tidal Ponds on Kiawah Island, South Carolina
Connie Moy	*(MES)*	Marine Biology	Development and Validation of an Estuarine Biotic Integrity Index for South Carolina Tidal Creeks
Gretchen Hay	*MES (2001)*	Geology	Modeling the Habitat Characteristics of Tidal Creeks Used by Recreationally Important Juvenile Finfish with a Geographic Information System
Scott Rutzmoser	*MES (2001)*	Geology	Assessing the percent cover of Phragmites austalis in the Ace Basin NERR, SC
Andrew Hulin	*MES (2000)*	Policy/Geology	Evaluating the Use of GIS and Remote Sensing for Use in Establishing Land-Use for Endangered Species Habitat
James Daugomah	*MES (2000)*	Geology	Natural and Anthropogenic Factors Affecting Spatial *Palaeomonetes pugio* Population Abundance in Murrells and North Inlet, SC
Dianna Alsup	*MES (1999)*	Geology	Succession in Abandoned Rice Fields: A Study of Changes to Plant Distribution in a Marsh Environment
Jaime Chose	*MES (1999)*	Geology	Parameters Influencing Bank Erosion in Two South Carolina Tidal Salt Marshes
Scott Bruemmer	*B.S.*	Geology	N/A
Prentiss Lund	*B.S.*	Geology	N/A
Siobhan O'Reilly-Green	*B.S. Candidate*	Geology	N/A
Amer Smailbegovic	*B.S.(1998)*	Geology	N/A
Megan Weiner	*B.S.(1998)*	Geol/Biology	N/A

Section V: Collaborations

NASA Centers

NASA Goddard Space Flight Center
NASA Stennis Space Flight Center
NASA Johnson Space Flight Center
NASA Langley Space & Research Center
NASA Marshall Space Flight Center

Business and Industry

Calmit Hyperspectral Aerial Monitoring Program
The Nature Conservancy
SMARTech, Charleston, SC – satellite ground station, Small Business
Geometrics, Myrtle Beach and Columbia, SC – geotechnical/civil engineering, Small Business

Other Federal

National Oceanic and Atmospheric Administration
Corps of Engineers

State Agencies

South Carolina Department of Natural Resources
South Carolina Department of Health and Environmental Control
South Carolina Department of Commerce

Non-government Organizations

Murrells Inlet 2007 Task Force
Charleston City Council

Section VI: Additional Uses of Data derived from this project

Classes using data

University of South Carolina (Jensen/Porter)
  Remote Sensing 751
  Remote Sensing 551
  Resource Management and Decision Making ENHS 775

College of Charleston (Runyon)
  Geomorphology GEOL225
  Introduction to Remote Sensing GEOL314
  Advanced Remote Sensing GEOL442
  Geographic Information Systems GEOL449

University of Charleston (Runyon)
  Applications in Remote Sensing EVSS642
  Geologic Applications in GIS EVSS 649

Appendix 1:

Land Use Modeling and Prediction Using an Artificial Neural Network

Jeffery S. Allen and Kang S. Lu
Strom Thurmond Institute, Clemson University, Perimeter Road, Clemson, SC 29634;
email: jeff@strom.clemson.edu klu@strom.clemson.edu

1 Introduction

One of the challenges of urban growth simulation is to identify and determine the rules to be used in a model that fit the unique geographic environment (Batty, 1998; Wu, 2002). Regardless of the approach and the form that a model may take, these rules are either conceptually preset by urban experts or empirically derived from case studies. Experts such as Von Thunen (1826) in the field of urban economics strived to use deterministic rules and a select few variables in modeling urban space. Their models succeeded to varying degrees in explaining some spatial phenomena but failed in practical applications because they all oversimplified the urban reality (Lee, 1973; Sui, 1997). The complexity of urban systems also makes it difficult, if not impossible, to derive universal rules for building a knowledge-based expert system that is applicable everywhere like those in the medical science even though some attempts have been made in this direction (Pijanowski et al., 1997, Allen and Lu, 2003). It is only possible or more appropriate to empirically derive the regionalized or localized rules that govern each of the spatially differentiated urban systems.

All empirical models rely on sample data for training or calibrating and assume that rules or relationships, often in terms of coefficients or weights, revealed from these data remain to be true within a certain geographic domain for a given time period. Although there are many methods available for deriving the coefficients or weights for conceptual models, they mainly fall into two groups: conventional statistical techniques and innovative neural networks. Among statistical models, logistic regression has been popular for several reasons (see McMillan, 1989; Landis & John, 1997; Allen, Lu, and Potts, 2002; Wu, 2002; Allen & Lu 2003). According to Allen and Lu (2003), the logistic framework is capable of handling discrete land use variables and the mix of both discrete and continuous independent variables; it is nonlinear in form to better represent the nature of the complex urban reality; it is flexible to be tailored to individual land use systems; and it is available within most statistical packages. However, due to both the complexity of urban land use systems and limitations of the model, it does not always provide satisfactory predictions, as several studies have shown (Landis, 1994, Allen & Lu, 2003). Like other mathematical models, the model assumes that all variables be independent from one another, which appears to contradict the hierarchical urban reality in which all factors are interrelated and interdependent. This leads to a search for alternative models such as neural networks based on the generic algorithms.

This past year, the land use project team explored the applicability of artificial neural networks in land use simulation, developed an operational neural net model for predicting urban growth, applied the model in the Myrtle Beach region of South Carolina, and tested its reliability and validity using both areal sample datasets and global sample datasets against the logistic regression.

2 Artificial neural networks

Neural network computing and generic algorithms have been proposed as possible alternative approaches to handle the uncomputability of complex systems (Sui 1997). Although the first neural networks model appeared in the early 1940s (McCulloch & Pitts, 1943), they were mainly applied in signal processing (Widrow & Stearns, 1985), control (Nguyen & Widrow, 1989, Miller, Sutton, & Werbos, 1990), pattern recognition (Le Cun et al., 1990), medicine (Anderson, 1986; Anderson, Golden, and Murphy, 1986; Hecht-Nilsen, 1990), speech production and recognition (Sijowski and Rosenberg, 1986; Lippmann, 1989), and business (Collins, Ghosh, and Scofield, 1988). Like the history of land use modeling, neural network studies were few in a period of quiet years in the 1970s after the first golden age of the 1950s and 1960s, but revitalized vigorously in the late 1980s and 1990s mainly due to the discovery of robust propagation training methods and the advent of computer technology (Fausett, 1994). However, it was not until the mid-1990s that neural networks were used in the field of land use modeling and resource management.

Openshaw (1993) started using a neural net for modeling spatial interaction. Wang (1994) used artificial neural networks in a geographical information system for agricultural land-suitability assessment. Gimblett et al. (1994) developed a forest management decision model based on neural networks and generic algorithms and tested the model in the Hoosier National Forest. Fischer and Gopa (1994) used an artificial neural network approach to the modeling of interregional telecommunication flows. Gong (1996) combined evidential reasoning and artificial neural network techniques for geological mapping. More recently, Yeh and Li (2002) used neural networks and cellular automata to simulate potential or alternative urban development patterns based on different planning objectives.

According to Kohonen (1988), neural networks are "massively parallel interconnected networks of simple (usually adaptive) elements and their hierarchical organizations which are intended to interact with other objects of the real world in the same way as the biological nervous systems do." The neural network model has certain advantages over mathematical methods (linear and nonlinear) in that it can handle interdependency among the factors. The model also differs from conventional rule-based expert systems in that rules governing the connections among neurons are generated by learning from examples rather than by the preset knowledge from experts. Previous studies indicate that neural networks provide superior levels of performance to those of conventional statistical models because they can well handle the uncertainties of spatial data. Neural networks also are open and flexible compared to other deterministic models in that they can be tailored to the available variables and datasets.

There are many types of neural networks that have been developed for addressing different problems. One of them is the backpropagation neural net that has the capacity to recognize and classify patterns through training or learning processes (Yeh and Li 2002). Figure 1 shows a multiplayer neural network. The net contains an input layer with multiple units, a hidden layer with multiple units, and an output layer with multiple units. Units between two adjacent layers are interconnected. Each unit from the input layer sends its signal to each unit of the hidden layer. Each hidden unit receives the signal from each input unit and sums the signal with different weights and applies an activation function and sends its own signal to each output unit. Each output unit receives a signal from each hidden layer and sums the signals with corresponding weights and computes the output. This process can repeat if there are more hidden layers. The weights can be determined using the robust backpropagation algorithm to be discussed next.

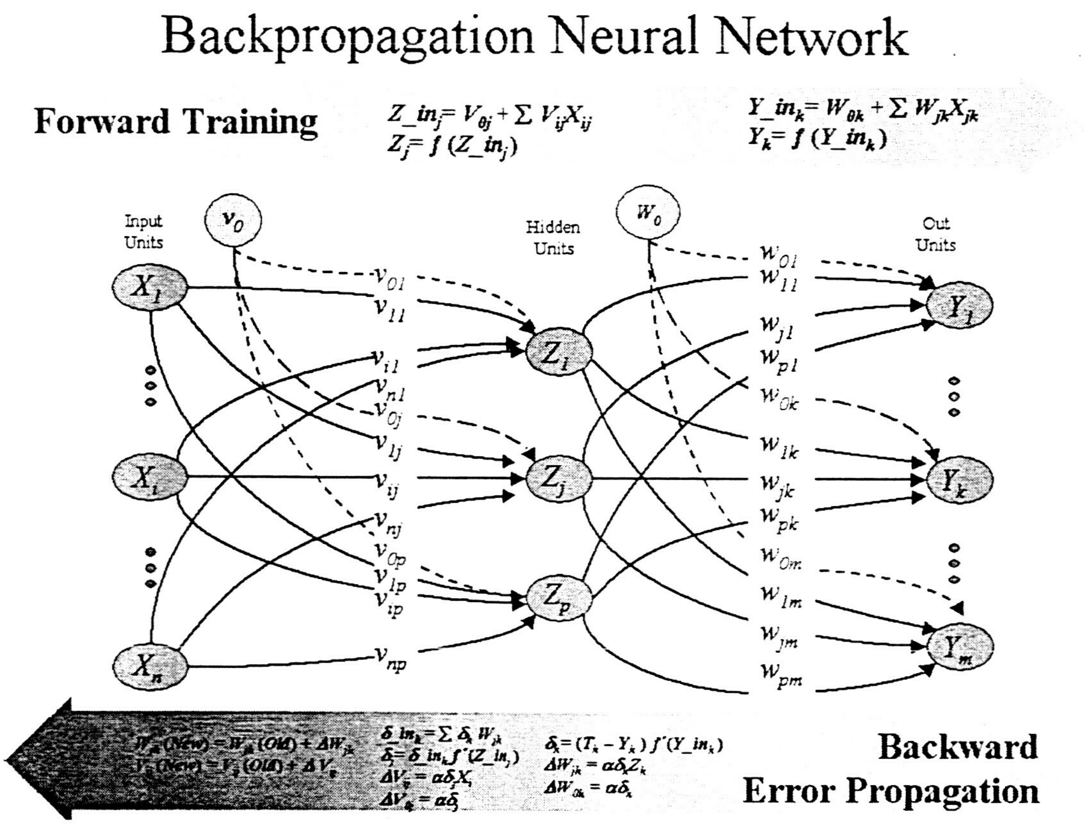

Figure 1. A multi-layer backpropagation neural network.

3 Backpropagation training algorithm

The training of a network by backpropagation involves three stages: the feedforward of the input training pattern, the backpropagation of the associated error, and the adjustment of the weights. There are many methods available. The algorithm described below is for a standard three layer backpropagation neural net.

The training starts with initialization of weights and bias by assigning a small random number to each of them. This can be achieved using the technique developed by Nguen-Widrow to keep random values between –0.5 and 0.5, as is commonly the case. For each record or training pattern in the dataset, the training will complete the following three stages. This will continue in an iterative fashion until the stop condition is met.

3.1 *Feedforward training*

During the feedforward, each input unit (X_i, $i = 1, \ldots, n$) receives signal x_i and broadcasts this signal to each of the hidden units. Each hidden unit (Z_j, $j = 1, \ldots, p$) sums its weighted input signals,

$$\overset{n}{\underset{i=1}{}}$$

$$z\_in_j = v_{0j} + \sum v_{ij}x_i$$

applies its activation function to compute its output signal,

$$z_j = f\,(z\_in_j),$$

and sends this signal to all units in the output layer. Each output unit (Y_k, $k = 1, \ldots, m$) sums its weighted input signals,

$$y\_in_k = w_{0k} + \sum_{j=1}^{p} w_{jk}\, z_j$$

applies its activation function to compute its output signal,

$$y_k = f\,(y\_in_k)$$

which is the response of the net for the given input pattern.

3.2 *Error Backpropagation*

During training, each output units compares its computed activation y_k with its target value t_k to determine the associated error for that pattern with that unit. Based on this error, the factor δ_k ($k = 1, \ldots, m$) is calculated. Each output unit (Y_k, $k = 1, \ldots, m$) receives a target pattern (t_k) corresponding to the input training pattern, computes its error information term

$$\delta_k = (t_k - y_k)\, f'\,(y\_in_k),$$

calculates its weight correction term (used to update w_{jk} later) with a learning rate α,

$$\Delta w_{jk} = \alpha\, \delta_k\, z_j,$$

calculates its bias correction term (used to update w_{0k} later),

$$\Delta w_{0k} = \alpha\, \delta_j\, z_j,$$

and sends to units in the layer below (the hidden units).

Each hidden unit (Z_j, $j = 1, \ldots, p$) sums its delta inputs (from units in the layer above)

$$\delta\_in_j = \sum_{k=1}^{m} \delta_k\, w_{jk}\ ,$$

multiplies by the derivative of its activation function to calculate its error inform term,

$$\delta_j = \delta\_in_j\, f'\,(z\_in_j),$$

calculates its weight correction term (used to update v_{ij} later) with a learning rate α ,

$$\Delta\, v_{ij} = \alpha\, \delta_j\, x_i,$$

calculates its bias correction term (used to update w_{0k} later),

$$\Delta v_{0j} = \alpha\, \delta_j.$$

3.3 *Updating weights and bias*

Once the weight adjustment terms are calculated, they can be used to update the weights and biases. For each output unit (Y_k, $k = 1, \ldots, m$), updates its bias and weights ($j = 1, \ldots, p$):

$$w_{jk} = w_{jk},(\text{old}) + \Delta w_{jk}$$

For each hidden unit (Z_j, $j = 1, \ldots, p$), updates its bias and weights ($i = 1, \ldots, n$):

$$v_{ij} = v_{ij}(\text{old}) + \Delta\, v_{ij}$$

One iteration through all the records in a dataset is called an epoch. Squared error e = $(t_k - y_k)(t_k - y_k)$ can be calculated for each epoch or after a few epochs. The stop condition can be set based on the maximum epochs, an error threshold, or when the squared error starts increasing in either the training dataset or testing dataset if applicable. Once the net is trained and biases and weights are obtained, the feedforward algorithm is used for prediction.

3.3 *Activation function*

According to Fausett (1994), an activation function for a backpropagation net should contain several important characteristics: It should be continuous, differentiable, and monotonically nondecreasing. Furthermore, for computational efficiency, it is desirable that its derivative be easy to compute. For the most commonly used activation functions, the value of the derivative can be expressed in terms of the value of the function. Usually, the function is expected to saturate, i.e., approach finite maximum and minimum values asymptotically.

One of the most typical activation functions is the binary sigmoid function, which has range of (0,1) and is defined as

$$f(x) = \frac{1}{\quad} .$$

with

$$f'(x) = f(x)\,[1 - f(x)].$$

The binary sigmoid can have its range expanded and shifted so that it maps the real numbers into the interval [*a*, *b*] for any a and b. To do so, given an interval [a, b], we define the parameters

$$\gamma = b - a,$$
$$\eta = -a.$$

Then the sigmoid function

$$g(x) = \gamma\, f(x) - \eta$$

has the desired property, namely, its range is (a, b). Furthermore, its derivative also can be expressed conveniently in terms of the function value as

$$g'(x) = \frac{1}{\gamma}[\eta + g(x)][\gamma - \eta - g(x)]$$

The steepness of the logistic sigmoid can be modified by a slope parameter σ. This more general sigmoid function (with range between 0 and 1) is

$$f(x) = \frac{1}{1 + \exp(-\sigma x)} .$$

with

$$f'(x) = \sigma f(x)\,[1 - f(x)].$$

or

$$g(x) = \gamma\, f(x) - \eta$$

$$= \frac{\gamma}{1 + \exp(-\sigma x)} - \eta$$

and

$$g'(x) = \frac{\sigma}{}\,[\eta + g(x)][\gamma - \eta - g(x)].$$

4 Operational model design

A neural net was designed to simulate and predict the probabilities of land transformation from the rural state to urban use. Land use was classified into only two categories: urban and non-urban, coded 1 and 0 respectively. Therefore, only one output unit is needed. Figure 2 depicts the backpropagation neural network land use model tailored to the unique environment of the Myrtle Beach region of South Carolina.

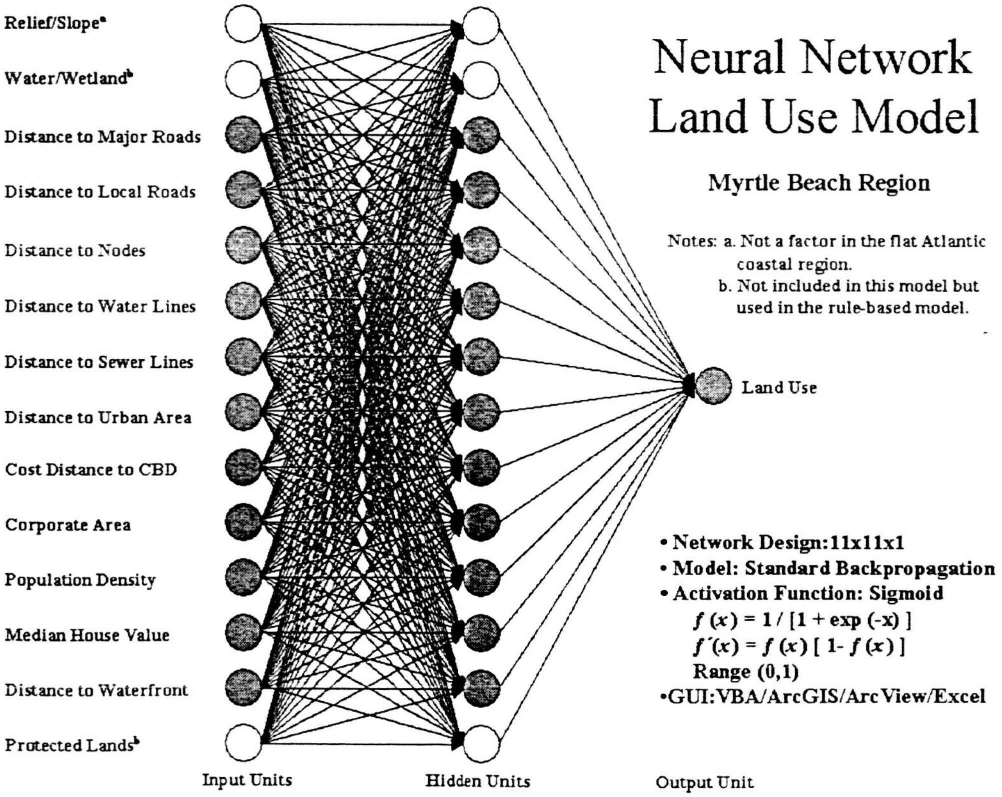

Figure 2. Neural network land use model for the Myrtle Beach region of South Carolina, USA.

The input units are the site attributes and environmental factors that affect land use decision making and spatial distribution (Batty and Xie, 1994; Wu and Webster, 1998, Landis and Zhang, 1997; Allen & Lu, 2003). They are grouped into five categories: market factors, physical suitability, service accessibility, initial conditions, and policy constraints. They represent the key aspects of social, economic, and environmental factors that affect land use and urban growth. In this study, a total of 14 predictor variables were used for building the logistic regression model and the neural network. Note that relief or slope is not a significant factor that causes the differentiation between land uses in this flat area on the Atlantic coast. It is also logical to exclude water features, wetlands, and protected lands first before generating sample datasets. Therefore, only 11 variables were actually used for analysis and the neural net has 11 active input units.

Units of the hidden layer can be set during the training process. For simplicity, 11 hidden units were used in the final model. To make the results comparable with those of the logistic regression model, binary sigmoid function was used as the activation function so that the output from the neural net would fall between 0 and 1. This can be treated as a land transition probability that is useful for simulation and prediction of future urban growth. The cutoff value for classification is 0.5, which is similar to that used in the logistic regression model. The cutoff values for simulating future urban growth were calculated based on the growth ratio as used in the previous two studies (Allen & Lu, 2003).

The graphic user interface of the neural network model was developed using Visual Basic 6.00 and runs on a PC. It was integrated with a land use module developed in ArcGIS/ArcView. GIS was used to generate training and testing samples and export them to the neural network model. The bias and weights obtained through the training or learning process were imported back to the GIS for a grid-based feedforward prediction so that the result can be mapped out or visualized. The operational neural network module provides the flexibility for users to select certain variables and set the corresponding units as desired. The output from the module is also in the Excel format and can be readily put in a word document, facilitating report and paper writing. Samples of the Graphic User Interface of the module are shown in Appendix A.

5 Stratified random sampling

Two sets of spatial data were prepared for the two baseline years, 1990 and 2000. The 2000 land use layer, which has only two classes, urban (1) and nonurban (0), was used as the target layer in the neural network model and dependent variable in the logistic model. Spatial data for 1990 were used for deriving datasets for the independent variables of the logistic model and the input units of the neural network model. The source data are shown in Table 1. Each variable grid was scaled to a range between 0-1 using the technique developed by Gong (1996). However, the range and minimum of each variable grid were stored in a separate file so that they could be retrieved and used for scaling the new set of grids for predicting the future growth. All of these data preparation processes were conducted within the ArcGIS (ESRI).

It is neither necessary nor desirable to use the entire dataset for training the neural networks. The number of training patterns needed, P, depends on the number of the weights to be trained, W, and the accuracy of classification expected, e. According to Fausett (1994), sample size or enough training patterns P can be determined by the condition

$$W/P = e.$$

or

$$P=W/e.$$

For a net with w = 144 and e = 0.1, 1440 cases or training patterns are required to be assured of classifying 90% of the testing patterns correctly, assuming that the net was trained to classify

95% of the training patterns correctly. With e = 0.05, the required training patterns are 2880. Due to spatial differentiation in urban growth, a sample size of 4000 cases was selected for both training and testing datasets.

A stratified random sampling method was used to extract subsets from the complete coverage. This method guarantees that the resultant samples represent different land use classes, different urban patterns, or different levels of urbanization in the region. There are many ways to accomplish this task. In this study, a large base sample set was created then was split into nine subsets in two different ways for two different purposes.

Table 1. **Operational predictor variables for the logistic model and network model.**

Variable Name	Major Data Source
Market factors	
Population density	Census Blockgroup (1990, 2000)
Housing unit value	Census Blockgroup (1990, 2000)
Physical suitability	
Water and wetland	NWI (1989) and Land Cover (1990 and 2000)
Slope /relief *	DEM (USGS)
Distance to waterfront	NWI (1989)
Service accessibility	
Distance to primary roads	Roads (USGS 1990, 2000)
Distance to local roads	Roads (USGS 1990, 2000)
Distance to major nodes	Roads (USGS 1990, 2000)
Distance to waterline	South Carolina Chambers of Commerce (1990)
Distance to sewage	
Cost distance to CBD	Multiple sources including roads (USGS 1990)
Initial conditions	
Distance to existing urban	Land Cover (1990, 2000)
Policy constraints	
Protected lands	Gap Analysis (USGS, 2003) (GA, NC, and SC)
Corporate area	Tiger/Lines (1990)

First, a cell-based technique was developed to randomly select individual cells from the 2000 land use grid of the region. With the help of an Avenue Script, the Grid.MakeRandom function of the Spatial Analyst of ArcGIS was used to generate a grid with uniformly distributed random values between 0 and 1. A subset of this grid, masked by the area of interest, was iteratively extracted either in the descending order or ascending order until a desired sample size (in number of cells or in percentage 25%) was obtained. This grid was reclassified to create a random mask grid. Then, the Grid.Sample function was used to convert all the variable grids (Table 1) into an ASCII format that can be used directly for the logistical analysis and network training.

From the above base sample dataset, which has 36,500 cases, nine subsets were created using a stratified method. Records of the dataset were numbered repeatedly from 1 to 9 and the records with the same number were extracted to form a subset with approximately 4072 cases. Each subset is capable of representing the whole population or urban reality in the region, but multiple datasets make it possible to use some for training and some for testing and to examine the global effect or strength of regional models. These subsets are called global samples.

The second nine subsets are called areal samples or local samples. They were extracted from the base set following the record order and each has 4000 cases. Because the records start from the upper left corner to the lower right corner of the region when a grid is converted to an ASCII file, the resultant datasets in essence are area-based, representing different spatial patterns of urban space in the region. They are, therefore, called areal samples. Based on the level of urbanization, areas that these subsets represent can be roughly grouped into four categories: (a) remote rural areas with scattered urban cells (<10%, 3 subsets); (b) less urbanized areas with small towns (10-20%, 2 subsets); (c) urban fringe areas around metropolitan centers (20-30%, 1 subset); and (d) urbanized areas with large green space (wetlands) along the coast (> 30%, 2 subsets). Although these classifications are quite arbitrary, they are useful for testing the reliability and validity of both models with a perspective of spatial variation.

6 Model training process

There are a total of 18 datasets in two categories, each category having 9 sets and each set having approximately 4000 cases. Both logistic regression and neural network were calibrated and trained with the each dataset while other sets in the same category were used for testing the validity of each model for different geographical areas, different spatial patterns, and different samples.

It was found that for each dataset, the logistic model was capable of generating the same regression coefficients and the same urban classifications regardless the number of runs or iterations. However, the results (network weights and classification accuracy) of the neural network model varied substantially with different runs and different parameters (such as error threshold, maximum epochs, and learning rates) for the same dataset. To be consistent, all trainings of the neural network started with maximum epochs of 3000, an error threshold of 0.05, and a learning rate of 0.2.

Five strategies were used to determine which results were to be used. First, if the prediction results were equal or better than those from the logistic model when the maximum epochs were reached and the training was stopped, the weights and classifications were used as the indicator of the power of the model. This was the case for 14 of 18 datasets. Second, when the error threshold was reached quickly and the training stopped as in 4 cases of global datasets, the results were saved but the model was retrained with an error threshold of 0.01. No training has reached that level of accuracy. Third, when the neural network generated a lower accuracy than the logistic model did for the first run, either maximum epochs were increased or the error threshold was lowered for continuous training to explore the potential of the neural network. No more than three additional runs were needed. Fourth, when the training failed in the first run as happened to two area-based datasets (area-sample 1 and area-sample 3) due to improper initial random weight or too few urban cases in the samples, additional runs were carried out. For area-sample 1, desired results were obtained after resetting the initials (or neural network parameters). For area-sample 3, the training became successful after the learning rate was reduced to 0.05. Finally, when the training failed in the first few runs and the technique mentioned above did not work, the dataset was split into two smaller sets of odd and even numbers. Each subset was used to train the neural network and the resultant weights were used as the initial weights for training the model again using the whole dataset. This was the case for area-based dataset 5.

7 Prediction success rates

7.1 *Global effects*

Both models were calibrated and tested using 9 sets of sample data representing the whole population of the region to examine to their global effects in terms of prediction success rates. Results are summarized in Table 2. As these sample datasets indicate, urban area in this region covers about 21.86-23.33% of the total land area. Both models generated fairly good overall predictions and nonurban predictions, with 88.21-90.01% and 94.46-95.88% respectively for the logistic model and 89.75-93.59% and 90.13-98.37% respectively for the neural network model (Figure 3 and Figure 4). However, the neural networks proved to be superior to the logistic regression model in all but one case. The largest improvement takes place in the urban category with an average 4.73 net percentage. This number becomes notably larger at 10.18 if sample dataset 7 is excluded. More importantly, the neural network has exhibited its capability to differentiate urban land use in the dominantly rural environments (Figures 3 through 6).

Table 2. **Comparison of prediction success rates between the neural networks and the logistic regression model as trained using the global sample datasets.**

Data				Predicted						
				Neural Networks			Logistic Regression			Net Change
Set	Land Use	N	(%)	Urban	Non-urban	Correct (%)	Urban	Non-urban	Correct (%)	
1	**Urban**	939	23.05	685	254	72.95	631	308	67.20	5.75
	Non-urban	3134	76.95	73	3061	97.67	148	2986	95.28	2.39
		4073				91.97			88.80	3.17
2	**Urban**	917	22.51	760	157	82.88	649	268	70.77	12.11
	Non-urban	3156	77.49	104	3052	96.70	139	3017	95.60	1.10
		4073				93.59			90.01	3.58
3[a]	**Urban**	925	22.72	699	226	75.57	640	285	69.19	6.38
	Nonurban	3147	77.28	87	3060	97.24	144	3003	95.42	1.82
		4072				92.31			89.46	2.85
4	**Urban**	890	21.86	675	215	75.84	577	313	64.83	11.01
	Nonurban	3182	78.14	61	3121	98.08	131	3051	95.88	2.20
		4072				93.22			89.10	4.12
5	**Urban**	940	23.08	710	230	75.53	646	294	68.72	6.81
	Nonurban	3132	76.92	105	3027	96.65	162	2970	94.83	1.82
		4072				91.77			88.80	2.97
6[a]	**Urban**	949	23.31	724	225	76.29	656	293	69.13	7.16
	Nonurban	3123	76.69	63	3060	97.98	173	2950	94.46	3.52
		4072				92.93			88.56	4.37
7	**Urban**	950	23.33	647	303	68.11	646	304	68.00	0.11
	Nonurban	3122	76.67	51	3071	98.37	153	2969	95.10	3.27
		4072				91.31			88.78	2.53
8	**Urban**	928	22.79	1326	162	89.11	614	314	66.16	22.95
	Nonurban	3144	77.21	248	2264	90.13	166	2978	94.72	-4.59
		4072				89.75			88.21	1.54
9	**Urban**	932	22.89	702	230	75.32	616	316	66.09	9.23
	Nonurban	3140	77.11	97	3043	96.91	143	2997	95.45	1.46
		4072				91.97			88.73	3.24

Note: (a) Training was successful after several trials; (b) Sample set 5 was first split into two subsets using one set for initial training. The resultant weights were used as initial training for the whole set.

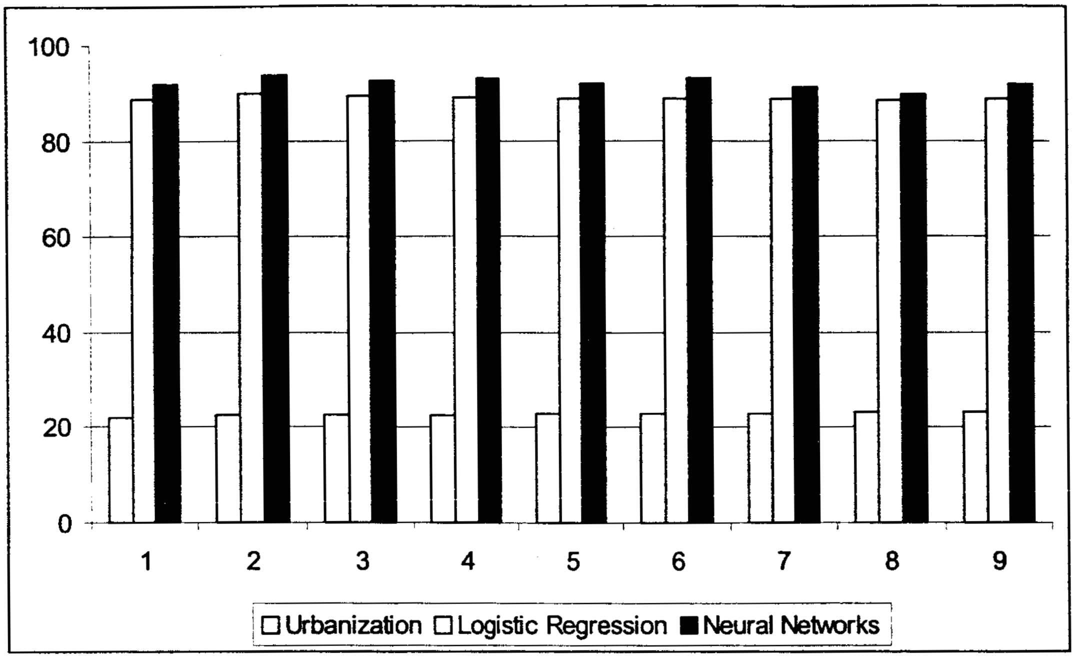

Figure 3. **Overall success rates of both urban and nonurban classifications as predicted by the neural networks and logistic regression using the global datasets.**

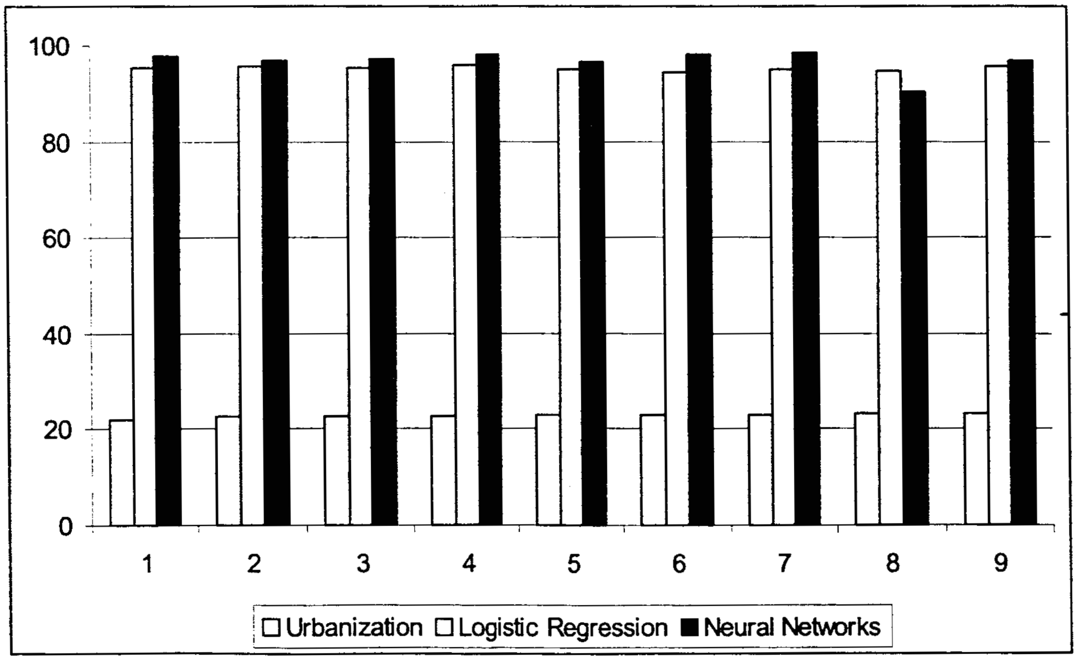

Figure 4. **Accuracy of classifications of nonurban use as predicted by the neural networks and logistic regression using the global datasets.**

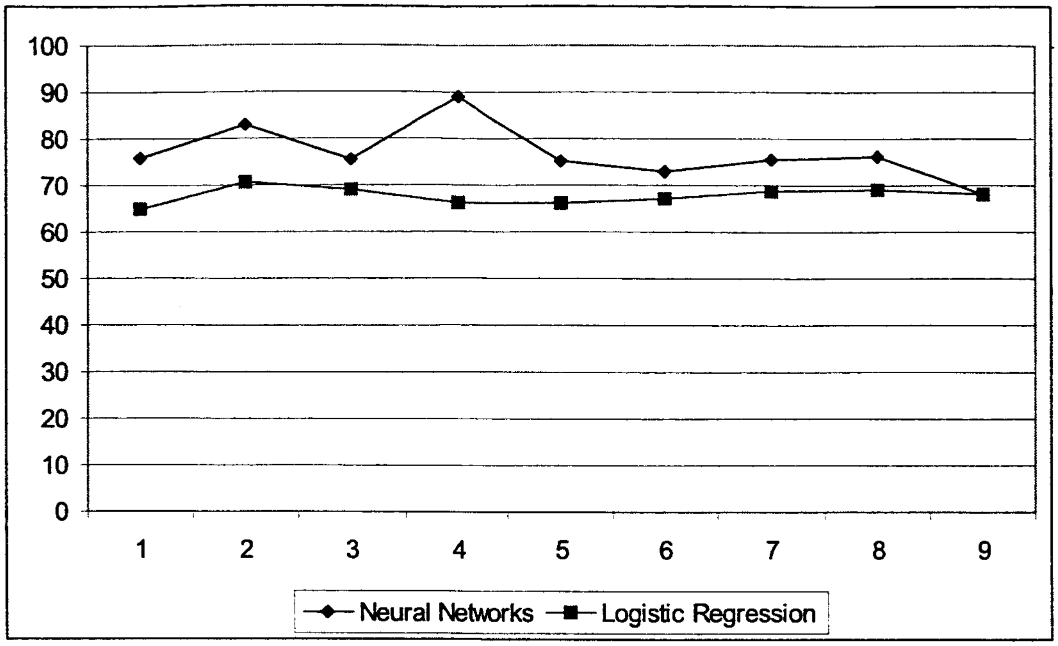

Figure 5. **Difference of classification accuracy between the neural networks and logistic regression against global datasets. The trend shows that as the area becomes more urbanized, the difference between the two models becomes smaller.**

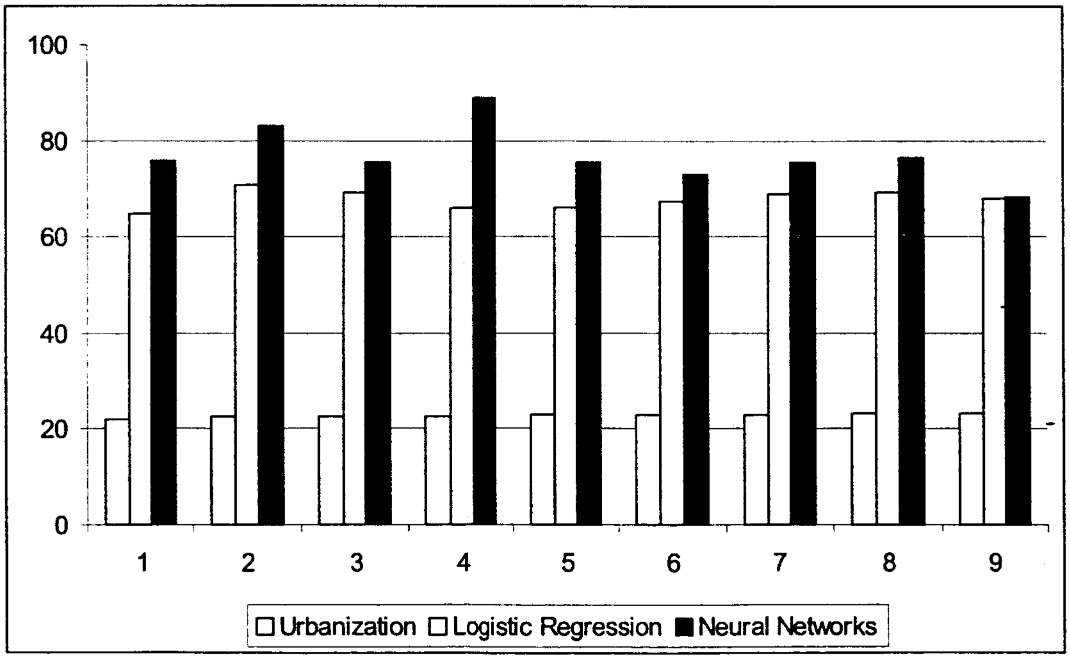

Figure 6. **Difference of classification accuracy between the neural networks and logistic regression against global datasets. The trend shows that as the area becomes more urbanized, the difference between the two models becomes smaller.**

The logistic model generated a slightly better prediction for the non-urban use (94.72% or 4.59 net change) at the cost of urban land use (66.16% or -22.95 net change). Although the neural networks were retrained with better predictions (urban 75.11%, nonurban 96.22%, and overall 91.40%) than those generated from the logistic model, the results of the first run were kept in the table because it raises an issue of neural network training to be discussed later.

Although prediction success rates vary substantially across different land use categories, the accuracy of prediction is similar across different datasets. This is also true with the testing results. Table 5 shows the classification accuracy for each dataset based on the model calibrated using the first dataset. The maximum standard deviation in prediction success rates (1.441) was found in the urban category with the smallest in the nonurban category. This was expected because the nonurban use is still the most dominant land use patterns in the region. It was found that for each testing global dataset, the prediction success rates in each category are slightly smaller than that for the training dataset, suggesting the neural network model best fit the dataset used for its training. Whether this is also true to the logistic model remained untested.

Table 3. **Prediction success rates of the neural network models trained by sample dataset 1 and tested by eight other sample datasets.**

Dataset	**Urban Cells**	**Nonurban Cells**	**Total Cases**	**Correctly Classified (%)** **Urban**	**Nonurban**	**Overall**
1	939	3134	4073	72.95	97.67	91.97
2	917	3156	4073	71.76	96.83	91.19
3	925	3147	4072	70.05	96.28	90.32
4	890	3182	4072	70.45	95.85	90.30
5	940	3132	4072	69.15	95.95	89.76
6	949	3123	4072	70.39	96.25	90.23
7	950	3122	4072	69.68	96.09	89.93
8	928	3144	4072	68.43	95.71	89.49
9	932	3140	4072	69.10	96.18	89.98
Mean				70.35	96.36	90.43
Min				68.43	95.71	89.49
Max				72.95	97.67	91.97
Standard Deviation				1.441	0.626	0.788

7.2 *Spatial differentiations*

Prediction success rates or classification accuracy was used as the measure of power or reliability of the two models of concern. For each area-based dataset, the overall success rate and the two categorical success rates were calculated for each model and the results were summarized in Table 4. In general, both models have obtained good or very good overall predictions for the nonurban land use with an average accuracy between 89.41% and 94.74%. Since the rural land covers more than a quarter of the total area in the region, prediction accuracy for non urban land use in terms of percentage correctly classified is often higher than for any other uses. Similarly, the difference in effectiveness between these two models is only marginal in both nonurban and all categories even though the average success rates of the neural network model are better than those of the logistic model (by 0.64 and 2.35 percentage points respectively.

Table 4. **Prediction success rates: binary logistic regression vs. backpropagation neural network using area-based samples.**

Data				Predicted						
				Neural Network			Logistic Regression			Net Change
Set	Land Use	N	(%)	Urban	Non-urban	Correct (%)	Urban	Non-urban	Correct (%)	
1[a]	Urban	152	3.73	92	60	60.53	43	109	28.29	32.24
	Non-urban	3919	96.27	5	3914	99.87	9	3910	99.77	0.10
		4071				98.40			97.10	1.30
2	Urban	569	14.23	472	97	82.95	396	173	69.60	13.35
	Non-urban	3431	85.78	81	3350	97.64	52	3379	98.48	-0.84
		4000				95.55			94.38	1.18
3	Urban	267	6.68	158	109	59.18	107	160	40.07	19.11
	Nonurban	3733	93.33	13	3720	99.65	2	3731	99.95	-0.30
		4000			97.15	96.95			95.95	1.00
4	Urban	470	11.75	329	141	70.00	80	390	17.02	52.98
	Nonurban	3530	88.25	48	3482	98.64	27	3503	99.24	-0.60
		4000				95.28			89.58	5.71
5[b]	Urban	324	8.10	164	160	50.62	66	258	20.37	30.25
	Nonurban	3676	91.90	26	3650	99.29	16	3660	99.56	-0.27
		4000				95.35			93.15	2.20
6	Urban	1181	29.53	770	411	65.20	786	395	66.55	-1.35
	Nonurban	2819	70.48	51	2768	98.19	258	2561	90.85	7.34
		4000				88.45			83.68	4.78
7	Urban	1587	39.68	1401	186	88.28	1290	297	81.29	6.99
	Nonurban	2413	60.33	551	1862	77.17	350	2063	85.50	-8.33
		4000				81.58			83.83	-2.25
8	Urban	1488	37.20	1326	162	89.11	1253	235	84.21	4.90
	Nonurban	2512	62.80	248	2264	90.13	339	2173	86.50	3.63
		4000				89.75			85.65	4.10
9	Urban	2337	50.18	2008	329	85.92	1980	357	84.72	1.20
	Nonurban	2320	49.82	392	1928	83.10	508	1812	78.10	5.00
		4657				84.52			81.43	3.09

Note: (a) Training was successful after several trials; (b) Sample set 5 was first split into two subsets and using one set for initial training. The resultant weights were used as initial training for the whole set.

As shown in Figures 7 through 9, the most remarkable improvement was found in the urban use category. For the nine area-based datasets, the average prediction accuracy is 74.42% for the neural network model, compared to 54.68% for the logistic model, which is an improvement of 17.74 percentage points. The largest improvement is by 52.98 percentage points in set number four. This suggests that the neural network model is superior in its ability to differentiate the urban land use from the nonurban use. On the other hand, the geographic variation of prediction success rates is relatively lower for the neural net (50.62-89.11%) than for the logistic model (17.07-84.72%). No accuracy is found

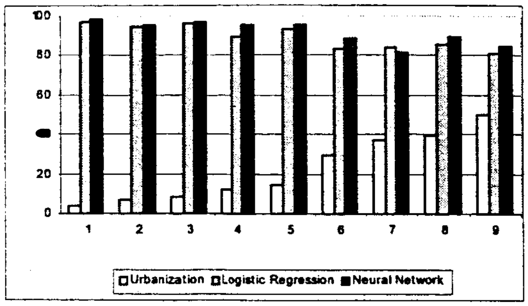

Figure 7. **Overall success rates for both urban and nonurban classifications as predictedby the neural networks and logistic regression using area-based datasets. (a) The datasets were ranked based on the level of urbanization and thus the series numbers are not the same as the sample numbers; (b) overall prediction accuracy tends to decline as the area is more urbanized; and (c) the improvement in prediction is only marginal.**

below 50% despite of great variation in the level of urbanization. All these indicate that the neural network-based prediction is also more stable and thus more reliable. In addition, the findings that success rates vary with different areas suggest that sub models or multiple models are needed for better approximation of a regional urban system. Existing land use models do not have the capability to apply different rules for addressing spatially differentiated patterns and temporally varying growth rates.

It is worth reporting that the classification accuracy also changes with training sample size. During the preliminary study, the base dataset was split into seven subsets with the largest one having 6657 cases while each of the rest have 5000 cases. This is the only dataset with which the neural network model was less successful in predicting urban use (-6.00) as shown in Table 5. Is this always true in more urbanized areas, or is it because the network was not adequately trained, or something else? To answer these questions, several other runs were performed. Some better results were obtained, but the accuracy was always smaller than that generated by the logistic model. The dataset was then broken into two smaller sub sets for retraining the net. To our surprise, the neural network model generated much better predictions in every category for each smaller subset than the logistic model did (Table 5). This appears to suggest that the smaller the sample size, the better the prediction based on the neural network. To further confirm this finding, other original datasets were subdivided and trained. Similar trends hold even though the difference varies from one case to another.

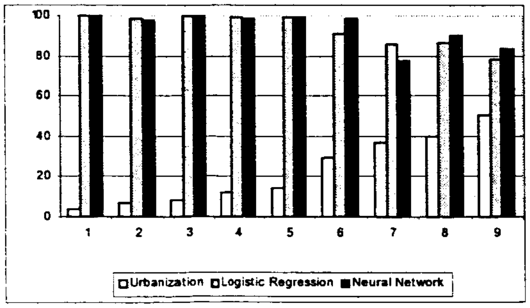

Figure 8. Success rates for nonurban use classifications as predicted by the neural networks and logistic regression using area-based datasets. (a) Both models have difficulties in differentiating the nonurban use form the urban use; (b) There is not significant difference in prediction accuracy between the two models.

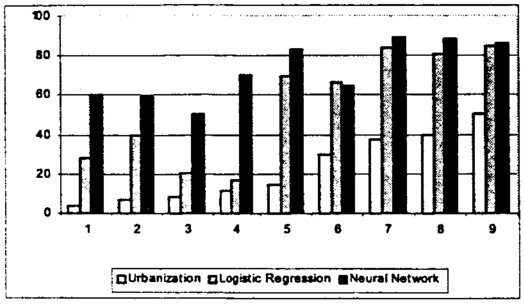

Figure 9. **Success rates of urban use classifications as predicted by the neural networks and logistic regression using area-based datasets. (a) The datasets were ranked based on the level of urbanization and thus the series numbers are not the same as the sample numbers; (b) the improvement of prediction becomes greater as the area represented by the sample become more rural.**

Table 5 **Prediction Success Rates: Binary Logistic Regression vs. Backpropagation Neural Network, Based on Split Smaller Samples**

Data				Predicted						
				Logistic Regression			Neural Network			Net Change
Set	Land Use	N	(%)	Urban	Non-urban	Correct (%)	Urban	Non-urban	Correct (%)	
7	Urban	3176	47.71	2751	425	86.60	2560	616	80.60	(-6.00)
	Nonurban	3481	52.29	681	2800	80.40	369	3112	89.40	9.00
		6657				83.40			85.20	1.80
7a	Urban	1658	55.29	1165	176	86.88	1232	109	91.87	4.99
	Non-urban	1341	44.71	239	1419	85.59	152	1506	90.83	5.24
		2999				86.16			91.30	5.14
7b	Urban	1823	49.84	1565	270	85.29	1597	238	87.03	1.74
	Non-urban	1835	50.16	428	1395	76.52	267	1556	85.35	8.83
		3658				80.92			86.19	5.27

7.3 *Predicted future growth*

The projected future population growth and urban area growth in Georgetown and Horry Counties is summarized in Table 6 through Table 9. Although the growth ratios in both counties are not as large as those in the Charleston region, they represent two unique growth patterns in coastal South Carolina. Georgetown County, which has strict zoning ordinances, has experienced little growth in both population and area over the last decade (Table 6 and Table 7). In fact, Georgetown's population increase over the past century, only ranks sixth among eight coastal counties in South Carolina. As a result, it has become the second smallest county in population in the coastal region. It is projected that its population will increase by only 3000 in the next thirty years. The urban area will expand by less than 5 square miles over the same period. On the contrary, Horry County exhibits an uncontrolled, sprawl growth pattern. It is the fastest growing county in the State of South Carolina. In 1900, Horry County's population was almost the same as Georgetown's population. It has increase 8.42 times by 2000. This growth rate ranks the first in the entire state. Over the last decade, its urban area increased by nearly 40 square kilometers. By year 2030, its urban area will expand from 142.84 km^2 in 2000 to 259.21 km^2 at the current pace and more likely triple to 484.65 km^2 at the 3:1 growth ratio (Table 8).

Figure 9 and Figure 10 show the spatial extent of historical urban growth during 1990-2000 and predicted urban growth through 2030. In comparison, predicted urban growth for the other two coastal regions is shown in Figure 12 and 13 in the Appendix. Urban sprawl in this region mainly took a zonal pattern expanding both ways along the coast and spreading toward inland towns along the major highways. This spatial trend is predicted to continue through 2030. Areas around the major road intersections along the US 17 Bypass will continue to be the hot growth spots in the region. Due to the constraint of wetland areas, no significant growth is anticipated in the stretch between the Myrtle Beach and North Myrtle Beach, but the upland or dry land areas along two major roads (US Hwy 501 and SC Hwy 9) leading inland will see significant urban developments. The triangle area, formed by US Hwy 501, US Hwy 17, SC HWY 707 and SC HWY 544, and SC Hwy 9, is the only large tract of physically developable land adjacent to the Myrtle Beach and thus is the prime target for future development. This will create significant pressure on the coastal ecosystems in that region. Summary tables about the future urban growth are shown in tables six through nine.

Table 6. **Projected urban area growth in square kilometers, Georgetown County, South Carolina, 1990-2030.**

Year	Population Growth	Urban Area Growth in Square Kilometers			
		Ratio 0.48:1	Ratio 1:1	Ratio 2:1	Ratio 3:1
1990	46302	22.11	22.11	22.11	22.11
1995	51050	23.03	23.03	23.03	23.03
2000	55797	23.95	25.17	27.32	29.46
2005	60544	24.87	27.32	31.60	35.88
2010	65291	25.79	29.46	35.88	42.31
2015	70038	26.70	31.60	40.17	48.73
2020	74785	27.62	33.74	44.45	55.16
2025	79532	28.54	35.88	48.73	61.58
2030	84279	29.46	38.03	53.02	68.01

Note: (a) Urban areas are calculated based on the projected population growth and the growth ratios; (b) urban area in the county will double in the next thirty years based on the 2:1 growth scenario.

Table 7. **Projected urban area growth in percentage, Georgetown County, South Carolina, 1990-2030.**

Year	Population Growth (%)	Urban Area Growth in Percentage (%)			
		Ratio 0.48:1	Ratio 1:1	Ratio 2:1	Ratio 3:1

1990					
1995	10.25	4.17	4.17	4.17	4.17
2000	20.51	8.33	13.86	23.55	33.23
2005	30.76	12.48	23.55	42.92	62.29
2010	41.01	16.63	33.23	62.29	91.36
2015	51.26	20.78	42.92	81.67	120.42
2020	61.52	24.93	52.61	101.04	149.48
2025	71.77	29.09	62.29	120.42	178.54
2030	82.02	33.24	71.98	139.79	207.60

Note: (a) Year 1990 was used as the starting baseline year for percentage calculation; (b) the ratio of urban area growth (%) to population growth (%) was 0.48: 1 for the period between 1990 and 2000.

Table 8. **Projected urban area growth in square kilometers, Horry County, South Carolina, 1990-2030.**

Year	**Population Growth**	**Urban Area Growth in Square Kilometers**		
		Ratio 1:1	**Ratio 2:1**	**Ratio 3:1**
1990	144053	104.06	104.06	104.06
1995	170341	123.45	123.45	123.45
2000	196629	142.84	142.84	142.84
2005	222917	162.24	180.82	199.81
2010	249205	181.63	218.80	256.78
2015	275493	201.03	256.78	313.75
2020	301781	220.42	294.76	370.71
2025	328069	239.82	332.73	427.68
2030	354357	259.21	370.71	484.65

Note: (a) Urban areas are calculated based on the projected population and growth ratios; (b) urban area in the county will triple in the next thirty years based on the 3:1 growth scenario.

Table 9. **Projected urban area growth in percentage, Horry County, South Carolina, 1990-2030.**

Year	**Population Growth**	**Urban Area Growth in Square Kilometers**		
		Ratio 1:1	**Ratio 2:1**	**Ratio 3:1**
1990				
1995	18.25	18.63	18.63	18.63
2000	36.50	37.27	37.27	37.27
2005	54.75	55.91	73.77	92.01
2010	73.00	74.54	110.26	146.76
2015	91.24	93.19	146.76	201.51
2020	109.49	111.82	183.26	256.25
2025	127.74	130.46	219.75	310.99
2030	145.99	149.10	256.25	365.74

Note: (a) Urban areas are calculated based on the projected population growth and the growth ratios; (b) urban area in the county will double in the next thirty years based on the 2:1 growth scenario.

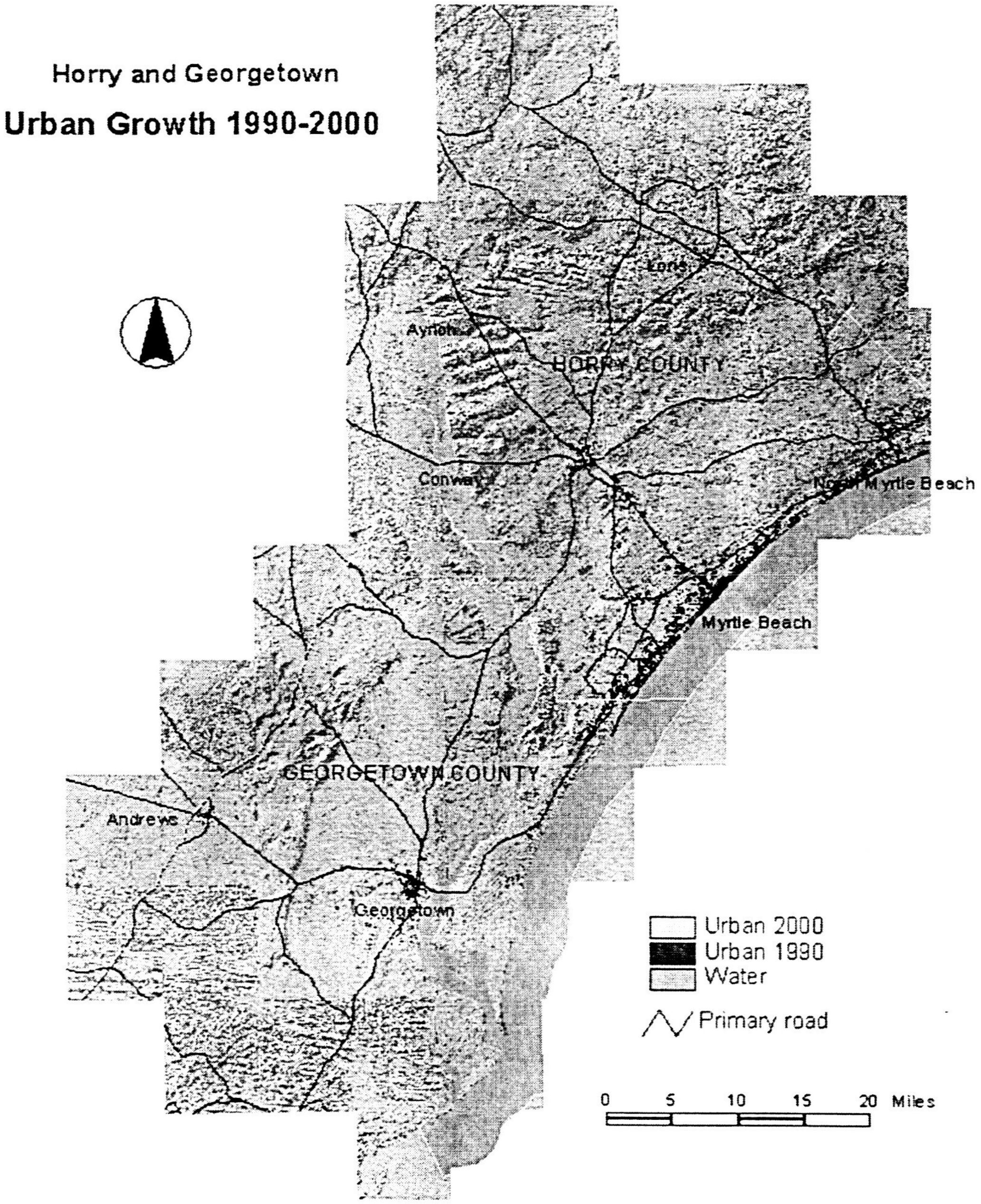

Figure 10. **Urban growth in the Georgetown-Horry region of South Carolina, 1990-2000**.

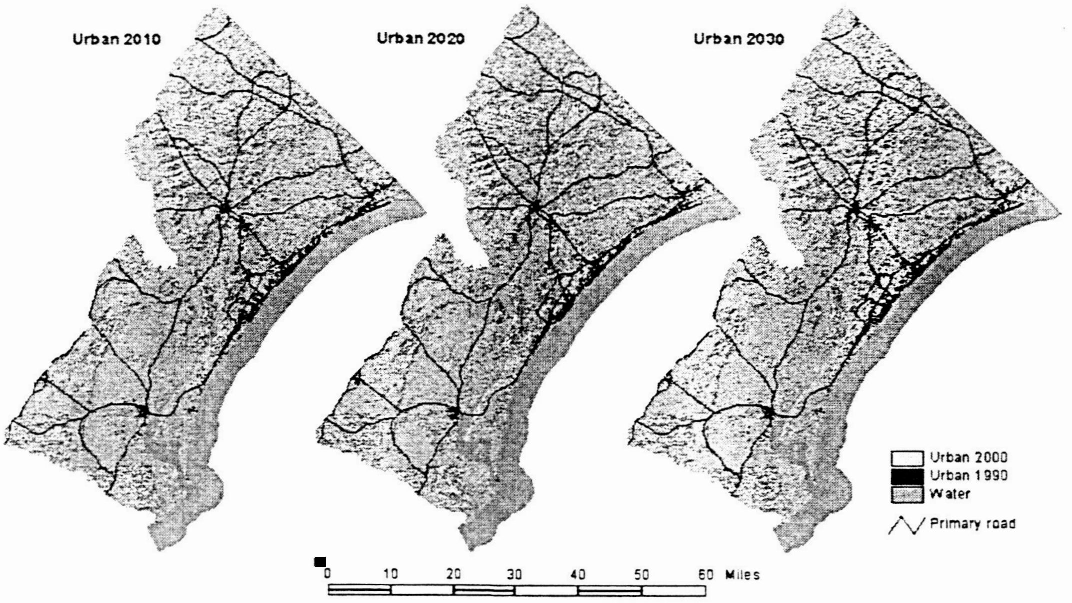

Figure 11. **Predicted urban growth in the Georgetown-Horry region of South Carolina, 2010-2030. Demand of future urban sizes in the Horry County was based on a 3:1 urban area-population growth ratio.**

7 Conclusions

The use of an appropriate relationship model is critical for reliable prediction of future urban growth. Identification of proper variables and mathematic functions and determination of the weights or coefficients are the key tasks for building such a model. Although the conventional logistic regression model is appropriate for handing land use problems, it appears insufficient to address the issue of interdependency of the predictor variables. This study used an alternative approach to simulation and modeling urban growth using artificial neural networks. It developed an operational neural network model trained using a robust backpropagation method. The model was applied in the Myrtle Beach region of South Carolina, and tested with both global datasets and areal datasets to examine the strength of both regional models and areal models. The results indicate that the neural network model not only has many theoretic advantages over other conventional mathematic models in representing the complex urban systems, but also is practically superior to the logistic model in its capability to predict urban growth with better accuracy and less variation. The neural network model is particularly effective in terms of successfully identifying urban patterns in the rural areas where the logistic model often falls short. It was also found from the area-based tests that there are significant intra-regional differentiations in urban growth with different rules and rates. This suggests that the global modeling approach, or one model for the entire region, may not be adequate for simulation of a urban growth at the regional scale. Future research should develop methods for identification and subdivision of these areas and use a set of area-based models to address the issues of multi-centered, intra-regionally differentiated urban growth.

Acknowledgements

This research was funded by the NASA EPSCOR program of South Carolina.

References

Allen, J. and K. Lu (2003). "Modeling and Prediction of Future Urban Growth in the Charleston Region of South Carolina: A GIS-based integrated approach". Conservation Ecology 8(2): 2.

Allen, Jeffery, Kang S. Lu, and Thomas D. Potts. 2002. A GIS-based analysis and prediction of land-use change in a coastal tourism destination area. In Miller, Marc I., Auyong, Jan, and Hadley, Nina P. (eds.). Proceedings of the 1999 International Symposium on Coastal and Marine Tourism: Balancing Tourism and Conservation. (26-29 April 1999, Vancouver, BC, Canada). Washington Sea Grant Program and School of Marine Affairs, University of Washington, Seattle, WA, Oregon Sea Grant College Program, Oregon State University, Corvallis, OR, and Oceans Blue Foundation, Vancouver, BC.

Anderson, J. A. (1986) Cognitive capaibiliti4s of a parallel system. In E. Bienestoch, F. Fogelman-Souli. & Weisbuch. Eds., Disordered systems and biological organization. NATO ASI Series. F20, Berlin: Springer-Verlag.

Anderson, J.A. R.M Golder, & G.L. Murphy. (1986) Concepts in distributed systems. In H. H. Szu. Ed., Optical and hybrid computing, 634:260-272. Bellington. WA: Society of Photo-Optical Instrumentation Engineers

Batty M, Xie Y (1994) From cells to cities. Environment and Planning B: Planning and Design 21:531-548

Collins, E., S. Ghosh. & C. L. Scofield (1988) An application of multiple neural nwtwork learning system to emulation fo mortgage underwriting judgements. IEEE international conference on neural networks, Sna Diego, CA, 11:459-466

Fausett L (1994) Fundamentals of neural networks: architectures, algorithms, and applications. Princeton Hall, Englewood Cliffs, New Jersey.

Gimblett, R. H., Ball, G. L., & Guisse, A W. (1994). Autonomous rule generation and assessment for complex spatial modeling. Landscape and Urban Planning, 30, 13-16.

Gong P (1990) Integrated analysis of spatial data from multiple sources: using evidential reasoning and artificial neural network techniques for geological mapping. Photogrammetric Engineering & Remote Sensing 62:513-523

Hecht-Nielsen. R. (1990) Neurocomputing. Reading, MA:Addison-Wesley

Kohonen, T. The 'Neural' phonetic typewriter. Computer, 21(3): 11-22

Landis, J. (1994). The California urban futures model: A new generation of metropolitan simulation models. Environment and Planning B, Planning and Design. 21, 399-420.

Landis, J., & Zhang, M. (1997). Modeling urban land use change: The next generation of the California urban future model. Paper submitted to the land use modeling workshop at USGS-EROS Data Center, June 5-6, Sioux Falls, South Dakota.

Li X, Yeh AGO (2000) Modeling sustainable urban development by the integration of constrained cellular automata and GIS. International Journal of Geographic information Science 14(2): 131-152

Lippmann, R. P. (1989) Review of neural networks for speech recognition. Neural Computation, 1:1-38

McCulloch, W.S., & Pitts W (1943) A logical calculus of the ideas immanent in nervous activity. Bulletin of Mathematical Biophysics, 5:115-133

Miller W T Sutton R S & Werbos P J (eds) (1990) Neural networks for control. Cambridge, MA:MIT Press.

Le Gun, Y, B. Boser, J. S. Denker, D. Henderson. R.E. Howard, W. Hubbard, & L D. Jackel (1990) Handwritten digit recognition with a backpropagation network. In D. S. Touretsky, ed., Advances in neural information processing systems 2. San Mateo, CA: Morgan Kaufman. Pp. 396-404

Nguyen D & B Widrow (1989) Fast learning in networks of locally tuned processing units. Neural Computation, 1:281-294

Openshaw S (1993) Modelling spatial interaction using a neural net. In: Fischer MM, Nijkamp P (eds) GIS Spatial modeling and policy. Springer, Berlin. Pp 147-164

Pijanowski, B. C. et al (1997). A land transformation model: Conceptual elements, spatial object class hierarchies, GIS command syntax and an application for Michigan's Saginaw Bay Watershed. Paper submitted to the land use modeling workshop at USGS EROS Data Center, June 5-6, Sioux Falls, South Dakota.

Sejnowski, T. J, & C.R. Rosenberg . (1986). Nettalk: aparallel network that learns to read aloud. The Hohns Hopkins University Electrical Engineering and Coputer Science Technial Report JHU/EECS-86/01. 32pp. Rprinted in Anderosn &Rosenfeld [1988]. Ppp.663-672

Sui, D. Z. (1997). The syntax and semantics of urban modeling: Versions vs. visions. Paper submitted to the land use modeling workshop at USGS EROS Data Center, June 5-6, Sioux Falls, South Dakota.

Von Thunen, J. H. (1826). Der Isolierte Staat in Beziehing auf Landwirtschatf und Nationaloknomie, Rostoch, Translated into English by Carla M. Wartenberg as The Isolated State, Permagon Press, Oxford, 1966.

Wang F (1994) The use of artificial neural networks in a geographical information system for agricultural land-suitability assessment. Environment and Planning A 26: 265-284

Webster CJ, Wu F (1999) Regulation, land-use mix and urban performance. Part 2: simulation. Environemnt and Planning A 31: 1529-1545

Widrow , B., & S. D. Stearns. (1985). Adaptive signal processing. Englewood Cliffs, NJ: Princeton-Hall.

Wu F, Webster CJ (1998) Simulation of land development through the integration of cellular automat and multicriteria evaluation. Environment and Planning B: Planning and Design 25:103-126.

Yeh AGO, Li X (2002) Urban simulation using neural networks and cellular automata for land use planning. In: Richardson D, Van Oosterom P (eds) Advances in Spatial Data Handling. Springer, Berlin, pp 452-464

Appendix A. Neural Network Module

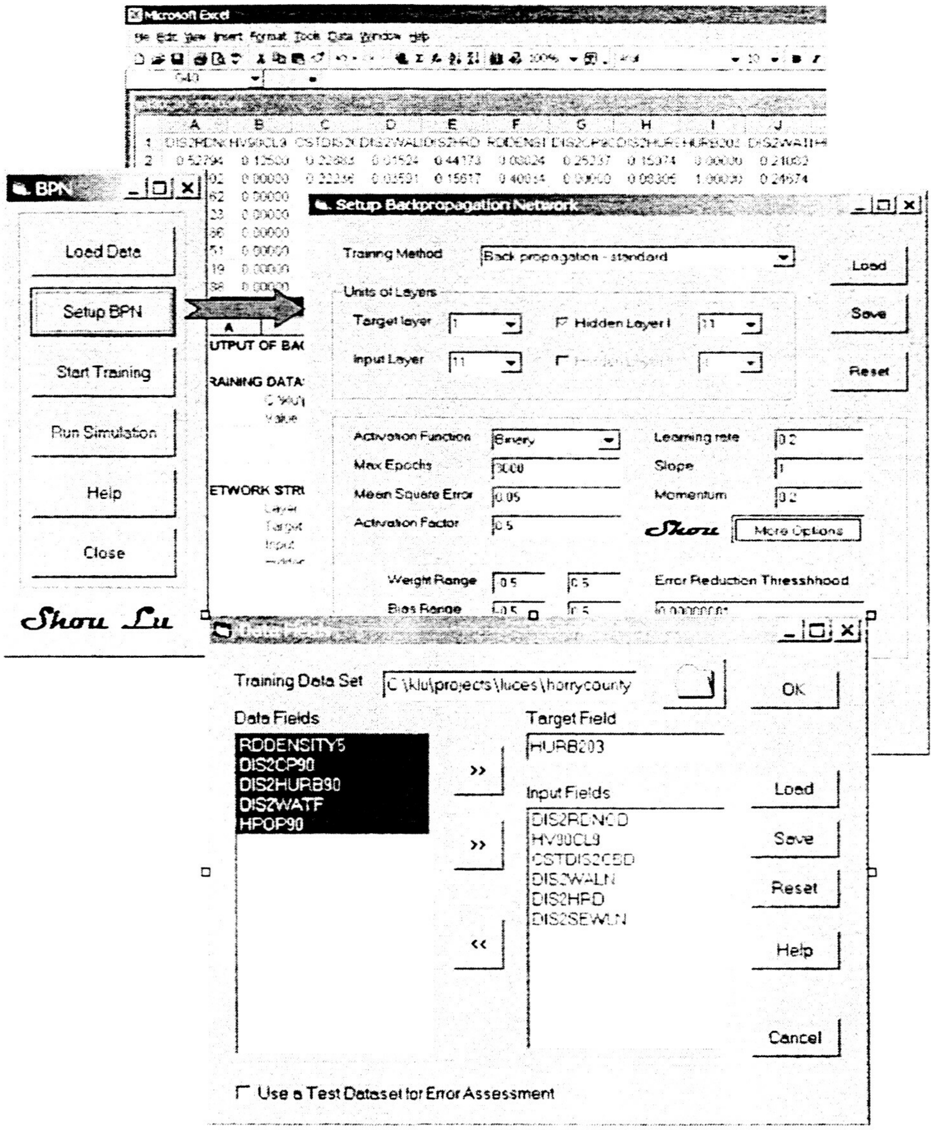

Training Method: Back propagation - standard

Units of Layers

Target layer: 1

Input Layer: 11

☑ Hidden Layer I: 11

☐ Hidden Layer II

Activation Function: Binary

Max Epochs: 3000

Mean Square Error: 0.05

Activation Factor: 0.5

Learning rate: 0.2

Slope: 1

Momentum: 0.2

Weight Range: -0.5 0.5

Bias Range: -0.5 0.5

Error Reduction Thresshhood: 0.00000001

Training Data Set: C:\klu\projects\luces\horrycounty

Data Fields:
RDDENSITY5
DIS2CP90
DIS2HURB90
DIS2WATF
HPOP90

Target Field: HURB203

Input Fields:
DIS2RDNCD
HV90CL9
CSTDIS2CBD
DIS2WALN
DIS2HRD
DIS2SEWLN

☐ Use a Test Dataset for Error Assessment

Figure 12. Sample graphic user interfaces of the neural network land use model.

Appendix A. Predicted urban growth in the BCD and BCJ regions

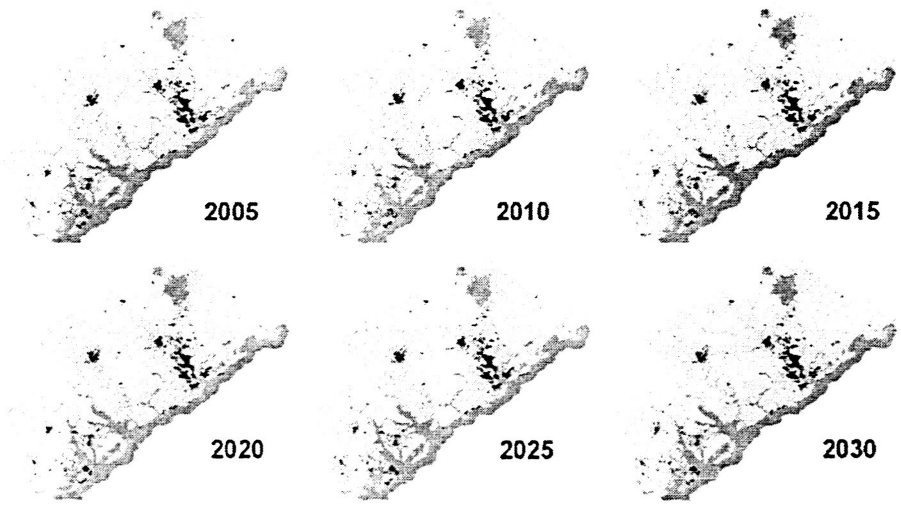

Figure 13. Predicted urban growth in the BCD (Berkeley, Charleston and Dorchester) and BCJ (Beaufort, Colleton and Jasper) regions of South Carolina, 2005-2030.

Figure 14. Predicted urban growth in 2030 in the BCD and BCJ region.